

**The Pennsylvania State University  
The Graduate School  
Department of Materials Science and Engineering**

**FABRICATION AND ELECTRICAL PROPERTIES OF  
TEXTURED  $\text{Sr}_{0.53}\text{Ba}_{0.47}\text{Nb}_2\text{O}_6$  CERAMICS PREPARED  
BY TEMPLATED GRAIN GROWTH**

**A Thesis in  
Materials Science and Engineering  
by**

**Cihangir Duran**

**© 2001 Cihangir Duran**

**Submitted in Partial Fulfillment  
of the Requirements  
for the Degree of**

**Doctor of Philosophy**

**December 2001**

**UMI Number: 3036024**

**UMI<sup>®</sup>**

---

**UMI Microform 3036024**

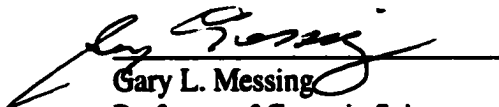
**Copyright 2002 by ProQuest Information and Learning Company.  
All rights reserved. This microform edition is protected against  
unauthorized copying under Title 17, United States Code.**

---

**ProQuest Information and Learning Company  
300 North Zeeb Road  
P.O. Box 1346  
Ann Arbor, MI 48106-1346**

We approve the thesis of Cihangir Duran:

Date of Signature



**Gary L. Messing**  
Professor of Ceramic Science and Engineering  
Thesis Co-Advisor  
Chair of Committee

August 20, 2001



**Susan Trolier-McKinstry**  
Associate Professor of Ceramic Science and Engineering  
Thesis Co-Advisor

Aug. 20, 2001



**Robert E. Newnham**  
Alcoa Professor Emeritus of Ceramic Science and Engineering

August 20, 2001



**L. Eric Cross**  
Evan Pugh Professor Emeritus of Electrical Engineering

August 20, 2001



**Clive A. Randall**  
Professor of Materials Science and Engineering

20 Aug 2001



**Long-Qing Chen**  
Associate Professor of Materials Science and Engineering  
Coordinator of Graduate Program  
Department of Materials Science and Engineering

Aug. 20, 2001

## ABSTRACT

$\text{Sr}_{0.53}\text{Ba}_{0.47}\text{Nb}_2\text{O}_6$  (SBN53) ceramics were textured by the templated grain growth (TGG), in a matrix of  $\text{SrNb}_2\text{O}_6$  and  $\text{BaNb}_2\text{O}_6$  powders. Acicular  $\text{KSr}_2\text{Nb}_5\text{O}_{15}$  (KSN) template particles, synthesized by a molten salt process, were used to texture the samples in the  $c$  direction (i.e., [001]). Template growth was assisted by adding  $\text{V}_2\text{O}_5$  as a liquid phase former for some compositions. The texture fraction also increased with higher sintering temperatures or times and with initial template concentration due to the preferential growth of the template particles.

When  $\text{V}_2\text{O}_5$  was present, SBN53 phase formation initiated on the KSN templates and texture development started at temperatures as low as  $950^\circ\text{C}$ . Phase formation in the  $\text{V}_2\text{O}_5$ -free samples, however, initiated in the matrix (i.e., independent of the KSN templates). The liquid phase adversely affected the template growth by favoring anisotropic grain growth in the matrix, which caused lower texture fraction and broader texture distribution in [001] at low template concentrations. Increased template-template interaction (e.g., tangling) during tape casting also resulted in broader texture distribution. Therefore, an optimum template content was found to be  $\sim 10\text{-}15$  wt%. However, a texture fraction of 0.93 to 0.98 was obtained using only 5 wt% templates when anisotropic matrix grain growth was prevented.

Phase evolution was studied in the randomly oriented samples as a function of quenching temperature, heating rate, and liquid phase, using KSN powder (rather than acicular particles) as a seed material. The formation temperature for SBN53 was lowered substantially by adding more seeds, decreasing the heating rate, and introducing a liquid.

The temperature decreased from 1260°C for the samples with no seeds to 1130°C for the samples with 15.4 wt% seeds + 0.8 mol % V<sub>2</sub>O<sub>5</sub> at a heating rate of 4 °C/min. For the V<sub>2</sub>O<sub>5</sub>-free samples, the activation energy was considerably lowered from 554 ± 15 kJ/mol for the samples with no seeds to 241 ± 17 kJ/mol for the samples with 15.4 wt% seeds.

The dielectric and piezoelectric properties were enhanced in samples with better orientation (i.e., high texture fraction ( $f$ ) and narrow degree of orientation parameter ( $r$ ) in the texture direction). The presence of nonferroelectric phases (V<sub>2</sub>O<sub>5</sub> or Nb<sub>2</sub>O<sub>5</sub>-based) at the grain boundaries suppressed the observed dielectric properties, especially at the transition temperature. Therefore, the maximum dielectric constant,  $K_{33}$ , was 7,900 in the V<sub>2</sub>O<sub>5</sub>-containing and 23,600 in the V<sub>2</sub>O<sub>5</sub>-free samples, both of which are low compared to single crystal ( $K_{33} = 81,000$ ). The ferroelectric transition temperature was found to be higher than that of SBN50 single crystals due to filling of interstitial sites with K<sup>+</sup> ions from the KSN templates and V<sup>5+</sup> ions from the liquid phase former. Dielectric spectra showed normal ferroelectric behavior for the V<sub>2</sub>O<sub>5</sub>-containing and weak relaxor behavior for the V<sub>2</sub>O<sub>5</sub>-free samples.

A model was developed to correlate the processing parameters (i.e.,  $f$  and  $r$ ) to the polarization. It was found that the remanent polarization ( $P_r$ ) increased sharply (after  $f = 0.5$ ) when the charge transfer (via percolation) between elongated grains was effectively established.

Polarization fatigue, caused by charge accumulation at defects such as grain boundaries and domain walls, decreased the remanent polarization on successive application of the field in the V<sub>2</sub>O<sub>5</sub>-free samples. V<sub>2</sub>O<sub>5</sub>-containing samples, however, did not experience any evidence of polarization fatigue due to more uniform cation

distribution. However, some samples showed aging in the form of “pinched” loops during polarization reversal, which was eliminated by increasing the number of driving field cycles.

The best room temperature electrical properties obtained in the  $c$  (polar) direction of TGG samples are the remanent polarization ( $P_r$ ) of  $20.3 \mu\text{C}/\text{cm}^2$ , an estimated saturation polarization ( $P_s$ ) of  $24 \mu\text{C}/\text{cm}^2$  (69-96% of single crystal), and the piezoelectric charge coefficient ( $d_{33}$ ) of  $88 \text{ pC}/\text{N}$  (80-98% of single crystal).

## TABLE OF CONTENTS

<b>LIST OF FIGURES</b>	<b>ix</b>
<b>LIST OF TABLES</b>	<b>xiv</b>
<b>ACKNOWLEDGEMENTS</b>	<b>xv</b>
<b>CHAPTER 1. STATEMENT OF THE PROBLEM AND</b>	
<b>THESIS ORGANIZATION</b>	<b>1</b>
1.1 STATEMENT OF THE PROBLEM	1
1.2 RESEARCH OBJECTIVES	3
1.3 THESIS ORGANIZATION	3
1.4 REFERENCES	5
<b>CHAPTER 2. INTRODUCTION AND BACKGROUND</b>	<b>7</b>
2.1 TEMPLATED GRAIN GROWTH	7
2.1.1 Application of Textured Microstructures	11
2.1.2 Requirements for TGG	12
2.1.3 Kinetics of Exaggerated Grain Growth	13
2.2 TUNGSTEN BRONZE (TB) STRUCTURE FAMILY	16
2.3 TEXTURED CERAMICS WITH TB STRUCTURE	19
2.4 PHASE FORMATION AND SINTERING OF SBN CERAMICS	22
2.5 REFERENCES	25
<b>CHAPTER 3. TEMPLATE PARTICLE SYNTHESIS IN THE</b>	
<b>SrO-Nb<sub>2</sub>O<sub>5</sub>-BaO SYSTEM</b>	<b>32</b>
3.1 INTRODUCTION	32
3.2 EXPERIMENTAL PROCEDURE	34
3.3 RESULTS AND DISCUSSION	35
3.3.1 Effect of Molten Salt Composition	35
3.3.2 Molten Salt Synthesis in KCl	36
3.3.3 Molten Salt Synthesis in SrCl <sub>2</sub> ·6H <sub>2</sub> O	41
3.3.4 Physical Separation of Anisotropic Particles	44
3.4 CONCLUSIONS	48
3.5 REFERENCES	49

<b>CHAPTER 4. REACTIVE SINTERING OF <math>\text{Sr}_{0.53}\text{Ba}_{0.47}\text{Nb}_2\text{O}_6</math> CERAMICS</b>	<b>52</b>
4.1 INTRODUCTION	52
4.2 EXPERIMENTAL PROCEDURE	54
4.3 RESULTS AND DISCUSSION	57
4.3.1 Densification and Reaction Kinetics in the Quenched Samples	57
4.3.1.1 Densification Behavior	57
4.3.1.2 Phase Formation	59
4.3.1.3 Reaction Kinetics	69
4.3.2 Densification and Microstructure Evolution in the Sintered Samples	72
4.3.2.1 Densification	72
4.3.2.2 Microstructure Evolution	76
4.4 CONCLUSIONS	81
4.5 REFERENCES	83
<b>CHAPTER 5. TEMPLATED GRAIN GROWTH OF <math>\text{Sr}_{0.53}\text{Ba}_{0.47}\text{Nb}_2\text{O}_6</math> CERAMICS WITH <math>\text{V}_2\text{O}_5</math> ADDITIVES</b>	<b>86</b>
5.1 INTRODUCTION	86
5.2 EXPERIMENTAL PROCEDURE	87
5.3 RESULTS AND DISCUSSION	93
5.3.1 Densification and Texture Development	93
5.3.2 Electrical Properties	111
5.3.2.1 Dielectric Properties	111
5.3.2.2 Switching, Piezoelectric, and Pyroelectric Properties	118
5.4 CONCLUSIONS	126
5.5 REFERENCES	129
<b>CHAPTER 6. TEMPLATED GRAIN GROWTH OF <math>\text{Sr}_{0.53}\text{Ba}_{0.47}\text{Nb}_2\text{O}_6</math> CERAMICS WITHOUT <math>\text{V}_2\text{O}_5</math> ADDITIVES</b>	<b>132</b>
6.1 INTRODUCTION	132
6.2 EXPERIMENTAL PROCEDURE	133
6.3 RESULTS	135
6.3.1 Densification and Phase Formation	135
6.3.2 Texture Development	137
6.3.3 Electrical Properties	147
6.3.3.1 Dielectric Properties	147
6.3.3.2 Switching and Piezoelectric Properties	151
6.4 DISCUSSION	155



6.4.1 Densification and Phase Formation	155
6.4.2 Texture Development	161
6.4.3 Electrical Properties	167
6.4.3.1 Dielectric Properties	167
6.4.3.2 Switching and Piezoelectric Properties	170
6.5 CONCLUSIONS	177
6.6 REFERENCES	181
<b>CHAPTER 7. SUMMARY AND FUTURE WORK</b>	<b>186</b>
7.1 SUMMARY	186
7.1.1 Template Particle Synthesis	186
7.1.2 Reactive Sintering of $\text{Sr}_{0.53}\text{Ba}_{0.47}\text{Nb}_2\text{O}_6$ Ceramics	187
7.1.3 Templated Grain Growth of $\text{Sr}_{0.53}\text{Ba}_{0.47}\text{Nb}_2\text{O}_6$ Ceramics	189
7.1.4 Electrical Properties of Textured $\text{Sr}_{0.53}\text{Ba}_{0.47}\text{Nb}_2\text{O}_6$ Ceramics	190
7.2 FUTURE WORK	192
7.2.1 Templated Grain Growth	192
7.2.2 Texture Characterization	192
7.2.3 Modeling of Electrical Properties	193
7.3 REFERENCES	196
<b>APPENDIX A: DETERMINATION OF CORRECTION FACTORS</b>	
<b>FOR STEREOLOGICAL ANALYSIS</b>	<b>197</b>
<b>APPENDIX B: AN EQUATION TO MODEL THE CORRELATION</b>	
<b>BETWEEN THE ELECTRICAL PROPERTIES AND</b>	
<b>PROCESSING PARAMETERS</b>	<b>200</b>

## LIST OF FIGURES

2.1	Texture development by TGG in a polycrystalline body.	9
2.2	Growth of a single crystal in a polycrystalline body by TGG.	10
2.3	Template growth based on Hennings' model.	14
2.4	Projection of tungsten bronze structure.	17
3.1	XRD pattern (top) and SEM micrograph (bottom) of SBN50 needles from a KCl+(S+B+N)50 mixture (R = 1) heat treated at 1100°C for 4 h (CR = 1). Peaks are indexed to the SBN50 composition.	37
3.2	Temperature-time diagram for the KCl+SN system (R = 1 and CR = 2). SN is SrNb <sub>2</sub> O <sub>6</sub> , KSN is KSr <sub>2</sub> Nb <sub>5</sub> O <sub>15</sub> , and SN* is Sr <sub>2</sub> Nb <sub>2</sub> O <sub>7</sub> . The ratio given is KSN/SN/SN*.	39
3.3	Phase and morphology evolution in KCl + SN system; (a) 900°C, (b) 1025°C, (c) 1050°C, and (d) 1100°C for 4 h. R = 1 and CR = 2.	40
3.4	Temperature-time diagram for the SrCl <sub>2</sub> · 6H <sub>2</sub> O + Nb <sub>2</sub> O <sub>5</sub> system (R = 2 and CR = 2). SN is SrNb <sub>2</sub> O <sub>6</sub> and SN* is Sr <sub>2</sub> Nb <sub>2</sub> O <sub>7</sub> . Ratio is SN/SN*.	42
3.5	Phase and morphology evolution in the SrCl <sub>2</sub> · 6H <sub>2</sub> O + Nb <sub>2</sub> O <sub>5</sub> system; (a) 4 h and (b) 8 h at 1050°C. R = 2 and CR = 2.	43
3.6	Effect of physical separation on the particles synthesized at 1100°C for 6 h ; (a) As-synthesized, (b) sediment, and (c) supernatant particles. R = 1 and CR = 2.	45
3.7	XRD pattern (top) and SEM micrograph (bottom) of KSN needles (sediment) from KCl + SN mixture (R = 1.25) heat treated at 1100°C for 6 h (CR = 2). Peaks are indexed to the KSN composition.	47
4.1	Densification graphs as a function of composition. Heating rate is 7°C/min.	58
4.2	Phase evolution in the RV0 samples as a function of quenching temperature. Heating rate is 4°C/min. • → SBN53, S → SN, B → BN, U → Unknown. α is given in %.	60

4.3	Phase evolution in the samples quenched from 1100°C. Heating rate is 4°C/min. • → SBN53, S → SN, B → BN, U → Unknown.	62
4.4	SrNb <sub>2</sub> O <sub>6</sub> (SN)-BaNb <sub>2</sub> O <sub>6</sub> (BN) binary phase diagram.	64
4.5	SBN53 formation ( $\alpha$ ) as a function of KSN content and heating rate.	66
4.6	SBN53 formation as a function of KSN content at a heating rate of 4°C/min.	68
4.7	Plot of $\ln(\beta \cdot (d\alpha/dT))$ vs. $1/T$ for the R0 samples as a function of $\alpha$ and $\beta$ .	70
4.8	Plot of $\ln(\beta \cdot (d\alpha/dT))$ vs. $1/T$ as a function of heating rate at a constant $\alpha = 50$ .	71
4.9	Densification graphs of the sintered samples as a function of (a) sintering temperature and (b) time. $\beta = 7$ °C/min.	73
4.10	Microstructure development in the V <sub>2</sub> O <sub>5</sub> -containing samples sintered at 1400°C for 4h; (a) RV0, (b) RV5, and (c) RV15.	77
4.11	Microstructure evolution in the R0 (left column) and R15 (right column) samples as a function of sintering temperature; (a and b) 1200°C, (c and d) 1300°C, and (e and f) 1400°C for 4 h.	78
4.12	Microstructure evolution in the R0 (left column) and R15 (right column) samples as a function of sintering time; (a and b) 1 min, (c and d) 12 h at 1400°C.	79
5.1	Sectioning of samples from sintered pieces.	89
5.2	(a) $\theta - 2\theta$ scan (e.g., standard XRD) and (b) $\omega$ scan (for rocking curve).	92
5.3	Densification graphs of the samples as a function of sintering time at 1400°C.	94
5.4	XRD patterns of the TV15 <sub>L</sub> samples after sintering for 4 h at; (b) 950°C, (c) 1100°C, (d) 1200°C, and (e) 1300°C. Curve "a" is for the random sample (heated at 1250°C for 5 h) and is given as an untextured reference pattern. Major SBN53 peaks are marked.	96
5.5	SEM pictures of the TV15// samples after sintering for 4 h; (a) 950°C, (b) 1200°C, (c) 1300°C, and (d) 1400°C.	97

5.6	SEM micrographs of the samples sintered at 1400°C for 4h; (a) TV5, (b) TV9, (c) TV12, (d) TV15, (e) TV5-9, and (f) TV5-15.	99
5.7	Effect of temperature on $K^+$ homogenization in TV15// samples after sintering 4h. (Bar = 20 $\mu\text{m}$ ).	103
5.8	Texture fraction ( $f$ ), calculated using the Lotgering factor, as a function of sintering temperature.	105
5.9	Orientation distribution curves for the $\perp$ -cut samples sintered at 1400°C for 4 h. The curves are March-Dollase fits to the corrected rocking curve data.	109
5.10	Density vs. texture fraction by the Lotgering factor.	110
5.11	(a) Temperature and crystallographic direction dependence of dielectric constant for the sample TV15, (b) dielectric loss in the $c$ direction ( $\perp$ cut), and (c) in the $a$ - $b$ plane ( $//$ cut). Random sample is RV15.	112
5.12	Dielectric constant as a function of sintering time for the TV5-9 $\perp$ samples. Samples were sintered at 1400°C.	114
5.13	Average $K_{\text{max}}$ as a function of initial template content and texture fraction (by the Lotgering factor) for the $\perp$ -cut samples.	116
5.14	Temperature dependence of the dielectric constant for samples sintered at 1400°C for 4h.	117
5.15	Change of average remanent polarization ( $P_r$ ) as a function of initial template content in the $c$ direction. Samples were sintered at 1400°C for 4 h.	119
5.16	P-E graph of the samples sintered at 1400°C for 4h. Random sample is RV15.	121
5.17	Change in the remanent polarization ( $P_r$ ) as a function of initial template content and texture fraction (by the Lotgering factor) for the $\perp$ -cut samples.	123
5.18	Change in the piezoelectric charge coefficient ( $d_{33}$ ) as a function of initial template content and texture fraction (by the Lotgering factor) for the $\perp$ -cut samples.	124

5.19	Pyroelectric coefficient as a function of temperature and crystallographic direction in the TV15 samples sintered 1400°C for 4 h. The random sample is RV15.	125
6.1	Densification of samples as a function of template concentration.	136
6.2	XRD patterns of the T9 $\perp$ samples after sintering for 4 h at; (b) 1200°C, (c) 1300°C, and (d) 1400°C. Curve “a” is for the random sample (heated at 1250°C for 5 h) and given as a untextured reference pattern. Major SBN53 peaks are marked.	138
6.3	Texture development in the T9// samples as a function of sintering conditions; (a) 1200°C for 4 h, (b) 1300°C for 4 h, (c) 1400°C for 1 min, and (d) 1400°C for 4 h.	139
6.4	Texture development as a function of template concentration after sintering at 1400°C for 12 h; (a) T5//, (b) T9//, (c) T12//, (d) T15//, and (e) T5-15//.	141
6.5	Texture fraction ( $f$ ), calculated using the Lotgering factor, as a function of (a) sintering temperature and (b) time.	145
6.6	Orientation distribution curves for the $\perp$ -cut samples sintered at 1400°C for 12 h. The curves are March-Dollase fits to the corrected rocking curve data.	146
6.7	Dielectric constant (a) and loss (b) as a function of sintering time and crystallographic (polar $c$ and nonpolar $a$ or $b$ ) direction for the T9 samples. Samples were sintered at 1400°C. The inset in (a) gives the data for measurements in the $a$ - $b$ plane.	148
6.8	Average $K_{\max}$ as a function of initial template content and texture fraction (by the Lotgering factor) for the $\perp$ -cut samples. Samples are $\geq 95\%$ dense.	150
6.9	Plot of $K_{\max}/K$ vs. $(T-T_{\max})^\gamma$ , with calculated values of degree of diffuseness ( $C/K_{\max}$ in °C), as a function of sintering conditions for the T9 $\perp$ samples. $f$ and $\gamma$ stand for the texture fraction and diffuseness coefficient, respectively.	152

6.10	Change of average remanent polarization ( $P_r$ ) as a function of initial template content in the $c$ direction; (a) Type A and (b) Type B. Samples were sintered at 1400°C for 12 h.	153
6.11	P-E hysteresis loops of the T5-15 samples sintered at 1400°C for 12 h and random (R15) sample sintered at 1350°C for 4 h.	154
6.12	(a) Change of average $P_r$ (Type B) as a function of initial template content and $f$ (by the Lotgering factor) and (b) normalized $P_r$ as a function of $f$ for the $\perp$ -cut samples. Samples are $\geq 95\%$ dense.	156
6.13	Change of average piezoelectric charge coefficient ( $d_{33}$ ) as a function of initial template content and texture fraction (by the Lotgering factor) for the $\perp$ -cut samples. Samples are $\geq 95\%$ dense.	158
6.14	Density vs. texture fraction (by the Lotgering factor) for the samples sintered at $1200 < T < 1450^\circ\text{C}$ for 1 min to 12 h.	165
7.1	Textured grain length (from stereological analysis) vs. texture fraction (from the Lotgering factor).	195
7.2	$D(\text{gb}) / K(\text{gb})$ vs. texture fraction for the V <sub>2</sub> O <sub>5</sub> -free and V <sub>2</sub> O <sub>5</sub> -containing samples. $\blacktriangle$ : T5 or TV5, $\blacklozenge$ : T15 or TV15, and $\blacksquare$ : T5-15 or TV5-15.	195

## LIST OF TABLES

2.1	The piezoelectric and electro-optic properties of tungsten bronze crystals.	20
4.1	Sample designation, KSN content, and additive contribution in SBN53.	56
4.2	Change in the diffraction angle ( $2\theta$ ) of the main peak (311) of the SBN.	65
5.1	Sample name, KSN concentration, and amount of $K_2O$ and $Nb_2O_5$ in SBN53. All samples have 0.8 mol % (0.37 wt%) $V_2O_5$ .	90
5.2	Summary of the average dimensions and texture for the TV9 and TV15 samples sintered between 1200°C and 1450°C.	106
5.3	Comparison of room temperature polarization values in the SBN ceramic literature.	122
5.4	The average room temperature dielectric and piezoelectric properties for random and textured samples sintered at 1400°C for 4 h.	127
6.1	Sample designation, KSN content, and additive contribution in SBN53 ceramics without $V_2O_5$ addition.	134
6.2	Summary of average dimensions as a function of sintering conditions and template concentration.	143
6.3	Estimated matrix composition before KSN-SBN solid solution formation starts.	162
6.4	Summary of processing (i.e., $f$ and $r$ ) and $P_r$ values used in Figure 6.12a for the $V_2O_5$ -free samples.	172
6.5	The average room temperature dielectric and piezoelectric properties for random and textured samples sintered at 1400°C for 12 h.	178

## **ACKNOWLEDGEMENTS**

I am grateful to Dr. Messing and Dr. McKinstry for their help, guidance, and patience in the last 5 years. They taught me how to solve the critical problems and do a job excellent. They have strongly encouraged me to develop my research skills.

I would like to thank my committee members, Dr. R. E. Newnham, Dr. L. E. Cross, and Dr. C. A. Randall, for their time, interest, and thoughtful questions and suggestions.

I thank Turkish Government (and Gebze Institute of Technology) for financially supporting me throughout my Ph.D. study.

I would like to thank all my friends from Turkey, Korea, India, China, the USA, and from other nations. Without them, I am sure that the life was going to be so boring in State College. I hope our friendships will last forever. In particular, I thank Huseyin Yilmaz for his help in modeling and Ed Sabolsky for his critical comments (and being the one who understands me). Koray Ozturk also deserves thanks for cutting my hair in the last 5 years. I am also grateful to MRL staff (Leah, Paul, Beth, Tim, Scott, Maria, Jeff, and many others) for making everything work well and in time.

My dad and mom, Ismet and Gulseren Duran, and my brother Cihan Duran have always had complete confidence in me and supported all the time. To me, this is the best gift to them.

Last, but definitely not least, I should thank my wife Sukran Duran for her patience, help, and love, and my daughter Irem Duran for being lovely all the time and sitting on my shoulders while I was writing my thesis.



## CHAPTER 1

### STATEMENT OF THE PROBLEM AND THESIS ORGANIZATION

#### 1.1 STATEMENT OF THE PROBLEM

The physical properties of materials can be optimized by controlling the microstructure. The conventional approach in ceramics has been to fabricate microstructures with small, equiaxed grains to obtain reproducibility, reliability, and predictability of properties in the fabrication of a large number of parts. Although most inorganic crystals exhibit anisotropy in structure, habit, and properties, property averaging in a randomly oriented ceramic prevents the harnessing of useful anisotropy observed in the single crystal form. This problem is most pronounced in materials with low symmetry crystal structures.

The tungsten bronze ferroelectrics are useful for electro-optic, piezoelectric, pyroelectric, millimeter wave, and photorefractive applications [1,2].  $\text{Sr}_{0.75}\text{Ba}_{0.25}\text{Nb}_2\text{O}_6$  (SBN75) single crystals have some of the largest known linear electrooptic coefficients [2,3]. Particularly, the application of optical phase conjugators for adaptive optics is important for high-power laser or microwave systems [4,5]. At the paraelectric to ferroelectric phase transition, one unique fourfold axis exists and  $180^\circ$  ferroelectric domain walls form during cooling (e.g., non- $180^\circ$  domain walls are absent) [6,7]. Therefore, high transverse fields can be applied without depoling tungsten bronze compositions such as  $\text{Sr}_{2-x}\text{Ca}_x\text{NaNb}_5\text{O}_{15}$  (SCNN),  $\text{Sr}_x\text{Ba}_{1-x}\text{Nb}_2\text{O}_6$  (SBN), and  $\text{Ba}_{2-x}\text{Sr}_x\text{K}_{1-y}\text{Na}_y\text{Nb}_5\text{O}_{15}$  (BSKNN). This means that a very high drive field can be applied

for shear mode transduction with the low loss levels, and, thus, these materials can be used for high power shear mode actuators [6].

Despite the recent progress in growing high quality tungsten bronze single crystals [2,8], the use of single crystals has been limited because of low mechanical strength, difficulty in fabrication, the presence of defects (e.g. striation bands) and compositional fluctuations, and a high price. Therefore, if SBN ceramics with properties close to single crystal values are fabricated, ceramics would be advantageous due to their ease of fabrication and shaping, thermal and stress resistance, and cost-effectiveness.

Abnormal grain growth and the high calcination temperatures of SBN ceramics with high Sr content make conventional sintering (e.g., of precalcined SBN powder) of SBN ceramics difficult [9]. Dense SBN ceramics were obtained by reactive sintering [10] but they show properties inferior to the single crystals because of the random orientation of grains.

Ceramics with preferred crystallographic orientation (i.e. texture) are known to have improved electrical and electromechanical properties in certain orientations. While processing of grain-oriented (or textured) tungsten bronze ceramics such as SBN30–SBN65 [11],  $\text{Pb}_{0.60}\text{Ba}_{0.40}\text{Nb}_2\text{O}_6$  [12], and  $\text{KSr}_2\text{Nb}_5\text{O}_{15}$  (KSN) [13] has been done by hot pressing and hot-forging, the resulting ceramics are limited by restrictions on the product shape, small production scale, high cost, and, in most cases, limited texture.

As an alternative to techniques such as hot pressing and hot forging, templated grain growth (TGG) is a pressureless sintering technique for inducing grain orientation in bulk, polycrystalline materials. The process entails providing a dense, fine-grained matrix for the growth of oriented, anisotropically-shaped (i.e. fiber, whisker, or platelet)

template particles dispersed in the matrix. By orienting the grains in the *c* direction using template particles, it should be possible to achieve improved directionally dependent electrical properties. It is expected that materials with a high degree of texture should have properties that are similar to those of single crystals of the same composition.

## **1.2 RESEARCH OBJECTIVES**

The primary objectives of this study are to develop high quality textured  $\text{Sr}_{0.53}\text{Ba}_{0.47}\text{Nb}_2\text{O}_6$  (SBN53) ceramics by templated grain growth (TGG), to measure the electrical properties as a function of crystallographic orientation (e.g., in the non-polar *a* (or *b*) and polar *c* directions), and finally, to develop processing-property relations for the textured samples. Samples with equiaxed grains and single crystals of similar compositions will be used to compare to the textured samples.

## **1.3 THESIS ORGANIZATION**

The availability of single crystal template particles is a key element in the fabrication of grain-oriented SBN53 ceramics by TGG. Therefore, acicular  $\text{KSr}_2\text{Nb}_5\text{O}_{15}$  (KSN) template particles were synthesized by molten salt synthesis (MSS). The reaction sequence and the effect of processing parameters such as salt to powder ratio, reaction temperature and time, and cooling rate on the morphology and phase-purity of the resulting particles are discussed in Chapter 3. It is also shown that physical separation of as-synthesized template particles by their differential settling rates in water helps separate the templates less than  $\sim 10 \mu\text{m}$  in length, which enables better orientation during tape casting.

In Chapter 4, the densification and kinetics of SBN53 phase formation in random samples (e.g., prepared with KSN powder additions instead of KSN templates) were described as a function of the KSN powder content, the presence and amount of a liquid phase (e.g.,  $V_2O_5$ ,  $Nb_2O_5$ ), and sintering conditions.  $V_2O_5$  was added to form a liquid at lower temperatures (the melting temperature is  $690^\circ\text{C}$ ). For the  $V_2O_5$ -free compositions, a liquid formed at  $\sim 1260\text{-}1350^\circ\text{C}$  due to excess  $Nb_2O_5$ , depending on the KSN seed content. The impact of the introduction of isostructural KSN seeds on the activation energy for phase formation was investigated. In addition, the intrinsic anisotropic grain growth in SBN53 is described in this chapter. An understanding of the requirements for grain growth enables careful control of TGG and the results obtained from the random samples form the basis for subsequent TGG experiments.

Chapters 5 and 6 are based on TGG and the electrical properties of SBN53 ceramics as a function of initial template concentration. Alignment of template particles in a fine matrix was achieved by tape casting, which gave rise to an axisymmetric (i.e., fiber) texture along the crystallographic  $c$  direction. Template growth was investigated as a function of sintering time and temperature. The amount of texture was determined by the Lotgering factor and stereology, and the distribution in the texture (e.g.,  $[001]$ ) direction was characterized by rocking curves. The dielectric and piezoelectric properties were measured in the polar  $c$  direction and in the non-polar  $a$ - $b$  plane, and then correlated with the texture fraction, degree of orientation, and grain boundary phases. Processing-property relation was developed by taking the polarization and texture distribution functions into account.

## **1.4 REFERENCES**

- 1 - S. N. Murty, K.V. R. Murty, K. C. Mouli, A. Bhanumathi, S. B. Raju, G. Padmavathi, and K. L. Murty, "Relaxor behavior in certain tungsten bronze ceramics", *Ferroelectrics*, 158, 325-330 (1994)**
- 2 - R. R. Neurgaonkar, W. K. Cory, J. R. Oliver, E. J. Sharp, G. L. Wood, and G. J. Salamo, "Growth and optical properties of ferroelectric tungsten bronze crystals," *Ferroelectrics*, 142, 167-88 (1993)**
- 3 - P. V. Lenzo, E. G. Spencer, and A. A. Ballman, "Electrooptic coefficients of ferroelectric strontium barium niobate," *Appl. Phys. Lett.*, 11, 23-24 (1967)**
- 4- C. R. Giuliano, "Applications of optical phase conjugation," *Phys. Today*, 34, 27-35 (1981)**
- 5- J. Feinberg, "Photorefractive nonlinear optics," *Phys. Today*, 41, 46-52 (1988)**
- 6- R. R. Neurgaonkar, J. R. Oliver, W. K. Cory, L. E. Cross, and D. Viehland, "Piezoelectricity in tungsten bronze crystals," *Ferroelectrics*, 160, 265-76 (1994)**
- 7- C. A. Randall, R. Guo, A. S. Bhalla, and L. E. Cross, "Microstructure-property relations in tungsten bronze lead barium niobate,  $Pb_{1-x}Ba_xNb_2O_6$ ," *J. Mater. Res.*, 6[8], 1720-28 (1991)**
- 8- R. R. Neurgaonkar, W. K. Cory, J. R. Oliver, M. Khoshnevisan, and E. J. Sharp, "Ferroelectric tungsten bronze crystals and their photorefractive applications," *Ferroelectrics*, 102, 3-14 (1990)**
- 9- N. S. VanDamme, A. E. Sutherland, L. Jones, K. Bridger, and S. R. Winzer, "Fabrication of optically transparent and electrooptic strontium barium niobate ceramics," *J. Am. Ceram. Soc.*, 74[8], 1785-92 (1991)**

- 10- W- J. Lee and T- T. Fang, "Densification and microstructural development of the reaction sintering of strontium barium niobate," *J. Am. Ceram. Soc.*, 81[4], 1019-24 (1998)
- 11- K. Nagata, Y. Yamamoto, H. Igarashi, and K. Okazaki, "Properties of the hot-pressed strontium barium niobate ceramics," *Ferroelectrics*, 38, 853-56 (1981)
- 12 - R. R. Neurgaonkar, J. R. Oliver, J. G. Nelson, and L. E. Cross, "Piezoelectric and ferroelectric properties of La-modified and unmodified tungsten bronze  $\text{Pb}_{0.60}\text{Ba}_{0.40}\text{Nb}_2\text{O}_6$  dense ceramics," *Mat. Res. Bull.*, 26, 771-77 (1991)
- 13 - T. Kimura, S. Saiubol, and K. Nagata, "Effect of grain orientation on the Curie temperature of  $\text{KSr}_2\text{Nb}_2\text{O}_{10}$  solid solutions," *J. Ceram. Soc. Japan, Int. Ed.*, 103[2], 132-37 (1995)

## **CHAPTER 2**

### **INTRODUCTION AND BACKGROUND**

#### **2.1 TEMPLATED GRAIN GROWTH**

In many cases, single crystals with useful piezoelectric, ferroelectric, optical, and superconducting properties have not been exploited because of the difficulty or high cost of conventional crystal growth techniques [1,2]. However, some materials lose their useful properties in randomly oriented polycrystalline ceramics. Sometimes, microstructures with randomly oriented anisotropic grains have been utilized to improve the properties, as in the case of  $\text{Si}_3\text{N}_4$  ceramics [3,4]. Anisotropic grain growth has been attributed either to anisotropic surface energies of different crystal planes that result from an anisotropic crystal structure or the poisoning of a few crystallographic planes by impurities that results in anisotropic grain boundary mobilities [5,6].

Several recent studies have focused on aligning (i.e., texturing) anisotropic grains to access anisotropic single crystal properties in polycrystalline ceramics. The shear forming of slurries that contain only anisotropically shaped particles (e.g., fiber, whisker, or platelet) results in highly oriented green bodies that produce strongly textured materials after sintering [7,8]. However, anisotropic particles do not pack very well during forming and inhibit densification by creating rigid networks (e.g., constrained sintering); therefore, pressure (hot pressing and sinter forging) or a liquid phase is required to attain high density.

Templated grain growth (TGG) is a relatively new, pressureless sintering technique for inducing grain orientation in bulk, polycrystalline materials. TGG entails

providing a dense, fine-grained matrix for the growth of oriented template particles dispersed in the matrix. Because template particles are separated by a matrix powder, rigid template networks do not form. Textured microstructures can be achieved by applying a field gradient (e.g., mechanical [9], magnetic [10], or temperature [11]) during fabrication. Common methods to apply a shear field to the slurry or matrix and align the templates are hot-forging [12], hot pressing [13], tape casting [9], dry pressing [14] and slip casting [15]. Texture development in a polycrystalline body is schematically presented in Figure 2.1 The initial microstructure consists of large template particles oriented in a fine matrix. In many cases, early microstructure development is characterized primarily by template elongation. When the template growth in the longitudinal direction is stopped (for example by impingement), growth continues in the thickness direction, which leads to thickening of the elongated grains.

Currently, the most prevalent commercial technique for producing high quality ferroelectric single crystals is top-seeded solution growth [2,16]. However, this method requires long periods of time at high temperature and careful control of complex processes (e.g. cooling rate, seed rotation rate, and atmosphere) which affect the quality of grown crystals and therefore result in high costs. TGG is also an alternative process for growing large single crystals. It involves contacting a single crystal "template" to a sintered polycrystalline matrix and then heating the assemblage to a temperature that promotes the migration of the single crystal boundary through the matrix. Single crystals of millimeter size can be grown by this method. Growing single crystals by TGG is schematically shown in Figure 2.2. When the seed crystal and the matrix are brought into contact, a single crystal with the same orientation as the seed crystal is produced by



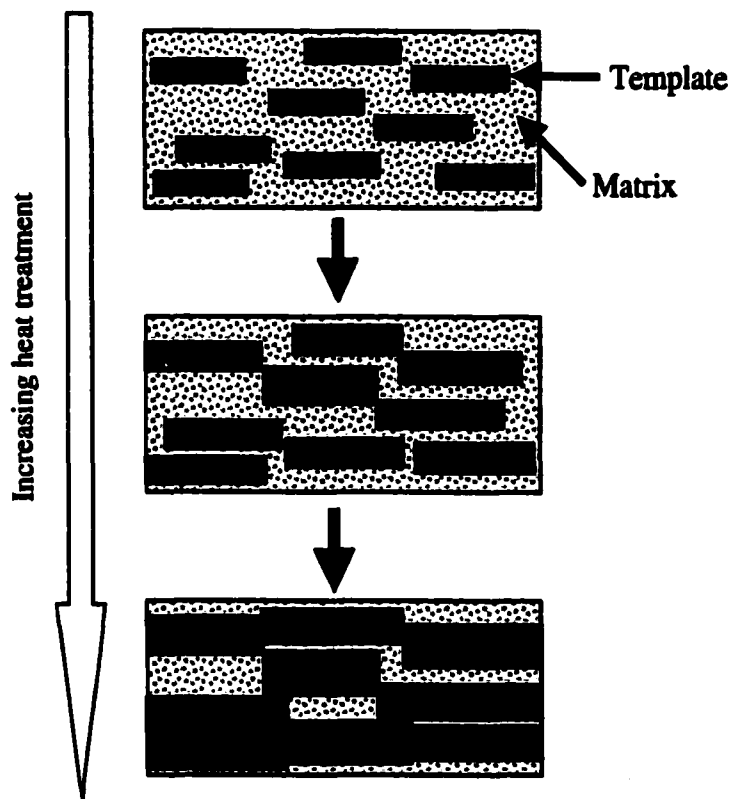
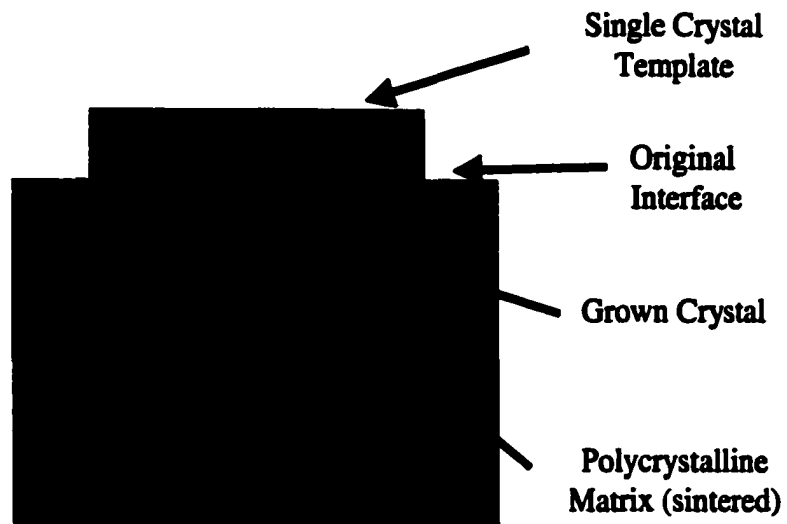


Figure 2.1 Texture development by TGG in a polycrystalline body.



**Figure 2.2 Growth of a single crystal in a polycrystalline body by TGG.**

directional growth of the interface into the polycrystalline matrix. The impetus for boundary migration comes from the grain boundary free energy, which increases with decreasing grain size [17,18]. Therefore, the grain size of the matrix plays an important role in successful crystal growth.

The TGG approach can be either homoepitaxial, in which the growing single crystal or textured ceramic has the same composition and crystal structure as the template material, or heteroepitaxial when the template material differs from the matrix materials [19,20].

### **2.1.1 Application of Textured Microstructures**

Textured ceramics hold promise for improved structural and functional properties. For example, the poling efficiency of textured ferroelectric ceramics, particularly in systems where the number of possible polarization directions is low, can be improved considerably [20]. The critical current density in superconductors [21] and ionic conductivity in  $\beta''$ -alumina [22] were enhanced by texturing. A fracture toughness of 6.3  $\text{MPa}\cdot\text{m}^{1/2}$  in textured  $\text{Al}_2\text{O}_3$  perpendicular to the basal surface was obtained compared to 3-4  $\text{MPa}\cdot\text{m}^{1/2}$  for equiaxed, fine-grained  $\text{Al}_2\text{O}_3$  [23]. Toughness increases due to crack deflection and bridging by the aligned anisotropic grains. TGG has been used to produce textured  $\text{Al}_2\text{O}_3$  [24], mullite [25],  $\text{Sr}_2\text{Nb}_2\text{O}_7$  [26],  $\text{Bi}_4\text{Ti}_3\text{O}_{12}$  [27],  $\text{Si}_3\text{N}_4$  [9], SiC [15], AlN-SiC [28] ceramics, and single crystal  $\text{Al}_2\text{O}_3$  [29], and  $\text{BaTiO}_3$  [19,30].

### **2.1.2 Requirements for TGG**

The critical factors that affect TGG can be summarized as follows: a dense, homogenous, and fine-grained matrix powder (to provide the driving force), morphologically stable template particles (or single crystals), an epitaxial match at the template/matrix interface, a mechanism for boundary migration (surface energy, kinetics, anisotropic template growth rate, and liquid phase), avoidance of exaggerated grain growth in the matrix, and uniform contact between the matrix and seed crystal. For a boundary to migrate (either for an oriented single crystal or many well-oriented template particles in a fine-grained matrix), the matrix should be dense and fine-grained since the energy for boundary migration arises from grain boundary free energy. Therefore, by starting with a fine grain size matrix, the grain boundary free energy is increased and the driving force for migration is maintained. The final texture also depends strongly on the initial number of template particles since the degree of grain orientation increases due to the growth of these particles. In addition, the relative size of the matrix and template particles during densification plays an important role in the texture development. In other words, templates must be large enough to initiate oriented grain growth in the matrix during heat treatment. Template particles must also be anisometric in shape so that they can be oriented in the matrix during forming. It has been found that template particles in the size range of 5 to 50  $\mu\text{m}$  resulted in successful texture development by TGG [15,31]. Template particles must be larger than the matrix grains because coarsening of the matrix grains during heat treatment reduces the thermodynamic driving force for the growth of template particles by decreasing the total grain boundary area. There is also a critical template content above which orientation of the texture direction broadens. This critical

template content varies depending on factors such as the matrix grain size, and the presence and amount of liquid content. It has been shown that template contents of around 5 to 10 vol% are adequate to induce highly textured microstructures [20,32,33].

### 2.1.3 Kinetics of Exaggerated Grain Growth

Since TGG relies on the preferential growth on the seed particles, it can be treated as a special case of exaggerated grain growth. When template growth is assisted by a liquid, the growth of templates occurs by solution-reprecipitation, in which small particles dissolve in a liquid due to their smaller size, and then reprecipitate on the larger template particles. If diffusion through this liquid layer is rate-controlling, a thinner layer would result in a steeper concentration gradient and faster mass transport kinetics. It has been discussed by Hennings *et al.* [34] for exaggerated grain growth in BaTiO<sub>3</sub> ceramics. Those authors considered that the growth of exaggerated grains was controlled by the supersaturation of the intergranular liquid phase which separates the matrix grains from each other and from the growing template grains (Fig. 2.3). The growth rate is driven by a constant gradient composed of the difference in solubility between the template and the matrix (i.e., supersaturation) across the intergranular liquid phase thickness ( $\delta$ ). From a solubility point of view, small spherical matrix grains have a slightly higher equilibrium solubility,  $c_r$ , than very large templates of solubility  $c_R$  (where  $c_r > c_R$ ). The Kelvin equation [35] can be modified to show the increased solubility of the smaller grains:

$$RT \ln \left( \frac{c_r}{c_R} \right) = \frac{2\gamma\Omega}{r} \quad (2.1)$$

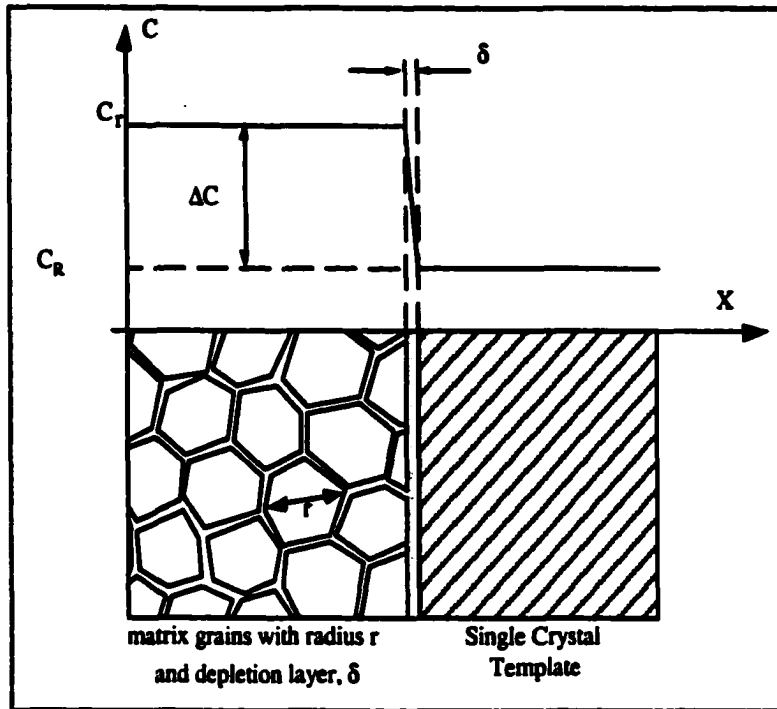


Figure 2.3 Template growth based on Hennings' model [34].

$$\frac{c_r}{c_R} = \exp\left(\frac{2\gamma\Omega}{RT_r}\right) \approx 1 + \frac{2\gamma\Omega}{RT_r} = 1 + \frac{\beta}{r} \quad (2.2)$$

$$\beta = \frac{2\gamma\Omega}{RT} \quad (2.3)$$

where  $R$  is the gas constant,  $\gamma$  the surface energy of the solid-liquid interface,  $T$  the temperature, and  $\Omega$  is the molar volume of the solid in contact with the liquid phase. It was assumed that all grains are wetted by a thin liquid film whose thickness,  $\delta$ , is a function of the volume of liquid phase. The concentration difference,  $\Delta c$ , and the average radius are assumed to be constant during this initial growth period [34].

$$\Delta c = c_r - c_R \approx c_R \beta / r \quad (2.4)$$

The concentration gradient of the solid dissolved in the liquid film is defined as:

$$dc/dx \approx \Delta c / \delta \quad (2.5)$$

The mass transport through the liquid film by diffusion is:

$$dm/dt = A\rho G = -AJ \quad (2.6)$$

where  $\rho$  is the density,  $m$  the mass,  $t$  the time,  $A$  the cross sectional area,  $G$  the growth rate, and  $J$  the flux per cross section and time:

$$J = -Ddc/dx \approx -D\Delta c / \delta \quad (2.7)$$

where  $D$  is the diffusion coefficient in the liquid. By combining Eqns. (2.4), (2.6) and (2.7), the growth rate or boundary migration of the crystal face is:

$$G = \left(\frac{Dc_R}{\rho\delta}\right) \left(\frac{\beta}{r}\right) \quad (2.8)$$

This equation shows that the growth rate is directly proportional to  $\gamma$ , and inversely proportional to both  $r$  and  $\delta$ . The crystal faces with the highest packing density

and the fewest unsaturated bonds will have the lowest  $\gamma$  and hence the slowest growth rates [1]. The presence of a liquid is necessary for boundary migration to occur; however, the diffusion is limited with increasing  $\delta$  due to decreased mobility. The grain boundary mobility can be increased considerably when the matrix grain size is in the submicron range and the advancing template face has a high surface energy (e.g., (111) vs. (100) in BaTiO<sub>3</sub>) [36]. In brief, the growth rate of a template is mostly influenced by changes in liquid layer thickness, matrix grain size, and template orientation.

## 2.2 TUNGSTEN BRONZE (TB) STRUCTURE FAMILY

The tungsten bronze family has an oxygen octahedral framework structure that is much more open than the perovskite structure [37]. The TB structure is characterized by oxygen octahedra linked at the corners to yield three different interstitial sites A, B, and C that extend through the structure along the 4-fold symmetry ( $z$ ) axis (or  $c$  direction) (Figure 2.4). The linkage is regular along the  $c$  axis, but markedly puckered in the  $a$  and  $b$  directions. The B cations are inside the oxygen octahedra. Tungsten bronze compositions are characterized by the chemical formulae  $(A_1)_4(A_2)_2C_4B_{10}O_{30}$  or  $(A_1)_4(A_2)_2B_{10}O_{30}$ , in which the A<sub>1</sub> cations are in the 15-fold coordinated site, the A<sub>2</sub> cations are in the 12-fold coordinated site, the C cations are in the 9-fold coordinated site, and the B cations are in two different 6-fold coordinated sites. The A sites (A<sub>1</sub>, A<sub>2</sub>) can be occupied by large monovalent (e.g., Na, K), divalent (e.g., Sr, Ba), or trivalent (e.g., La) ions, the two different B sites (B<sub>1</sub>, B<sub>2</sub>) are usually occupied by smaller, highly charged cations (e.g., Nb, Ta, W, Ti), and the C site may be vacant or occupied by small cations such as Li [37,38,39].



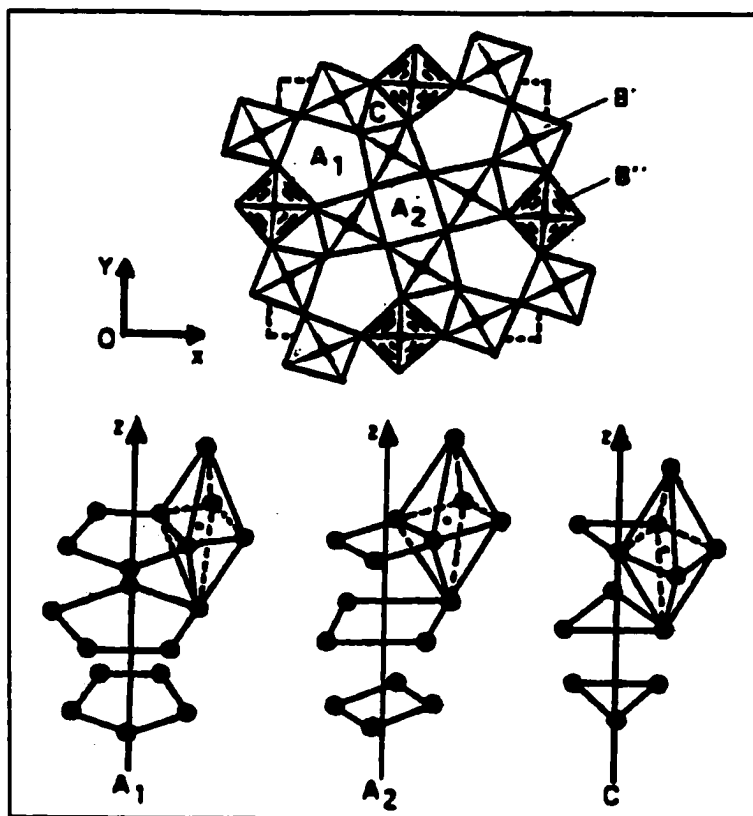


Figure 2.4 Projection of tungsten bronze structure [39].

TB crystals are in the prototypic point group  $4/mmm$ . The ferroelectric phase transition is from  $4/mmm$  to  $4mm$  (tetragonal-tetragonal) or from  $4/mmm$  to  $mm2$  (tetragonal-orthorhombic). The tetragonal TB family can be divided into four groups based on ferroelectric and optical studies [38,39];

1) Crystals with  $4mm$  symmetry and  $\langle 001 \rangle$  polar axis (e.g.,  $\text{Sr}_x\text{Ba}_{1-x}\text{Nb}_2\text{O}_6$ ,  $\text{KSr}_2\text{Nb}_3\text{O}_{13}$ ,  $\text{Ba}_6\text{Ti}_2\text{Nb}_3\text{O}_{30}$ ). These materials show large dielectric constants ( $K_{33}$ ), and electro-optic ( $r_{33}$ ) and piezoelectric strain ( $d_{33}$ ) coefficients. They have nearly cylindrical shapes (24-facets),  $T_c < 150^\circ\text{C}$ , and moderate polarization ( $P_3$ ).

2) Crystals with  $4mm$  symmetry and  $\langle 001 \rangle$  polar axis (e.g.,  $\text{Ba}_{2-x}\text{Sr}_x\text{K}_{1-y}\text{Na}_y\text{Nb}_3\text{O}_{13}$ ,  $\text{K}_3\text{Li}_2\text{Nb}_3\text{O}_{13}$ ). These materials show large  $r_{31}$ ,  $K_{11}$ , and  $d_{15}$ . They have square or octahedron shapes,  $T_c > 150^\circ\text{C}$ , and moderate polarization ( $P_3$ ).

3) Crystals with  $mm2$  symmetry and  $\langle 001 \rangle$  polar axis (e.g.,  $\text{Sr}_{2-x}\text{Ca}_x\text{NaNb}_3\text{O}_{13}$ ). These materials show large  $r_{15}$ ,  $r_{33}$ ,  $d_{15}$ , and  $d_{33}$ . They have cylindrical shapes,  $T_c \sim 200\text{--}300^\circ\text{C}$ , and large polarization ( $P_3$ ).

4) Crystals with  $mm2$  symmetry and  $\langle 001 \rangle$  or  $\langle 010 \rangle$  polar axis (e.g.,  $\text{Pb}_2\text{KNb}_3\text{O}_{13}$ ,  $\text{Pb}_4\text{Ba}_{1-x}\text{Nb}_2\text{O}_6$ ). These materials show large  $r_{31}$ ,  $K_{11}$ , and  $d_{15}$ . They have  $T_c \sim 350^\circ\text{C}$  and large polarization ( $P_3$ ).

$\text{Sr}_x\text{Ba}_{1-x}\text{Nb}_2\text{O}_6$  (SBN) is a ferroelectric solid solution, where  $x = 0.25\text{--}0.75$ . It is the best example of a material with high  $K_{33}$ ,  $r_{33}$ , and  $d_{33}$  [39-42]. SBN single crystals have a distinct growth habit with 24 well-defined facets with definite crystallographic orientation [39]. SBN single crystals are useful for electro-optic (e.g., optical wave guide, switches, and modulators), piezoelectric, pyroelectric (e.g., uncooled IR detectors), millimeter wave (e.g., optical computing and modulators), photorefractive (e.g., image

processing, 3-D storage, phase conjugation), and surface acoustic wave (e.g., filters and resonators, delay lines) applications [39,40,43].  $\text{Sr}_{0.75}\text{Ba}_{0.25}\text{Nb}_2\text{O}_6$  (SBN75) single crystals have some of the largest known linear electrooptic coefficients [39,44]. The piezoelectric and electro-optic properties of tungsten bronze crystals are summarized in Table 2.1. For SBN, the Curie temperature decreases with increasing Sr content, and the dielectric spectra changes from normal to relaxor ferroelectric [45].

Tungsten bronzes are referred to as either “filled” or “unfilled” bronzes when the C sites are vacant and the A sites are either fully, or partially occupied, respectively. For example,  $\text{Pb}_3\text{Nb}_{10}\text{O}_{30}$  and  $(\text{Sr},\text{Ba})_3\text{Nb}_{10}\text{O}_{30}$  have A sites which are only 5/6 filled. In SBN,  $\text{Ba}^{2+}$  predominantly occupies the 15-fold coordinated site since  $\text{Ba}^{2+}$  (1.74 Å) is substantially larger than  $\text{Sr}^{2+}$  (1.54 Å) [39]. Therefore,  $\text{Sr}^{2+}$  occupies either the  $A_1$  site or a combination of the  $A_1$  and  $A_2$  sites depending on the composition. In SBN34, for example, the Sr/Ba ratio on the  $A_1$  site reaches 0, which means  $\text{Sr}^{2+}$  occupies only the  $A_2$  site [46]. This disordered atomic arrangement of  $\text{Sr}^{2+}$ ,  $\text{Ba}^{2+}$ , and vacancies on the A sites has been related to the diffuse phase transition [47]. The  $A_1$ ,  $A_2$ , and C sites can be filled by alkali and alkaline earth metal ions, leading to a large family of solid solutions. Therefore, a wide spectrum of Curie temperatures and dielectric constants are observed in this family [48,49].

### 2.3 TEXTURED CERAMICS WITH TB STRUCTURE

Grain-oriented tungsten bronze ceramics have been fabricated by several techniques without using template particles. Neurgaonkar *et al.* [50] hot-forged  $\text{Pb}_{0.60}\text{Ba}_{0.40}\text{Nb}_2\text{O}_6$  (PBN60) and La-doped PBN60 ceramics. They obtained improved

Table 2.1. The piezoelectric and electro-optic properties of tungsten bronze crystals (From ref. 38).

Crystal	$T_c$ , °C	Electro-optic coeff. $\times 10^{-12}$ m/V	Piezoelectric coeff. pC/N (25°C)	Dielectric Constant (25°C)
$\text{Sr}_{0.75}\text{Ba}_{0.25}\text{Nb}_2\text{O}_6$ (SBN75)	56	$r_{33} = 1350$	$d_{33} = 670$	$K_{33} = 3000$
$\text{Sr}_{0.60}\text{Ba}_{0.40}\text{Nb}_2\text{O}_6$ (SBN60)	75	$r_{33} = 420$	$d_{33} = 180$	$K_{33} = 1000$
$\text{Sr}_{0.50}\text{Ba}_{0.50}\text{Nb}_2\text{O}_6$ (SBN50)	128	$r_{33} = 210$	$d_{33} = 110$	$K_{33} = 450$
$\text{Ba}_{2-x}\text{Sr}_x\text{K}_{1-y}\text{Na}_y\text{Nb}_5\text{O}_{15}$ (BSKNN-1)	209	$r_{33} = 100$	$d_{15} = 80$	$K_{11} = 370$
$\text{Ba}_{2-x}\text{Sr}_x\text{K}_{1-y}\text{Na}_y\text{Nb}_5\text{O}_{15}$ (BSKNN-2)	178	$r_{33} = 160$	$d_{15} = 200$	$K_{11} = 690$
			$d_{33} = 80$	$K_{33} = 190$
$\text{Ba}_{2-x}\text{Sr}_x\text{K}_{1-y}\text{Na}_y\text{Nb}_5\text{O}_{15}$ (BSKNN-3)	180	$r_{33} = 210$	$d_{15} = 93$	$K_{11} = 750$
$\text{Sr}_{2-x}\text{Ca}_x\text{NaNb}_5\text{O}_{15}$ (SCNN)	270	$r_{33} = 650^*$	$d_{33} = 270$	$K_{33} = 1740$
		$r_{51} = 450^*$	$d_{15} = 248$	$K_{11} = 1700$
$\text{Pb}_{0.60}\text{Ba}_{0.40}\text{Nb}_2\text{O}_6$ (PBN60)	300	$r_{51} = > 1800^*$	$d_{15} = > 300$	$K_{11} = 1900$
$\text{K}_3\text{Li}_2\text{Nb}_5\text{O}_{15}$ (KLN)	405	$r_{51} = 100$	$d_{15} = 147$	$K_{11} = 350$
$\text{Sr}_2\text{KNb}_5\text{O}_{15}$ (SKN)	157	$r_{33} = 210$	$d_{33} = 95$	$K_{33} = 1100$
$(\text{Ba},\text{Sr})_6\text{Ti}_2\text{Nb}_8\text{O}_{30}$ (BSTN)	114	$r_{33} = 300^*$	$d_{33} = 125$	$K_{33} = 345$
$\text{Ba}_2\text{NaNb}_5\text{O}_{15}$ (BNN)	560	$r_{33} = 48$	$d_{33} = 20$	$K_{33} = 47$
		$r_{51} = 94$	$d_{15} = 45$	$K_{11} = 240$

\* Calculated values

anisotropic dielectric and piezoelectric properties with respect to the randomly oriented ceramic. However, the saturation polarization ( $P_{\text{sat}}$ ) remained well below the single crystal values ( $24 \mu\text{C}/\text{cm}^2$  vs.  $60\text{-}70 \mu\text{C}/\text{cm}^2$ ). Kimura *et al.* [51] applied 1-stage and 2-stage hot pressing (HP) techniques to improve grain orientation and the dielectric properties of  $\text{KSr}_2\text{Nb}_5\text{O}_{15}$  ceramics. Grain orientation was highly improved by 2-stage hot pressing from 23 to 86% (measured by the Lotgering factor). Nagata *et al.* [52] hot-pressed  $\text{Sr}_x\text{Ba}_{1-x}\text{Nb}_2\text{O}_6$  ceramics, where  $x = 0.30\text{-}0.65$ , to improve the optical and electrical properties, but their piezoelectric values remained well below the single crystal values. Slightly anisotropic properties were obtained in directions perpendicular ( $\perp$ ) and parallel ( $\parallel$ ) to the hot pressing direction. For example, they reported maximum dielectric constants ( $K_{\text{max}}$ ) of 4,400 ( $\perp$ ) and 3,000 ( $\parallel$ ), and remanent polarizations ( $P_r$ ) of  $2.1 \mu\text{C}/\text{cm}^2$  ( $\perp$ ) and  $1.6 \mu\text{C}/\text{cm}^2$  ( $\parallel$ ). In a recent paper [20], Duran *et al.* reported enhanced electrical properties in highly textured  $\text{Sr}_{0.53}\text{Ba}_{0.47}\text{Nb}_2\text{O}_6$  (SBN53) ceramics fabricated by TGG, using  $\text{KSr}_2\text{Nb}_5\text{O}_{15}$  particles as templates. Highly grain-oriented ceramics ( $> 90\%$  as measured by the Lotgering factor) had  $K_{\text{max}} = 7,550$  ( $\parallel$  to the texture direction) and 600 ( $\perp$  to the texture direction),  $P_r = 13.2 \mu\text{C}/\text{cm}^2$  ( $\parallel$ ) and  $1 \mu\text{C}/\text{cm}^2$  ( $\perp$ ),  $P_{\text{sat}} = 21 \mu\text{C}/\text{cm}^2$  ( $\parallel$ ) (60-85% of single crystal value), and a piezoelectric strain coefficient ( $d_{33}$ ) =  $78 \text{ pC}/\text{N}$  ( $\parallel$ ) (70-85% of single crystal value).

## 2.4 PHASE FORMATION AND SINTERING OF SBN CERAMICS

Fang *et al.* [53] studied the formation mechanism of  $\text{Sr}_{0.5}\text{Ba}_{0.5}\text{Nb}_2\text{O}_6$  (SBN50) ceramics from the respective oxides. They proposed the following reaction sequence based on the XRD analysis;  $\text{BaCO}_3$  or  $\text{SrCO}_3$  reacts with  $\text{Nb}_2\text{O}_5$  to form  $\text{Ba}_5\text{Nb}_4\text{O}_{15}$  or  $\text{Sr}_5\text{Nb}_4\text{O}_{15}$ , respectively, on heating to 600-900°C for 2 h. These phases react with the remaining  $\text{Nb}_2\text{O}_5$  to yield final intermediate products of  $\text{BaNb}_2\text{O}_6$  (BN) and  $\text{SrNb}_2\text{O}_6$  (SN) after calcining at 800-1100°C for 2 h. The final product SBN50 forms by gradual consumption of SN and BN between 1000 and 1150°C.

The formation fraction of SBN phase decreases with increasing Sr concentration and increases with increasing calcination temperature [47,53,54]. The difficulty of forming SBN with higher Sr contents (e.g., SBN75) at lower calcination temperatures was attributed to increasing lattice distortion resulting from the high concentration of  $\text{Sr}^{2+}$  ions in the  $A_1$  site of the tetragonal tungsten bronze (TTB) structure [53,54] (because the space of the  $A_1$  site is relatively larger than the  $\text{Sr}^{2+}$  ions). The highly distorted lattice can make the diffusion of ions, especially larger  $\text{Ba}^{2+}$ , more difficult. Therefore, a higher calcination temperature is needed for full TTB structure formation. For example, complete SBN50 formation takes place at 1230°C compared to 1300°C in SBN60 and 1400°C in SBN70 for the same heating rate of 20°C/min. The activation energy of phase formation was reported to be 735, 900, and 1300 kJ/mole for SBN50, SBN60, and SBN70, respectively [54].

SBN ceramics have been sintered by conventional and reactive routes. In solid state powder processing, unreacted oxides are likely due to incomplete calcination,

leading to compositional heterogeneity in the system. Lee *et al.* [55,56] showed in the conventional sintering of SBN60 ceramics that heterogeneities could cause liquid phase formation at temperatures lower than the sintering temperature required for densification. They found by TEM that the  $\text{Nb}_2\text{O}_5/(\text{SrO}+\text{BaO})$  ratio is different between the grains ( $<1$ ) and grain boundaries ( $>1$ ). Therefore, the resulting grain boundaries are  $\text{Nb}_2\text{O}_5$ -rich, which leads to liquid phase formation at  $T \geq 1260^\circ\text{C}$ . It was reported that the temperature at which the liquid phase forms decreases with increasing excess  $\text{Nb}_2\text{O}_5$  [57]. This liquid phase formation gives rise to a duplex microstructure consisting of millimeter-sized grains together with smaller grains. Cracking, caused by excessive localized grain growth in the microstructure, takes place due to high internal stresses. The result is low density ceramics. Similar abnormal grain growth behavior was also observed in other tetragonal tungsten bronze ceramics such as  $(\text{Pb},\text{Ba})\text{Nb}_2\text{O}_6$  and  $(\text{K},\text{Sr})\text{Nb}_5\text{O}_{15}$  (KSN) [58,59].

One way to retard the onset temperature at which liquid forms in conventional sintering is to presinter a compact below the actual sintering temperature. It was found in KSN ceramics that presintering delayed abnormal grain growth by limiting particle coarsening and pore growth during prefiring; and this reduced the number of nucleation sites for abnormal grain growth [58].

An alternative way to obtain dense SBN ceramics without abnormal grain growth is reactive sintering [60]. This is a process in which chemical reaction of the starting powders and densification of the powder compact are both achieved in the same heating cycle. The reaction and densification may occur either in sequence, simultaneously, or by some combination of the two [60,61]. Due to the complexity of the mechanisms during reactive sintering, suitable reactants are very important to obtain high density and a

uniform microstructure. In SBN, reactive sintering occurs by reaction of  $\text{SrNb}_2\text{O}_6$  (SN) and  $\text{BaNb}_2\text{O}_6$  (BN). Phase formation is initiated by forming necks between particles in the early stage of reactive sintering. Compositional homogenization takes place as interdiffusion occurs through these necks, which helps eliminate or retard uncontrolled liquid formation due to local composition variations. Densification occurs very rapidly following homogenization as a result of the high driving force from the porous, fine-grained, and uniform microstructure [60].

It has been variously reported that the desired SBN composition can form either directly or via intermediate SBN compositions. Fang *et al.* [53] reported that when SBN50-SBN75 compositions were calcined at  $1150^\circ\text{C}$  for 2 h from the respective oxides, phase pure SBN50 was formed. However, compositions with higher Sr contents (e.g., SBN60 and SBN75) had some unreacted SN. The amount of unreacted SN increased with the Sr content. It was suggested that SBN with lower Sr content forms first, and then reacts with the remaining SN to form the final SBN60 or SBN75 with increasing temperature. However, Lee and Fang [59] indicated that the shift of the major peak of the developed SBN at different reaction stages of reactive sintering is due to lattice mismatch between SBN and residual SN (or BN), and penetration of  $\text{Sr}^{2+}$  and  $\text{Ba}^{2+}$  ions through the SBN during the reaction. These results suggest that reactive sintering and calcination may change the sequence the desired SBN forms.



## 2.5 REFERENCES

- 1- D. Elwell and H. J. Scheel, *Crystal growth from high temperature solutions*, Academic Press, London (1975)
- 2- A. Linz, V. Belruss, and C. S. Naiman, "Solution-growth perovskites," *J. Electrochem. Soc.*, 112[6], 60C-66C (1965)
- 3- E. Tani, S. Umebayashi, K. Kishi, K. Kobayashi, and M. Nishijima, "Gas pressure sintering of  $\text{Si}_3\text{N}_4$  with concurrent addition of  $\text{Al}_2\text{O}_3$  and 5 wt% rare earth oxide: high fracture toughness  $\text{Si}_3\text{N}_4$  with fiber-like structure," *Am. Ceram. Soc. Bull.*, 65 [9], 1311-15 (1986)
- 4 - P. F. Becher, "Microstructural Design of Toughened Ceramics," *J. Am. Ceram. Soc.*, 74 [2], 255-69 (1991)
- 5 - J. D. Powers and A. M. Glaeser, "Grain boundary migration in ceramics," *Interface Science*, 6, 23-29 (1998)
- 6 – H. Emoto and M. Mitomo, "Control and characterization of abnormally grown grains in silicon nitride ceramics," *J. Eur. Ceram. Soc.*, 17, 797-804 (1997)
- 7 - H. Watanabe, T. Kimura, and T. Yamaguchi, "Sintering of platelike bismuth titanate powder compacts with preferred orientation," *J. Am. Ceram. Soc.*, 74 [1], 139-47 (1991)
- 8 - S. Swartz, W. A. Schulze, and J. V. Biggers, "Fabrication and electrical properties of grain oriented  $\text{Bi}_4\text{Ti}_3\text{O}_{12}$  ceramics," *Ferroelectrics*, 38, 765-68 (1981)
- 9 - K. Hirao, M. Ohashi, M. E. Brito, and S. Kanzaki, "Processing strategy for producing highly anisotropic silicon nitride," *J. Am. Ceram. Soc.*, 78[6], 1687-90 (1995)

- 10 - A. Holloway, R. W. McCallum, and S. R. Arrasmith, "Texture development due to preferential grain growth of Ho-Ba-Cu-O in 1.6-T magnetic field," *J. Mater. Res.*, 8[4], 727-733 (1993)
- 11 - A. Halliyal, A. S. Bhalla, and R. E. Newnham, "Polar glass ceramics-A new family of electroceramic materials: Tailoring the piezoelectric and pyroelectric properties," *Mat. Res. Bull.*, 18[8], 1007-19 (1983)
- 12 - T. Takenaka and K. Sakata, "Grain orientation and electrical properties of hot-forged  $\text{Bi}_4\text{Ti}_3\text{O}_{12}$  Ceramics," *Jap. J. Appl. Phys.*, 19[1], 31-39 (1980)
- 13 - H. Igarashi, K. Matsunaga, T. Taniai, and K. Okazaki, "Dielectric and piezoelectric properties of grain-oriented  $\text{PbBi}_2\text{Nb}_2\text{O}_9$  ceramics," *Am. Ceram. Soc. Bull.*, 57[9], 815-17 (1978)
- 14 - E. Suvaci, M. M. Seabaugh, and G. L. Messing, "Reaction-based processing of textured alumina by templated grain growth," *J. Eur. Ceram. Soc.*, 19 [13-14], 2465-74 (1999)
- 15 - M. D. Sacks, G. W. Scheiffele, and G. A. Staab, "Fabrication of textured silicon carbide via seeded anisotropic grain growth," *J. Am. Ceram. Soc.*, 79[6], 1611-16 (1996)
- 16 - D. Rytz, B. A. Wechsler, C. C. Nelson, and K. W. Kirby, "Top-seeded solution growth of  $\text{BaTiO}_3$ ,  $\text{KNbO}_3$ ,  $\text{SrTiO}_3$ ,  $\text{Bi}_{12}\text{TiO}_{20}$  and  $\text{La}_{2-x}\text{Ba}_x\text{CuO}_4$ ," *J. Crystal Growth*, 99[4], 864-68 (1990)
- 17 - S. Matsuzawa and S. Mase, "Method for producing a single crystal of ferrite," *U.S. Patent 4339301* (July 13, 1982)

- 18 - T. Yamamoto and T. Sakuma, "Fabrication of barium titanate single crystals by solid-state grain growth," *J. Am. Ceram. Soc.*, 77 [4], 1107-9 (1994)
- 19 - P. W. Rehrig, S. E. Park, S. Trolier-McKinstry, G. L. Messing, B. Jones, and T. R. Shrout, "Piezoelectric properties of zirconium-doped barium titanate single crystals grown by templated grain growth," *J. Appl. Phys.*, 86[3], 1657-61 (1999)
- 20 - C. Duran, S. Trolier-McKinstry, G. L. Messing, "Fabrication and electrical properties of textured  $\text{Sr}_{0.53}\text{Ba}_{0.47}\text{Nb}_2\text{O}_6$  ceramics by templated grain growth," *J. Am. Ceram. Soc.*, 83[9], 2203-13 (2000)
- 21 - C. Takahashi, M. Nagano, Y. Wakiya, T. Kato, and K. Kato, "Anisotropy of critical current density in Bi-2223/Ag tapes," *Advances in Superconductivity VII. Proceedings of the 7<sup>th</sup> International Symposium on Superconductivity*, 75-81 (1995)
- 22 - G. E. Youngblood and R. S. Gordon, "Texture-Conductivity Relationships in Polycrystalline Lithia-Stabilized  $\beta$ "-Alumina," *Ceram. Internat.*, 4[3], 93-98 (1978)
- 23 - M. M. Seabaugh, "Texture development in liquid phase sintered alpha alumina via anisotropic template growth," Ph.D. Thesis, The Pennsylvania State University (1998)
- 24 - D. Brandon, D. Chen, and H. Chan, "Control of texture in monolithic alumina," *Mat. Sci. Eng. A195*, 189-96 (1995)
- 25 - S.H. Hong, G. L. Messing, "Development of textured mullite by templated grain growth," *J. Am. Ceram. Soc.*, 82[4], 867-72 (1999)
- 26 - B. Brahmaroutu, G. L. Messing, S. Trolier-McKinstry, and U. Selvaraj, "Templated grain growth of textured  $\text{Sr}_2\text{Nb}_2\text{O}_7$ " *Proceedings of the Tenth IEEE Int. Symp. on Appl. of Ferroelectrics*, Edited by B. Kulwicki, A. Amin, and A. Safari, Vol. 2, 883-86 (1996)

- 27** - J. A. Horn, S. C. Zhang, U. Selvaraj, G. L. Messing, and S. Trolier-McKinstry, "Templated grain growth of textured bismuth titanate," *J. Am. Ceram. Soc.*, 82[4], 921-26 (1999)
- 28** - M. S. Sandlin and K. J. Bowman, "Textures in AlN-SiC composite ceramics"; pp. 263-268 in *Mat. Res. Soc. Symp. Proc.*, Vol. 327, *Covalent Ceramics II, Non-Oxides*. Material Research Society, Pittsburgh, PA (1994)
- 29** - C. Scott, J. Strok, and L. Levinson, "Solid state thermal conversion of polycrystalline alumina to sapphire using a seed crystal," *U.S. Pat. No. 5 549 746* (1996)
- 30** - T. Yamamoto and T. Sakuma, "Fabrication of barium titanate single crystals by solid-state grain growth," *J. Am. Ceram. Soc.*, 77[4], 1107-109 (1994)
- 31** - M. M. Seabaugh, I. H. Kerscht, and G. L. Messing, "Texture development by templated grain growth in liquid-phase sintered  $\alpha$ -alumina," *J. Am. Ceram. Soc.*, 80[5], 1181-88 (1997)
- 32** - B. Brahmaraoutu, "Templated grain growth of textured strontium niobate ceramics" Ph.D. Thesis, The Pennsylvania State University (1999)
- 33** - E. Suvaci and G. L. Messing, "Critical factors in the templated grain growth of textured reaction-bonded alumina," *J. Am. Ceram. Soc.*, 83[8], 2041-48 (2000)
- 34** - D. F. K. Hennings, R. Janssen and P. J. L. Reynen, "Control of liquid-phase enhanced discontinuous grain growth in barium titanate," *J. Am. Ceram. Soc.*, 70[1], 23-7 (1987)
- 35** - P. C. Hiemenz, "The Kelvin Equation," pp. 303-6 in *Surface Chemistry*, Vol. 2, New York (1986)

- 36 - P. W. Rehrig, "Templated grain growth of BaTiO<sub>3</sub>-based perovskite single crystals," Ph.D. Thesis, The Pennsylvania State University (1999)
- 37- Encyclopedia of Chemical Technology, 3<sup>rd</sup> Edition, John Wiley & Sons Inc., Vol. 10, pp.14-15.
- 38- R. R. Neurgaonkar, J. R. Oliver, W. K. Cory, L. E. Cross, and D. Viehland, "Piezoelectricity in tungsten bronze crystals," *Ferroelectrics*, 160, 265-76 (1994)
39. R. R. Neurgaonkar, W. K. Cory, J. R. Oliver, E. J. Sharp, G. L. Wood, and G. J. Salamo, "Growth and optical properties of ferroelectric tungsten bronze crystals," *Ferroelectrics*, 142, 167-88 (1993)
40. S. N. Murty, K.V. R. Murty, K. C. Mouli, A. Bhanumathi, S. B. Raju, G. Padmavathi, and K.L. Murty, "Relaxor behavior in certain tungsten bronze ceramics," *Ferroelectrics*, 158, 325-330 (1994)
41. A. M. Glass, "Investigation of the electrical properties of Sr<sub>1-x</sub>Ba<sub>x</sub>Nb<sub>2</sub>O<sub>6</sub> with special reference to pyroelectric detection," *J. Appl. Phys.*, 40[12], 4699-713 (1969)
42. A. A. Ballman and H. Brown, "The growth and properties of strontium barium metaniobate, Sr<sub>1-x</sub>Ba<sub>x</sub>Nb<sub>2</sub>O<sub>6</sub>, a tungsten bronze ferroelectric," *J. Cryst. Growth*, 1, 311-18 (1967)
- 43- R. R. Neurgaonkar, W. F. Hall, J. R. Oliver, W. W. Ho, and W. K. Cory, "Tungsten bronze Sr<sub>x</sub>Ba<sub>1-x</sub>Nb<sub>2</sub>O<sub>6</sub>: A case history of versatility," *Ferroelectrics*, 87, 167-79 (1988)
44. P. V. Lenzo, E.G. Spencer, and A. A. Ballman, "Electrooptic coefficients of ferroelectric strontium barium niobate," *Appl. Phys. Lett.*, 11, 23-24 (1967)

- 45- D. Viehland, Z. Xu, and W-H. Huang, "Structure-property relationships in strontium barium niobate; I- Needle-like nanopolar domains and the metastably-locked incommensurate structure," *Phil. Mag. A*, 71[2], 205-17 (1995)
46. R. Guo, A. S. Bhalla, G. Burns, and F. H. Dacol, "Studies on annealing and quenching of strontium barium niobate (SBN) single crystals: A-site cation ordering-disordering effect," *Ferroelectrics*, 93, 397-405 (1989)
47. N. S. VanDamme, A. E. Sutherland, L. Jones, K. Bridger, and S. R. Winzer, "Fabrication of optically transparent and electrooptic strontium barium niobate ceramics," *J. Am. Ceram. Soc.*, 74[8], 1785-92 (1991)
48. A. Bhanumathi, S. N. Murty, K. Umakantham, K. C. Mouli, G. Padmavathi, K. T. Rao, and V. Syamalamba, "Ferroelectric properties of tungsten bronze ceramics" *Ferroelectrics*, 102, 173-81 (1990)
49. S. N. Murty, K. Umakantham, K.V.R. Murthy, K. C. Mouli, G. Padmavathi, and K. L. Murty, "Effect of different cations on the ferroelectric properties of modified strontium barium niobate ceramics," *J. Mat. Sci. Letters*, 11, 607-609 (1992)
50. R. R. Neurgaonkar, J. R. Oliver, J. G. Nelson, and L. E. Cross, "Piezoelectric and ferroelectric properties of La-modified and unmodified tungsten bronze  $Pb_{0.60}Ba_{0.40}Nb_2O_6$  dense ceramics," *Mat. Res. Bull.*, 26, 771-77 (1991)
51. T. Kimura, S. Saiubol, and K. Nagata, "Effect of grain orientation on the Curie temperature of  $KSr_2Nb_2O_9$  solid solutions," *J. Ceram. Soc. Japan, Int. Ed.*, 103[2], 132-37 (1995)
52. K. Nagata, Y. Yamamoto, H. Igarashi, and K. Okazaki, "Properties of the hot-pressed strontium barium niobate ceramics," *Ferroelectrics*, 38, 853-56 (1981)

- 53- T-T. Fang, N-T. Wu, and F-S. Shiau, "Formation mechanism of SBN ceramic powders," *J. Mater. Sci. Letters*, 13, 1746-48 (1994)
- 54- W-J. Lee and T-T. Fang, "Nonisothermal reaction kinetics of  $\text{SrNb}_2\text{O}_6$  and  $\text{BaNb}_2\text{O}_6$  for the formation of  $\text{Sr}_x\text{Ba}_{1-x}\text{Nb}_2\text{O}_6$ ," *J. Am. Ceram. Soc.*, 81[1], 193-99 (1998)
- 55- H-Y. Lee and R. Freer, "The mechanism of abnormal grain growth in  $\text{Sr}_{0.6}\text{Ba}_{0.4}\text{Nb}_2\text{O}_6$  ceramics," *J. Appl. Phys.* 81[1], 376-82 (1997)
- 56- H-Y. Lee and R. Freer, "Abnormal grain growth and liquid-phase sintering in  $\text{Sr}_{0.6}\text{Ba}_{0.4}\text{Nb}_2\text{O}_6$ , (SBN40) ceramics," *J. Mater. Sci.*, 33, 1703-708 (1998)
- 57- J. R. Carruthers and M. Grasso, "Phase equilibria relations in the ternary system  $\text{BaO-SrO-Nb}_2\text{O}_5$ ," *J. Electrochem. Soc.: Solid State Science*, 117[11], 1426-30 (1970)
- 58- T. Kimura, S. Miyamoto, and T. Yamaguchi, "Microstructure development and dielectric properties of potassium strontium niobate ceramics," *J. Am. Ceram. Soc.*, 73[1], 127-30 (1990)
- 59- T. Hiroshima, K. Tanaka, and T. Kimura, "Effects of microstructure and composition on the Curie temperature of lead barium niobate solid solutions," *J. Am. Ceram. Soc.*, 79[12], 3235-42 (1996)
- 60- W-J. Lee and T-T. Fang, "Densification and microstructural development of the reaction sintering of strontium barium niobate," *J. Am. Ceram. Soc.*, 81[4], 1019-24 (1998)
- 61- W.-S. Hong, L.C. De Jonghe, X. Yang, and M. Rahaman, "Reaction sintering of  $\text{ZnO-Al}_2\text{O}_3$ ," *J. Am. Ceram. Soc.*, 78[12], 3217-24 (1995)

## CHAPTER 3

### TEMPLATE PARTICLE SYNTHESIS IN THE SrO-Nb<sub>2</sub>O<sub>5</sub>-BaO SYSTEM

#### 3.1 INTRODUCTION

Anisometric single crystal particles (e.g., templates) are very important in the fabrication of textured ceramics by templated grain growth (TGG) [1]. The initial template orientation in the green ceramic and the relative growth rate of templates during sintering determines the degree of texture that is developed during TGG. Therefore, template size and morphology affect the amount of growth and final texture. Highly textured ceramics have been fabricated by TGG using whiskers or platelets [2-5]. These template shapes are suitable for orientation by tape casting or extrusion [6,7]. The morphology and crystal symmetry of the templates determine the texture direction. By regulating the morphology of templates and suitably orienting them in the matrix, it is possible to fabricate one dimensionally oriented (fiber textured) [1,8]) or even three dimensionally oriented (sheet textured) [9]) ceramics that could exhibit properties close to single crystals of the same composition. The requirements for the template particles can be summarized as: (i) larger size relative to the matrix grains, (ii) anisometric morphology, (iii) morphological stability in the matrix, (iv) epitaxial relationship to the final phase, and (v) cost-effective synthesis method.

Solution growth [10,11,12] and hydrothermal [13,14] techniques are two common methods to synthesize single crystal particles. For materials which melt incongruently or exhibit low temperature phase transitions, flux growth can be very useful in effecting crystal growth at temperatures far below the melting point of the product phase. For



example, reactive solvents in the hydrothermal technique increase the solubility of the material that is sparingly soluble in an ordinary solution below the boiling temperature [13,14]. An alternative method is molten salt synthesis (MSS). This process is based on the use of a molten salt solvent to act as the medium of reaction between the constituent oxides (e.g., reactants). MSS has been used extensively to prepare ferrites [15], titanates [16], niobates [17,18,19], and mullite [20]. The desired compound will form if it is thermodynamically more stable than the reactants. In addition, the higher the product stability, the lower the molten salt solubility relative to the reactants. The solubility of oxides in molten salts varies greatly, from less than  $1 \times 10^{-10}$  mole fraction to more than 0.5 mole fraction, and is typically  $1 \times 10^{-3}$  to  $1 \times 10^{-7}$  mole fraction [21]. However, because of the small diffusion distances in an intimate mix of the reactants, and the relatively high mobility of species ( $1 \times 10^{-5}$  to  $1 \times 10^{-8}$  cm<sup>2</sup>/sec compared to as low as  $1 \times 10^{-18}$  cm<sup>2</sup>/sec in the solid state), complete reaction is accomplished in a relatively short time [21]. It is desirable to have a molten salt viscosity of ~ 1-100 mPa·s because high viscosity can retard the growth process [12]. The reaction proceeds by supersaturation of the molten salt solvent by the reactants with respect to the product compound, which precipitates from the solution. This process continues to consume reactant until a residual concentration remains in solution commensurate with its intrinsic solubility in the melt, as determined by the solubility product, typically  $< 1 \times 10^{-3}$  mole fraction [21]. The requirements of the molten salt solvent are; (i) it should not undergo any undesirable side reactions with the reactants, product compounds, and crucible material, (ii) the salt solvent should possess sufficient aqueous solubility so that it can be removed by simple washing, (iii) the salt must have a low melting temperature [12,17,21]. The vapor

pressure of the salt must be low at the reaction temperature to prevent salt evaporation, which causes surface crystallization, and to maintain a constant salt bath chemistry [12]. Some of the disadvantages of MSS process are the possible inclusion of the salt ions in the product, precipitation of inseparable impurity phases, and relatively slow growth rates compared to crystallization from pure melts. Therefore, it is advantageous to have a common cation between the salt and the solute to minimize contamination by other metal ions [9].

Molten salt synthesis was chosen to form the anisometric particles in this work. In particular, the aim was to synthesize large, acicular template particles (e.g.,  $\text{SrNb}_2\text{O}_6$ ,  $\text{Sr}_{0.50}\text{Ba}_{0.50}\text{Nb}_2\text{O}_6$ , and  $\text{KSr}_2\text{Nb}_5\text{O}_{15}$  (isostructural with SBN)) that are suitable for orientation and templated grain growth of SBN53 ceramics.

### 3.2 EXPERIMENTAL PROCEDURE

Alkaline and alkaline earth metal chloride salts such as KCl (Alfa Products), NaCl (Alfa Products), LiCl (Baker Analyzed), and  $\text{SrCl}_2 \cdot 6\text{H}_2\text{O}$  (Aldrich) were used to synthesize anisometric particles in the SrO-BaO-Nb<sub>2</sub>O<sub>5</sub> system. As constituent oxides, SrCO<sub>3</sub> (Alfa Products), BaCO<sub>3</sub> (J. T. Baker), Nb<sub>2</sub>O<sub>5</sub> (Ceramic grade, H.C. Starck), SrNb<sub>2</sub>O<sub>6</sub> (SN), and Sr<sub>0.50</sub>Ba<sub>0.50</sub>Nb<sub>2</sub>O<sub>6</sub> (SBN50) powders were used. SN was prepared by ball milling SrCO<sub>3</sub> and Nb<sub>2</sub>O<sub>5</sub> for 24 h in ethanol using zirconia balls. The ethanol was evaporated during fast stirring to avoid differential settling. The powder mixtures were dried at 100°C for 24 h, and calcined at 1050°C for 5 h. SBN50 was prepared in the same way as SN by mixing SrCO<sub>3</sub> (S), Nb<sub>2</sub>O<sub>5</sub> (N), and BaCO<sub>3</sub> (B), and then calcining at

1200°C for 5 h. X-ray diffractometry (XRD) showed the formation of single phase SN and SBN powders.

For each mixture, the metal salts and reactant(s) at different salt to powder ratios (R) by weight were hand-ground in a mortar and pestle for 30 min and then put into an Al<sub>2</sub>O<sub>3</sub> crucible. The crucible was covered with a flat Al<sub>2</sub>O<sub>3</sub> lid and sealed with Al<sub>2</sub>O<sub>3</sub> cement (Saint-Gobain/Norton Industrial Ceramic Corporation) to minimize salt evaporation. The assemblage was heated at 5°C/min to 900-1100°C and held for 1 to 6 h, and then cooled to ambient temperature at a cooling rate (CR) of 1 to 3°C/min. As-synthesized single crystal particles were washed ~8 times with hot deionized water, and sonicated for 20 min to dissolve the remaining salt on the particles and to deagglomerate the clumped needles. As-synthesized particles were characterized for phase formation and morphology by using XRD and scanning electron microscopy (SEM).

### **3.3 RESULTS AND DISCUSSION**

#### **3.3.1 Effect of Molten Salt Composition**

Since anisometric particles are required for TGG templates, the initial screening was done on the basis of particle morphology. LiCl + SBN50 mixtures (R = 1) formed cubic LiNbO<sub>3</sub> particles when heated to 800 - 1100°C and held for 6 h (CR = 2). Small needlelike SBN50 particles ( $\leq 3 \mu\text{m}$  in length) were obtained in NaCl + (SrO+BaO+Nb<sub>2</sub>O<sub>5</sub>)50 or NaCl + SBN50 mixtures (R = 1) heat-treated at 1100°C for 4 h (CR = 2). Reacting NaCl + SN mixtures (R = 1) from 900 to 1100°C for 4 h (CR = 2) yielded single phase SN, but with equiaxed morphology. No shifts in the XRD peak

positions (with respect to the positions given in the respective JCPDS cards) of the SBN50 and SN were observed. Because anisometric particles could not be synthesized using either LiCl or NaCl salts, further efforts were concentrated on the KCl and  $\text{SrCl}_2 \cdot 6\text{H}_2\text{O}$  salts because they have common cations to the product phases.

### 3.3.2 Molten Salt Synthesis in KCl

To prepare acicular SBN50 particles, SBN50 or (S+B+N)50 powders were mixed with KCl at various salt to powder ratios (e.g.,  $R = 1$  to 2.5) and then heat-treated at  $1100^\circ\text{C}$  for 3 to 8 h ( $CR = 1$  to 3). Figure 3.1 depicts the XRD pattern (indexed to the SBN50 composition (JCPDS # 39-265)) and SEM micrograph of SBN50 needles from KCl + (S+B+N)50 mixture ( $R = 1$ ) synthesized at  $1100^\circ\text{C}$  for 4 h ( $CR = 1$ ). Once formed, the SBN50 needles were always  $\leq 3 \mu\text{m}$  in length regardless of the  $R$ ,  $CR$ , and SBN form (e.g., precalcined or individual oxides), which indicates that SBN50 is not very soluble in KCl.

In order to increase the size of the particles, seeded MSS was performed. Equal weights of needlelike SBN50 (Fig. 3.1) and (S+B+N)50 were mixed with KCl ( $R = 1$ ) and then reacted at  $1100^\circ\text{C}$  for 4 h. Again, single phase SBN needles  $\leq 3 \mu\text{m}$  in length were obtained even at a very slow cooling rate of  $1^\circ\text{C}/\text{min}$ . This suggests that the final product phase (or seed) does not behave as nucleation sites for further growth, and that the nucleation frequency to form SBN50 from the reactant oxides is higher. A slight shift in the XRD peak positions was observed, which may indicate that either SBN forms with a different Sr/Ba ratio (other than SBN50) or  $\text{K}^+$  incorporates into the SBN lattice.

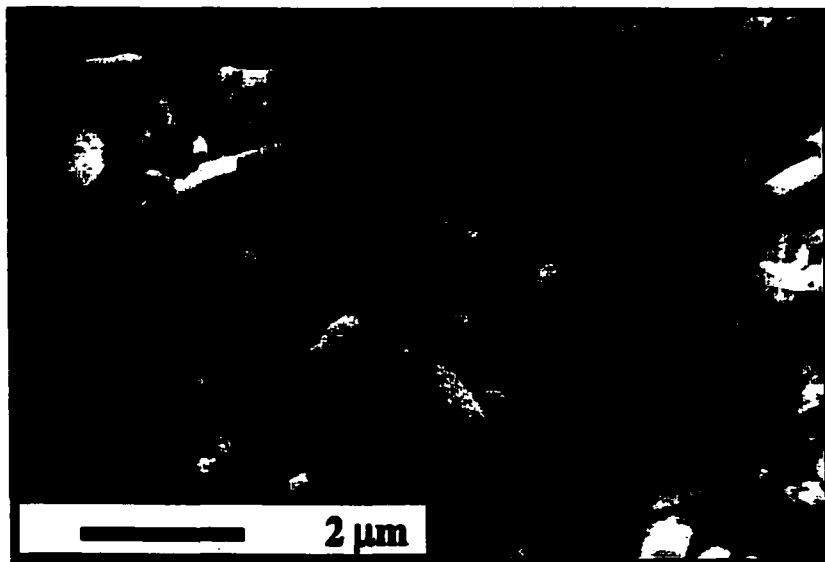
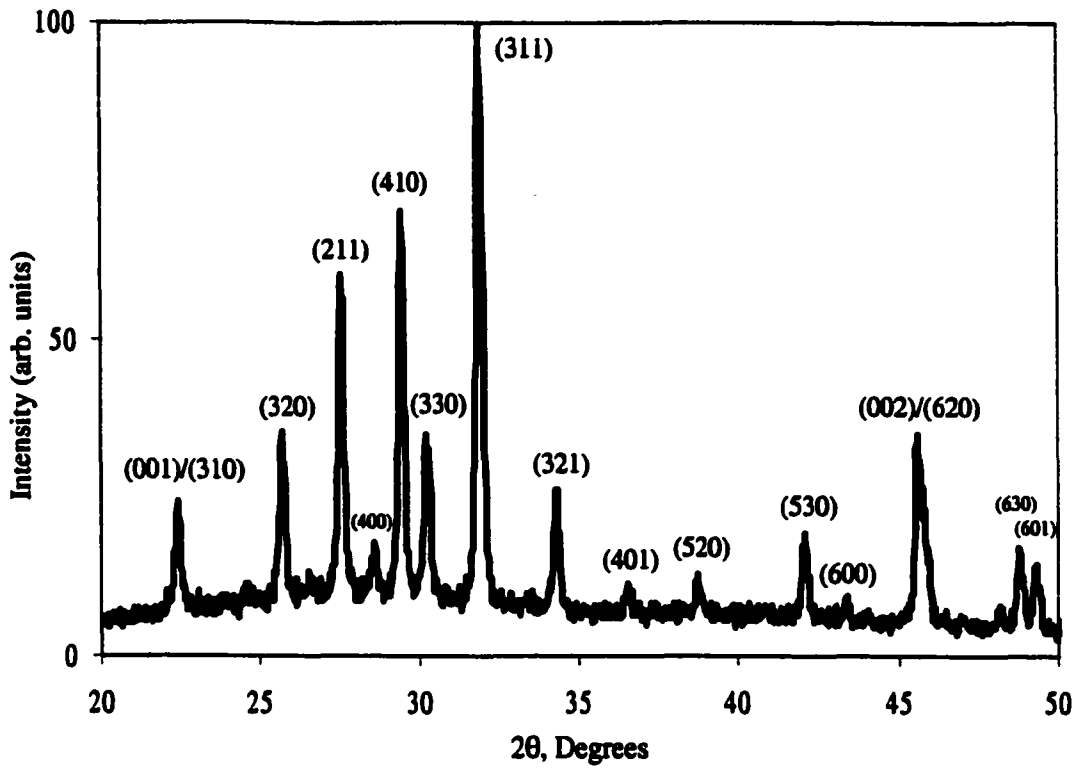
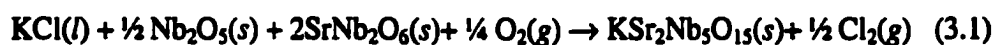


Figure 3.1. XRD pattern (top) and SEM micrograph (bottom) of SBN50 needles from a  $\text{KCl}+(\text{S}+\text{B}+\text{N})50$  mixture ( $R = 1$ ) heat treated at  $1100^\circ\text{C}$  for 4 h ( $\text{CR} = 1$ ). Peaks are indexed to the SBN50 composition.

Figure 3.2 shows a temperature-time diagram for the KCl + SN system ( $R = 1$  and  $CR = 2$ ). The numbers at each point indicate the ratio of  $KSN/SN/Sr_2Nb_2O_7$  ( $SN^*$ ), which was qualitatively determined from the main XRD peak heights. Figure 3.3 shows the phase and morphology evolution as a function of reaction temperature (for 4 h). With increasing temperature and time, first KSN and then  $SN^*$  start to form, and they increase in amount. This may indicate that SN has some solubility in the molten KCl. At 900 and 1000°C, only SN is present in the form of  $\sim 1 \mu m$  equiaxed particles (Fig. 3.3a). SrO has a solubility of  $\sim 0.2 \text{ g}/(100 \text{ g of KCl})$  at 800°C and  $1 \text{ g}/(100 \text{ g of KCl})$  at 1100°C [22]. Therefore, an appreciable amount of Sr-rich  $SN^*$  forms at higher temperatures and longer times. This may take place either by diffusion of strontium and oxygen ions onto the SN particles or by a solid-state reaction between SrO and SN.

$Nb_2O_5$  is reported to be insoluble in alkaline chlorides [23]. Therefore, KSN may possibly form by



It seems that KSN formation is a melt-aided reaction rather than a crystallization process. No phases in the K-Nb system were observed by XRD, which indicates that KSN forms directly according to Eqn. (3.1). The reaction takes place at the bottom of the crucible due to the density difference between the salt (1.98 g/cc) and the solid phases (density ( $Nb_2O_5$ ) = 4.47 g/cc and  $SN = 5.16 \text{ g/cc}$ ). Note that the KSN needles (Fig. 3.3b-d) appear to be thicker due to aggregation of several individual needles, possibly due to multiple nucleation sites when the KSN phase forms. At 1100°C (Fig. 3.3d), acicular particles range from 3 to 20  $\mu m$  in length. Smaller particles are the unreacted SN phase.

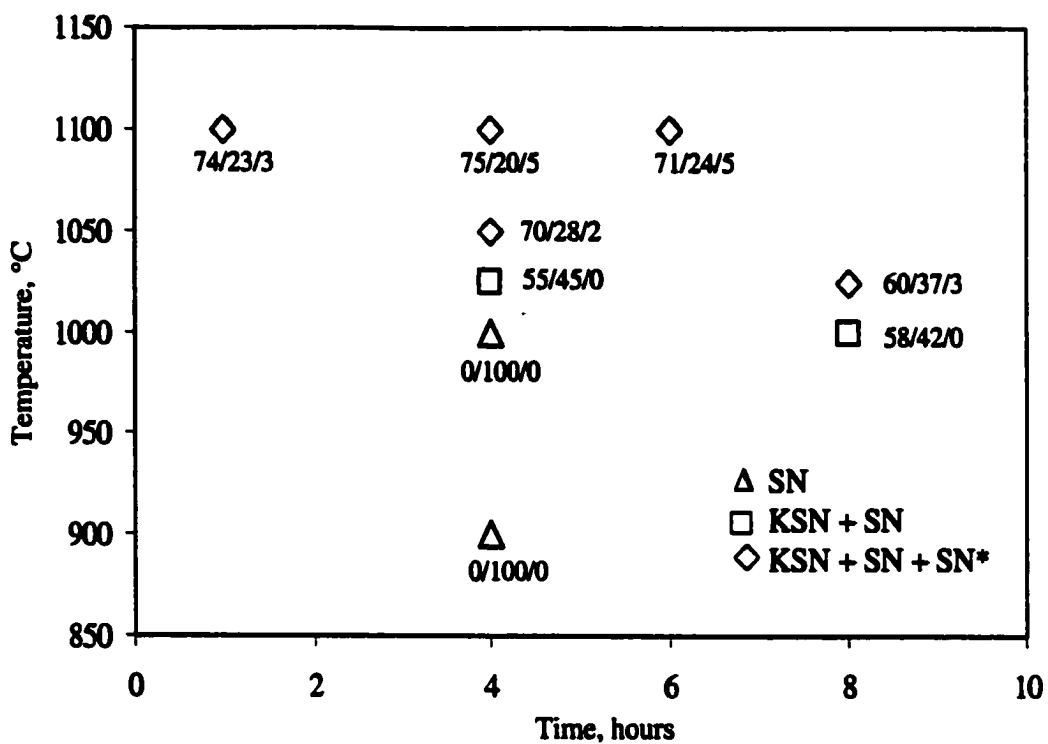


Figure 3.2. Temperature-time diagram for the KCl+SN system ( $R = 1$  and  $CR = 2$ ). SN is  $\text{SrNb}_2\text{O}_6$ , KSN is  $\text{KSr}_2\text{Nb}_5\text{O}_{15}$ , and SN\* is  $\text{Sr}_2\text{Nb}_2\text{O}_7$ . The ratio given is KSN/SN/SN\*.

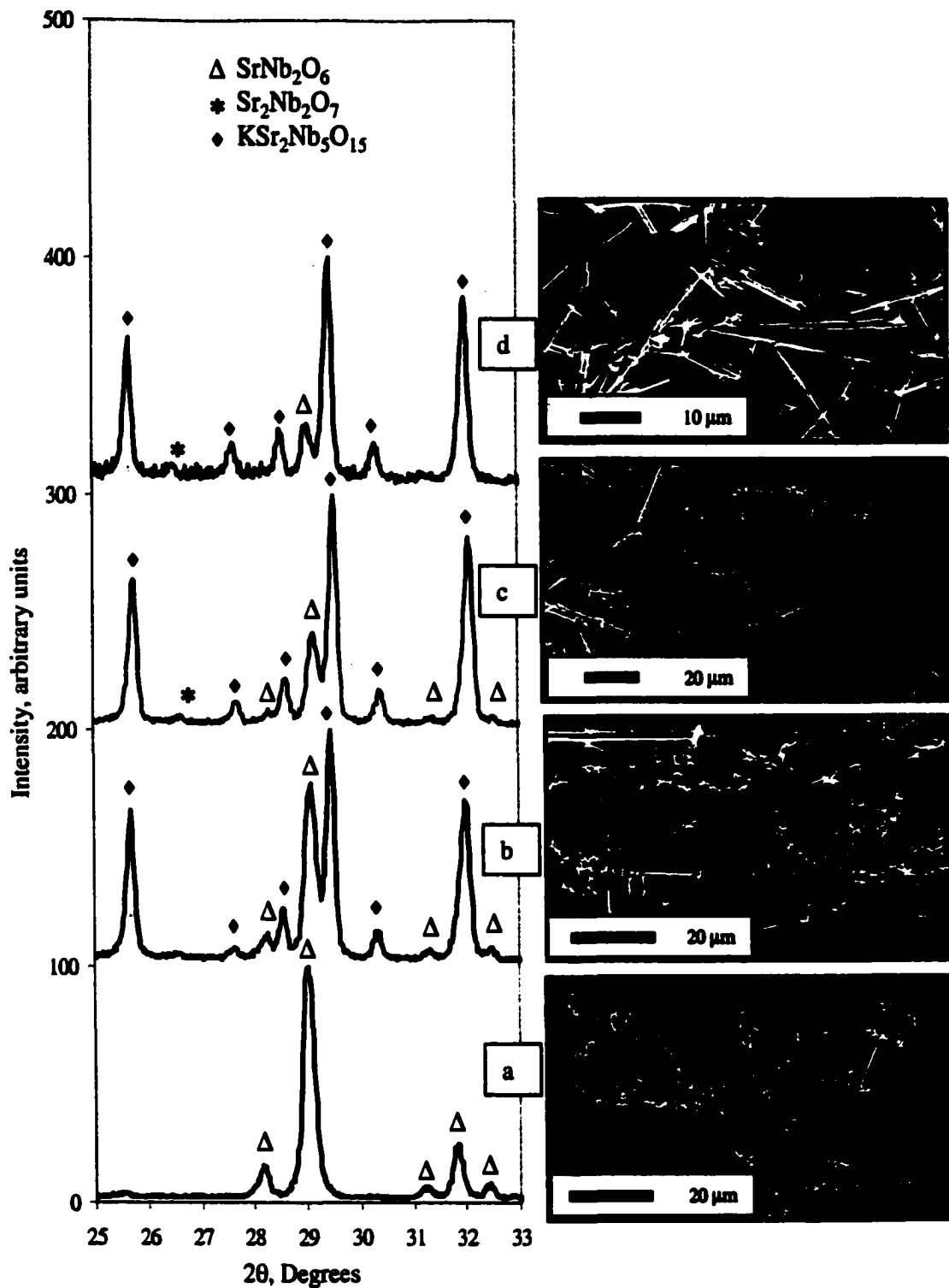


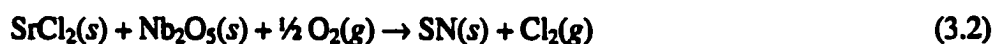
Figure 3.3. Phase and morphology evolution in KCl + SN system; (a) 900°C, (b) 1025°C, (c) 1050°C, and (d) 1100°C for 4 h.  $R = 1$  and  $CR = 2$ .



Decreasing R to 0.6 at 1100°C resulted in considerable reduction of the KSN phase (47/50/3) due to lower potassium ion concentration in the medium. In addition, more needles were stuck together when less liquid was present.

### 3.3.3 Molten Salt Synthesis in SrCl<sub>2</sub>·6H<sub>2</sub>O

Figure 3.4 shows a temperature-time diagram for the SrCl<sub>2</sub>·6H<sub>2</sub>O + N system (R = 2 and CR = 2). R = 2 was selected because the salt behaves both as a reaction medium and the Sr<sup>2+</sup> ion source for the product phase. The numbers at each point again indicate the fractional ratio of SN/SN\* phases. SN\* formation takes place with increasing reaction temperature and time. Figure 3.5 shows the phase and morphology evolution as a function of reaction time at 1050°C. In contrast to small, equiaxed SN in the KCl system (Fig. 3.3a), acicular SN particles were synthesized in the SrCl<sub>2</sub>·6H<sub>2</sub>O system because particle growth in the molten salt tends to reflect the crystal symmetry (SN is an orthorhombic crystal). The needles vary greatly in size and small ones (~1-3 μm) are lumpy at 900°C (for 1 h) but they grow in size with temperature and time (Figure 3.5a). After 8 h of reaction time, big SN\* particles with an irregular morphology were formed (Fig. 3.5b). Brahmaroutu *et al.* [19] determined by thermogravimetry and XRD that the possible reactions in the SrCl<sub>2</sub> + N (4:1 molar ratio or R = 2.5) system are:



SN forms at about 550-750°C by a solid-state process (the melting temperature of SrCl<sub>2</sub> is 875°C) (Eqn. 3.2). Reaction of SN and SrCl<sub>2</sub> above the melting temperature results in

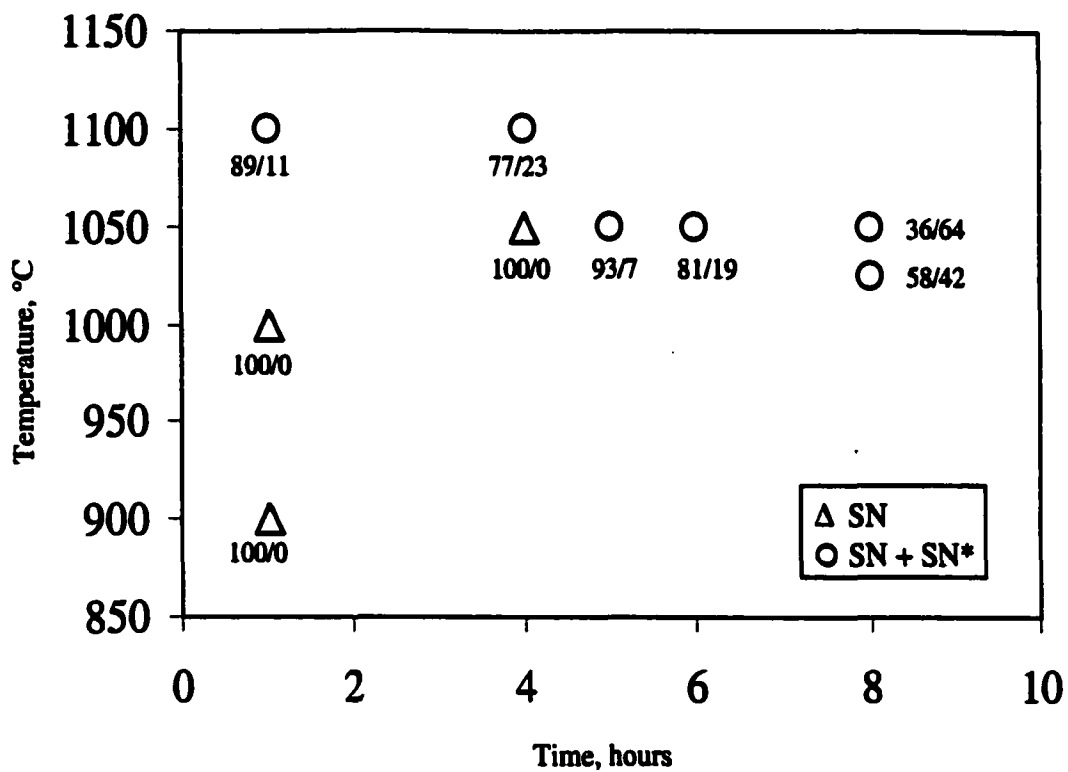


Figure 3.4. Temperature-time diagram for the  $\text{SrCl}_2 \cdot 6\text{H}_2\text{O} + \text{Nb}_2\text{O}_5$  system ( $R = 2$  and  $CR = 2$ ). SN is  $\text{SrNb}_2\text{O}_6$  and SN\* is  $\text{Sr}_2\text{Nb}_2\text{O}_7$ . Ratio is SN/SN\*.

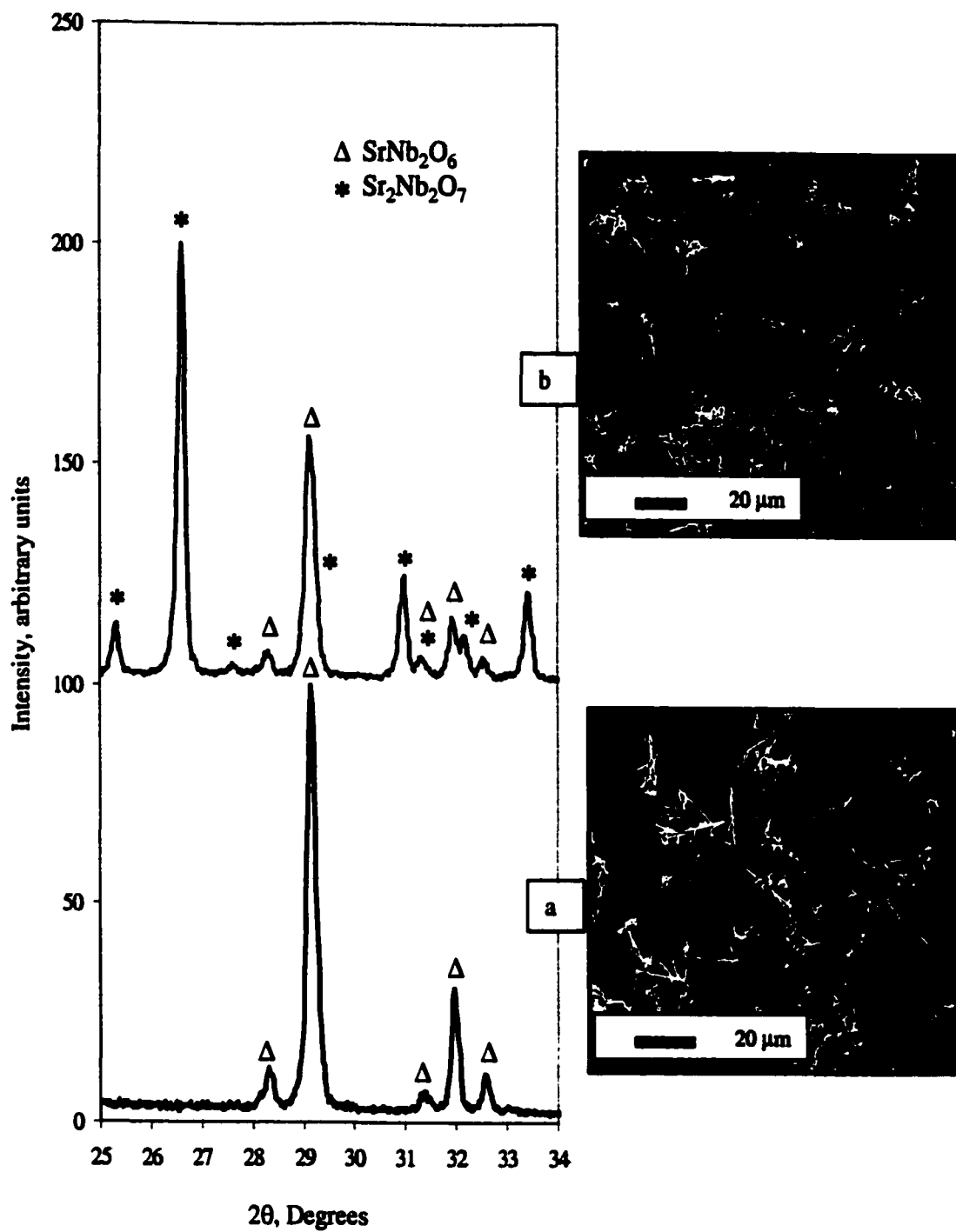


Figure 3.5. Phase and morphology evolution in the  $\text{SrCl}_2 \cdot 6\text{H}_2\text{O} + \text{Nb}_2\text{O}_5$  system; (a) 4 h and (b) 8 h at  $1050^\circ\text{C}$ .  $R = 2$  and  $\text{CR} = 2$ .

the formation of Sr-rich SN\* (Eqn. 3.3). In our case, the retardation of SN\* formation to higher temperatures and times (Fig. 3.4) is due to a lower SrCl<sub>2</sub> + N ratio (2:1 molar ratio or R = 1.2 by weight, excluding H<sub>2</sub>O). They also reported that formation of SN and SN\* depends on the initial SrCl<sub>2</sub>:N ratio. Diffusivity of Sr<sup>2+</sup> and O<sup>2-</sup> ions near the surface of the SN particles is the rate-limiting step. Since diffusion increases with reaction conditions, so does SN\* formation. These results indicate that the kinetics of the different reactions and relative thermodynamic stability of the phases at various reaction conditions control phase formation in this system.

### 3.3.4 Physical Separation of Anisotropic Particles

A simple sedimentation method was used to separate smaller SN particles from the KSN and SN\* because it is very difficult to orient templates with low aspect ratio during tape casting. After washing, as-synthesized particles were sonicated for 20 min., and the supernatant was removed quickly with a pipette after several minutes. Figure 3.6 shows the effect of separation on particles synthesized at 1100°C for 6 h (R = 1 and CR = 2). As-synthesized particles have a relative KSN/SN/SN\* ratio of 71/24/5 (Fig. 3.2) and SEM shows that there are many smaller (e.g., SN) particles (Fig. 3.6a). After separation, large KSN needles and blade-like SN\* particles (arrowed in Fig. 3.6b) remained as sediment and smaller SN particles remained suspended in the supernatant (Fig. 3.6c). The peak ratio is 63/36/1 for the supernatant and 73/15/12 for the sediment particles, which shows that particles with low aspect ratio can be separated by this method. Note that SN\* particles synthesized in the KCl + SN system have a well-defined rectangular-platelet

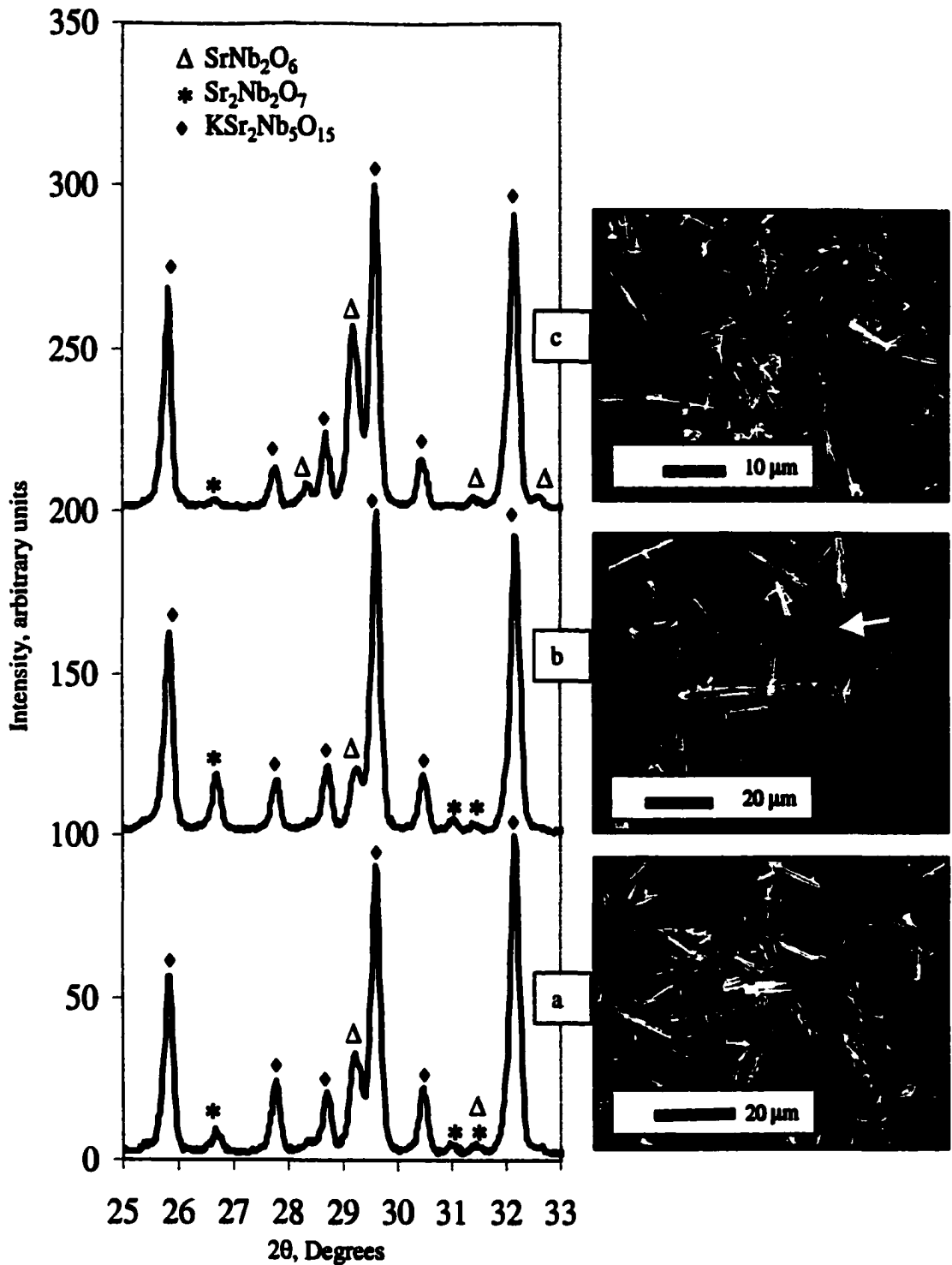


Figure 3.6. Effect of physical separation on the particles synthesized at 1100°C for 6 h ; (a) As-synthesized, (b) sediment, and (c) supernatant particles.  $R = 1$  and  $CR = 2$ .

morphology compared to the large, irregularly shaped SN\* in the  $\text{SrCl}_2 \cdot 6\text{H}_2\text{O} + \text{N}$  system (Fig. 3.5b).

It was seen in the KCl + SN system that the KCl salt behaves as both a reaction medium and the  $\text{K}^+$  source for KSN template formation. Although the alumina crucible was sealed with alumina cement to minimize salt evaporation, it was very difficult to retain the salt at high reaction temperatures due to its high vapor pressure. Evaporation of the salt reduces the number of the  $\text{K}^+$  ions available for the KSN needle formation according to Eqn. (3.1). To compensate for the evaporation, the salt to powder ratio was increased to 1.25, and then the mixture was reacted at  $1100^\circ\text{C}$  for 6 h (CR = 2). Figure 3.7 shows KSN particles after the physical separation. XRD shows that the relative peak ratio is 93/0/7, that is, there was no SN detected by XRD. The pattern is indexed to the KSN composition (JCPDS Card # 34-108). The most intense peak is (410), instead of (311)/(420), and the intensity of (211) decreases by more than half, which indicates that the fiber axis is along the crystallographic [001]. The SEM micrograph shows that the acicular particles are not clumped and range from 10 to 30  $\mu\text{m}$  in length. Therefore, in TGG experiments, acicular KSN particles were used because these particles are more uniform and the easier to reproduce in size relative to SBN50 and SN needles. In addition, KSN is isostructural with SBN (tetragonal tungsten bronze structure) with a polar axis in the  $c$  direction (i.e., [001]) and the lattice parameter difference between them is less than 0.5% in both  $a$  (or  $b$ ) and  $c$  directions at room temperature [24,25].

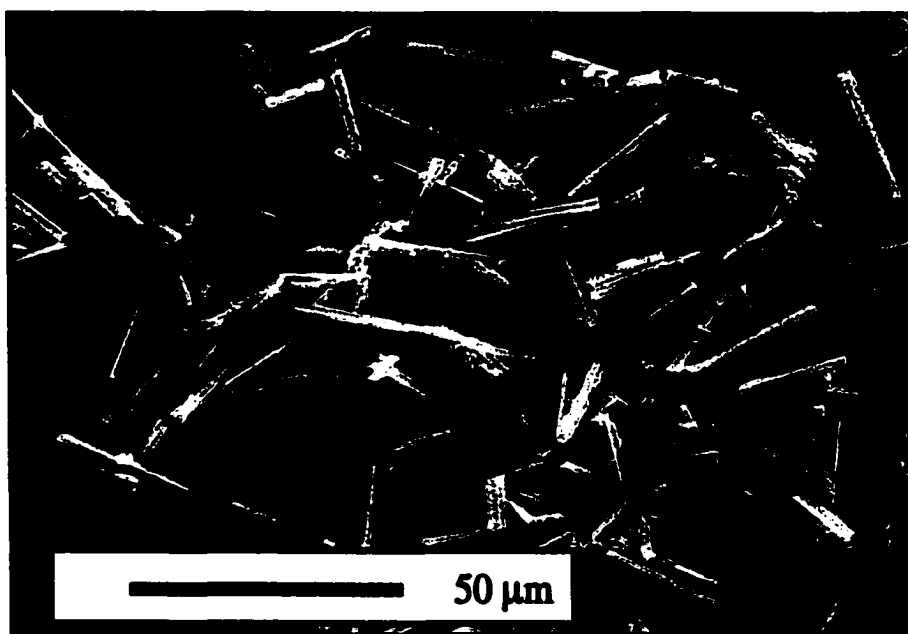
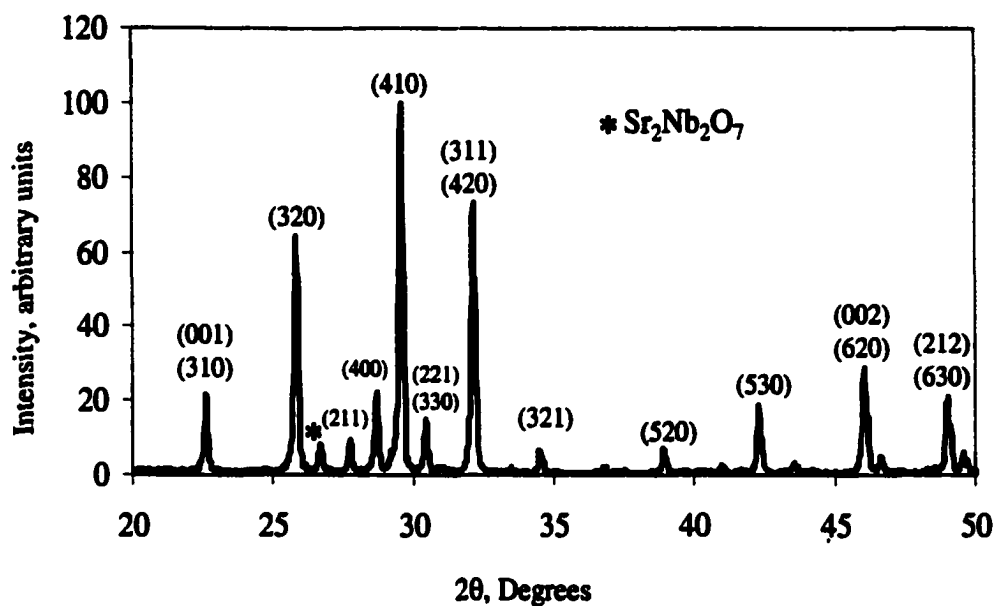


Figure 3.7. XRD pattern (top) and SEM micrograph (bottom) of KSN needles (sediment) from KCl + SN mixture ( $R = 1.25$ ) heat treated at  $1100^{\circ}\text{C}$  for 6 h ( $\text{CR} = 2$ ). Peaks are indexed to the KSN composition.

### 3.4 CONCLUSIONS

Particles (i.e., templates for TGG) such as  $\text{KSr}_2\text{Nb}_5\text{O}_{15}$ ,  $\text{Sr}_{0.5}\text{B}_{0.5}\text{Nb}_2\text{O}_6$ , and  $\text{SrNb}_2\text{O}_6$  were synthesized in the SrO-BaO-Nb<sub>2</sub>O<sub>5</sub> system, using alkaline (LiCl, NaCl, and KCl) and alkaline earth ( $\text{SrCl}_2 \cdot 6\text{H}_2\text{O}$ ) salts. No anisotropic particles were obtained using LiCl or NaCl salts. In the  $\text{SrCl}_2 \cdot 6\text{H}_2\text{O} + \text{Nb}_2\text{O}_5$  system (salt to powder ratio = 2), acicular  $\text{SrNb}_2\text{O}_6$  particles formed by a solid state reaction of the salt and Nb<sub>2</sub>O<sub>5</sub>. Large, irregularly-shaped (Sr-rich)  $\text{Sr}_2\text{Nb}_2\text{O}_7$  particles formed with increasing reaction temperature and time. Small but finite solubility of SrO in the KCl +  $\text{SrNb}_2\text{O}_6$  system (ratio = 1) favored the formation of acicular  $\text{KSr}_2\text{Nb}_5\text{O}_{15}$  and blade-like  $\text{Sr}_2\text{Nb}_2\text{O}_7$  particles (at higher temperatures).  $\text{SrNb}_2\text{O}_6$  particles were fine (~1 μm) for all conditions examined. KCl evaporation limited complete KSN formation but increasing the KCl content (ratio = 1.25) yielded more KSN. The physical separation of as-synthesized particles by differential settling in water eliminated almost all of the unreacted, smaller SN particles. Therefore, the KSN needles were selected as the most suitable templates for SBN53 matrix crystallization during TGG process.



### 3.5 REFERENCES

- 1- E. M. Sabolsky, A. R. James, S. Kwon, S. Trolier-McKinstry, and G. L. Messing, "Piezoelectric properties of <001> textured  $\text{Pb}(\text{Mg}_{1/3}\text{Nb}_{2/3})\text{O}_3\text{-PbTiO}_3$  ceramics," *Appl. Phys. Letters*, 78[17], 2551-53 (2001)
- 2 – K. Hirao, T. Nagaoka, M. E. Brito, and S. Kanzaki, "Microstructure control of silicon nitride by seeding with rodlike  $\beta\text{-Si}_3\text{N}_4$  particles," *J. Am. Ceram. Soc.*, 77[7], 1857-62, (1994)
- 3 – M. J. Sacks, G. W. Scheiffele, and G. A. Staab, "Fabrication of textured silicon carbide via seeded anisotropic grain growth," *J. Am. Ceram. Soc.*, 79[6], 1611-16, (1996)
- 4 – M. M. Seabaugh, I.H. Kerscht, and G. L. Messing, "Texture development by templated grain growth in liquid-phase-sintered  $\alpha$ -alumina," *J. Am. Ceram. Soc.*, 80[5], 1181-85, (1997)
- 5 – S.-H. Hong and G. L. Messing, "Development of textured mullite by templated grain growth," *J. Am. Ceram. Soc.*, 82[4], 867-72, (1999)
- 6 – H. Watanabe, T. Kimura, and T. Yamaguchi, "Particle orientation during tape casting in the fabrication of grain-oriented bismuth titanate," *J. Am. Ceram. Soc.*, 72[2], 289-93, (1989)
- 7 – C. G. Kang and S. S. Kang, "Effect of extrusion on fiber orientation and breakage of alumina short fiber composites," *J. Composite Mater.*, 28[2], 155-66, (1994)
- 8- C. Duran, S. Trolier-McKinstry, and G. L. Messing, "Fabrication and electrical properties of textured  $\text{Sr}_{0.53}\text{Ba}_{0.47}\text{Nb}_2\text{O}_6$  ceramics by templated grain growth," *J. Am. Ceram. Soc.*, 83[9], 2203-13 (2000)

- 9- B. Brahmaroutu, "Templated grain growth of textured strontium niobate ceramics," Ph.D. Thesis, The Pennsylvania State University (1999)
- 10- D. Elwell and H. J. Scheel, *Crystal growth from high-temperature solutions*, Academic Press, London (1975)
- 11- A. Linz, V. Belruss, and C. S. Naiman, "Solution-growth perovskites," *J. Electrochem. Soc.*, 112[6], 60-66C, (1965)
- 12- B. N. Roy, *Crystal growth from melts: Applications to growth of groups 1 and 2 crystals*, John Wiley & Sons Ltd., New York (1992)
- 13- S-I. Hirano, "Hydrothermal processing of ceramics," *Ceramic Bull.*, 66[9], 1342-50 (1987)
- 14- W. J. Dawson, J. C. Preston, and S. L. Swartz, "Processing issues of hydrothermal synthesis of dielectric powders," pp. 27-32 in *Ceramic Powder Science IV*, Vol.32, American Ceramic Society, Westerville, OH (1991)
- 15- R. H. Arendt, "The molten salt synthesis of single magnetic domain  $\text{BaFe}_{12}\text{O}_{19}$  and  $\text{SrFe}_{12}\text{O}_{19}$  crystals," *J. Solid State Chem.*, 8, 339-47 (1973)
- 16 - A. Aboujalil, J. P. Deloume, F. Chassagneux, J. P. Scharff, and B. Durand, "Molten salt synthesis of lead titanate ( $\text{PbTiO}_3$ ), Investigation of the reactivity of various titanium and lead salts with molten alkali-metal nitrides," *J. Mater. Chem.*, 8, 1601-606 (1998)
- 17- K. H. Yoon, Y. S. Cho, and D. H. Kang, "Review: Molten salt synthesis of lead-based relaxors," *J. Mater. Sci.*, 33, 2977-84 (1998)
- 18- C. C. Li, C. C. Chiu, and S. B. Desu, "Formation of lead niobates in molten salt systems," *J. Am. Ceram. Soc.*, 74, 42-47 (1991)

- 19** – B. Brahmaraoutu, G. L. Messing, and S. Trolier-McKinstry, “Molten salt synthesis of anisotropic  $\text{Sr}_2\text{Nb}_2\text{O}_7$  particles,” *J. Am. Ceram. Soc.*, 82, 1565-68 (1999)
- 20**- S. Hashimoto and A. Yamaguchi, “Synthesis of needlelike mullite particles using potassium sulfate flux,” *J. Eur. Ceram. Soc.*, 20, 397-402 (2000)
- 21**-R. H. Arendt, J. H. Rosolowski, and J. W. Szymaszek, “ PZT ceramics from molten salt solvent synthesized powders”, *Mat. Res. Bull.*, 14, 703-709 (1979)
- 22** - A. Packter, “The crystallization of alkaline-earth metal oxides from metal chloride melts: solubility-temperature phase diagram analyses and preliminary experimental studies,” *Krist. Tech.*, 15[4], 413-20 (1980)
- 23** – G. Picard and P. Bocage, “The niobium chemistry in molten LiCl + KCl eutectic,” *Mater. Sci. Forum*, 73-75, 505-12 (1991)
- 24**- R. R. Neurgaonkar, W. K. Cory, and J. R. Oliver, “Growth and applications of ferroelectric tungsten bronze family crystals,” *Ferroelectrics*, 51, 3-8 (1983)
- 25**- R. R. Neurgaonkar, J. R. Oliver, and L. E. Cross, “Ferroelectric properties of tetragonal tungsten bronze single crystals,” *Ferroelectrics*, 56, 31-36 (1984)

## CHAPTER 4

### REACTIVE SINTERING OF $\text{Sr}_{0.53}\text{Ba}_{0.47}\text{Nb}_2\text{O}_6$ CERAMICS

#### 4.1 INTRODUCTION

Reactive sintering is a process in which chemical reaction and densification are both achieved in the same heat treatment. The two steps can occur in sequence or concurrently, or some combination of these, depending on the material and processing variables [1]. For example, smaller particle size or external pressure increases the densification rate compared to the reaction rate [2].

Typically, reactive sintering is done by sintering either the constituent oxides or intermediate products [3,4], which eliminates the prereaction (or calcination) step(s) and imparts an additional driving force for sintering due to the free energy of the chemical reaction. However, difficulty and complexity in controlling the reaction processes may outweigh these advantages [1]. Yangyun and Brook [2], for example, reported that reaction sintering does not usually yield a chemically homogenous product with controlled microstructure. They further proposed that products with a high density and controlled microstructure can be obtained if the densification takes place before the chemical reaction. However, Rahaman and De Jonghe [1] found in  $\text{ZnO-Fe}_2\text{O}_3$  that the fundamental concept in reaction sintering is the degree of microstructural disruption caused by the chemical reaction because, in the case of no microstructural disruption, sintered ceramics with high density and controlled grain size are not dependent on whether the reaction occurs prior to, or after, the densification.

Reactive sintering has been applied to the sintering of  $(\text{Sr,Ba})\text{Nb}_2\text{O}_6$  (SBN) ceramics and was found to be better than conventional sintering in that the latter resulted in low densification and cracking due to abnormal grain growth [4-6]. In SBN formation from its respective oxides,  $\text{SrNb}_2\text{O}_6$  (SN) and  $\text{BaNb}_2\text{O}_6$  (BN) were reported to be the final reaction products [7]. Phase formation takes place by forming necks between the particles in the early stage of reactive sintering, and then compositional homogenization (e.g., chemical reaction) takes place as interdiffusion of ions occurs through these necks. It was found that the densification occurs very rapidly following homogenization as a result of the high driving force for the porous, fine-grained, and uniform microstructure [4].

In this chapter, the densification and kinetics of phase formation in SBN53 will be reported as a function of initial  $\text{KSr}_2\text{Nb}_3\text{O}_{15}$  (KSN) seed content (0 to 15.4 wt%) at constant heating rates of 4, 7, and 10 °C/min. KSN is a suitable seed material for SBN crystallization during reactive sintering because KSN has the same crystal structure (i.e., tetragonal tungsten bronze) as SBN and the lattice parameter difference between them is less than 0.5% in both  $a$  and  $c$  directions at room temperature [8,9]. It has also been shown that SBN60 single crystals can be used as a seed material to grow KSN single crystals by the Czochralski technique [10].

The effect a liquid phase on densification and reaction kinetics was also considered. In the literature, liquid phase sintering of SBN ceramics has been attempted, both intentionally and unintentionally, to promote densification at lower temperatures. Lee and Freer [5,6] reported that  $\text{Nb}_2\text{O}_5$ -excess grain boundaries gave rise to unintentional liquid formation at temperatures  $\geq 1260^\circ\text{C}$  in the conventional sintering of

SBN60 ceramics. Nishiwaki *et al.* [11-13] conventionally sintered SBN30 ceramics in the presence of PbO, Bi<sub>2</sub>O<sub>3</sub>, Nb<sub>2</sub>O<sub>5</sub>, and V<sub>2</sub>O<sub>5</sub> (0.5 or 1 mol %) and found that only Nb<sub>2</sub>O<sub>5</sub> and V<sub>2</sub>O<sub>5</sub> accelerated densification. Therefore, in this work V<sub>2</sub>O<sub>5</sub> and excess Nb<sub>2</sub>O<sub>5</sub> were used as liquid phase formers.

Fundamentally, the goal of this work was to determine how seeding and the presence of a liquid phase change the temperature for densification and phase transformation. Microstructure evolution was also studied. The electrical properties of random ceramics will be given in comparison to those of textured samples in Chapters 5 and 6.

## 4.2 EXPERIMENTAL PROCEDURE

SrNb<sub>2</sub>O<sub>6</sub> (SN) and BaNb<sub>2</sub>O<sub>6</sub> (BN) powders were used to prepare Sr<sub>0.53</sub>Ba<sub>0.47</sub>Nb<sub>2</sub>O<sub>6</sub> (SBN53) ceramics by reactive sintering. SN and BN were prepared separately by ball milling SrCO<sub>3</sub> (Alfa) or BaCO<sub>3</sub> (J.T. Baker) and Nb<sub>2</sub>O<sub>5</sub> (H.C. Starck, Ceramic grade) for 24 h in ethanol using zirconia balls. The ethanol was evaporated during fast stirring to avoid differential settling. The powder mixtures were dried at 100°C for 24 h, and calcined at 1050°C for 5 h. Using the same procedure, KSN powder was prepared by the solid state reaction of K<sub>2</sub>CO<sub>3</sub> (J. T. Baker), SrCO<sub>3</sub>, and Nb<sub>2</sub>O<sub>5</sub> at 1250°C for 5 h in a closed Al<sub>2</sub>O<sub>3</sub> crucible. X-ray diffraction (XRD) showed the formation of SN, BN, and KSN after calcination.

Appropriate amounts of SN, BN, and KSN powders were mixed with a vinyl-based (Ferro 73210) binder solution and (Ferro M1111) modifier (Electronic Materials Division, MSI products group, San Marcos, CA) for tape casting. For some compositions,

$V_2O_5$  (0.85 mole %) was added as a liquid phase former during sintering. Table 4.1 summarizes the sample designation, KSN concentration, and initial amount of additives in the SBN53 samples. Extra BN powder was added to the slurry to compensate for the strontium and niobium introduced by the KSN seeds. However, the potassium and some of the excess niobium from the KSN could not be removed from the final composition. Therefore, the concentration of  $K_2O$  and  $Nb_2O_5$  increases with increasing KSN concentration. The slurry was prepared by ball milling the powder mixture, binder solution, and modifier for 24 h in toluene using 1-mm zirconia balls. Tape casting for each slurry was performed on a glass substrate at a casting speed of 7 cm/sec and a blade gap of 200  $\mu\text{m}$ . After 24 h drying at room temperature, tapes were cut and laminated at 83 MPa. Organics were burned out by heating at 0.5  $^{\circ}\text{C}/\text{min}$  to 500 $^{\circ}\text{C}$  and then holding for 2 h.

For kinetic analysis, the samples were heated at 4, 7, and 10  $^{\circ}\text{C}/\text{min}$  to temperatures between 900 and 1450 $^{\circ}\text{C}$ , and then air-quenched. Initial and final dimensions in the thickness direction were measured and the amount of shrinkage was calculated. The sample density was determined by the Archimedes technique. The quenched samples were ground for XRD analysis. The scan rate was 1 $^{\circ}2\theta$  per min with a step size of 0.02 $^{\circ}$ . The strongest line intensities of SBN ( $2\theta = 32.054^{\circ}$ ) (JCPDS # 39-265), KSN ( $2\theta = 32.077^{\circ}$ ) (JCPDS # 34-108), SN ( $2\theta = 29.211^{\circ}$ ) (JCPDS # 28-1243), and BN ( $2\theta = 28.245^{\circ}$ ) (JCPDS # 32-77) were integrated to find the peak areas, using curve fitting. For BN, the second most intense peak was used because the main BN peak at  $2\theta = 29.625^{\circ}$  corresponds to the second most intense peaks of SBN and KSN. The fraction of SBN53 formed was calculated by comparing the integrated peak areas of the

**Table 4.1 Sample designation, KSN content, and additive contribution in SBN53.**

Sample Designation*	V <sub>2</sub> O <sub>5</sub> , wt%	KSN content, wt%	Additive Contribution, wt%	
			K <sub>2</sub> O	Nb <sub>2</sub> O <sub>5</sub>
R0	0	0	0	0
RV0	0.37			
R5	0	5	0.26	0.72
RV5	0.37			
R9	0	9.1	0.47	1.32
RV9	0.37			
R15	0	15.4	0.80	2.23
RV15	0.37			

\* R and RV denote V<sub>2</sub>O<sub>5</sub>-free and V<sub>2</sub>O<sub>5</sub>-containing samples, respectively.



(SBN and/or KSN) to SN + BN. For the compositions without KSN seeds (e.g., R0 and RV0), only the SBN peaks were used to determine the extent of phase formation. However, for the others, the sum of the SBN and KSN main peaks was used because their  $2\theta$  peak positions are too close to be distinguished.

A nonisothermal reaction kinetics equation, proposed by Lee and Fang [14], was used to find the activation energy. For a constant heating rate,  $\beta$ :

$$\ln [\beta \cdot (d\alpha/dT)] = \ln [A f(\alpha)] + (- Q/RT) \quad (4.1)$$

where A is a frequency factor, Q is the activation energy, R is the gas constant, T is the absolute temperature, and  $\alpha$  is the reaction fraction. The function  $f(\alpha)$  can be dependent on the particle size. The activation energy can be found by plotting  $\ln [\beta(d\alpha/dT)]$  vs.  $1/T$  at different heating rates for a constant  $\alpha$  value.

For sintering experiments, samples were heated at 7 °C/min to 1200-1400°C for 1 min to 12 h. For microstructure analysis, samples were polished to 0.3  $\mu\text{m}$  using fine  $\text{Al}_2\text{O}_3$  powder and then thermally etched 100°C below the sintering temperature for 1h.

## 4.3 RESULTS AND DISCUSSION

### 4.3.1 Densification and Reaction Kinetics in the Quenched Samples

#### 4.3.1.1 Densification Behavior

Figure 4.1 shows the densification behavior as a function of quenching temperature and composition, at a heating rate ( $\beta$ ) of 7 °C/min. The relative density was calculated based on the density of the SBN52 single crystal (5.33 g/cc) [25], which is close to the composition of interest. R0 and R15 samples have a steep increase in

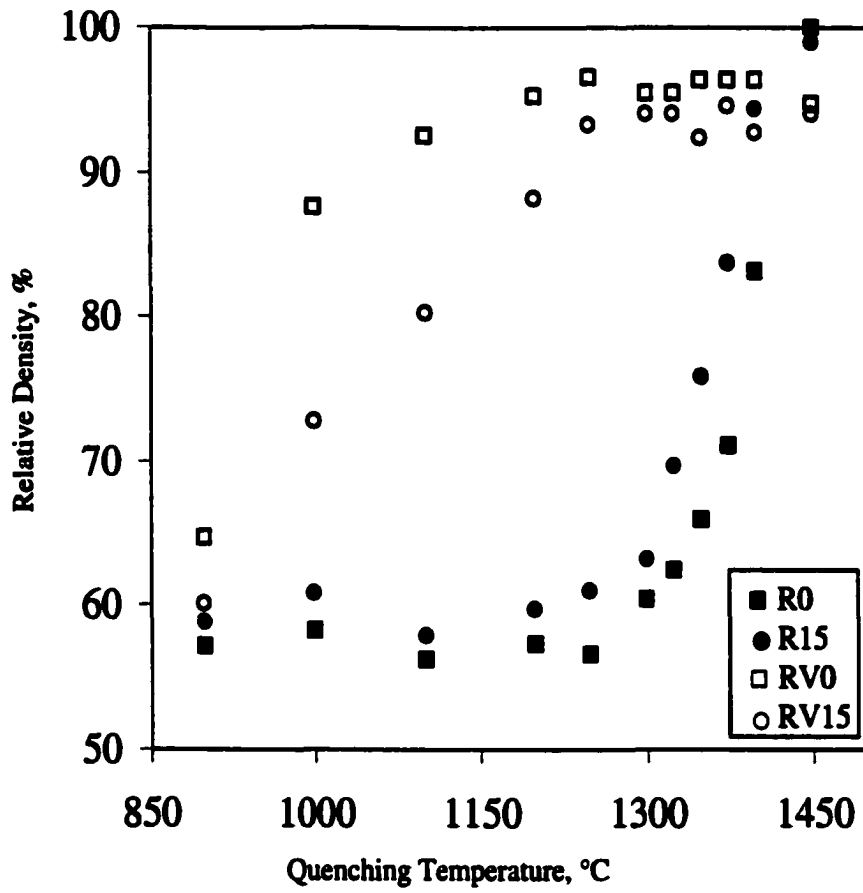


Figure 4.1. Densification graphs as a function of composition. Heating rate is 7°C/min.

densification after 1250 and 1200°C, respectively, and reach full density above 1400°C. Densification in the RV0 and RV15 samples, however, starts much earlier (just after 900°C) and increases continuously until 1200-1300°C, depending on the KSN content, and then remains constant. The onset of early densification in the RV0 and RV15 samples can be attributed to the melting of V<sub>2</sub>O<sub>5</sub> at 690°C. The density slightly increases with decreasing heating rate. It was found that KSN slows densification in the V<sub>2</sub>O<sub>5</sub>-containing samples, and improves it in the V<sub>2</sub>O<sub>5</sub>-free samples. The other samples with various amounts of KSN show trends in between the end member compositions. These data will be discussed in Section 4.3.2.1 together with the sintered samples.

All samples had nearly 17% shrinkage in the thickness direction upon full densification. In addition, densification curves indicate that there is no volumetric expansion during reactive sintering.

#### 4.3.1.2 Phase Formation

Figure 4.2 shows the XRD patterns for the RV0 samples at various stages of reaction fraction ( $\alpha$ ) at  $\beta = 4$  °C/min. The XRD pattern of the sample after burnout (500°C) is given as a reference for the  $\alpha = 0$  case. The amount of SBN53 increases with the reaction temperature. At 900°C, an unknown phase starts to appear and, at the same time, BN peaks disappear. The amount of this unknown phase first increases up to 1000°C and then gradually disappears at higher temperature. The other characteristic is that peak positions of the unknown phase steadily shift to higher diffraction angles with

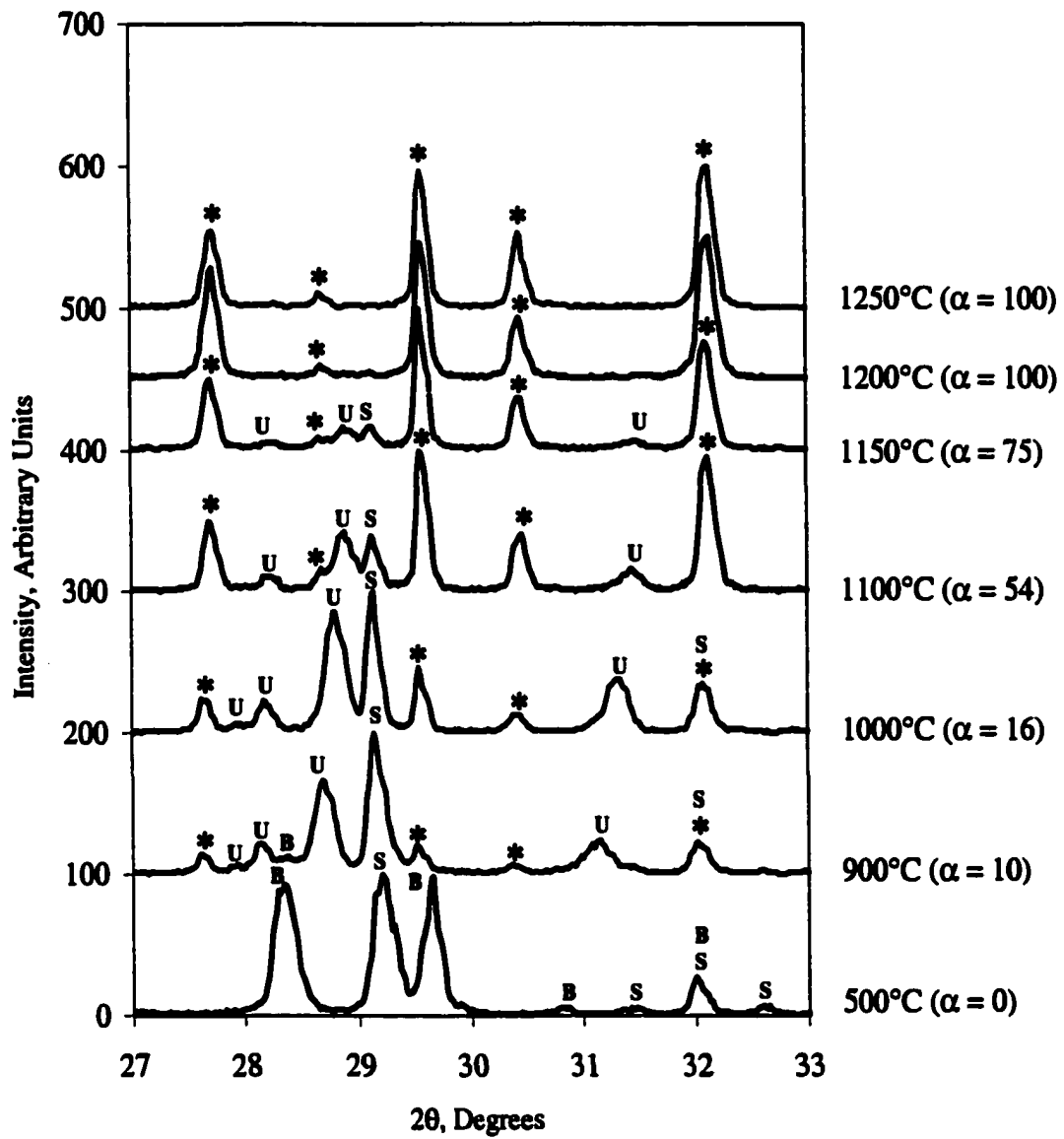


Figure 4.2. Phase evolution in the RV0 samples as a function of quenching temperature. Heating rate is 4°C/min. \* → SBN53, S → SN, B → BN, U → Unknown.  $\alpha$  is given in %.

temperature. Note that the integrated peak area of the most intense unknown phase was also taken into account in the calculation of  $\alpha$ .

Figure 4.3 shows that a higher seed content, assisted by a liquid, increases  $\alpha$  considerably (e.g., R0 vs. RV15 at the same temperature (1100°C)). It is apparent that the unknown phase also forms in the R0 samples but the BN peaks do not disappear. In both cases, the amount of the unknown phase decreases with increasing seed content and temperature, and its formation is almost independent of the heating rate. No phases in the SrO-BaO-Nb<sub>2</sub>O<sub>5</sub>-V<sub>2</sub>O<sub>5</sub> system were found to match the unknown phase.

The existence of the unknown phase has not been reported in the literature. Fang *et al.* [7] proposed that BaNb<sub>2</sub>O<sub>6</sub> (BN) and SrBa<sub>2</sub>O<sub>6</sub> (SN) are the last intermediate products in SBN50 formation from the respective oxides and that they form at 800-1100°C. The SBN50 forms by gradual consumption of SN and BN between 1000-1150°C. Nishiwaki *et al.* [11] reported that SrNb<sub>2</sub>V<sub>2</sub>O<sub>11</sub> and BaNb<sub>2</sub>V<sub>2</sub>O<sub>11</sub> form at 700 to 800°C and melt at around 900°C when V<sub>2</sub>O<sub>5</sub> (1 mol %) is present. In this study, however, the unknown phase forms even in the V<sub>2</sub>O<sub>5</sub>-free compositions, although the amount is small compared to the V<sub>2</sub>O<sub>5</sub>-containing samples. This indicates that the presence of a liquid favors the formation of this phase. The possible formation mechanism may be as follows; here it is assumed that the niobium ion diffusion is the rate-limiting species in sintering of SBN ceramics [15]. Because the strontium ion is smaller than the barium ion, strontium ions diffuse faster. Therefore, the unknown phase might form on the surface of the BN particles, and this process is accelerated by the liquid phase. The evidence is that the BN peaks disappear in the V<sub>2</sub>O<sub>5</sub>-containing samples (i.e., RV0 to RV15) and the intensity of the BN peaks decreases considerably in the V<sub>2</sub>O<sub>5</sub>-free samples (i.e., R0 to

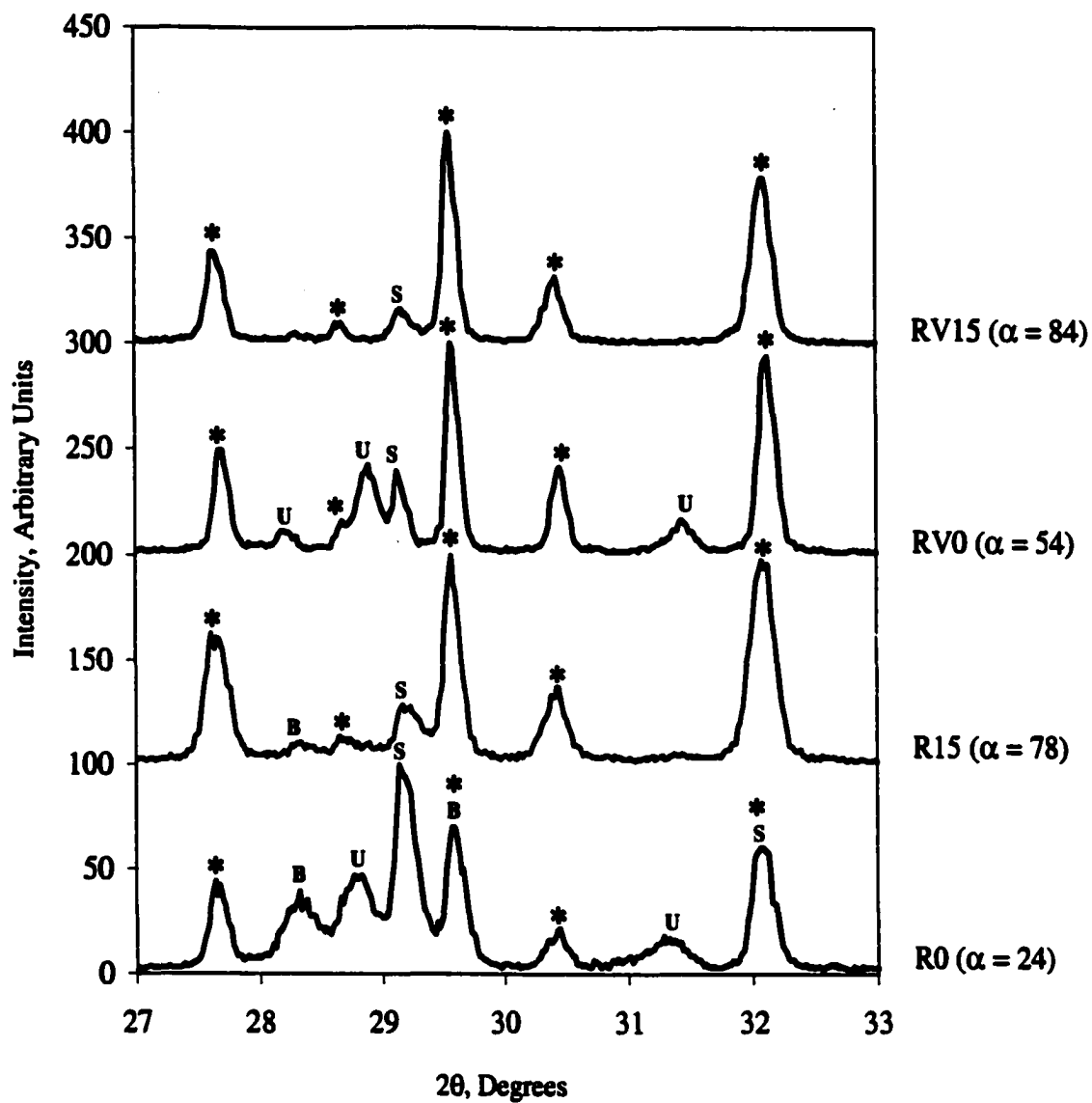


Figure 4.3. Phase evolution in the samples quenched from 1100°C. Heating rate is 4°C/min. \* → SBN53, S → SN, B → BN, U → Unknown.

R15). The formation of the unknown phase is consistently suppressed with increasing seed content (see Fig. 4.3) and, furthermore, is almost nonexistent in the R15 samples. The isostructural KSN seeds apparently prevent the formation of this phase and promote SBN53 formation. The SN-BN binary phase diagram [16] in Figure 4.4 shows that SN has some solubility in the BN and vice versa. SN and BN do not have the TTB structure as SBN. For example, SN has an orthorhombic crystal structure ( $a = 11$ ,  $b = 7.71$ , and  $c = 5.6$  Å (JCPDS# 28-1243)), BN has a monoclinic crystal structure ( $a = 10.43$ ,  $b = 6.03$ , and  $c = 3.95$  Å (JCPDS# 32-77)), and SBN50 has a tetragonal crystal structure ( $a = 12.46$  and  $c = 3.95$  Å (JCPDS# 39-265)). The unknown phase does not appear to be a solid solution based on BN, since the unknown phase XRD peaks do not show a 1:1 correspondence with BN. The lattice parameter of the unknown phase changes as the reaction temperature increases because the peak positions shift continuously to higher diffraction angles. More study is required to identify this unknown phase.

Table 4.2 shows the variation in the diffraction angle of the main peak (311) of SBN as a function of  $\alpha$  and composition at  $\beta = 4$  °C/min. The change in the diffraction angle ( $\Delta 2\theta$ ) between  $\alpha = 20$ -30 and 100 is very small, which indicates that the desired SBN composition forms directly, rather than via a variety of intermediate SBN solid solutions (i.e., other than SBN53). A similar result was also observed by Lee and Fang [4]. They also suggested that penetration of strontium and barium ions through the SBN phase during the reaction can cause a slight shift in the main peak position.

Figure 4.5 shows the reaction fraction ( $\alpha$ ) of SBN53 as a function of heating rate and seed content. The lines are drawn to guide the eye. The curves show a sigmoidal shape. For each composition,  $\alpha$  decreases with increasing heating rate at the same

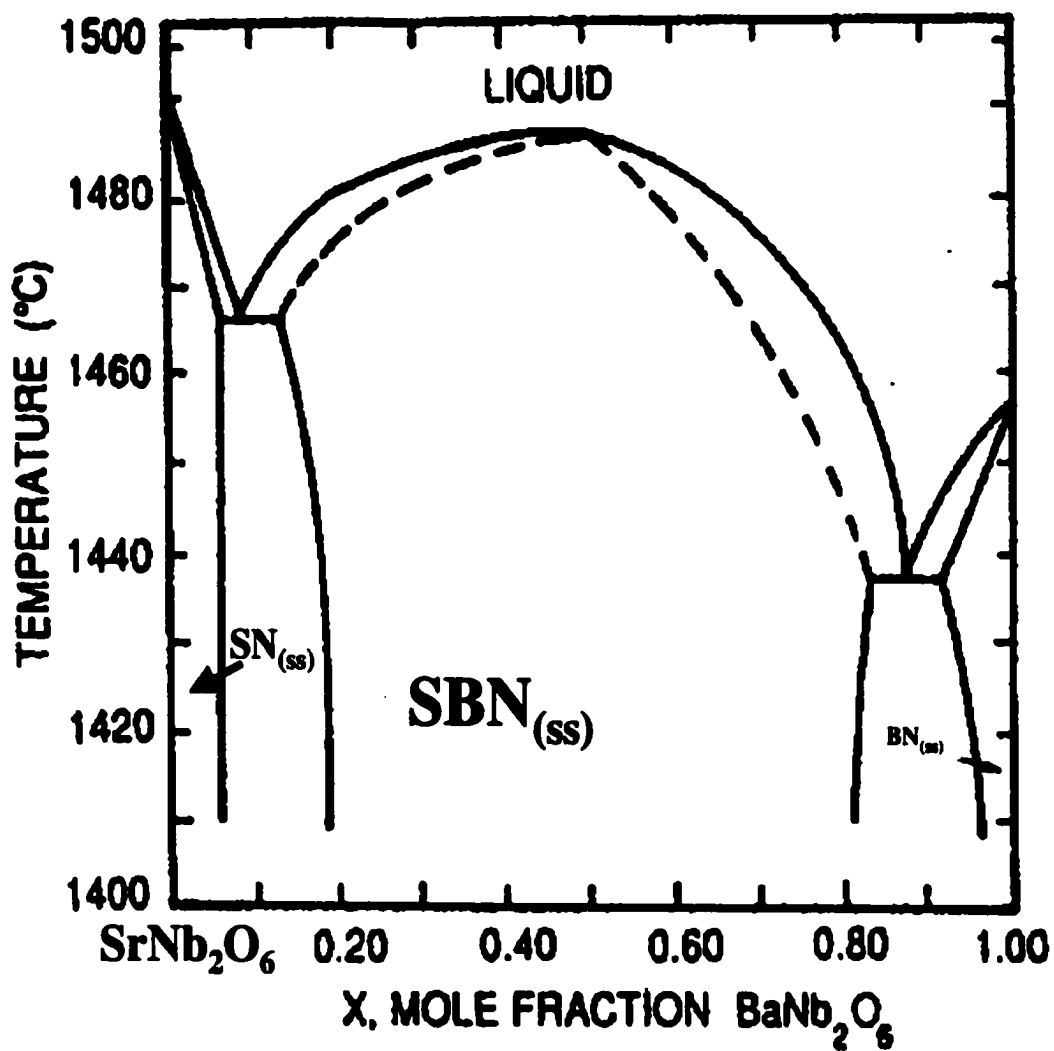


Figure 4.4. SrNb<sub>2</sub>O<sub>6</sub> (SN)-BaNb<sub>2</sub>O<sub>6</sub> (BN) binary phase diagram (From ref. 16).



**Table 4.2. Change in the diffraction angle ( $2\theta$ ) of the main peak (311) of the SBN.**

$\alpha$ <sup>#</sup>	R0 (°)	RV0 (°)	R15 (°)	RV15 (°)
20-30	32.06	32.08	32.14	32.08
70-80	32.10	32.10	32.08	32.10
100	32.14	32.14	32.12	32.10
$\Delta 2\theta$ <sup>*</sup> (°)	0.08	0.06	0.02	0.02

<sup>#</sup> At  $\beta = 4$  °C/min

<sup>\*</sup> Between  $\alpha$  values of 20-30 and 100

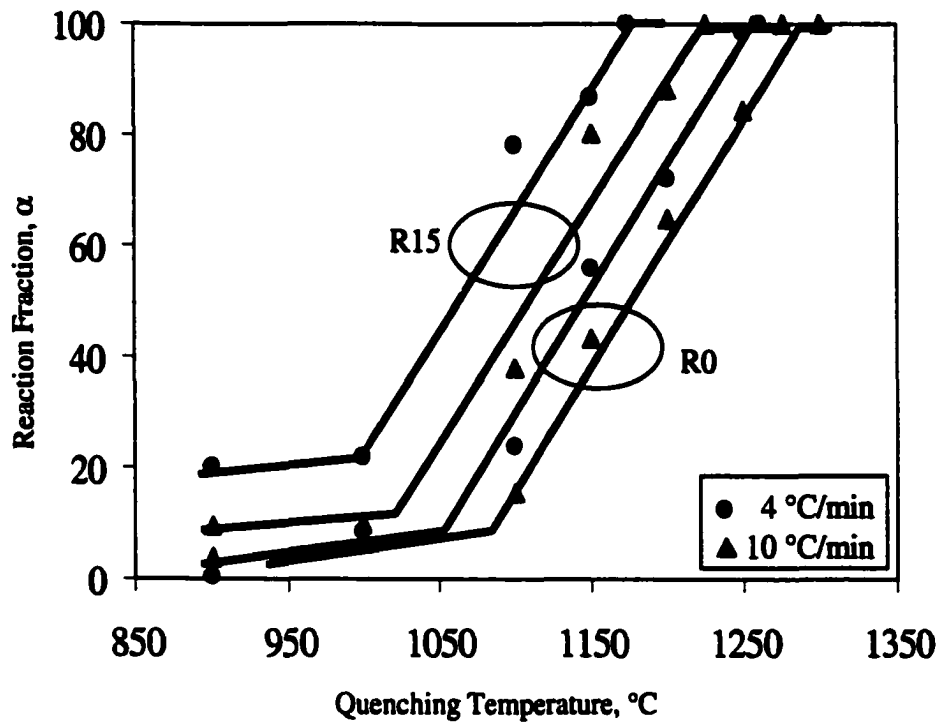


Figure 4.5. SBN53 formation ( $\alpha$ ) as a function of KSN content and heating rate.

temperature. In addition, increasing the seed content accelerates  $\alpha$  sharply; that is, SBN53 formation is promoted with increasing seed content and decreasing heating rate. For example, the R15 samples reach  $\alpha = 100$  at 1175°C ( $\beta = 4$  °C/min) compared to 1260°C ( $\beta = 4$  °C/min) and 1275°C ( $\beta = 10$  °C/min) in the R0 samples. Also, the temperature at which detectable reaction ( $\alpha \cong 20$ ) occurs decreases with increasing seed content. Figure 4.6 indicates that introduction of a liquid during the reaction drastically improves  $\alpha$  at lower temperatures ( $\beta = 4$  °C/min). The lines are again drawn to guide the eye. For instance, the phase formation is complete at 1260°C for the R0 samples and 1130°C for the RV15 samples. These results indicate that the phase formation gets easier because the liquid phase provides a path for faster transport and that the KSN seed particles lower the activation energy for the SBN formation by epitaxy.

Comparison of the densification (Fig. 4.1) and phase formation (Fig. 4.6) behaviors reveals that the presence of a liquid during the reaction sintering changes the sequence of whether the densification or the phase formation takes place first. For example, densification starts after 1250°C and phase formation ( $\alpha = 100$ ) is complete at 1275°C for the R0 samples ( $\beta = 7$  °C/min), which shows that phase formation is initiated prior to the densification. However, the densification and phase formation take place simultaneously in the RV0 samples because when the phase formation is finished at 1225°C ( $\beta = 7$  °C/min), the samples have already reached  $\geq 95$  % relative density. In both cases, ceramics with  $\geq 95$  % relative density were obtained, which indicates that it is not very critical whether the densification occurs prior to, simultaneously, or after the phase formation during the reactive sintering of SBN ceramics.

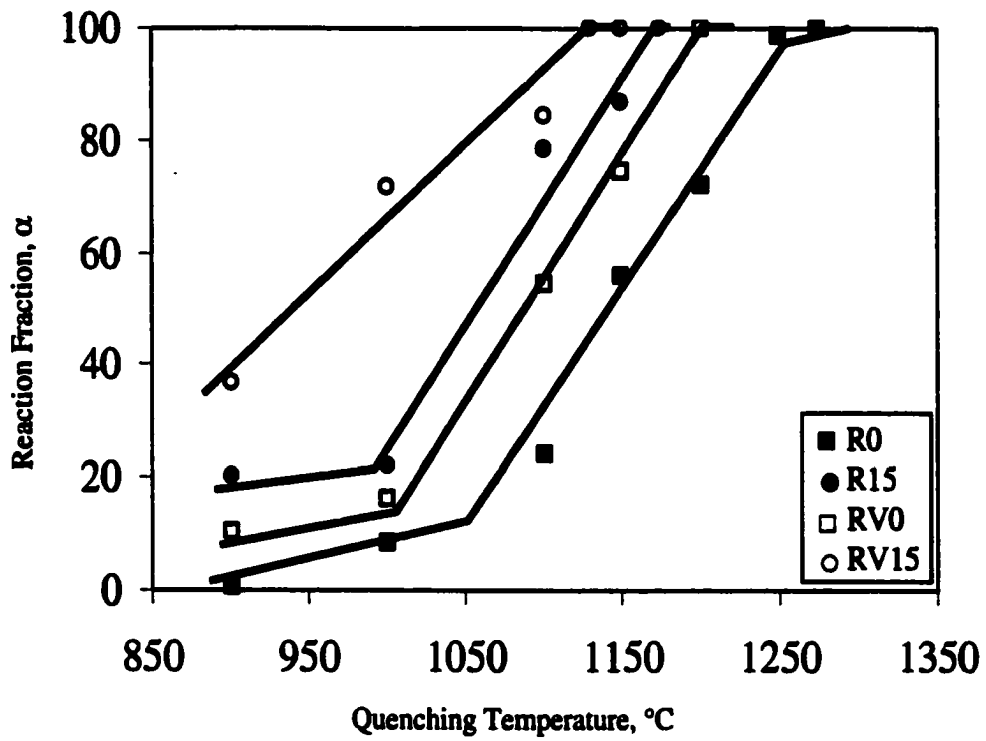


Figure 4.6. SBN formation as a function of KSN content at a heating rate of  $4^{\circ}\text{C}/\text{min}$ .

### 4.3.1.3 Reaction Kinetics

The activation energy was calculated using Eqn. (4.1) for the R0-R15 samples because the particle size increases only slightly ( $\sim \leq 2\text{-}3\ \mu\text{m}$ ) with temperature during SBN53 formation. Therefore, the  $f(\alpha)$  term can be considered constant at a fixed value of  $\alpha$  [14]. For the RV0-RV15 samples, however, particle (or grain) size changes considerably with temperature due to the melting of  $\text{V}_2\text{O}_5$  at  $690^\circ\text{C}$ , and hence the  $f(\alpha)$  term may not be constant.

Figure 4.7 shows a plot of  $\ln [\beta(d\alpha/dT)]$  vs.  $1/T$  at  $\beta = 4, 7, \text{ and } 10\ ^\circ\text{C}/\text{min}$  for the R0 samples at  $\alpha$  of 30, 50, and 70. The lines are results of linear curve fitting to experimental data at a given  $\alpha$ . The  $(d\alpha/dT)$  can be calculated from the slope of the lines in the  $\alpha$  vs.  $T$  plots (i.e., curve fitting to the linear section in Fig. 4.5). For each composition, the lines are parallel to each other at constant  $\alpha$ , which shows that one mechanism dominates during the reaction. Lee and Fang [14] also observed parallel lines for SBN50 to SBN70 compositions. Figure 4.8 indicates that the slope decreases with increasing KSN seed content. The activation energy calculated from the slopes of the  $\ln [\beta(d\alpha/dT)]$  vs.  $1/T$  plots is  $554 \pm 15\ \text{kJ/mol}$  for the R0,  $239 \pm 36\ \text{kJ/mol}$  for the R9, and  $241 \pm 17\ \text{kJ/mol}$  for the R15 samples. This result shows that introduction of isostructural KSN seed particles drastically decreases the energy barrier for SBN53 formation. An activation energy of  $735\ \text{kJ/mol}$  was reported for SBN50 formation in the literature [14]. The lower activation energy (i.e.,  $554 \pm 15\ \text{kJ/mol}$  for R0) obtained in this study may be

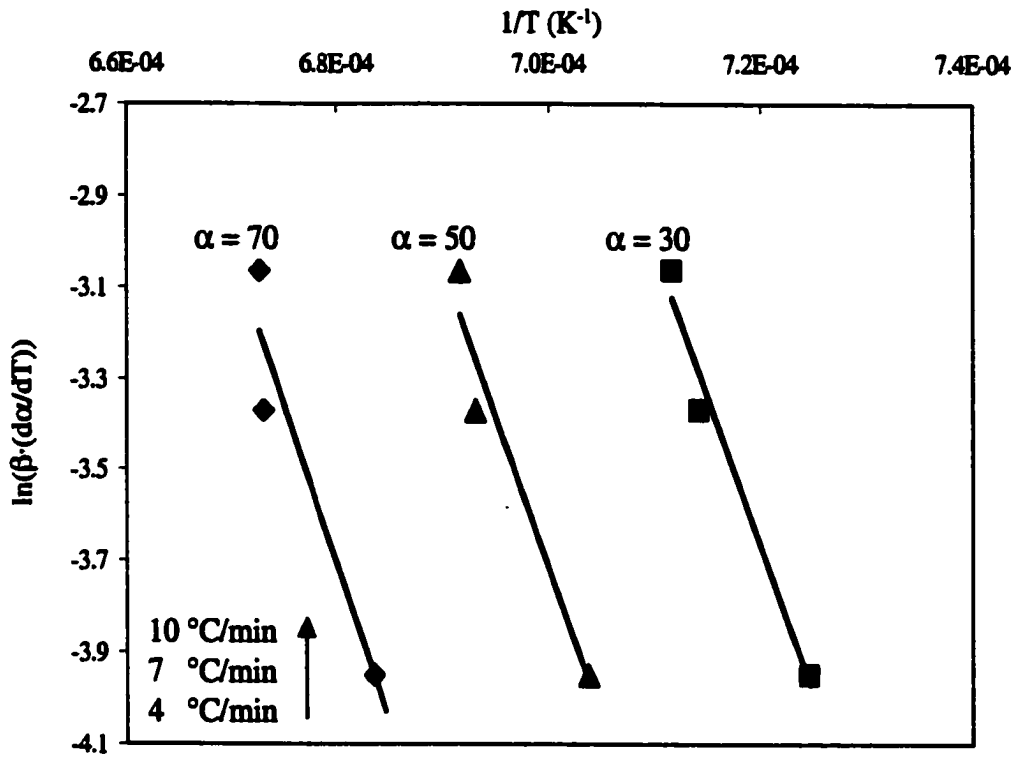


Figure 4.7. Plot of  $\ln(\beta \cdot (d\alpha/dT))$  vs.  $1/T$  for the R0 samples as a function of  $\alpha$  and  $\beta$ .

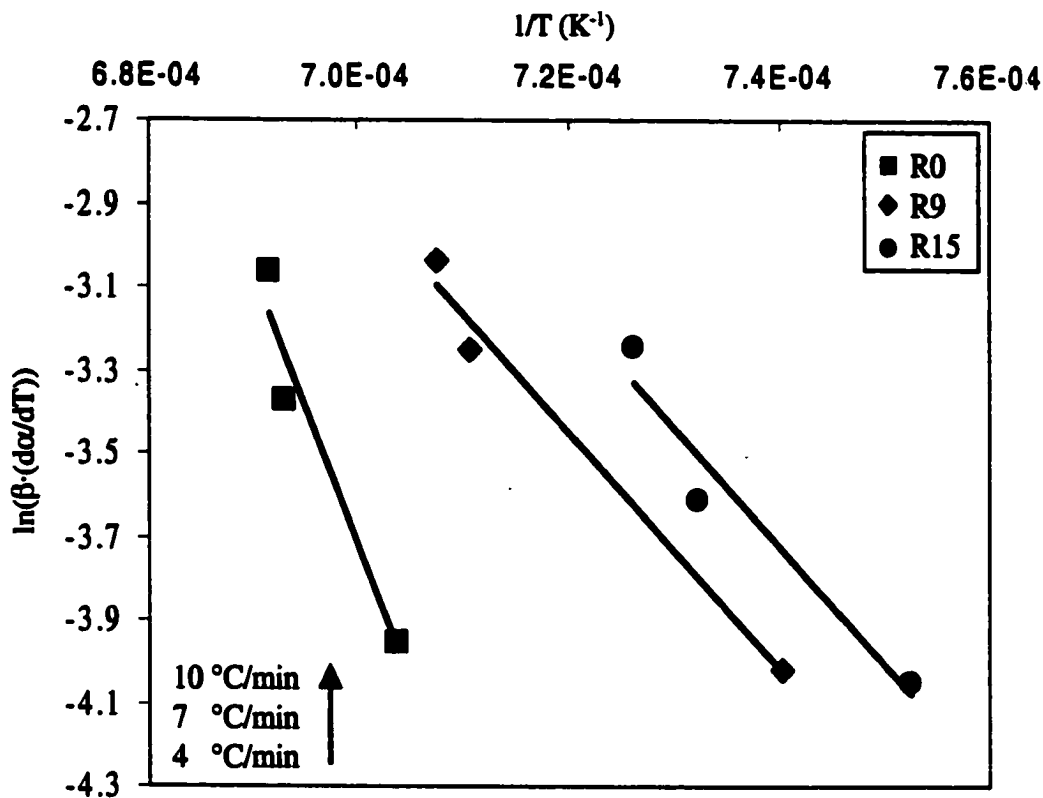


Figure 4.8. Plot of  $\ln(\beta \cdot (d\alpha/dT))$  vs.  $1/T$  as a function of heating rate at a constant  $\alpha = 50$ .

attributed to the difference in the processing variables such as green body formation (tape casting vs. dry pressing), initial particle size and mixing of the reactants.

It is expected that the  $V_2O_5$ -containing samples (RV0 to RV15) would have a lower activation energy because the liquid enables faster transport for SBN formation during the reaction. This conclusion is supported by the fact that the RV0 and RV15 samples have  $\alpha = 100$  at lower temperatures than R0 or RV0, as seen in Figure 4.6.

### **4.3.2 Densification and Microstructure Evolution in the Sintered Samples**

#### **4.3.2.1 Densification**

Figure 4.9 shows the densification behavior as a function of sintering conditions and composition. The RV0-RV15 samples have almost constant density (93-95%) between 1200 to 1450°C after sintering for 4 h due to the liquid phase sintering, which is consistent with Figure 4.1. The sintered R0-R15 samples reach maximum density (97-99%) at 1350°C (Fig. 4.9a) compared to 1400-1450°C for the quenched samples (Fig. 4.1), due to the longer hold times. Note that they have ~60% relative density at 1200°C. The densities of the sintered samples remain almost constant ( $\geq 93\%$ ) with sintering time at 1400°C except for samples R0 and R9 (Fig. 4.9b). These samples require longer time to reach higher densities.

Comparison of Figure 4.1 and Figure 4.9a indicates that the density decreases with increasing KSN content in the RV0-RV15 samples (Fig. 4.1) and vice versa in the R0-R15 samples (Fig. 4.9a). This difference in the densification behaviors stems mainly



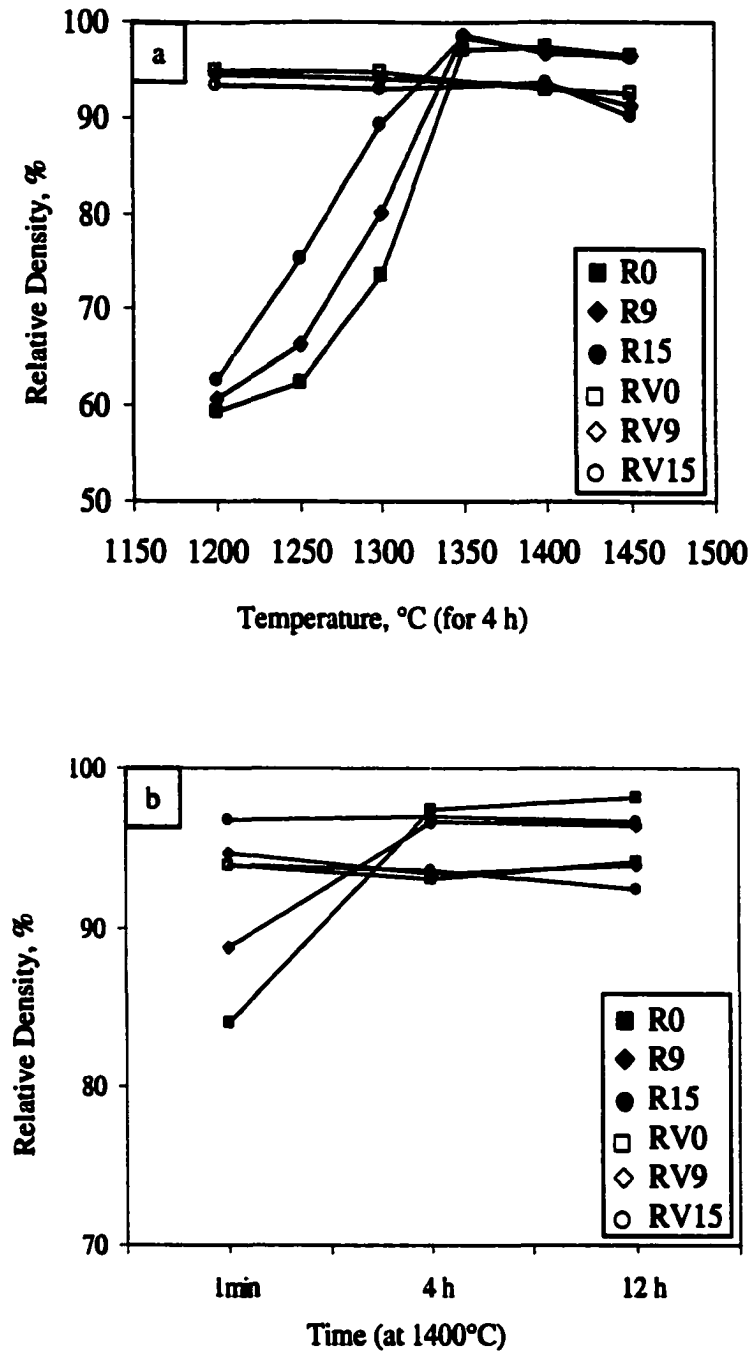


Figure 4.9. Densification graphs of the sintered samples as a function of (a) sintering temperature and (b) time.  $\beta = 7^\circ\text{C}/\text{min}$ .

from the presence of a liquid phase and homogenization of ions in the tungsten bronze structure.

A liquid phase is present all the time for the RV0-RV15 samples due to the melting of  $V_2O_5$  at  $690^\circ\text{C}$ . For the R0-R15 samples, however, a liquid forms due to excess  $Nb_2O_5$  introduced from the KSN seeds. Therefore, with increasing KSN content, the liquid amount increases and its formation temperature decreases. The liquid formation due to excess  $Nb_2O_5$  was observed in conventional sintering of SBN60 ceramics [5,6], and the details were given in section 2.4 of Chapter 2. For the KSN-free samples (i.e., R0 and RV0), SN and BN react to form SBN in a single homogenization step. For the KSN-containing samples, however, the first homogenization step is again the formation of SBN in which, depending on the seed content, SBN either nucleates on the seed particles and/or forms between SN and BN. The second reaction is the formation of the solid solution between SBN and KSN, during which excess  $Nb_2O_5$  forms the liquid phase for the R0-R15 samples.

The homogenization process is closely related to the crystal structure. There are six interstitial (A) sites in the TTB structure, five of which are occupied by Sr/Ba ions [17]. Also, the  $K^+$  ions go to vacant A sites and fill the structure. Because the  $A_1$  site (15-fold coordination) is larger than the  $A_2$  site (12-fold coordination), relatively bigger ions like  $Ba^{2+}$  and  $K^+$  ions presumably prefer to occupy the  $A_1$  sites and smaller  $Sr^{2+}$  ions occupy either the  $A_2$  site or a combination of  $A_2$  and  $A_1$  sites. As the KSN content changes, the distribution of these ions and remaining vacant sites may change in the A sites. For example, the lattice will be distorted more as the fraction of  $Sr^{2+}$  ions increases on the  $A_1$  site because the size of this site is relatively larger than the  $Sr^{2+}$  ion. Fang *et al.*

[7] reported that a high concentration of  $\text{Sr}^{2+}$  ions in the  $\text{A}_1$  site makes the formation of SBN difficult at low calcination temperatures due to increased lattice distortion. If  $\text{K}^+$  ions occupy the  $\text{A}_2$  site, then additional KSN content might promote lattice distortion. The more-distorted lattice would make the diffusion of ions through the product layer more difficult. This might account for slower densification in the RV0-RV15 samples with increasing KSN content (Fig. 4.1). The homogenization of SN and BN to form a SBN53 phase in the RV0 samples is faster compared to the additional  $\text{K}^+$  homogenization with increasing KSN content. Particle rearrangement due to liquid formation can also promote densification at lower temperatures compared to the R0-R15 samples (see Fig. 4.1).

Because the R0-R15 samples do not have a liquid at lower temperatures, the compositional homogenization to form SBN53 and the subsequent solid solution with KSN takes place in the solid state after  $1200^\circ\text{C}$ . Therefore, a sharp chemical gradient difference between different regions promotes the diffusion of the ions in the absence of a liquid. Lee and Fang [4] stated that the densification rate of reaction-sintered SBN50 and SBN60 samples could be pronouncedly enhanced when the homogenization is almost completed. The reason is that homogenization due to a chemical gradient does not change the state of the microstructure because it happens through the necks. For example, Figures 4.11a and b show that a uniform, highly porous, and fine grain microstructure is retained during the homogenization steps. Interdiffusion is a dominant process when the necks form because the material transport due to the chemical gradient is more important than the material flow due to the surface curvature [18]. When the necks grow larger, the interdiffusion of ions becomes easier and predominant, which stops additional sintering

until the homogenization is further advanced [4,19]. After the disappearance of the chemical gradient, the retained high surface area microstructure induces a high driving force for further densification, which can sharply increase the density. Because the temperature at which SBN53 formation is complete decreases with increasing KSN seed content (e.g., 1210°C for the R15 and 1275°C for the R0 samples ( $\beta = 7 \text{ }^\circ\text{C}/\text{min}$ )), the density increases sharply after 1200°C for the R15 samples. In contrast, densification is retarded to higher temperatures with decreasing seed content (i.e., at  $T \leq 1350^\circ\text{C}$  in Fig. 4.9a).

Therefore, the amount of liquid phase, the temperature at which it forms, and the possibility of  $\text{K}^+$  contribution to the lattice distortion are all competing processes. Each is dependent on the presence and amount of the KSN phase, which markedly affects the densification behavior of the SBN ceramics. It is evident from Figures 4.1 and 4.9 that the presence of a liquid is the major contributor to attain a high density at lower temperatures.

#### 4.3.2.2 Microstructure Evolution

Figure 4.10 shows the microstructure development in the  $\text{V}_2\text{O}_5$ -containing samples sintered at 1400°C for 4 h. The samples have elongated grains of various aspect ratios due to liquid phase sintering. They have the same characteristic microstructures irrespective of sintering temperature and time. Figures 4.11 and 4.12 show the microstructure evolution for the R0 and R15 samples as a function of sintering temperature and time, respectively. The other random samples have microstructure evolutions in between these two compositions, depending on the KSN concentration. At

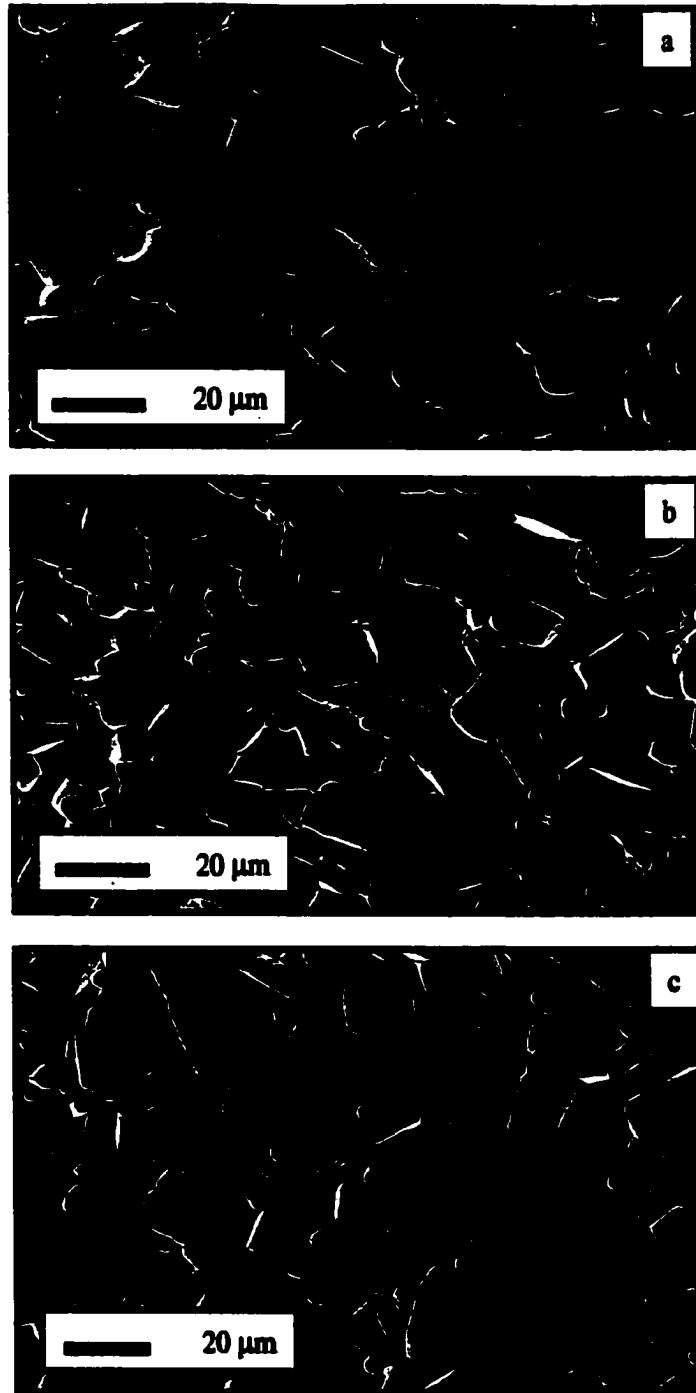


**Figure 4.10. Microstructure development in the  $V_2O_5$ -containing samples sintered at  $1400^\circ\text{C}$  for 4h; (a) RV0, (b) RV5, and (c) RV15.**

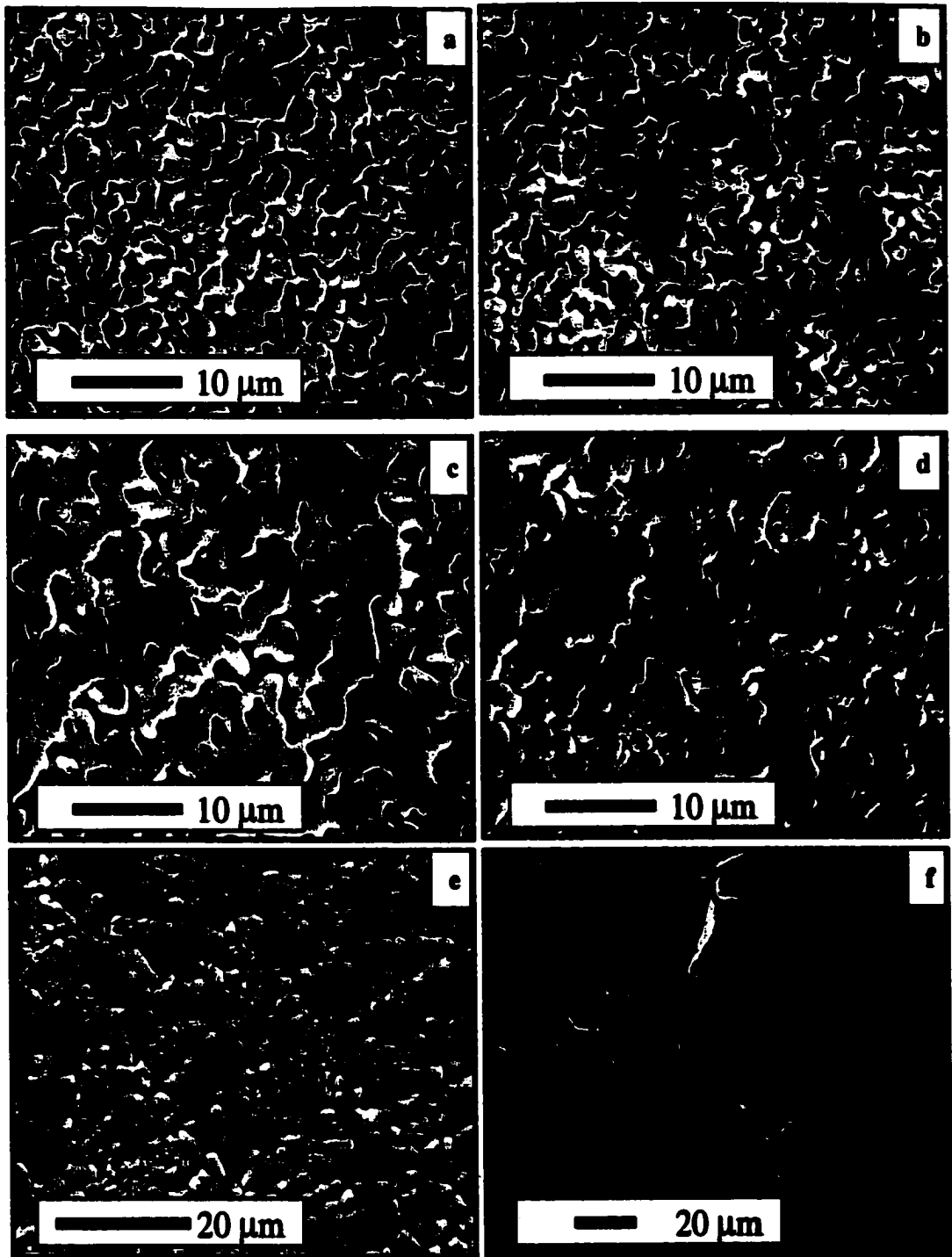


**Figure 4.11.** Microstructure evolution in the R0 (left column) and R15 (right column) samples as a function of sintering temperature; (a and b) 1200°C, (c and d) 1300°C, and (e and f) 1400°C for 4 h .

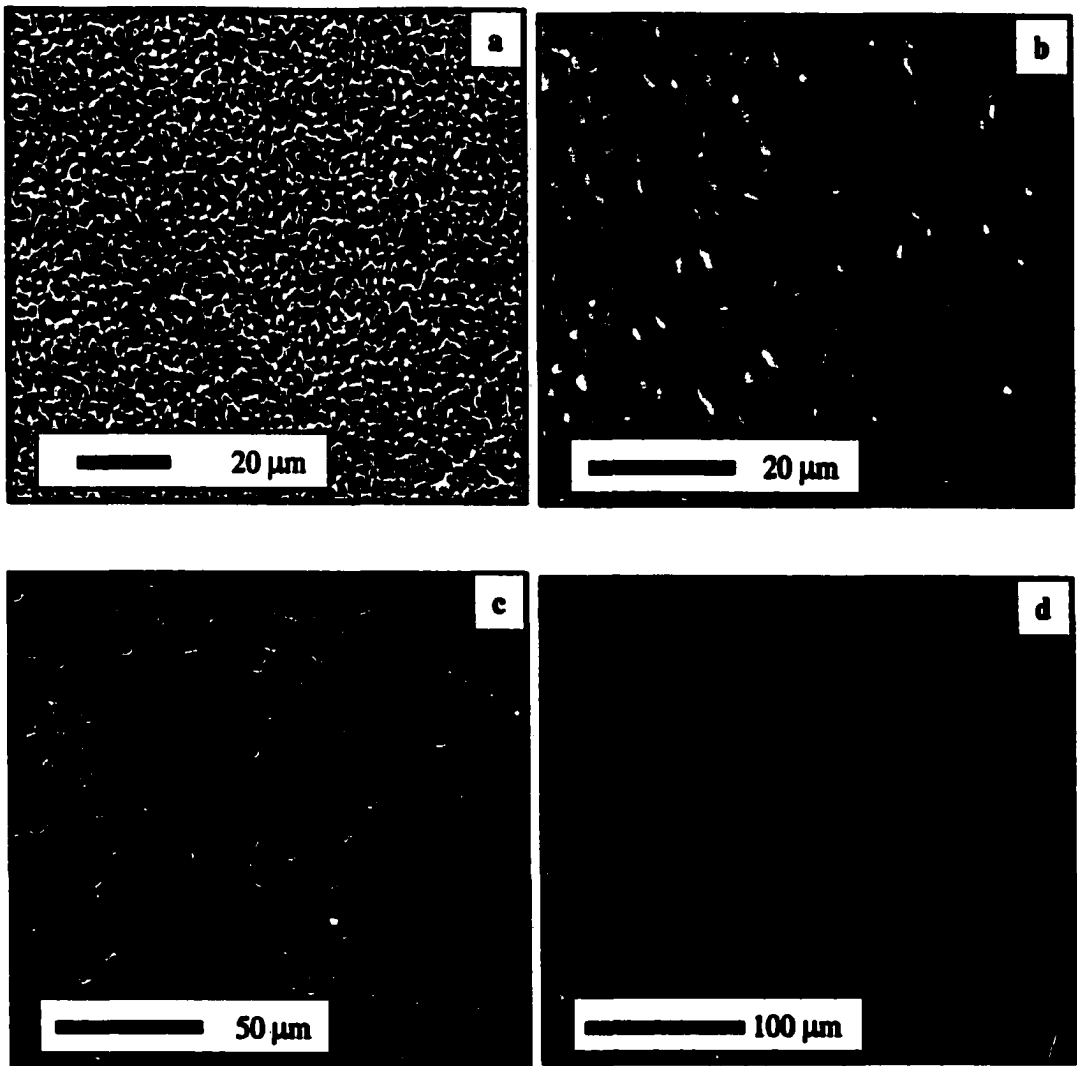


**Figure 4.12. Microstructure evolution in the R0 (left column) and R15 (right column) samples as a function of sintering time; (a and b) 1 min, (c and d) 12 h at 1400°C.**

1200°C, samples show very porous microstructures and fine grain sizes (~ 2 μm). With increasing temperature, neck growth continues and the sintering rate rises. At 1300°C, the pore structure is closed and is mostly concentrated at the triple points in the R15 sample, while R0 shows open porosity. The presence of small (~2 μm) and relatively larger grains (~5 μm) suggests that a bimodal grain size distribution start to appear in the R15 sample. Figures 4.12a and b show that the R15 sample has very dense microstructure after sintering 1 min at 1400°C compared to very fine and porous microstructure for the R0 sample. The microstructures of the R15 sample at high temperatures and times (Figs. 4.11f and 4.12d) show a duplex microstructure consisting of mm-sized grains together with smaller grains. Cracking (possibly due to polishing or the higher internal stress generated by the grain size difference) and spherical porosity entrapped within the big grains are easily observable.

Despite the homogenization step, the R0 samples show abnormal grain growth behavior as seen in Figure 4.12c. This suggests that, even in a stoichiometric mixture of SN+BN, abnormal grain growth can be observed, though at high sintering temperatures and times (e.g., T >1400°C for 12 h). Abnormal grain growth in the R15 sample, for example, started earlier (e.g., after sintering at 1400°C for 4h) due to the higher liquid phase content (e.g., more excess Nb<sub>2</sub>O<sub>5</sub>). The duplex microstructure formation in these samples can be attributed to the non-uniform wetting of the grains by the liquid. That is, grain growth localizes before the liquid spreads out, which causes liquid phase sintering in selected parts of the specimen. As seen for the R15 sample in Figure 4.12b, a bimodal grain size distribution is observed after sintering for 1 min at 1400°C. The presence of a liquid film increases the grain boundary mobility by providing a path for rapid diffusion,



especially for the wetted grains. This gives rise to the formation of very big grains (>100  $\mu\text{m}$ ) and entrapped porosity within these grains. Similar microstructure evolution was also reported in conventional sintering of SBN60 ceramics [5,6].

Microstructural evolution indicates that samples with high density and uniform grain size are obtained at different KSN contents. Abnormal grain growth in the R0-R15 samples takes place because of off-stoichiometric grain boundary phases, only when the samples are overheated.

#### 4.4 CONCLUSIONS

$\text{Sr}_{0.53}\text{Ba}_{0.47}\text{Nb}_2\text{O}_6$  (SBN53) ceramics were reactively sintered from  $\text{SrNb}_2\text{O}_6$  (SN) and  $\text{BaNb}_2\text{O}_6$  (BN) powders.  $\text{KSr}_2\text{Nb}_5\text{O}_{15}$  (KSN) was used as a seed material to accelerate the SBN53 formation.

An unknown phase started to form in the samples during the SBN53 formation. The amount of this phase was greater in the  $\text{V}_2\text{O}_5$ -containing samples, and decreased with increasing seed content and reaction temperature.

$\text{V}_2\text{O}_5$ -containing samples densified at lower temperatures due to the  $\text{V}_2\text{O}_5$  liquid phase and they reached maximum density at  $T \leq 1250^\circ\text{C}$ , compared to  $T \geq 1350^\circ\text{C}$  in the  $\text{V}_2\text{O}_5$ -free samples. The heating rate did not affect the densification much, except that the density was slightly higher at lower heating rates.

The presence of a liquid changed the sequence of the reactive sintering. In the  $\text{V}_2\text{O}_5$ -containing samples, densification and phase formation occurred simultaneously. In the  $\text{V}_2\text{O}_5$ -free samples, however, the phase formation was completed before densification. In both cases, ceramics with  $\geq 95\%$  relative density were obtained,

indicating that it is not critical whether the densification or phase formation takes place first.

The formation temperature for SBN53 was lowered substantially by adding more seeds, decreasing the heating rate, and introducing a liquid. For example, the temperature decreased from 1260°C for the samples with no seeds to 1130°C for the samples with 15.4 wt% seeds + 0.8 mol % V<sub>2</sub>O<sub>5</sub> at a heating rate of 4 °C/min. For the V<sub>2</sub>O<sub>5</sub>-free samples, the activation energy was lowered from 554 ± 15 kJ/mol for the samples with no seeds to 241 ± 17 kJ/mol for the samples with 15.4 wt% seeds. In addition, for all compositions, the SBN53 was formed directly, rather than via a variety of intermediate SBN solid solutions (i.e., other than SBN53).

Samples with high density and uniform grain size were obtained at different KSN contents. Unlike the V<sub>2</sub>O<sub>5</sub>-containing samples, abnormal grain growth in the V<sub>2</sub>O<sub>5</sub>-free compositions took place because of off-stoichiometric grain boundary phases, only when the samples were oversintered.

#### 4.5 REFERENCES

- 1- M. N. Rahaman and L.C. De Jonghe, "Reaction sintering of zinc ferrite during constant rates of heating," *J. Am. Ceram. Soc.*, 76[7], 1739-44 (1993)
- 2- S. Yangyun and R. J. Brook, "Preparation of zirconia-toughened ceramics by reaction sintering," *Sci. Sintering*, 17[1], 35-47 (1985)
- 3- W.-S. Hong, L.C. De Jonghe, X. Yang, and M. N. Rahaman, "Reaction sintering of ZnO-Al<sub>2</sub>O<sub>3</sub>," *J. Am. Ceram. Soc.*, 78[12], 3217-24 (1995)
- 4- W.-J. Lee and T.-T. Fang, "Densification and microstructural development of the reaction sintering of strontium barium niobate," *J. Am. Ceram. Soc.*, 81[4], 1019-24 (1998)
- 5- H.-Y. Lee and R. Freer, "The mechanism of abnormal grain growth in Sr<sub>0.6</sub>Ba<sub>0.4</sub>Nb<sub>2</sub>O<sub>6</sub> ceramics," *J. Appl. Phys.* 81[1], 376-82 (1997)
- 6- H.-Y. Lee and R. Freer, "Abnormal grain growth and liquid-phase sintering in Sr<sub>0.6</sub>Ba<sub>0.4</sub>Nb<sub>2</sub>O<sub>6</sub>, (SBN40) ceramics," *J. Mater. Sci.*, 33, 1703-08 (1998)
- 7- T.-T. Fang, N.-T. Wu, and F.-S. Shiau, "Formation mechanism of SBN ceramic powders," *J. Mater. Sci. Letters*, 13, 1746-48 (1994)
- 8- R. R. Neurgaonkar, W.K. Cory, and J. R. Oliver, "Growth and applications of ferroelectric tungsten bronze family crystals," *Ferroelectrics*, 51, 3-8 (1983)
- 9- R. R. Neurgaonkar, J. R. Oliver, and L.E. Cross, "Ferroelectric properties of tetragonal tungsten bronze single crystals," *Ferroelectrics*, 56, 31-36 (1984)
- 10- R. R. Neurgaonkar, W. W. Ho, W. K. Cory, W. F. Hall, and L. E. Cross, "Low and high frequency dielectric properties of ferroelectric tungsten bronze Sr<sub>7</sub>KNb<sub>3</sub>O<sub>15</sub> crystals," *Ferroelectrics*, 51, 185-91 (1984)

- 11- S. Nishiwaki, J. Takahashi, and K. Kodaira, "The effect of  $V_2O_5$  addition on ferroelectric properties of  $Sr_{0.3}Ba_{0.7}Nb_2O_6$  ceramics," *J. Ceram. Soc. Japan*, Int. Edition, 103, 1233-36 (1995)
- 12- S. Nishiwaki, J. Takahashi, and K. Kodaira, "Effect of additives on microstructure development and ferroelectric properties of  $Sr_{0.3}Ba_{0.7}Nb_2O_6$  ceramics," *Jpn. J. Appl. Phys.*, 33, 5477-81 (1994)
- 13- S. Nishiwaki, J. Takahashi, and K. Kodaira, "Synthesis and phase transition of ferroelectric  $Sr_{0.2}Ba_{0.8}Nb_2O_6$  with  $V_2O_5$  addition," *J. Ceram. Soc. Japan*, Int. Edition, 104, 413-16 (1996)
- 14- W-J. Lee and T-T. Fang, "Nonisothermal reaction kinetics of  $SrNb_2O_6$  and  $BaNb_2O_6$  for the formation of  $Sr_xBa_{1-x}Nb_2O_6$ ," *J. Am. Ceram. Soc.*, 81[1], 193-99 (1998)
- 15- W-J. Lee and T-T. Fang, "Effect of the strontium:barium ratio and atmosphere on the sintering behavior of strontium barium niobate," *J. Am. Ceram. Soc.*, 81[2], 300-304 (1998)
- 16- J. R. Carruthers and M. Grasso, "Phase equilibria relations in the ternary system  $BaO-SrO-Nb_2O_5$ ," *J. Electrochem. Soc.: Solid State Science*, 117[11], 1426-30 (1970)
- 17- R. R. Neurgaonkar, W. K. Cory, J. R. Oliver, E. J. Sharp, G. L. Wood, G. J. Salamo, "Growth and optical properties of ferroelectric tungsten bronze crystals," *Ferroelectrics*, 142, 167-188 (1993)
- 18- P. F. Stablein Jr. and G. C. Kuczynski, "Sintering in multicomponent metallic systems," *Acta Metall.*, 11, 1327-37 (1963)

**19- G. C. Kuczynski, "Sintering in multicomponent systems," pp. 685-711 in *Sintering and Related Phenomena*. Edited by G.C. Kuczynski, N.A. Hooton, and C.F. Gibbon, Gordon and Breach, NY (1967)**

**CHAPTER 5**  
**TEMPLATED GRAIN GROWTH OF  $\text{Sr}_{0.53}\text{Ba}_{0.47}\text{Nb}_2\text{O}_6$  CERAMICS**  
**WITH  $\text{V}_2\text{O}_5$  ADDITIVES**

**5.1 INTRODUCTION**

Electroceramics are used in a variety of applications such as sensors, actuators, capacitors, and varistors. In these applications, the ceramic microstructure is usually equiaxed, randomly oriented grains. Ferroelectric transducers require poling to obtain useful piezoelectric properties. Poling is difficult for some ferroelectric ceramics (i.e., uniaxial ceramics like SbSI [1]) because the symmetry-related orientations available for the spontaneous polarization are limited. Thus, ceramics with preferred crystallographic orientation (i.e. texture) are one way to improve electrical and electromechanical properties. Texturing piezoelectric ceramics may enable access to the directionally dependent properties and ultimately to a property set similar to that of single crystals. As an alternative to techniques such as hot pressing and hot forging, templated grain growth (TGG) offers the possibility of fabricating grain-oriented polycrystalline ceramics which exhibit single crystal-like properties.

In this chapter, the fabrication, texture characterization, and electrical properties of grain-oriented  $\text{Sr}_{0.53}\text{Ba}_{0.47}\text{Nb}_2\text{O}_6$  (SBN53) ceramics by TGG are described. 0.8 mol %  $\text{V}_2\text{O}_5$  was added to form a liquid. Acicular  $\text{KSr}_2\text{Nb}_5\text{O}_{15}$  (KSN) particles were utilized to texture SBN53 ceramics. These particles are suitable template particles for matrix recrystallization because KSN has the tungsten bronze structure with a polar axis in the *c* direction as in SBN and the lattice parameter difference between them is less than 0.5%

in both  $a$  and  $c$  directions at room temperature [2,3]. Texture development, as well as the dielectric, piezoelectric, and pyroelectric properties, was investigated as a function of initial template concentration, sintering conditions, crystallographic direction, and the degree of orientation. For comparison, random samples with the same compositions were prepared using solid state synthesized  $\text{KSr}_2\text{Nb}_3\text{O}_{15}$  powder (see Chapter 4).

## 5.2 EXPERIMENTAL PROCEDURE

SBN53 ceramics were prepared by reactive sintering of  $\text{SrNb}_2\text{O}_6$  (SN) and  $\text{BaNb}_2\text{O}_6$  (BN) powders. The synthesis of SN and BN was given in Chapter 4. Appropriate amounts of SN and BN were mixed with a vinyl-based (Ferro 73210) binder solution (35.1wt%) and (Ferro M1111) modifier (1.3 wt%) (Electronic Materials Division, MSI products group). Extra BN powder was added to the slurry to compensate for the SN from the template particles.  $\text{V}_2\text{O}_5$  (0.8 mole %) was added as a liquid former during sintering. The powder and template slurries were prepared separately to avoid whisker breakage during milling. The powder slurry was prepared by ball milling the powder mixture, binder solution, and modifier for 24 h in toluene using 1-mm zirconia balls. The template slurry, consisting of 5 to 15.4 wt% template particles, was mixed in toluene with the same binder solution and stirred for 24 h. The powder and template slurries were then mixed and stirred for 24 h.

Tape casting for each slurry was done on a glass substrate at a casting speed of 7 cm/sec and a blade gap of 200  $\mu\text{m}$ . After 24 h drying at room temperature, tapes were cut and laminated at 83 MPa, and then burned out at 500°C for 2 h with a heating rate of 0.5°C/min to prevent cracking and delamination. Samples were sintered between 1100°

and 1450°C for 4 to 12 h. Sections, as shown in Figure 5.1, were cut parallel (*//*) and perpendicular (*⊥*) to the casting direction from the textured samples to measure electrical properties in the *a-b* (non-polar) plane and the *c* (polar) direction, respectively. Table 5.1 summarizes the sample designation and initial amounts of K<sub>2</sub>O and Nb<sub>2</sub>O<sub>5</sub> from the KSN templates. T refers to textured samples. All samples have 0.8 mol % (0.37 wt%) V<sub>2</sub>O<sub>5</sub>. Extra BN powder was added to the slurry to compensate for the strontium and niobium introduced by the KSN seeds. However, the potassium and some of the excess niobium from the KSN could not be removed from the final composition. Therefore, the concentration of K<sub>2</sub>O and Nb<sub>2</sub>O<sub>5</sub> increases with increasing KSN concentration. For the TV5-9 and TV5-15 samples, only 5 wt% KSN templates were used. However, their compositions were adjusted to TV9 and TV15, respectively, by adding K<sub>2</sub>O and Nb<sub>2</sub>O<sub>5</sub> according to the additive difference.

The surfaces of the samples were polished to 10 μm prior to the electrical measurements. For microstructure analysis, samples were polished to 0.3 μm using fine Al<sub>2</sub>O<sub>3</sub> powder and then thermally etched 100°C below the sintering temperature for 1 h. The density was determined by the Archimedes technique. Elemental mapping analysis was performed on the thermally etched samples using an Energy Dispersive Spectroscopy (EDS) attached to a Field Emission Scanning Electron Microscopy.

Crystallographic texture was characterized using the  $\theta$ - $2\theta$  scan ( $2\theta$  ranges from 20 to 50°) on the  $\perp$ -cut samples and the texture fraction, using the Lotgering factor, was calculated:

$$f = (P - P^0) / (1 - P^0) \quad (5.1)$$



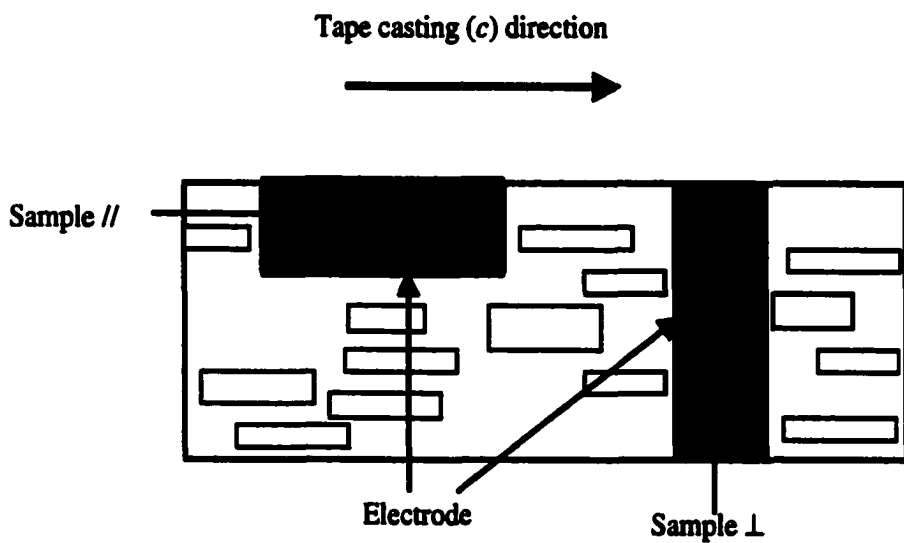


**Figure 5.1. Sectioning of samples from sintered pieces.**

**Table 5.1. Sample name, KSN concentration, and amount of K<sub>2</sub>O and Nb<sub>2</sub>O<sub>5</sub> in SBN53.**

**All Samples have 0.8 mol % (0.37 wt%) V<sub>2</sub>O<sub>5</sub>.**

<b>Sample Designation</b>	<b>KSN content, wt%</b>	<b>Additive Contribution, wt%</b>	
		<b>K<sub>2</sub>O</b>	<b>Nb<sub>2</sub>O<sub>5</sub></b>
<b>TV5</b>	<b>5</b>	<b>0.26</b>	<b>0.72</b>
<b>TV9</b>	<b>9.1</b>	<b>0.47</b>	<b>1.32</b>
<b>TV12</b>	<b>12</b>	<b>0.62</b>	<b>1.74</b>
<b>TV15</b>	<b>15.4</b>	<b>0.80</b>	<b>2.23</b>
<b>TV5-15</b>	<b>5</b>	<b>0.80</b>	<b>2.23</b>
<b>TV5-9</b>	<b>5</b>	<b>0.47</b>	<b>1.32</b>

where  $P$  and  $P^o$  are  $[I_{(001)}+I_{(002)}]/\sum I_{(hkl)}$  in the textured and random cases, respectively. Scanning Electron Microscopy (SEM) micrographs of //cut samples were used to characterize the morphological texture and anisometric grain dimensions. The major and minor axis of the grains were measured and analyzed using stereological analysis software [4]. Anisometric grains were defined as those with an aspect ratio  $\geq 2$ . The fraction of oriented material was determined by measuring the area fraction of anisotropic grains. The measured dimensions were corrected, using a stereological correction factor (See Appendix A). The crystallographic orientation distribution was obtained from rocking-curve (or  $\omega$  scan) measurements [5], using the (002) SBN peak on the  $\perp$ -cut samples. The range in specimen tilt was  $-23^\circ$  to  $+23^\circ$ , the step size was  $0.02^\circ$ , and the dwell time was 0.5 s. The rocking curves were corrected for background, absorption, and defocus using TexturePlus software [11]. These corrections can be viewed as dividing the measured rocking curve intensities by a “random” rocking curve calculated using the  $\theta$ - $2\theta$  scan of the Bragg peak [5]. The orientation distribution was calculated by fitting corrected rocking curves to the March-Dollase equation [7,8]:

$$Q(f,r,\alpha) = f ( r^2 \cos^2 \alpha + r^{-1} \sin^2 \alpha )^{-3/2} + ( 1-f ) \quad (5.2)$$

where  $f$  is the texture fraction,  $r$  is the degree of orientation, and  $\alpha$  is the misalignment angle from the texture direction (e.g., [001]). The  $r$  parameter is closely related to the width of the texture distribution of the anisotropic grains and ranges from  $r = 1$  for random to  $r = 0$  for perfectly textured materials. Schematic views of  $\theta$ - $2\theta$  scan (for the Lotgering factor) and  $\omega$  scan (for the rocking curve) are shown in Figure 5.2.

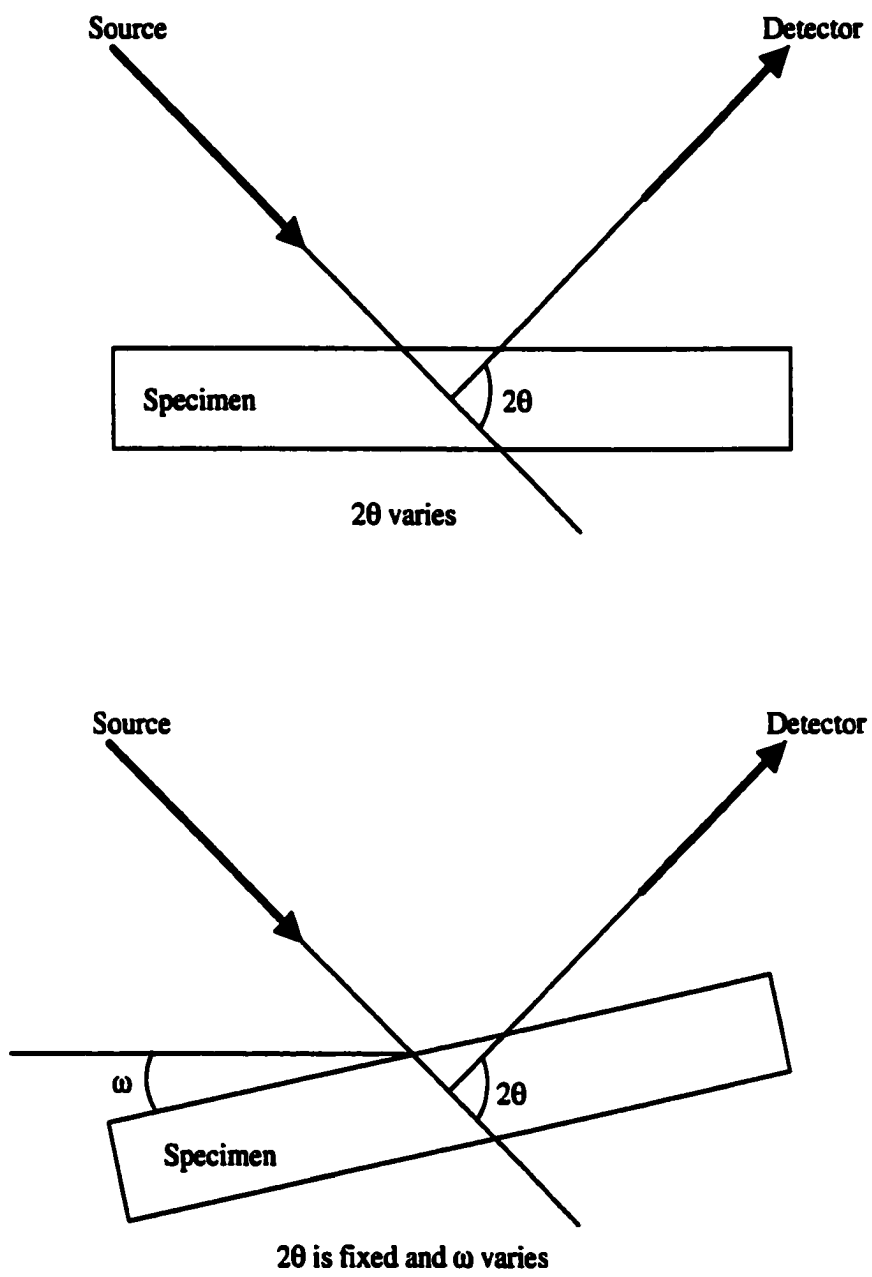


Figure 5.2. (a)  $\theta - 2\theta$  scan (e.g., standard XRD) and (b)  $\omega$  scan (for rocking curve).

For dielectric, piezoelectric, and pyroelectric measurements, samples were electroded with sputtered platinum. The temperature dependence of the dielectric constant and loss tangent was measured using a Hewlett Packard 4284A precision inductance-capacitance-resistance (LCR) meter at frequencies of 1 to 100 kHz and at 1 Volt. Before each run, samples were heated to 300°C to depole them, and then data were recorded during cooling to room temperature at 2°C/min. The polarization and coercive field were determined from polarization-electric field (P-E) hysteresis loops recorded at 10 Hz, using a Sawyer-Tower circuit. The fatigue behavior of the samples as a function of cycle was also measured using the same P-E circuit at 50 kV/cm, 10 Hz, and 25°C. The poling was performed by applying 20 kV/cm at ~10-15°C above the Curie temperature for 15 min and then cooling to room temperature while maintaining the field. The piezoelectric charge coefficient,  $d_{33}$ , of poled samples was measured 24 h after poling, using a Berlincourt  $d_{33}$  meter (Model ZJ-2) operating at 100 Hz. The saturation polarization,  $P_{\infty}$ , and pyroelectric coefficient were determined as the poled samples were heated from room temperature to 250°C at 3°C/min., using a Hewlett Packard 4140B picoammeter. Prior to the measurements, the samples were short-circuited to neutralize any space charge accumulated at the metal/dielectric interface.

## **5.3 RESULTS AND DISCUSSION**

### **5.3.1 Densification and Texture Development**

Figure 5.3 shows the densification graphs of the samples sintered at 1400°C from 1 min to 12 h. The density increases slightly with sintering time and decreases with increasing KSN content. 15.4 wt% KSN containing samples (i.e., TV15 and TV5-15)

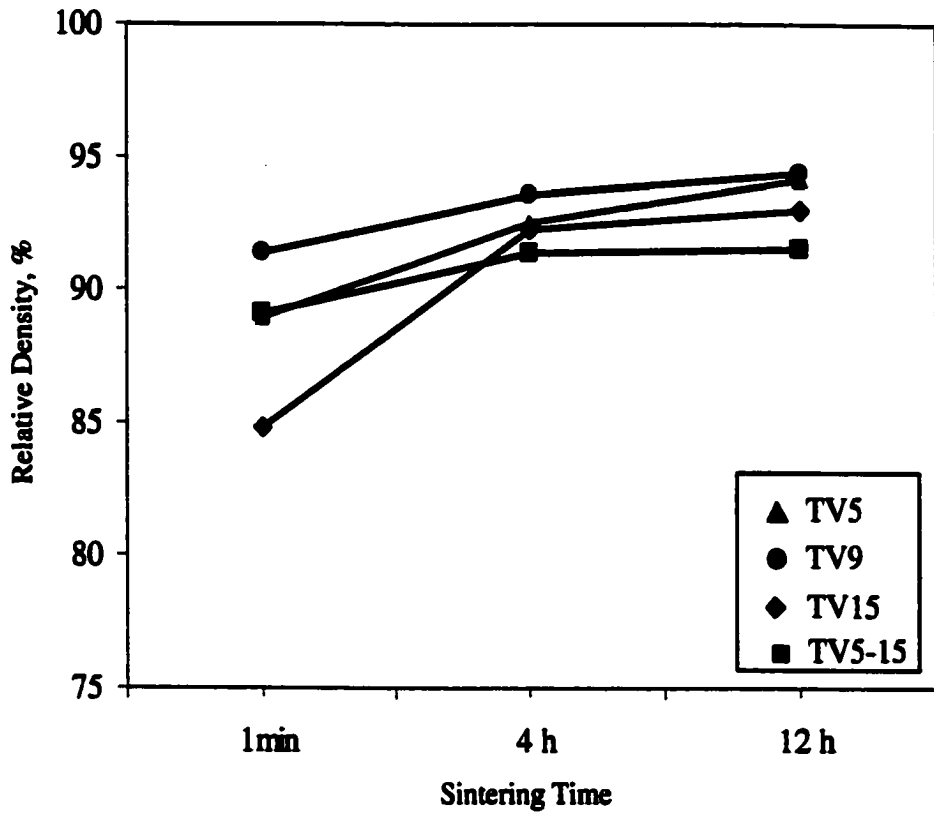


Figure 5.3. Densification graphs of the samples as a function of sintering time at 1400°C.

reached lower densities. As mentioned in Chapter 4 for the random samples, densification is retarded to higher temperatures with increasing KSN content, possibly due to the compositional homogenization between the SBN and KSN. Ceramics sintered at 1300°C for 4h reached a relative density of 88-92% due to the presence of a liquid. The formation of a liquid phase in SBN containing  $V_2O_5$  was reported to occur through a series of intermediate steps [9,10]. It was reported [9,11] that  $V^{5+}$  is rarely dissolved in the tungsten bronze structure and precipitates as separate islands at the triple junctions after sintering. For all samples, a single-phase tetragonal tungsten bronze (TTB) structure was obtained after sintering at 1100°C for 4h.

Figure 5.4 shows crystallographic texture development in the TV15 samples ( $\perp$  cut) as a function of sintering temperature, as well as a reference pattern of random SBN53. The  $\{00l\}$  peaks start to dominate the diffraction pattern at temperatures as low as 950°C, even though the phase formation is not fully completed. This suggests that the texture development commences early due to the presence of a liquid ( $V_2O_5$  melts at 690°C). After 1100°C, the relative intensity ratio of  $\{00l\}$  peaks to  $\{hkl\}$  peaks stays almost constant. Figure 5.5 shows that morphological texture development increases with increasing sintering temperature in the TV15 samples ( $//$  cuts). Initially aligned template particles consumed the matrix grains and started to impinge on each other with increasing temperature, which causes grain growth to slow down.

Figure 5.6 compares the texture development as a function of initial template content. Samples were sintered at 1400°C for 4 h. Morphological texture development in the  $c$  direction improves as the template concentration increases for the TV5-TV15 samples (Figs. 5.6a-d). In Chapter 4, it was shown that random samples with  $V_2O_5$ ,

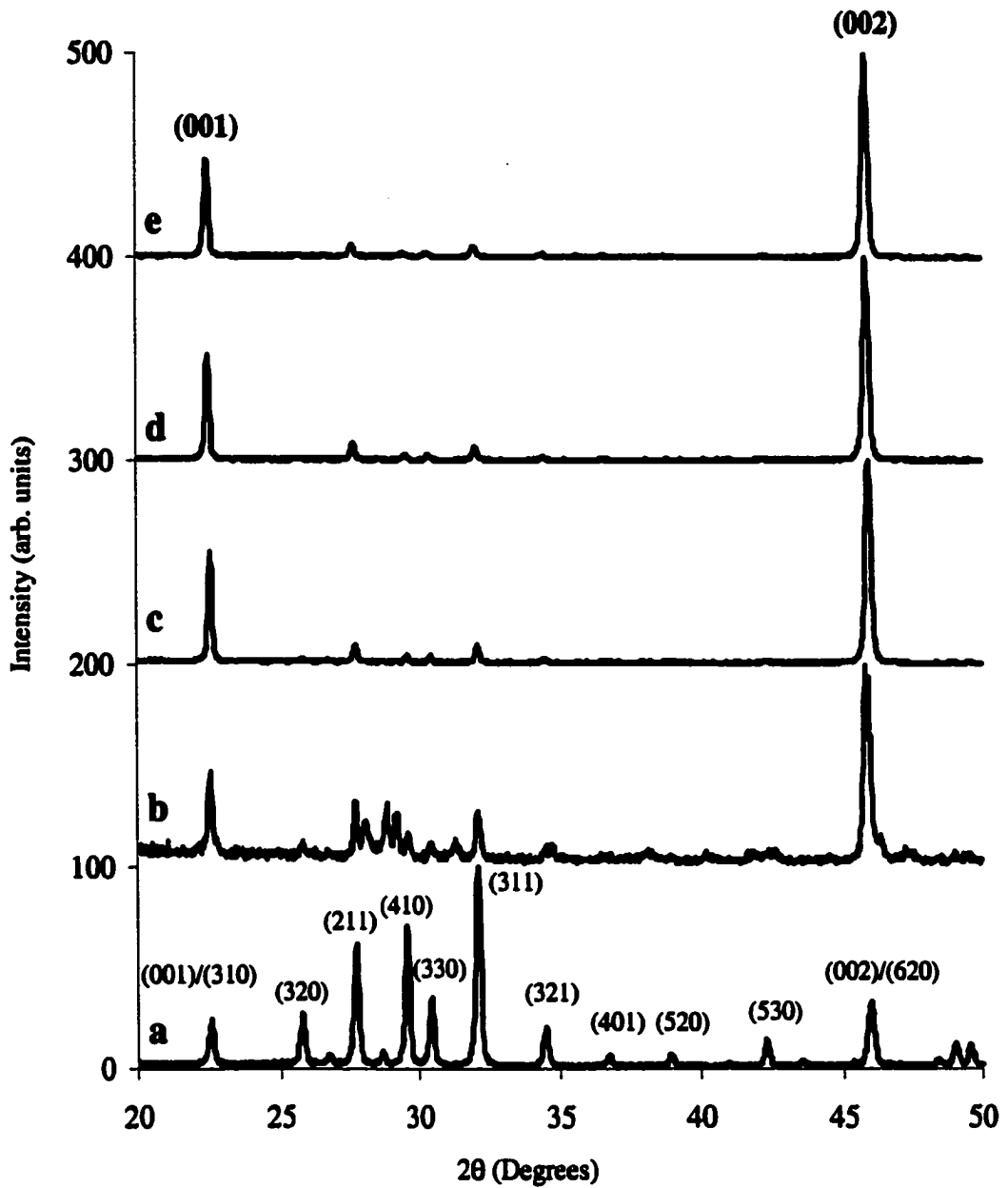
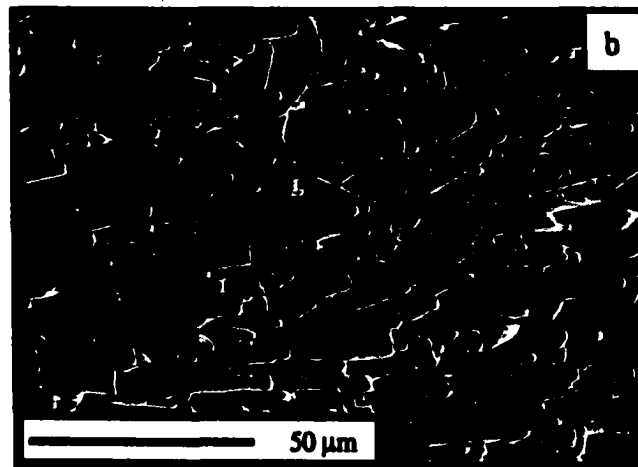
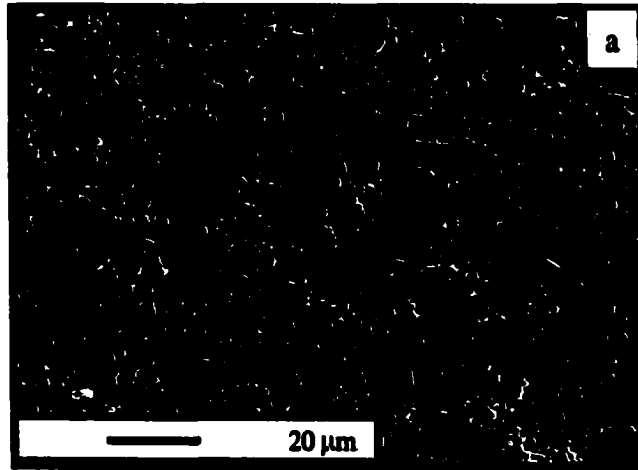
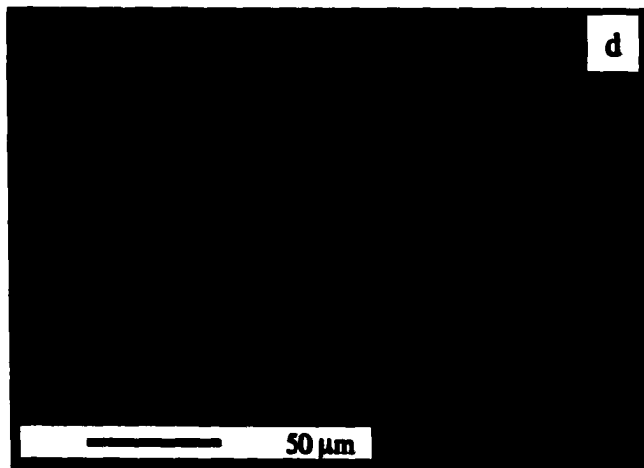
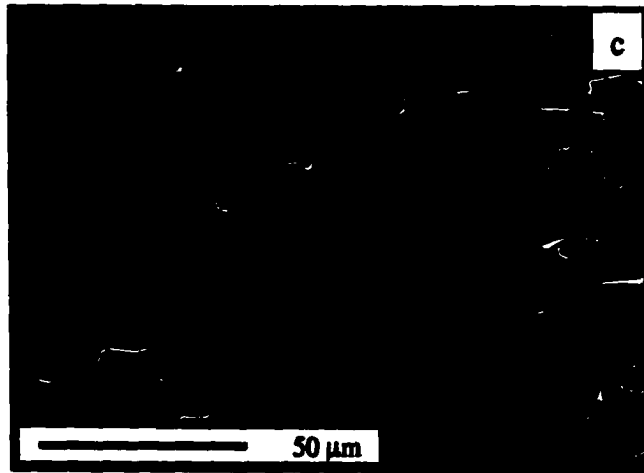


Figure 5.4. XRD patterns of the TV15L samples after sintering for 4 h at; (b) 950°C, (c) 1100°C, (d) 1200°C, and (e) 1300°C. Curve "a" is for the random sample (heated at 1250°C for 5 h) and is given as an untextured reference pattern. Major SBN53 peaks are marked.





**Figure 5.5. SEM pictures of the TV15// samples after sintering for 4 h; (a) 950°C, (b) 1200°C, (c) 1300°C, and (d) 1400°C.**



**Figure 5.5. Continued.**

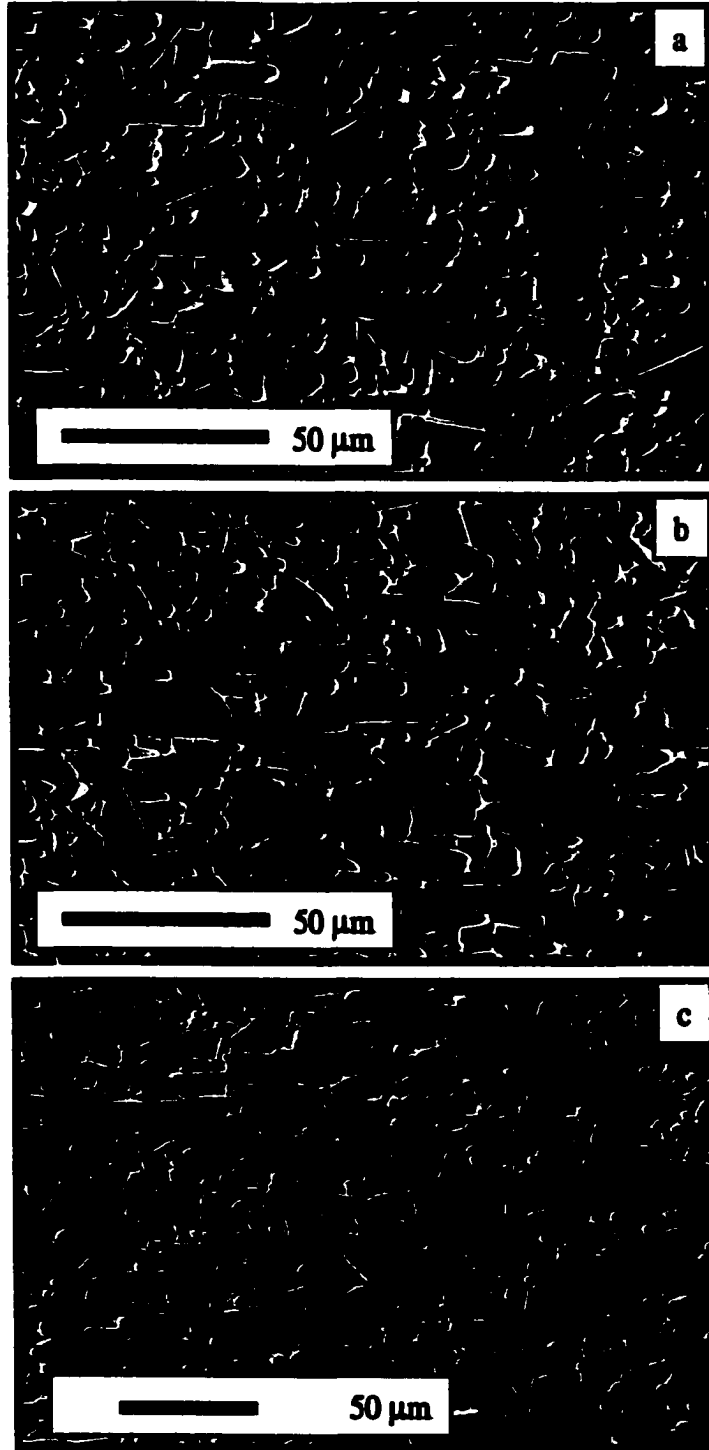


**Figure 5.6. SEM micrographs of the samples sintered at 1400°C for 4h; (a) TV5, (b) TV9, (c) TV12, (d) TV15, (e) TV5-9, and (f) TV5-15.**

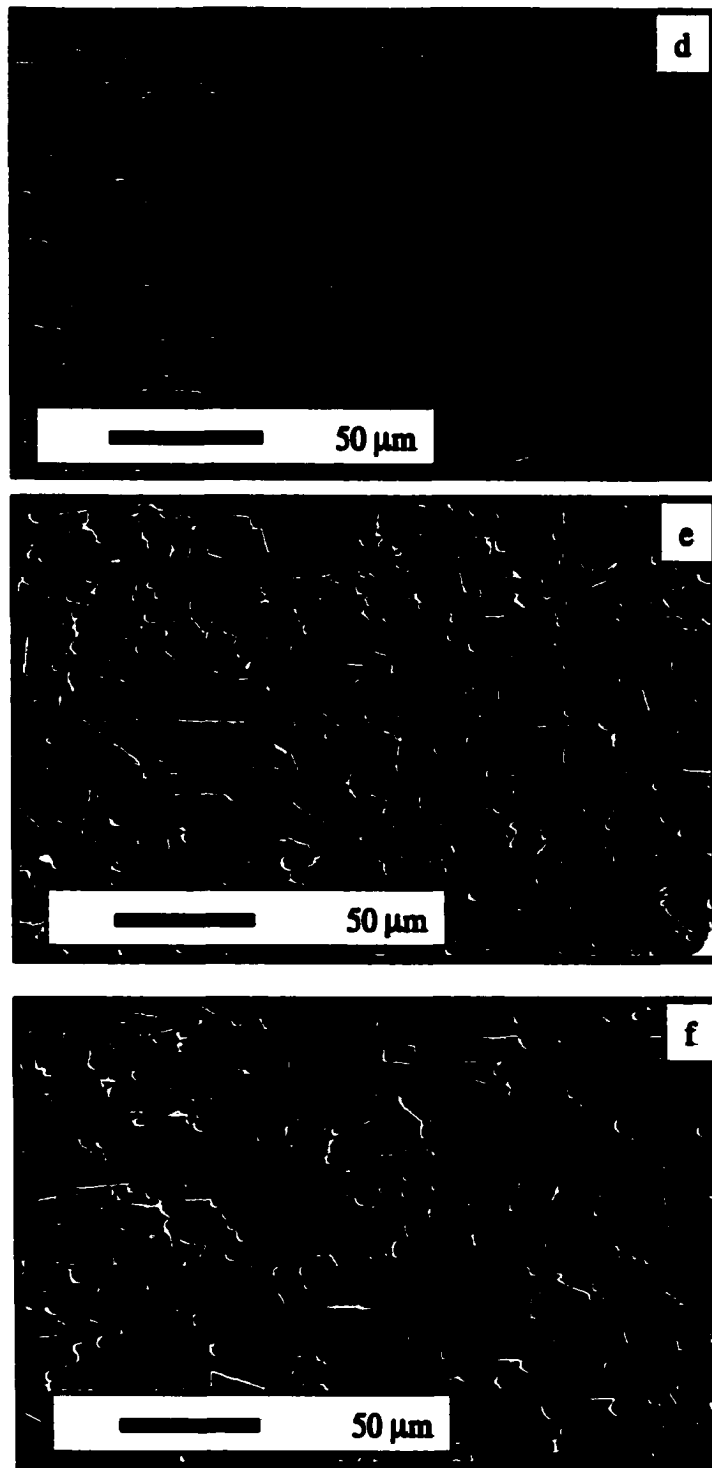


**Figure 5.6. Continued.**

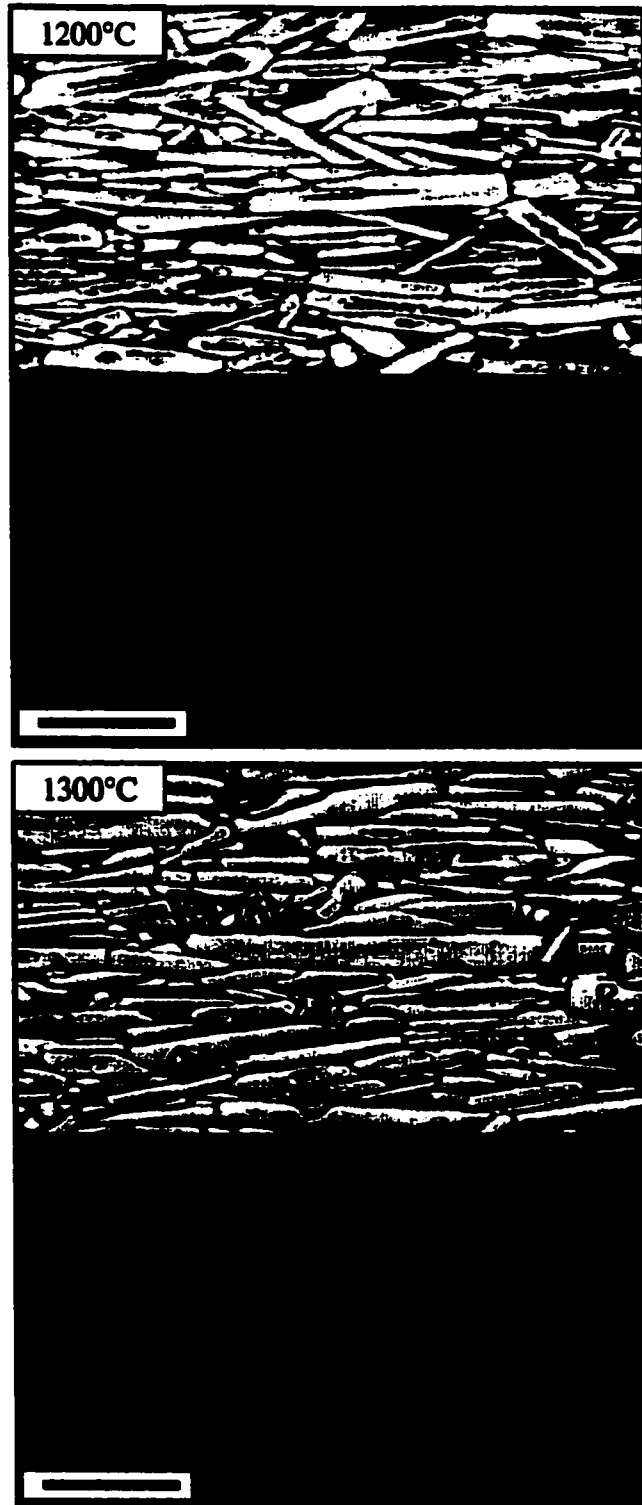
underwent anisotropic grain growth because of the liquid phase. Growth of the anisotropic grains occurs by solution-precipitation in which small particles dissolve in the liquid phase due to their smaller size, and then reprecipitate on the larger particles [12]. For TGG, the liquid facilitates preferential growth of template particles at the expense of matrix grains. Consequently, the aspect ratio of the template particles must be high and the matrix grain size must be as fine as possible at the time of densification. Samples with low template content such as TV5 and TV9 were not as strongly textured due to the lower fraction of template particles combined with anisotropic grain growth in the matrix. Matrix grain growth competes with the anisotropically growing grains by decreasing the total grain boundary area, and thereby decreasing the driving force for TGG. Increasing the template concentration (i.e., TV15 in Fig. 5.6d) resulted in better texture development because the larger number of template particles consumed the fine-grained matrix in less time because of the smaller inter-template spacing. Figures 5.6e and 5.6f show that the TV5-9 and TV5-15 samples are highly textured despite their low template contents (i.e., 5 wt%), as compared to TV5 (Fig. 5.6a). The possible reason may be the retardation of matrix densification (and possible grain growth) due to the compositional homogenization step (see Chapter 4 for details) because these samples have  $K_2O$  and  $Nb_2O_5$  in the matrix (see Table 5.1). Therefore, template growth is highly favored at low temperatures in the presence of a liquid before the matrix grain growth starts. At later stages, off-axis anisotropic grain growth in the matrix is minimized by impingement with the templates, and the matrix grains are aligned in the direction of template particles.

Figure 5.7 shows the effect of temperature on  $K^+$  homogenization in the TV15// samples.  $K^+$  ions are shown as the white areas on the maps. At 1200°C, the  $K^+$  ions are mainly found in the elongated grains (especially in thicker ones) but the distribution homogenizes with increasing temperature. At 1450°C, for example, there seems to be no segregated  $K^+$  ions in the elongated grains.

Figures 5.4 to 5.7 indicate that SBN53 formation from SN and BN takes place primarily on the template (e.g. KSN) particles. Depending on the frequency of the template particles, SBN formation also takes place in the matrix. Because the liquid phase promotes anisotropic grain growth, SBN53 formation and subsequent grain growth in the matrix is much faster in the samples with lower template content (except for the TV5-9 and TV5-15 samples) due to the larger inter-template spacing, which can cause wider orientation distributions for the  $c$  (polar) direction and thus deteriorate the electrical properties, as will be seen later.

Texture analysis was performed on the  $\perp$ -cut samples, using the Lotgering factor (Fig. 5.8). Texture fraction ( $f$ ) increases substantially with increasing template content for the TV5-TV15 samples. For example, the TV5 samples reached  $f = 0.56$  whereas an  $f = 0.93$  was obtained in the TV15 samples at 1400°C. In addition,  $f$  does not change much with temperature. For instance, the TV5-15 samples has  $f = 0.91$  at 1200°C and 0.93 at 1400°C after sintering for 4 h.

Anisotropic grain dimensions in the TV9 and TV15 samples (// cuts) were calculated by stereological analysis. Table 5.2 summarizes the average values between 1200°C and 1450°C. The average grain thickness and length increase with increasing temperature but the average aspect ratio decreases slightly in both samples. When growth



**Figure 5.7.** Effect of temperature on  $K^+$  homogenization in TV15// samples after sintering 4h. (Bar = 20  $\mu\text{m}$ ).

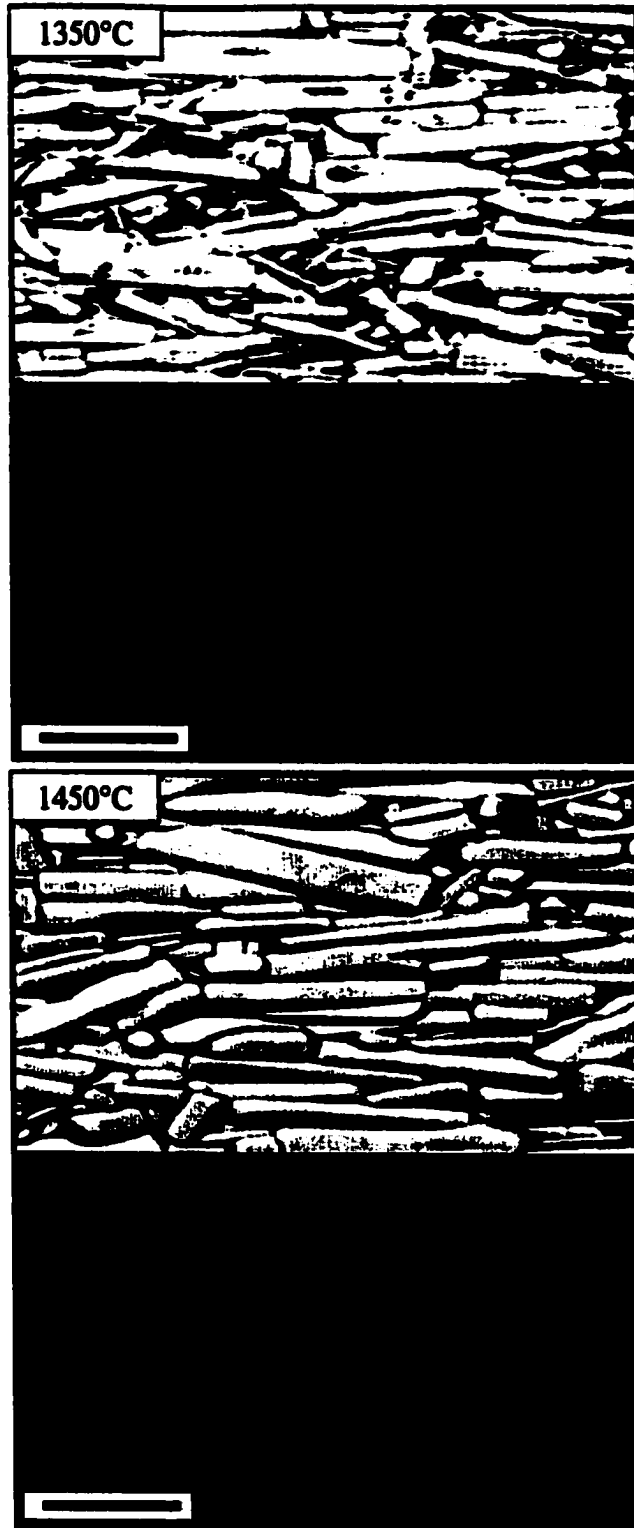


**Figure 5.7. Continued.**



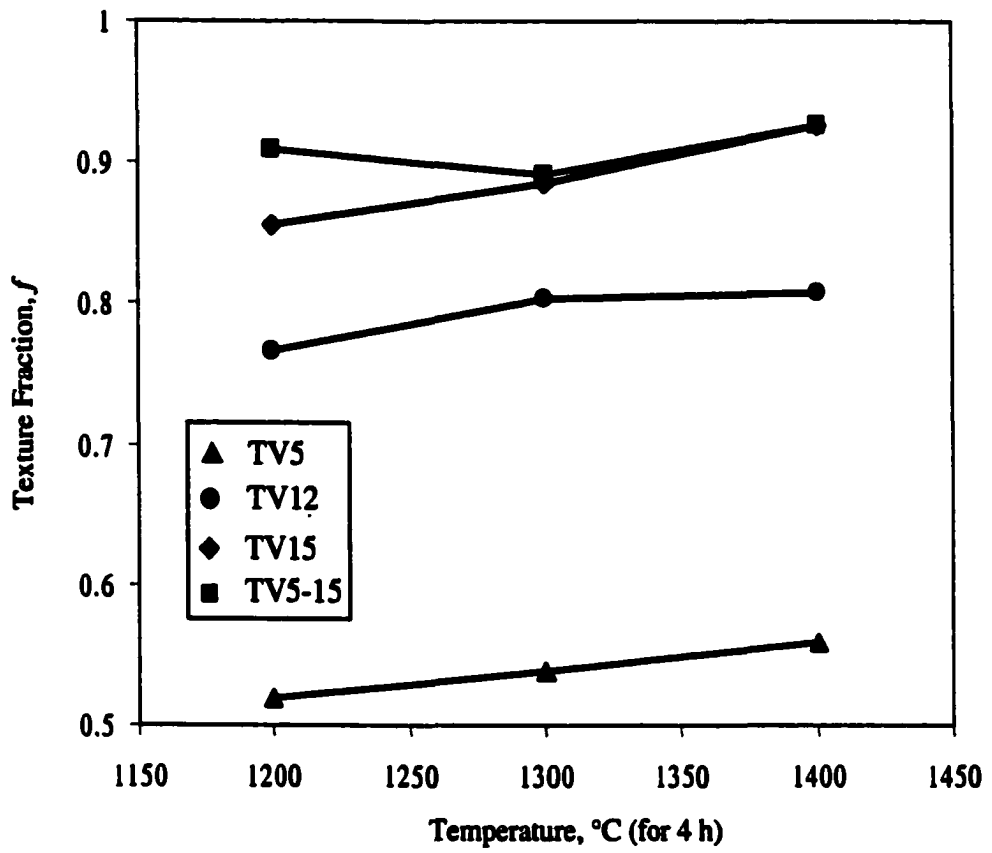


Figure 5.8. Texture fraction ( $f$ ), calculated using the Lotgering factor, as a function of sintering temperature.

**Table 5.2. Summary of the average dimensions and texture for the TV9 and TV15 samples sintered between 1200°C and 1450°C.**

Sample	Average Thickness, $\mu\text{m}$		Average Length, $\mu\text{m}$		Average Aspect Ratio		Textured Fraction	
	1200°C	1450°C	1200°C	1450°C	1200°C	1450°C	1200°C	1450°C
TV9	2.0	3.2	9.8	14.6	4.9	4.6	0.42	0.53
TV15	2.7	3.9	14.4	18.7	5.3	4.8	0.74	0.82

in the longitudinal direction is obstructed either by impingement with other growing template particles (See Figures 5.6d-f) or large matrix grains (See Figures 5.6a-c), grain growth continues in other directions, leading to thickening of the needle-shaped grains. The TV9 samples show smaller average values in length, thickness, and aspect ratio, which implies that impingement due to the matrix grains starts earlier. The evidence is that random (e.g., untemplated) samples show strong anisotropic grain growth (See Chapter 4), which can easily compete with (and hinder) template growth unless such growth is avoided by template growth.

The texture fraction as determined by stereological analysis (e.g., 0.82 at 1450°C) is lower than the Lotgering factor (e.g. 0.92 at 1450°C). This may be because grains with aspect ratios  $< 2$  were not measured although they may be crystallographically oriented in the *c* direction. While stereology is a valid characterization of texture, experimental error is introduced as a result of some of the assumptions for measurements [5]. Anisotropically-shaped grains whose shape arises from factors other than crystallography (e.g. by grain accommodation) cannot be separated from the template grains by SEM observation and, thus, are included in the measurements. The crystallographic orientation of these grains is likely more random than the anisotropically-shaped grains (e.g. in samples with 9.1 wt% templates). It is also possible that texture has developed in the sample matrix. In this case, a fraction of the matrix grains can be crystallographically oriented, but do not have an anisotropic morphology, and therefore are not included in the morphological analysis. Finally, during sectioning of samples, a number of anisotropic grains in the sample will be cut such that they project an isotropic cross section. These grains would not be counted in the measurement of the anisotropic fraction. These

considerations reveal that a somewhat different orientation distribution is obtained by the stereological technique, which results in a lower calculated volume fraction of template grains.

Although the Lotgering factor is a simple method to qualitatively characterize the texture fraction, it does not provide information about the distribution of angles in the materials, which is very important in processing-texture-property relationships. Therefore, the texture distribution in the  $c$  (e.g., texture or [001]) direction was determined from rocking curves. Figure 5.9 shows a graph of orientation distribution curves as a function of the angle  $\alpha$  for the samples sintered at 1400°C for 4 h. The curves on the plot are the result of curve-fitting to Eqn. (5.1). The  $r$  parameters are given on the plot. The correlation coefficient ( $R^2$ ) is  $\geq 0.95$  for each curve. The  $r$  value increases with decreasing template content. As seen in Figure 5.6a for TV5 sample, there are considerable amounts of off-axis elongated grains from the matrix, which gives rise to an increase in the  $r$  parameter, and correspondingly the widening of orientation distribution about the texture direction.

Figure 5.10 shows the texture evolution as a function of densification for the samples sintered between 1200 to 1450°C for various times. It is apparent that  $f$  remains almost constant for each composition. This result suggests that texture evolution starts earlier than the densification due to the presence of a liquid in the system that facilitates template growth by a solution-precipitation mechanism, as mentioned earlier.

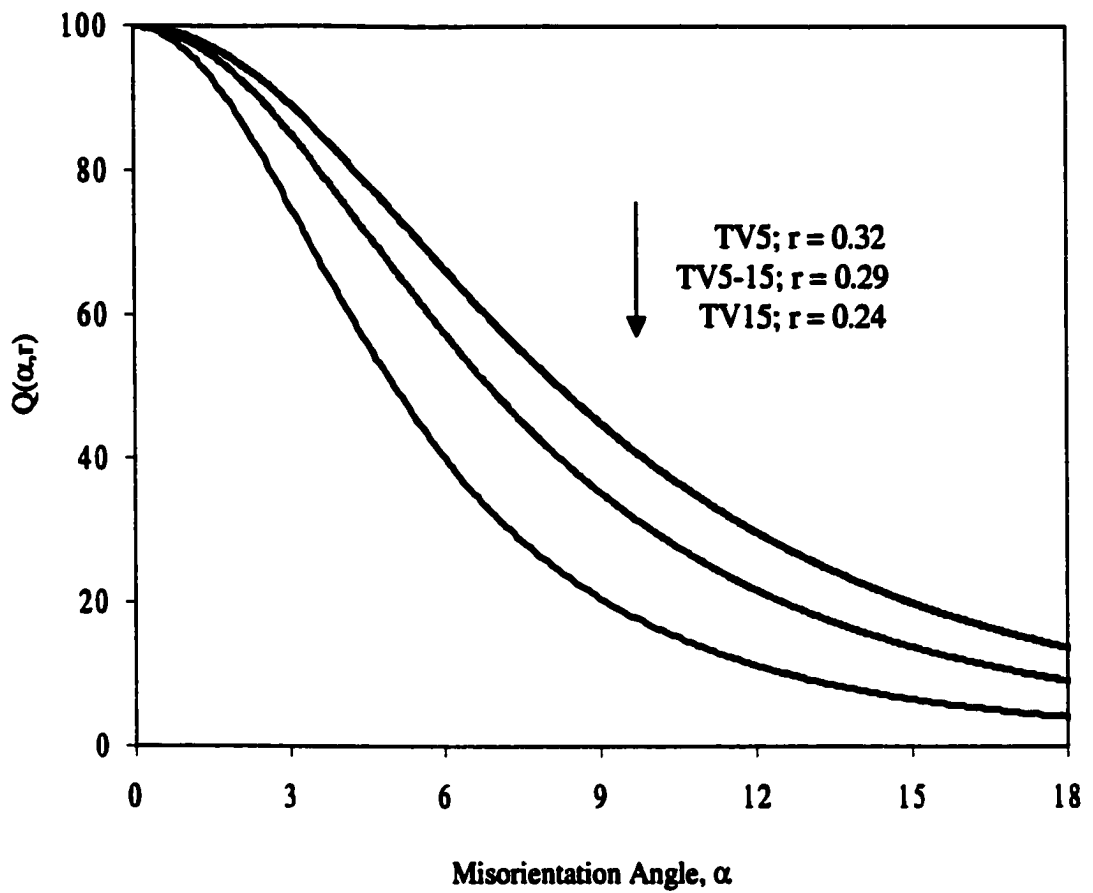


Figure 5.9. Orientation distribution curves for the  $\perp$ -cut samples sintered at 1400°C for 4 h. The curves are March-Dollase fits to the corrected rocking curve data.

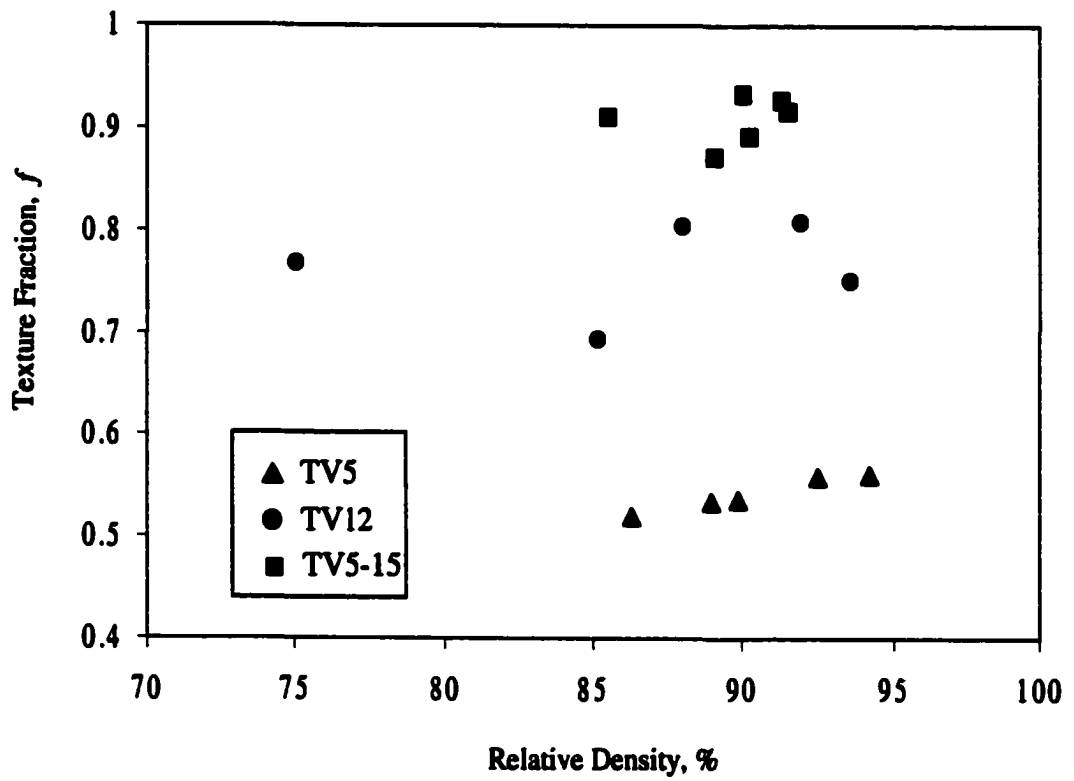


Figure 5.10. Density vs. texture fraction by the Lotgering factor.

## **5.3.2 Electrical Properties**

### **5.3.2.1 Dielectric Properties**

Figure 5.11 shows the orientation and temperature dependence of the dielectric constant and dielectric loss at different frequencies for sample TV15 sintered at 1400°C for 4 h. The dielectric constant at room temperature in  $\perp$  cuts (770) is higher than for either the  $\parallel$  cuts (370) or the random ones (430), which is consistent with the known dielectric anisotropy of SBN single crystals. Very high anisotropy in the dielectric constant between  $\perp$  and  $\parallel$  cut samples can be observed at  $T_c$  (e.g.,  $K_{\max} = 7,600$  vs. 540). The dielectric loss increased sharply in the  $a$ - $b$  plane as temperature increased (Figures 5.11b and c), presumably because the electrical conductivity in the  $a$ - $b$  plane ( $\parallel$  cuts) is higher than the  $c$  direction ( $\perp$  cuts) in SBN.

Figure 5.12 compares the dielectric spectra as a function of sintering time (1 min to 12 h) at 1400°C for the TV5-9 $\perp$  samples. The dielectric constant improves with sintering time, but, at the same time,  $T_c$  remains almost the same (i.e., between 141.5 to 143.7°C).  $K_{\max}$  increases from 4,970 to 7,120 because of the improved orientation in the  $c$  direction as the sintering time at 1400°C is increased from 1 min to 12 h. That is,  $f$  is 0.88 for 1 min and 0.93 for 12 h of sintering.

SBN is a relaxor ferroelectric as long as the Sr/Ba ratio is  $>0.34/0.66$ . The relaxor characteristics become more pronounced as the Sr/Ba ratio increases. As seen from Figure 5.11a and 5.12, the SBN53 samples showed relatively little dispersion, which can be attributed to the homogenous distribution of cations (especially  $K^+$ ) within the TTB structure due to the liquid phase sintering. Above  $T_c$ , the dielectric constant decreases

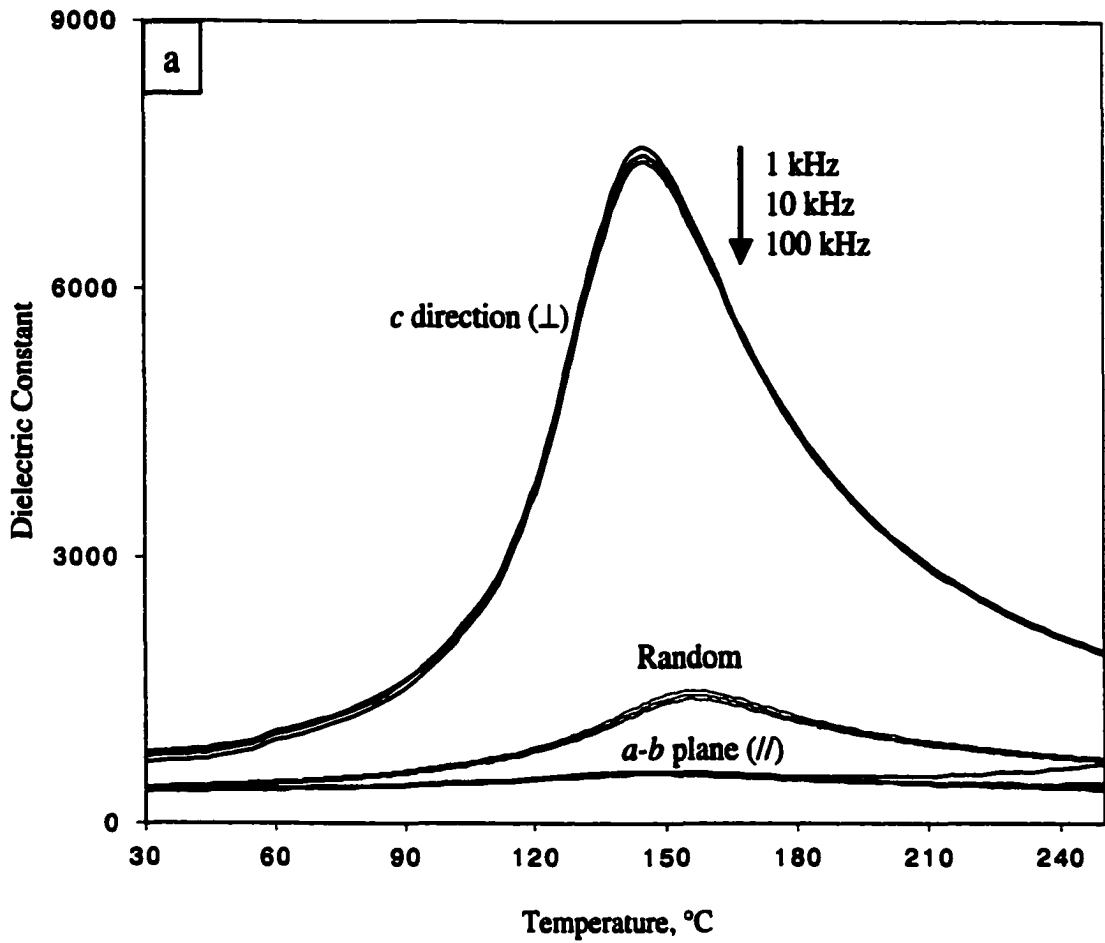


Figure 5.11. (a) Temperature and crystallographic direction dependence of dielectric constant for the sample TV15, (b) dielectric loss in the  $c$  direction ( $\perp$  cut), and (c) in the  $a$ - $b$  plane ( $//$  cut). Random sample is RV15.



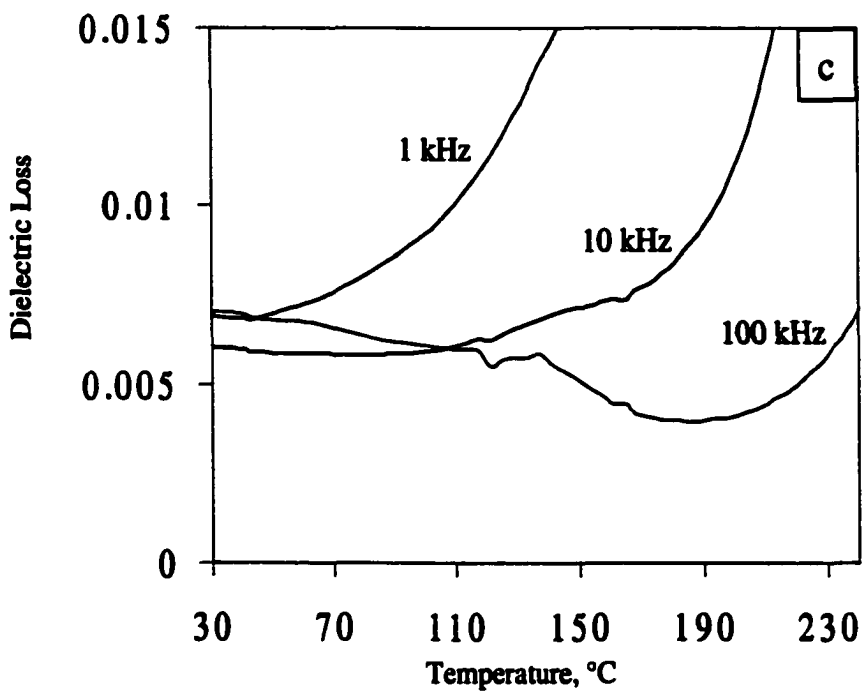
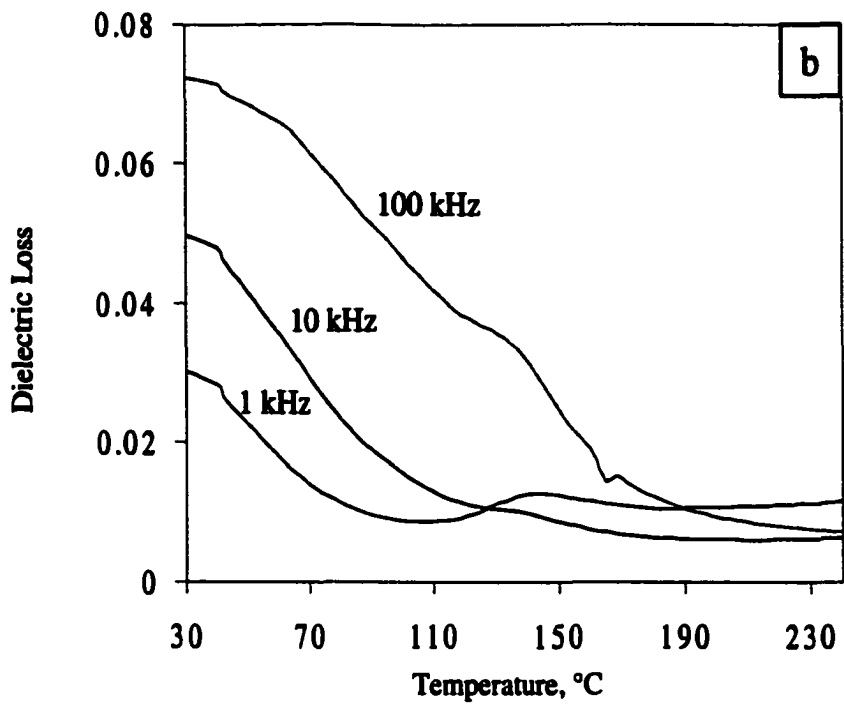


Figure 5.11. Continued.

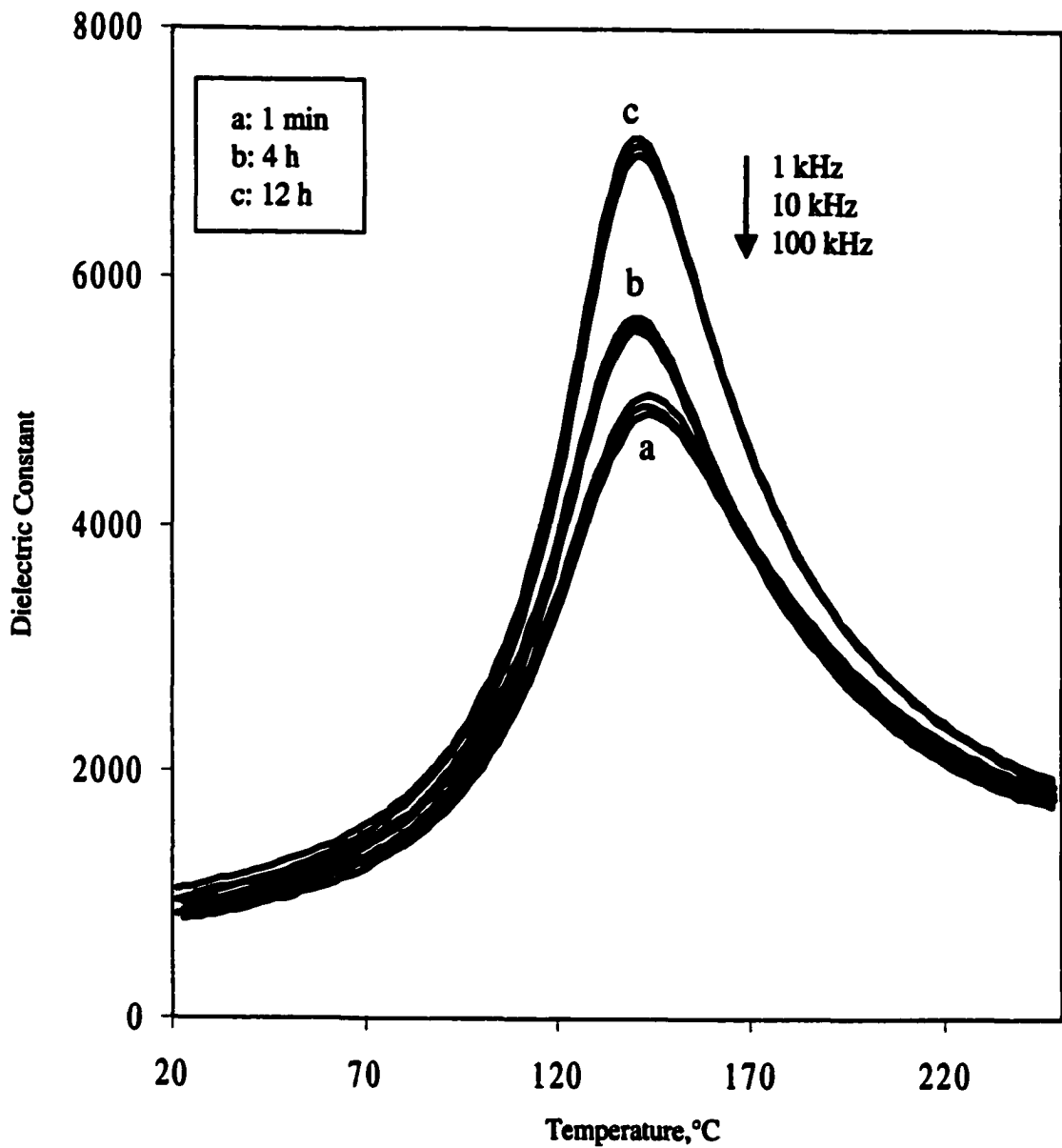


Figure 5.12. Dielectric constant as a function of sintering time for the TV5-9L samples. Samples were sintered at 1400°C.

slightly with increasing frequency due to the gradual loss of the space charge contribution to the permittivity.

Figure 5.13 shows that the average (i.e., arithmetic mean of at least 3 measurements on different samples)  $K_{\text{max}}$  improves sharply with increasing  $f$ . The best dielectric constant is obtained in the TV15 $\perp$  samples ( $K_{\text{max}} = 7,900$ ) because, from a processing point of view, it was found that the TV15 samples have attained a high  $f$  (0.91) (Fig. 5.8) with a low  $r$  parameter (0.24) (Fig. 5.9), as compared to the TV5-TV12 samples. However, this maximum value is well below the single crystal values. For example,  $K_{\text{max}} = 81,000$  [13] and 40,000-63,000 [13,14] were measured for the SBN50 and SBN60 single crystals, respectively. The average  $K_{\text{max}}$  for the random samples (i.e., RV5-RV15) is  $\sim 1430$ .

Lower dielectric properties in textured samples can be attributed to the existence of possible nonferroelectric grain boundary phase(s). Figure 5.14 proves for the R0 (no  $V_2O_5$  and template) and RV0 (no template) samples sintered at 1400°C for 4h that the RV0 sample shows consistently lower dielectric constants than the R0 sample that did not contain vanadium. This suggests that there may be a continuous non-ferroelectric layer of vanadium-rich compound(s) at the grain boundaries, which considerably suppress the observed dielectric properties, especially at the  $T_{\text{max}}$ . The same phenomenon is expected to occur in the templated samples containing vanadium oxide sintering aids. This would account for the low permittivities at  $T_c$  relative to single crystals. The TV5-15 samples probably have much thicker grain boundaries because excess  $Nb_2O_5$  is present both in the elongated grains and matrix grains (while the  $Nb_2O_5$  is contained only in the elongated grains in the TV5-TV15 samples). Therefore, the TV5-15 samples had a slightly lower

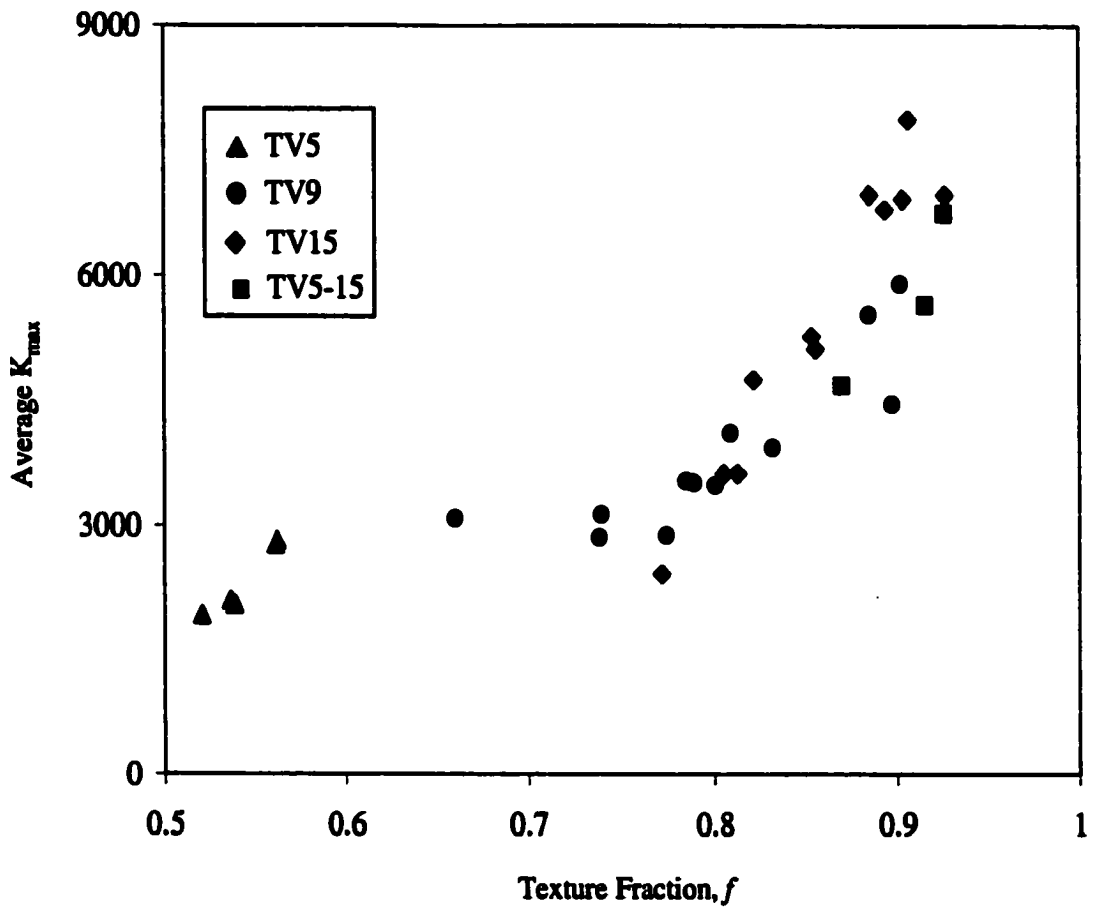


Figure 5.13. Average  $K_{max}$  as a function of initial template content and texture fraction (by the Lotgering factor) for the L-cut samples.

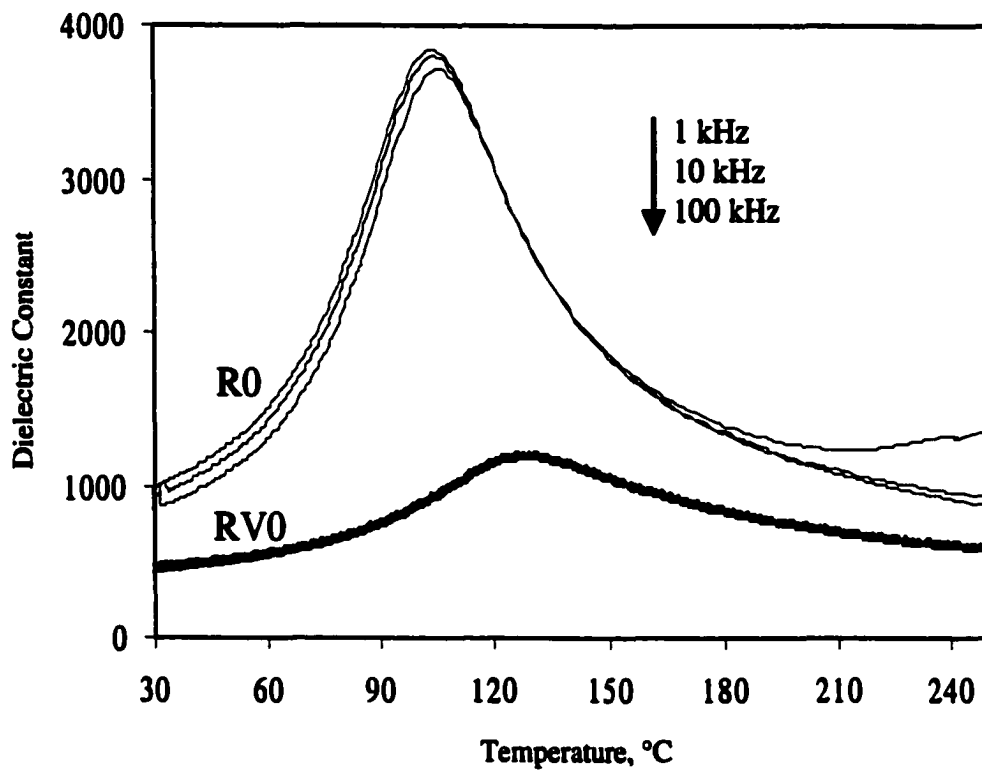


Figure 5.14. Temperature dependence of the dielectric constant for samples sintered at 1400°C for 4h.

$K_{\infty}$  (6,750) although they had a high  $f$  (0.93) and low  $r$  (0.29). A qualitative estimation of grain boundary thickness will be given in Chapter 7. Porosity also decreases the  $K$  values.

All of the samples have higher  $T_c$  values (e.g., 135.5°C for TV5 and 151.6 °C for TV5-15 after sintering for 4 h at 1400°C) than pure SBN50 single crystals (115-128°C) [2,13,15-18]. When alkali elements, such as  $\text{Na}^+$ ,  $\text{K}^+$ , are present in the structure, they partially or fully occupy the interstitial sites without vacancy formation [19,20] and cause  $T_c$  to increase, which stabilizes the ferroelectric structure.  $T_c$  increases due to the increased degree of filling of interstitial sites as the amount of KSN increases. In addition, a small incorporation of vanadium ions into the C sites may cause  $T_c$  to increase due to the stuffing effect (See Figure 5.14). For all samples, the Curie-Weiss constant is on the order of  $2 \times 10^5$  °C.

#### 5.3.2.2 Switching, Piezoelectric, and Pyroelectric Properties

Polarization-electric field (P-E) hysteresis loops were recorded at room temperature and at a frequency of 10 Hz. Figure 5.15 indicates that the remanent polarization ( $P_r$ ) increases with the applied field and template content. For example,  $P_r$  is  $5.1 \mu\text{C}/\text{cm}^2$  for the TV5,  $12.5 \pm 0.6 \mu\text{C}/\text{cm}^2$  for the TV15, and  $13.2 \pm 0.7 \mu\text{C}/\text{cm}^2$  for the TV5-15 samples at 50 kV/cm. Samples did not reveal any evidence of polarization fatigue on successive application of the field. For example,  $P_r$  remained almost the same for the TV15 $\perp$  sample after 140,000 cycles at 10 Hz, 50 kV/cm, and room temperature. However, some samples experienced aging in the form of “pinched” P-E loops, which was eliminated by increasing the number of driving field cycle.

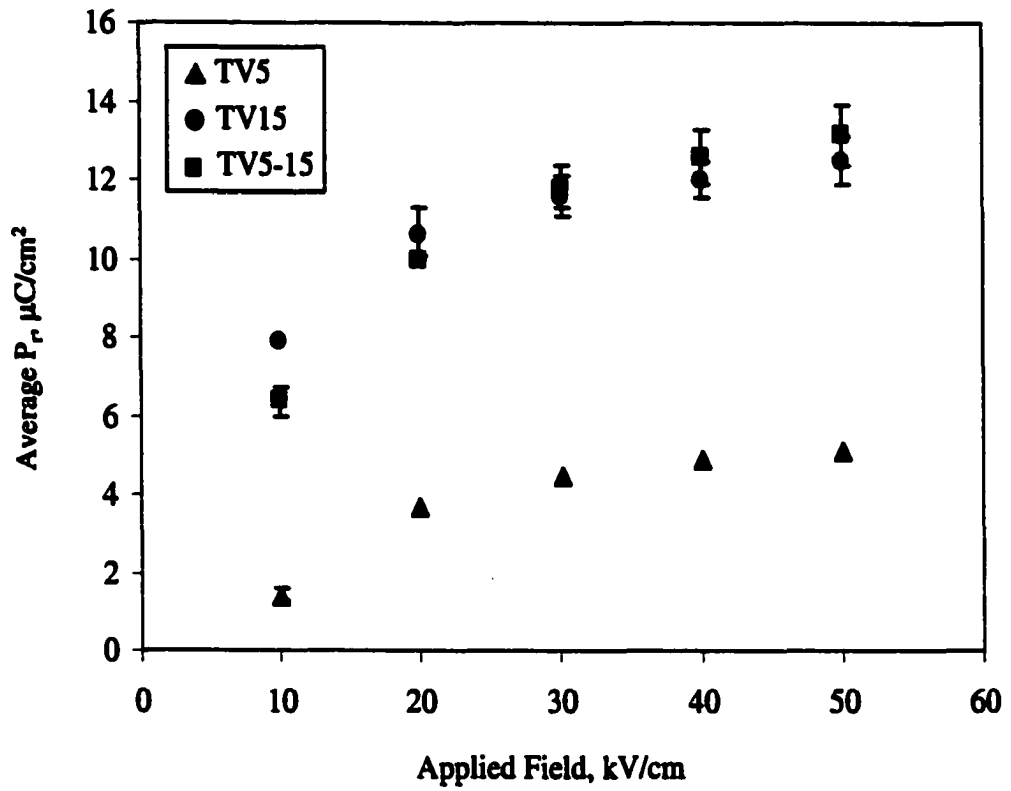


Figure 5.15. Change of average remanent polarization ( $P_r$ ) as a function of initial template content in the  $c$  direction. Samples were sintered at  $1400^\circ\text{C}$  for 4 h.

Figure 5.16 compares the hysteresis loops of samples TV15 ( $\perp$  and  $\parallel$  cuts) and RV15. A  $P_r$  of  $13.2 \mu\text{C}/\text{cm}^2$  and a saturation polarization ( $P_m$ ) of  $21 \mu\text{C}/\text{cm}^2$  (estimated from pyroelectric measurements) were obtained in  $\perp$  cuts (polar  $c$  direction). These values are much higher than the values reported for randomly oriented SBN ceramics (See Table 5.3).  $P_r = 2.6 \mu\text{C}/\text{cm}^2$  for the RV15 and  $1.1 \mu\text{C}/\text{cm}^2$  for the TV15// (nonpolar  $a$ - $b$  plane) were measured, which indicates that textured samples show very high anisotropy.

The change of average  $P_r$  and piezoelectric charge coefficient ( $d_{33}$ ) as a function of  $f$  and composition in the  $c$  direction is given in Figures 5.17 and 5.18, respectively. For comparison, SBN50 single crystal properties are also given. SBN50 single crystals have an average saturation polarization ( $P_m$  or  $P_s$ ) =  $27.4 \mu\text{C}/\text{cm}^2$  (it ranges from 25 to  $35 \mu\text{C}/\text{cm}^2$ , depending on the quality of the grown crystal) [18,21,24] and  $d_{33} = 97 \text{ pC}/\text{N}$  (it ranges from 90 to  $110 \text{ pC}/\text{N}$ ) [2,18,23-25]. In TGG ceramics, the  $P_r$  and  $d_{33}$  improve with increasing  $f$ . Compositions having a higher  $f$  (i.e.,  $> 0.9$ ) and lower  $r$  (i.e.,  $< 0.3$ ), such as TV15 and TV5-15, attained the maximum average  $P_r$  ( $13.2 \mu\text{C}/\text{cm}^2$ ) and  $d_{33}$  ( $88 \text{ pC}/\text{N}$ ) values. The  $P_m$  of  $21 \mu\text{C}/\text{cm}^2$  is close to the single crystal values. In addition,  $d_{33}$  is very high due to the higher dielectric constant and polarization induced by the strong grain orientation, and is comparable to the single crystals. A model equation (see Appendix B) was developed to correlate the measured  $P_r$  to  $r$  and  $f$ , and is given in detail together with the  $\text{V}_2\text{O}_5$ -free compositions in Chapter 6.

The increase in the saturation polarization with increasing texture resulted in improved pyroelectric properties. Figure 5.19 shows the pyroelectric coefficient as a function of temperature and crystallographic direction for the TV15 and RV15 samples.



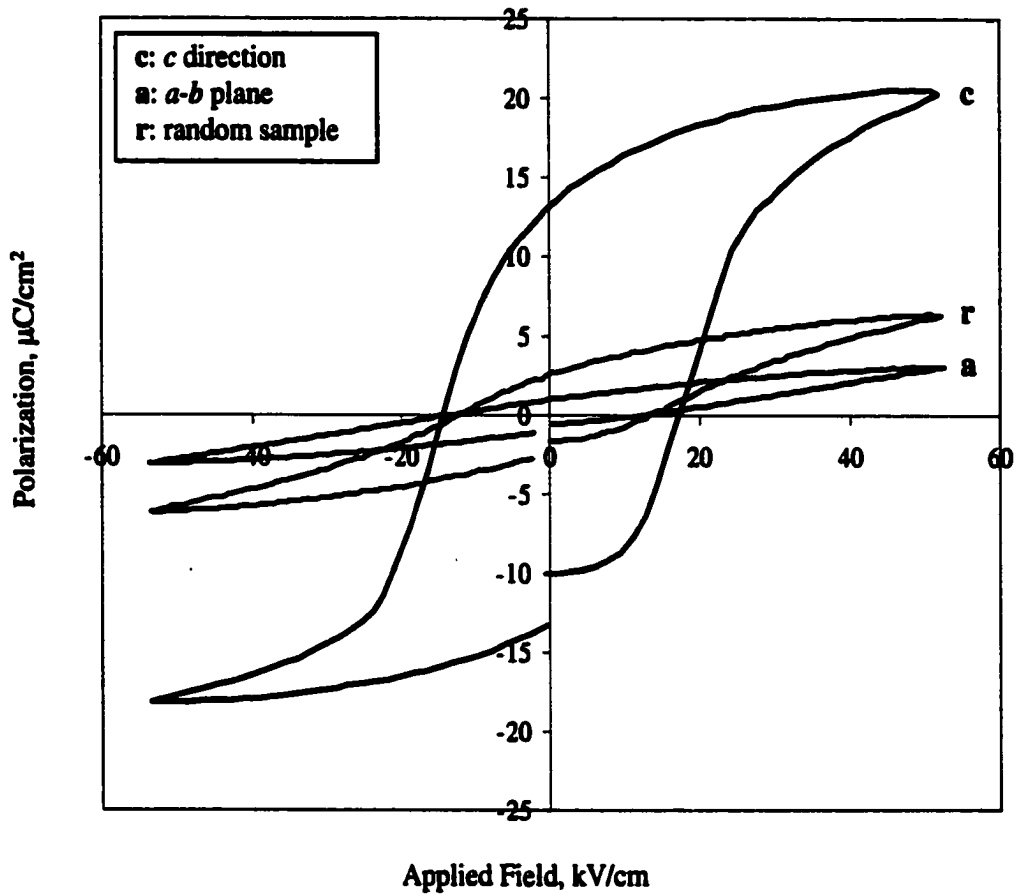


Figure 5.16. P-E graph of the samples sintered at 1400°C for 4h. Random sample is RV15.

**Table 5.3. Comparison of room temperature polarization values in the SBN ceramic literature.**

Composition	$P_r, \mu\text{C}/\text{cm}^2^*$	$P_{\text{sat}}, \mu\text{C}/\text{cm}^2^\#$	Reference
SBN50	-	6.5	24
$(\text{Sr}_{0.65}\text{Ba}_{0.225}\text{Li}_{0.2})\text{Nb}_2\text{O}_6$	2	-	29
Hot-pressed SBN30	2.9	-	6
Hot-pressed SBN40	2.5	-	
Hot-pressed SBN50	2.1	-	
SBN20 + 1 mol% $\text{V}_2\text{O}_5$	-	6.1 (at 50°C)	16
SBN30 + 1 mol% $\text{V}_2\text{O}_5$	-	6.1	14
SBN30	-	1.9	
SBN50	-	3.6	30

\*Remanent polarization

# Saturation polarization

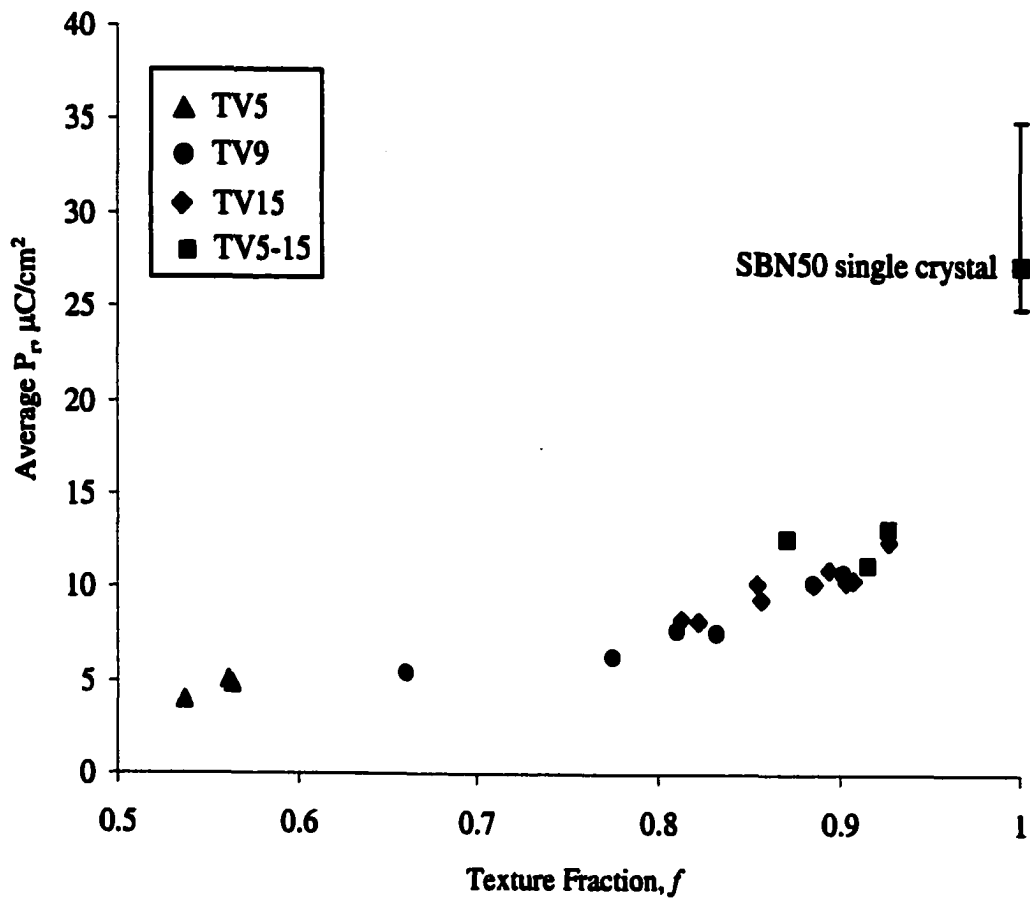


Figure 5.17. Change in the remanent polarization ( $P_r$ ) as a function of initial template content and texture fraction (by the Lotgering factor) for the  $\perp$ -cut samples.

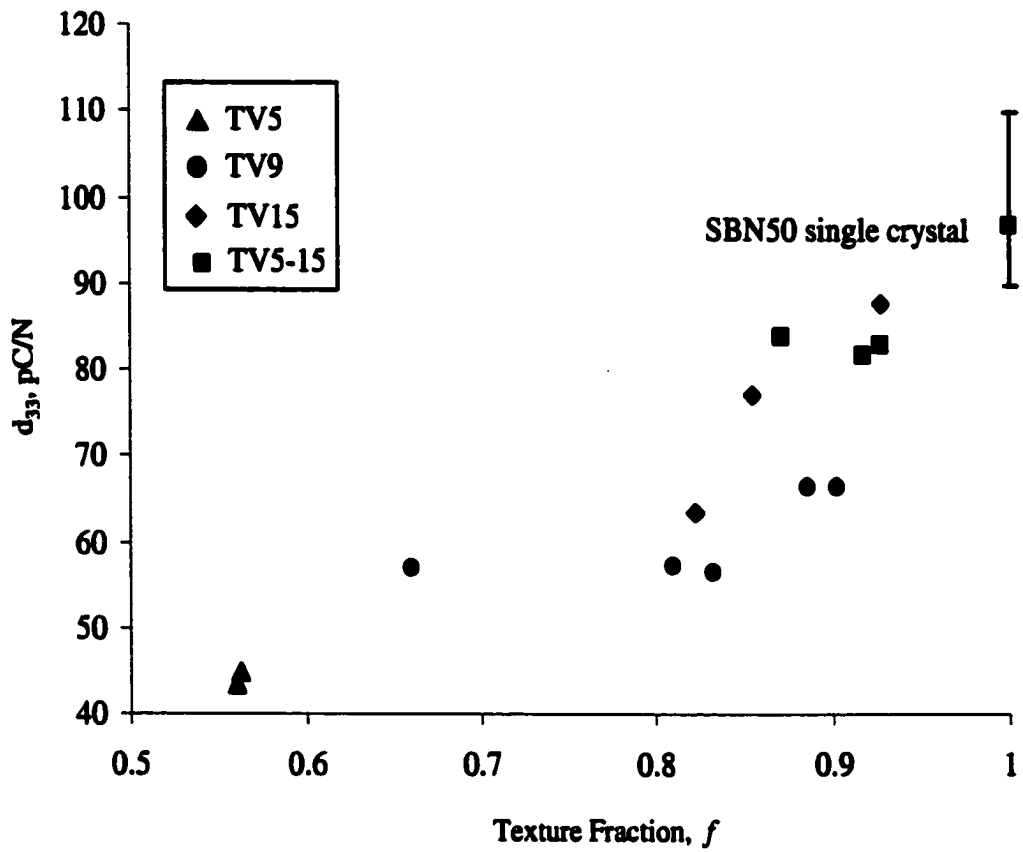


Figure 5.18. Change in the piezoelectric charge coefficient ( $d_{33}$ ) as a function of initial template content and texture fraction (by the Lotgering factor) for the  $\perp$ -cut samples.

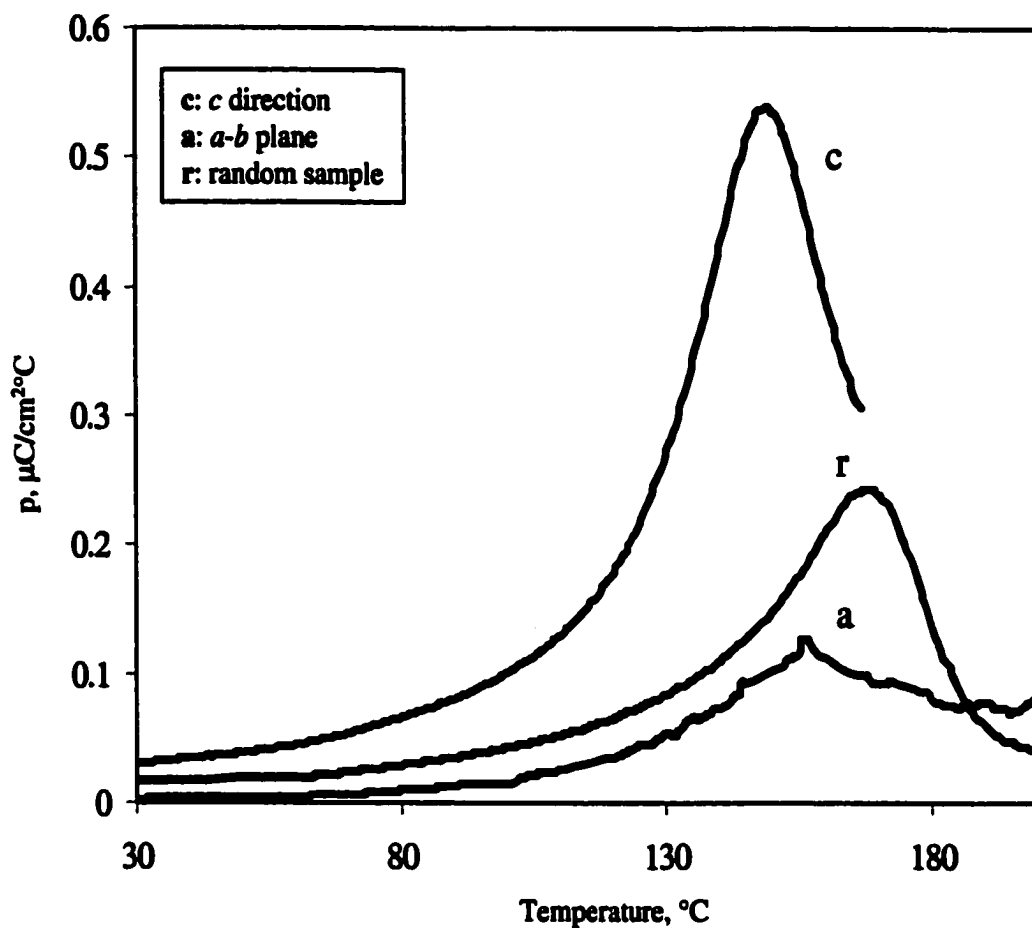


Figure 5.19. Pyroelectric coefficient as a function of temperature and crystallographic direction in the TV15 samples sintered 1400°C for 4 h. The random sample is RV15.

The pyroelectric current was found to be reversible for the heating and cooling runs up to 80°C, which means the measured data are not dominated by thermally stimulated current. The best room temperature pyroelectric coefficient of  $2.9 \times 10^{-2} \mu\text{C}/\text{cm}^2\text{C}$  was found in the TV15L. The reported pyroelectric coefficient for SBN50 single crystals is  $5.6 \times 10^{-2} \mu\text{C}/\text{cm}^2\text{C}$  [26]. The lower value for the TGG samples is due, in part, to their higher  $T_c$ 's.

The pertinent average room temperature dielectric and piezoelectric properties for random and textured samples sintered at 1400°C for 4 h are summarized in Table 5.4 as a function of crystallographic direction and composition. These results show that the electrical properties are considerably improved, compared to randomly oriented samples, and highly anisotropic properties can be achieved in the samples textured by TGG.

#### 5.4 CONCLUSIONS

Textured  $\text{Sr}_{0.53}\text{Ba}_{0.47}\text{Nb}_2\text{O}_6$  (SBN53) ceramics were successfully fabricated by templated grain growth (TGG), using acicular  $\text{KSr}_2\text{Nb}_5\text{O}_{15}$  (KSN) particles as templates for grain growth and  $\text{V}_2\text{O}_5$  as a liquid former. Specimens sintered at 1400°C for 12 h reached ~95% of the theoretical density. SBN53 phase formation initiated on the KSN templates and texture development started at temperatures as low as 950°C, even before the phase formation was completed (by  $T = 1100^\circ\text{C}$ ), due to melting of  $\text{V}_2\text{O}_5$  at 690°C. As sintering temperature and initial template concentration increased, the textured fraction ( $f$ ) also increased due to the preferential growth of template particles. Samples with low template content (5 and 9.1 wt%) were not as strongly textured due to the lower fraction of template particles and had wider orientation distributions in the  $c$  (or texture) direction due to anisotropic grain growth in the matrix. An  $f = 0.56$  and  $r = 0.32$  for the 5

**Table 5.4. The average room temperature dielectric and piezoelectric properties for random and textured samples sintered at 1400°C for 4 h.**

Sample	$T_c$ °C	$K_{max}$	K at 25°C	$\tan\delta$ (%)	$d_{33}$ , pC/N	$P_r$ , $\mu\text{C}/\text{cm}^2$	$E_c$ , kV/cm
RV0	127	1190	530	1.7	43	1.7	10.8
RV5	132	1410	510	2.7	35	1.9	10.9
TV5//	131	1235	530	2	25	2.1	12.5
TV5 $\perp$	136	2780	780	2.4	43	5.1	10.2
RV9	142	1440	490	2.1	37	2.2	11.8
TV9//	134	785	500	1.2	14	1.1	10.7
TV9 $\perp$	139	5520	1070	4.3	66	10.2	8.5
RV15	152	1440	430	2.5	40	2.5	12.6
TV15//	146	540	370	0.7	3	1.1	13.3
TV15 $\perp$	148	7000	770	3.6	88	12.5	11.6
TV5-9//	127	795	500	1.6	5	1.0	10.4
TV5-9 $\perp$	142	5450	1010	4.6	82	10.3	9.8
TV5-15//	151	730	445	1.7	4	1.2	12.1
TV5-15 $\perp$	152	6750	840	4.9	83	13.2	10.4

$T_c$ : Temperature at the  $K_{max}$ ; measured at 1 kHz during cooling.

$P_r$  and  $E_c$ : Measured at room temperature and 10 Hz, for an applied field of 50 kV/cm.

$K_{max}$  and K at 25°C: Measured at 1 kHz during cooling.

$\tan\delta$  (%): Measured at room temperature and 1 kHz during cooling.

$d_{33}$ : At 100 Hz and room temperature, after poling at 20 kV/cm at temperatures ~ 10-15°C above  $T_c$ .

wt%, and  $f = 0.93$  and  $r = 0.24$  for the 15 wt% templates were obtained at 1400°C. However, highly textured samples ( $f = 0.93$  and  $r = 0.29$ ) were obtained with only 5 wt% templates when the matrix grain growth was delayed by adding  $K_2O$  and  $Nb_2O_5$  to the matrix.  $K^+$  ions from the templates homogenized through the matrix with sintering temperature, and the homogenization was completed at  $T \geq 1350^\circ\text{C}$ .

Samples with a high  $f$  and small  $r$  exhibited better electrical properties. Existence of a non-ferroelectric vanadium-containing phase at the grain boundaries caused the dielectric constant to decrease. Therefore, a maximum  $K_{33} = 7,900$  was obtained which is only 10% of the single crystal value.  $T_c$  was found to be higher than that of single crystals due to the presence of  $K^+$  ions from KSN templates and incorporation of vanadium ions from the liquid phase former. The best room temperature electrical properties obtained in the  $c$  (polar) direction were  $P_r = 13.9 \mu\text{C}/\text{cm}^2$ ,  $P_m = 21 \mu\text{C}/\text{cm}^2$  (60-84% of single crystal),  $d_{33} = 88 \text{ pC}/\text{N}$  (80-98% of single crystal), and  $p_3 = 2.9 \times 10^{-2} \mu\text{C}/\text{cm}^2\text{C}$  (52% of single crystal). Samples did not reveal any evidence of polarization fatigue on successive application of the field. However, some samples experienced an aging effect in the form of “pinched” loops during polarization reversal, which was eliminated by increasing the number of driving field cycles.

These electrical properties are much greater than the reported values in SBN ceramic literature (over the whole solid solution range), which makes the TGG approach viable for fabricating ceramics with single crystal-like properties.



## 5.5 REFERENCES

- 1- K. Shoji and Y. Uehara, "Grain orientation of SbSI ceramics," *Japan. J. of Appl. Phys.*, 30[9B], 2315-17 (1991)
- 2 - R. R. Neurgaonkar, W. K. Cory, and J. R. Oliver, "Growth and applications of ferroelectric tungsten bronze family crystals," *Ferroelectrics*, 51, 3-8 (1983)
- 3 - R. R. Neurgaonkar, J. R. Oliver, and L. E. Cross, "Ferroelectric properties of tetragonal tungsten bronze single crystals," *Ferroelectrics*, 56, 31-36 (1984)
- 4 - NIH Image, V.1.56, by W. Rasband, National Institute of Health, USA.
- 5 - M. M. Seabaugh, M. D. Vaudin, J. P. Cline, and G. L. Messing, "Comparison of texture analysis techniques for highly oriented  $\alpha$ -Al<sub>2</sub>O<sub>3</sub>," *J. Am. Ceram. Soc.*, 83[8], 2049-54 (2000)
- 6- M. D. Vaudin, "TexturePlus," National Institute of Standards and Technology, Ceramics Division, Gaithersburg, MD.
- 7 - A. March, "Mathematische Theorie der Regelung nach der Korngestalt bei Affiner Deformation," *Z. Kristallogr.*, 81, 285-297 (1932)
- 8 - W. A. Dollase, "Correction of intensities for preferred orientation in powder diffractometry: Application of the March model," *J. Appl. Cryst.*, 19, 267-72 (1986)
- 9- S. Nishiwaki, J. Takahashi, and K. Kodaira, "The effect of V<sub>2</sub>O<sub>5</sub> addition on ferroelectric properties of Sr<sub>0.3</sub>Ba<sub>0.7</sub>Nb<sub>2</sub>O<sub>6</sub> ceramics," *J. Ceram. Soc. Japan*, Int. Edition, 103, 1233-36 (1995)
- 10- V. K. Trunov, E. V. Murashova, Y. V. Oboznenko, Y. A. Velikodnyi, and L. N. Kinzhibaio, "The BaO-V<sub>2</sub>O<sub>5</sub>-Nb<sub>2</sub>O<sub>5</sub> system," *Russ. J. Inorg. Chem.*, 30, 269-71 (1985)

- 11- S. Nishiwaki, J. Takahashi, and K. Kodaira, "Synthesis and phase transition of ferroelectric  $\text{Sr}_{0.2}\text{Ba}_{0.8}\text{Nb}_2\text{O}_6$  with  $\text{V}_2\text{O}_5$  addition," *J. Ceram. Soc. Japan*, Int. Edition, 104, 413-16 (1996)
- 12- M. M. Seabaugh, I. H. Kerscht, and G. L. Messing, "Texture development by templated grain growth in liquid-phase sintered  $\alpha$ -alumina," *J. Am. Ceram. Soc.*, 80[5], 1181-88 (1997)
- 13- A. M. Glass, "Investigation of the electrical properties of  $\text{Sr}_{1-x}\text{Ba}_x\text{Nb}_2\text{O}_6$  with special reference to pyroelectric detection," *J. Appl. Phys.*, 40[12], 4699-713 (1969)
- 14 - R. R. Neurgaonkar, W. W. Ho, W. K. Cory, W. F. Hall, and L. E. Cross, "Low and high frequency dielectric properties of ferroelectric tungsten bronze  $\text{Sr}_7\text{KNb}_3\text{O}_{13}$  crystals," *Ferroelectrics*, 51, 185-91 (1984)
- 15- R. R. Neurgaonkar, W. K. Cory, J. R. Oliver, E. J. Sharp, G. L. Wood, and G. J. Salamo, "Growth and optical properties of ferroelectric tungsten bronze crystals," *Ferroelectrics*, 142, 167-88 (1993)
- 16- R. Guo, A. S. Bhalla, G. Burns, and F. H. Dacol, "Studies on annealing and quenching of strontium barium niobate (SBN) single crystals: A-site cation ordering-disordering effect," *Ferroelectrics*, 93, 397-405 (1989)
- 17- M. DiDomenico, Jr. and S. H. Wemple, "Oxygen-octahedra ferroelectrics. I. Theory of electro-optical and nonlinear optical effects," *J. App. Phys.*, 40[2], 720-34 (1969)
- 18- R. R. Neurgaonkar, W. F. Hall, J. R. Oliver, W. W. Ho, and W. K. Cory, "Tungsten bronze SBN: A case history of versatility," *Ferroelectrics*, 87, 167-79 (1988)

- 19-** S. N. Murty, K. V. R. Murty, K. C. Mouli, A. Bhanumathi, S. B. Raju, G. Padmavathi, and K.L. Murty, "Relaxor behaviour in certain tungsten bronze ceramics," *Ferroelectrics*, 158, 325-30 (1994)
- 20-** K. Umakantham, S. N. Murty, K. S. Rao, and A. Bhanumathi, "Effect of rare-earth ions on the properties of modified SBN ceramics," *J. Mater. Sci. Letters*, 6, 565-67 (1987)
- 21-** S. B. Deshpande, H. S. Potdar, P. D. Godbole, and S. K. Date, "Preparation and ferroelectric properties of SBN50 ceramics," *J. Am. Ceram. Soc.*, 75[9], 2581-85 (1992)
- 22-** I. Camlibel, "Spontaneous polarization measurements in several ferroelectric oxides using a pulsed-field method," *J. Appl. Phys.*, 40[4], 1690-93 (1969)
- 23-** R. R. Neurgaonkar, J. R. Oliver, W. K. Cory, and L.E. Cross, D. Viehland, "Piezoelectricity in tungsten bronze crystals," *Ferroelectrics*, 160, 265-76 (1994)
- 24-** S. T. Liu, "Pyroelectric properties of dislocation-free ferroelectric SBN50 crystals," *Ferroelectrics*, 22, 709-10 (1978)
- 25-** T. W. Cline, L. E. Cross, and S. T. Liu, "Dielectric behaviour of SBN50 crystals," *J. Appl. Phys.* 49[7], 4298-4300 (1978)
- 26-** S. T. Liu, R. B. Maciolek, J. D. Zook, and B. Rajagopalan, "Electrooptic and ferroelectric effect in La-doped SBN single crystals," *Ferroelectrics*, 87, 265-69 (1988)

## CHAPTER 6

### TEMPLATED GRAIN GROWTH OF $\text{Sr}_{0.53}\text{Ba}_{0.47}\text{Nb}_2\text{O}_6$ CERAMICS

#### WITHOUT $\text{V}_2\text{O}_5$ ADDITIVES

##### 6.1 INTRODUCTION

In the preceding chapter, the TGG and the electrical properties of  $\text{V}_2\text{O}_5$ -doped  $\text{Sr}_{0.53}\text{Ba}_{0.47}\text{Nb}_2\text{O}_6$  (SBN53) ceramics were investigated. Acicular  $\text{KSr}_2\text{Nb}_5\text{O}_{15}$  (KSN) particles (5 to 15.4 wt%) were used as templates for grain growth. It was found that texture development started at  $T < 1000^\circ\text{C}$  due to melting of  $\text{V}_2\text{O}_5$  at  $690^\circ\text{C}$ . The liquid phase also promoted anisotropic grain growth in the matrix, which interfered with template growth and, particularly at low template loadings, caused broadening of the orientation distribution about the polar axis. Highly grain-oriented ceramics ( $f \sim 0.93$  as measured by the Lotgering factor) had 60-84% of single crystal saturation polarization and 80-98% of single crystal strain coefficient ( $d_{33}$ ) in the polar ( $c$ ) direction. However, the peak dielectric properties were much lower than the single crystal values due to the presence of  $\text{V}_2\text{O}_5$ -based non-ferroelectric phase(s) on the grain boundaries.

In this chapter, densification, texture development, and microstructure evolution in a reactive matrix is investigated as a function of KSN template content (5 to 15.4 wt%) and sintering conditions (1200 to  $1450^\circ\text{C}$  for 1 min to 12 h). Template growth was investigated in undoped and  $\text{Nb}_2\text{O}_5$ -rich matrices (i.e., no  $\text{V}_2\text{O}_5$  addition). The processing and electrical properties of textured SBN53 are compared to those of random samples, textured samples prepared with  $\text{V}_2\text{O}_5$  (See Chapter 5), and single crystals. A method is

proposed to model the polarization behavior as a function of processing parameters ( $f$  and  $r$ ).

## 6.2 EXPERIMENTAL PROCEDURE

$\text{SrNb}_2\text{O}_6$  (SN) and  $\text{BaNb}_2\text{O}_6$  (BN) powders were used to prepare SBN53 ceramics by reactive sintering. The synthesis of KSN templates was described in Chapter 3 and the synthesis of SN and BN matrix powders was described in Chapter 4. Procedures to orient the template particles in a mixture of SN and BN were described in Chapter 5. Table 6.1 summarizes the sample designation, KSN concentration, and initial amounts of additives in the SBN53 samples without  $\text{V}_2\text{O}_5$  addition. T refers to textured samples. For the T5-9 and T5-15 samples, only 5 wt% KSN templates were used. However, their compositions were adjusted to T9 and T15, respectively, by adding  $\text{K}_2\text{O}$  and  $\text{Nb}_2\text{O}_5$  according to the additive difference.

The dielectric constants of normal ferroelectric ceramics can be expressed by the Curie-Weiss law above  $T_c$  (or  $T_{\text{max}}$ ). However, the broad dielectric spectra of the relaxor ferroelectrics follow a quadratic law [1]. To quantify the phase transition modes for the intermediate type ferroelectrics (e.g., neither normal nor relaxor), a power law combining the Curie-Weiss and the quadratic laws was proposed by Uchino and Nomura [2], and is given as;

$$1 / K = (1 / K_{\text{max}}) + [(T - T_{\text{max}})^\gamma] / C \quad (6.1)$$

where  $K$  is the dielectric constant at  $T$ ,  $K_{\text{max}}$  is the dielectric constant at  $T_{\text{max}}$ ,  $\gamma$  is a diffuseness coefficient, and  $C$  is the Curie-Weiss constant. Eqn. (6.1) describes a normal ferroelectric when  $\gamma = 1$  (the Curie-Weiss law) and a relaxor ferroelectric when  $\gamma = 2$  (the

**Table 6.1 Sample designation, KSN content, and additive contribution in SBN53 ceramics without V<sub>2</sub>O<sub>5</sub> addition.**

Sample Designation	KSN content, wt%	Additive Contribution, wt%	
		K <sub>2</sub> O	Nb <sub>2</sub> O <sub>5</sub>
T5	5	0.26	0.72
T9	9.1	0.47	1.32
T12	12	0.62	1.74
T15	15.4	0.80	2.23
T5-9	5	0.47	1.32
T5-15	5	0.80	2.23

quadratic law).  $\gamma$  is determined from the slope of  $\log(1/K-1/K_{\infty})$  vs.  $\log(T-T_{\infty})$ . If both sides are multiplied by  $K_{\infty}$ , Eqn. (6.1) becomes;

$$K_{\infty} / K = 1 + [K_{\infty} (T - T_{\infty})^{\gamma}] / C \quad (6.2)$$

$C / K_{\infty}$  is a relative measure of the degree of diffuseness and is obtained from the slope of  $(K_{\infty} / K)$  vs.  $(T-T_{\infty})^{\gamma}$  [3].

Polarization-electric field (P-E) hysteresis loops were recorded in two different ways; in the first, the maximum voltage was increased sequentially (e.g., 10, 20, 30 kV/cm) (Type A) for the same sample and for the second one, the sample was depoled by annealing at 500°C for 1 h before each new measurement (Type B). The poling was performed by applying 10 kV/cm at ~10-15°C above the Curie temperature for 15 min and then cooling to room temperature while maintaining the field.

The other procedures were described in Chapter 5.

## 6.3 RESULTS

### 6.3.1 Densification and Phase Formation

Figure 6.1 shows the densification behavior of the samples as a function of sintering conditions and template concentration. The relative density was calculated based on the density of an SBN52 single crystal (5.33 g/cc) [4], which is close to the composition of interest. Densification increases sharply from 1200 to 1300°C and then levels off with further heating ( $\geq 94\%$ ). Densification is slower for the T5-15 samples below 1300°C. For sintering at 1400°C, the densities were nearly the same in samples

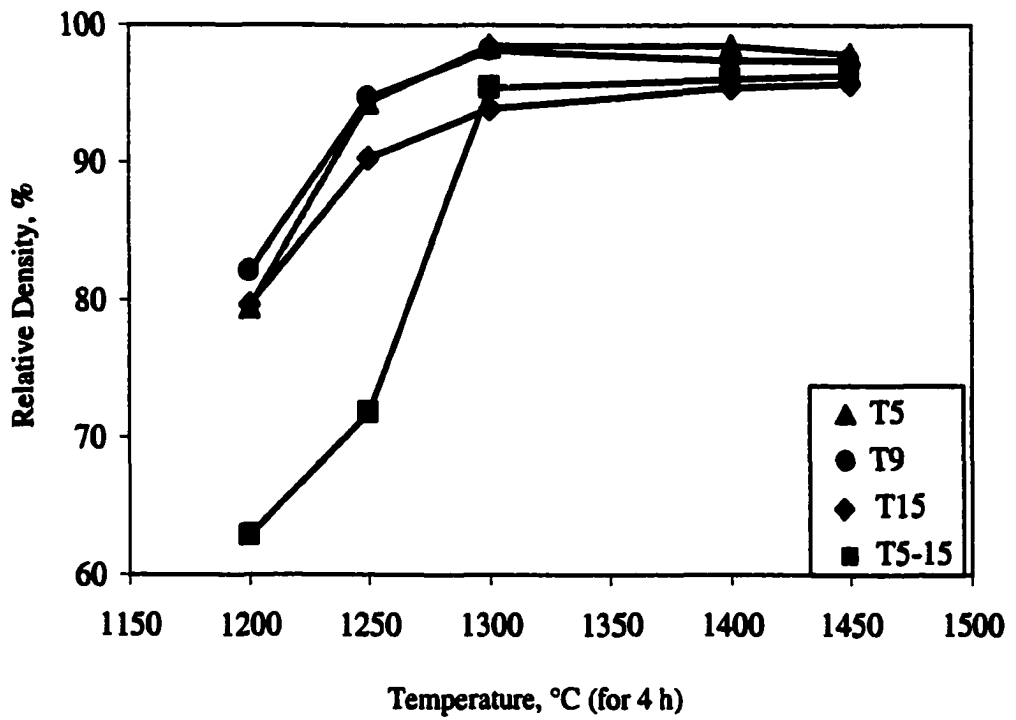


Figure 6.1 Densification of samples as a function of template concentration.



heat-treated between 1 min and 12 h. All samples transformed to the tetragonal tungsten bronze (TTB) structure by  $T = 1200^{\circ}\text{C}$ .

### 6.3.2 Texture Development

Figure 6.2 shows XRD patterns of the T9 samples ( $\perp$  cut) as a function of sintering temperature as well as a reference pattern of random SBN53 (R0 sample sintered at  $1250^{\circ}\text{C}$  for 5 h). For the T9 samples, the  $\{00l\}$  peaks dominate the diffraction pattern as the sintering temperature increases. Figure 6.3 shows that morphological texture development increases with increasing sintering temperature and/or time ( $//$  cuts). At  $1200^{\circ}\text{C}$ , the matrix is still very porous and there is no overgrowth on KSN templates. During matrix densification, the porosity concentrates in areas near template particles (Figs. 6.3b and c).

Figure 6.4 compares the effect of template concentration on texture development in the samples sintered at  $1400^{\circ}\text{C}$  for 12 h. For the T5-T15 samples (Figs. 6.4a-d), 5 wt% templates is insufficient for the full texture development. There are also some relatively small, elongated grains in the matrix (particularly  $< 10\ \mu\text{m}$ ) that are off-axis to the casting direction. Elongated grains are larger in dimension with decreasing template content. In addition, porosity in the samples increases with the template content. Note that there is no entrapped porosity within the elongated grains except for the T5-15 sample. In addition, elongated grains are much bigger in the T5-15// sample (Fig. 6.4e).

Table 6.2 shows a summary of average grain dimensions obtained from stereological analysis (See Appendix A). The average grain thickness and length increase

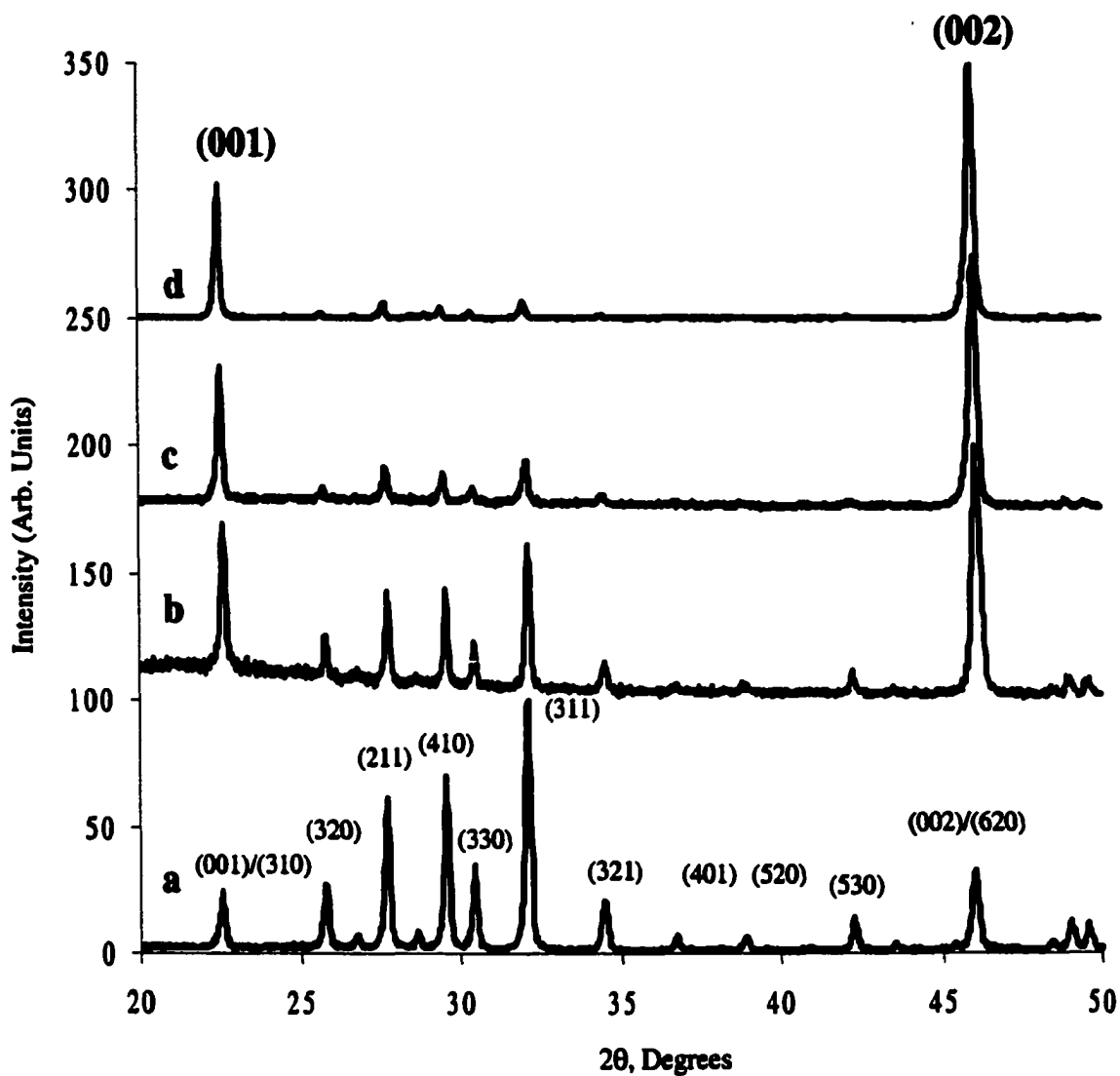
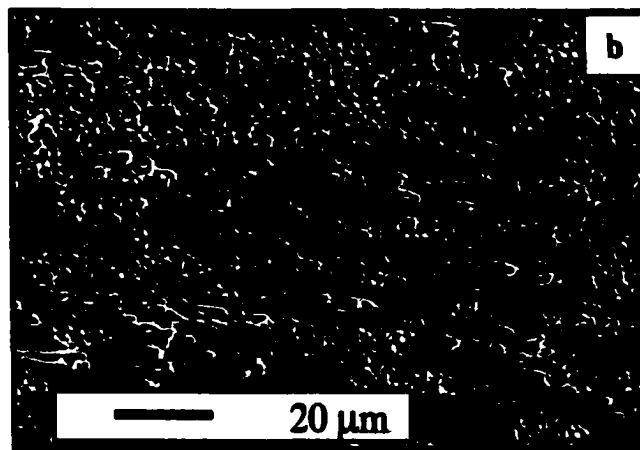
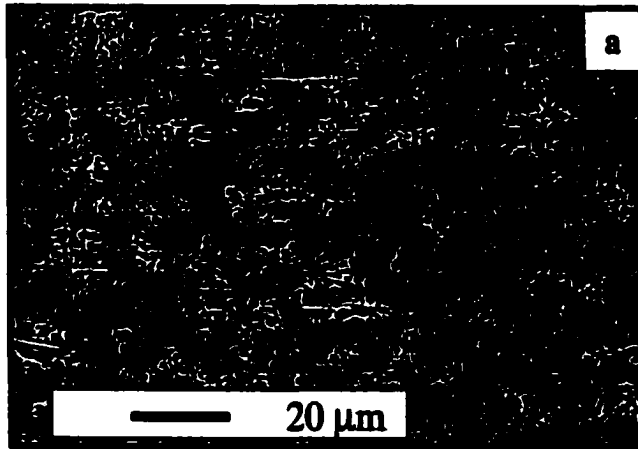
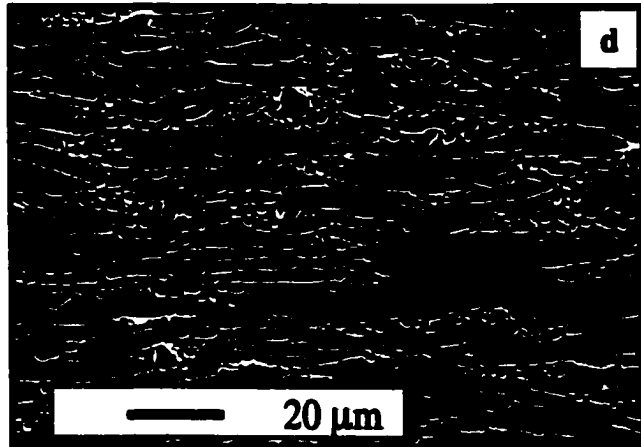
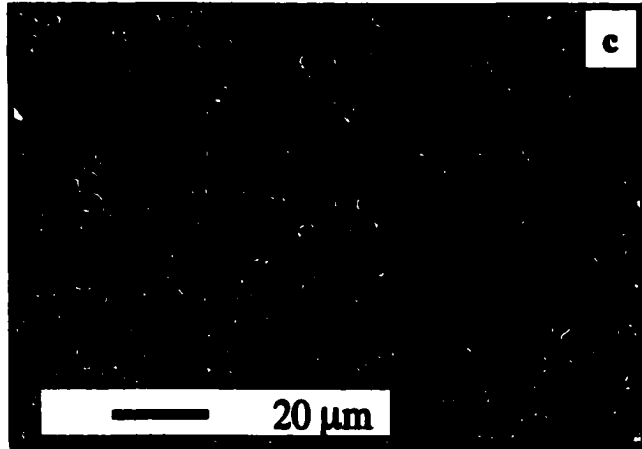


Figure 6.2 XRD patterns of the T9L samples after sintering for 4 h at; (b) 1200°C, (c) 1300°C, and (d) 1400°C. Curve "a" is for the random sample (heated at 1250°C for 5 h) and given as a untextured reference pattern. Major SBN53 peaks are marked.



**Figure 6.3** Texture development in the T9// samples as a function of sintering conditions; (a) 1200°C for 4 h, (b) 1300°C for 4 h, (c) 1400°C for 1 min, and (d) 1400°C for 4 h.



**Figure 6.3 Continued.**

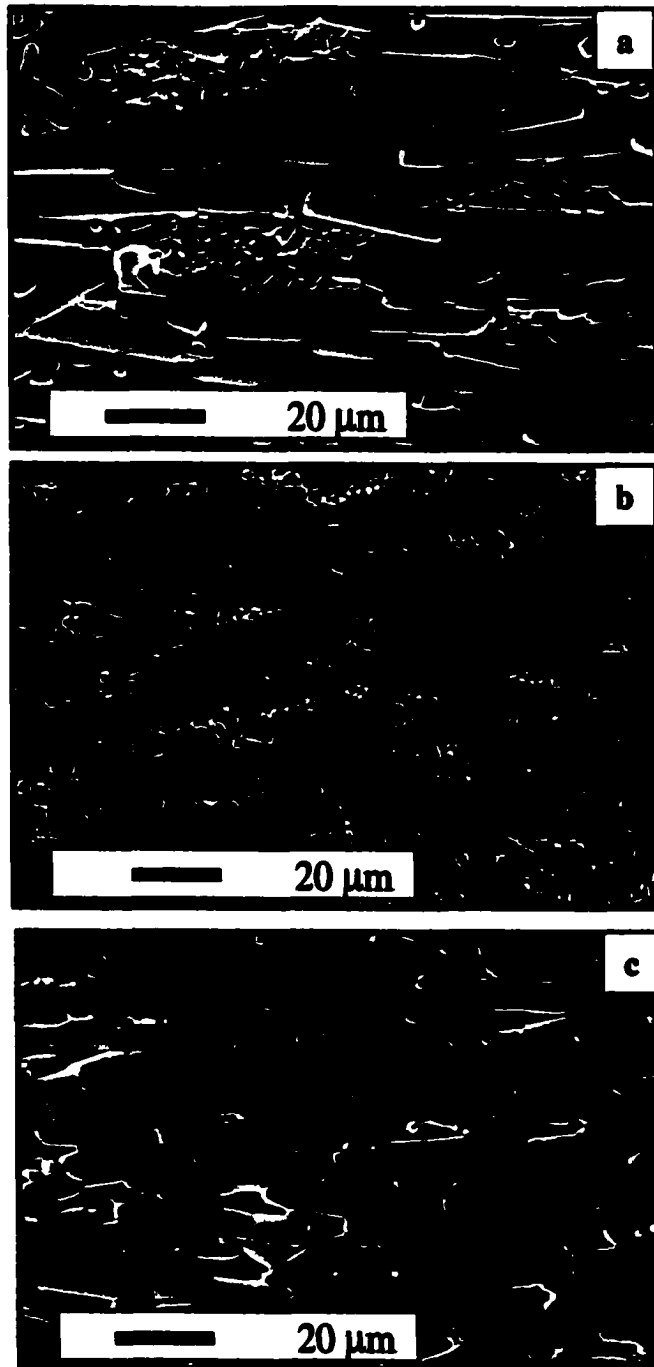


**Figure 6.4** Texture development as a function of template concentration after sintering at 1400°C for 12 h; (a) T5//, (b) T9//, (c) T12//, (d) T15//, and (e) T5-15//.

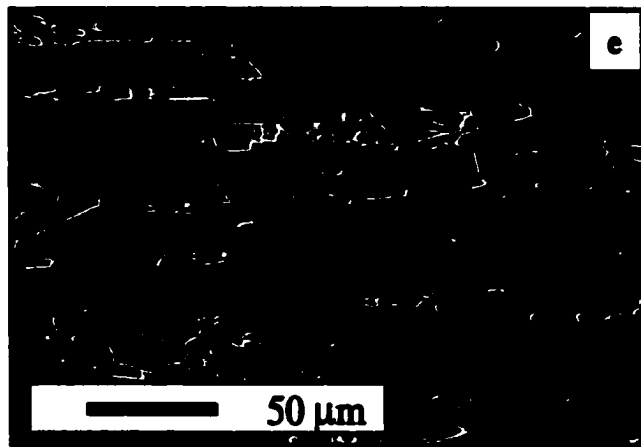
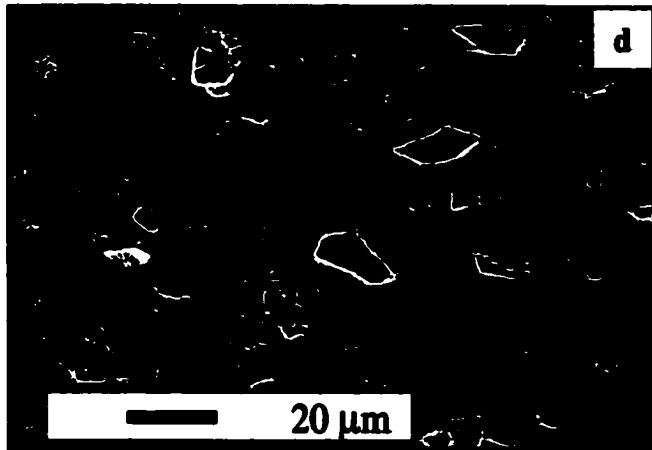


**Figure 6.4 Continued.**

**Table 6.2 Summary of average dimensions as a function of sintering conditions and template concentration.**

Sample	Average length, $\mu\text{m}$			Average thickness, $\mu\text{m}$			Average aspect ratio		
	1300°C	1400°C	1400°C	1300°C	1400°C	1400°C	1300°C	1400°C	1400°C
	4 h	4 h	12 h	4 h	4 h	12 h	4 h	4 h	12 h
T5	10.0	14.9	23.8	2.1	2.9	4.2	4.8	5.1	5.7
T9	8.8	12.7	16.8	2.0	2.5	3.1	4.4	5.1	5.4
T15	9.8	11.8	13.8	2.1	2.6	3.1	4.7	4.5	4.5
T5-15	15.3	19.9	35.7	3.6	3.5	5.7	4.3	5.7	6.3

with increasing temperature and/or time for all the samples, but the increment in the average aspect ratio is slight. The T5-15 samples have higher average values in length, thickness, and aspect ratio.

Crystallographic texture analysis was performed on the *c*-axis oriented samples ( $\perp$  cuts) by comparing the relative intensities of  $\{00l\}$  peaks with the  $\{hkl\}$  peaks in the random and oriented cases (Figure 6.5), using the Lotgering factor (Eqn. 5.1 in Chapter 5). The texture fraction ( $f$ ) increases with increasing sintering temperature and time for all the samples. The T5-15 samples attained  $f = 0.98$  after sintering at  $1400^{\circ}\text{C}$  for 12 h, compared to 0.61 for the T5 samples.

The Lotgering factor is a simple method to qualitatively characterize  $f$ . It, however, does not provide information about the texture distribution in the materials. Therefore, the texture distribution in the *c* (e.g., texture) axis was determined from rocking curves, as mentioned in Chapter 5. Figure 6.6 shows a graph of orientation distribution curves as a function of the angle  $\alpha$  for the samples sintered at  $1400^{\circ}\text{C}$  for 12 h. The curves on the plot are the result of curve-fitting to Eqn. 5.2 in Chapter 5. The  $r$  parameters are given on the plot. The correlation coefficient ( $R^2$ ) is  $\geq 0.95$  for each curve. The  $r$  value increases with increasing template content. Increase in the  $r$  parameter corresponds to widening of the orientation distribution curve about the texture direction (i.e.,  $[001]$ ).



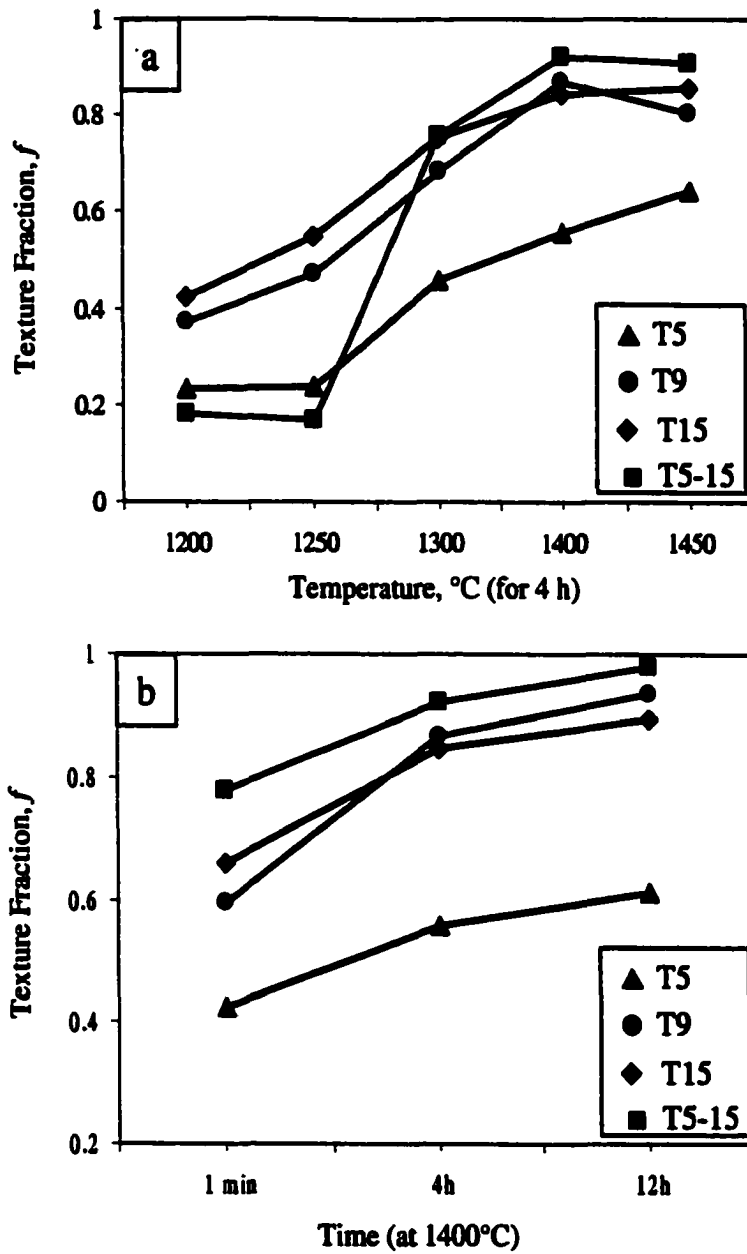


**Figure 6.5** Texture fraction ( $f$ ), calculated using the Lotgering factor, as a function of (a) sintering temperature and (b) time.

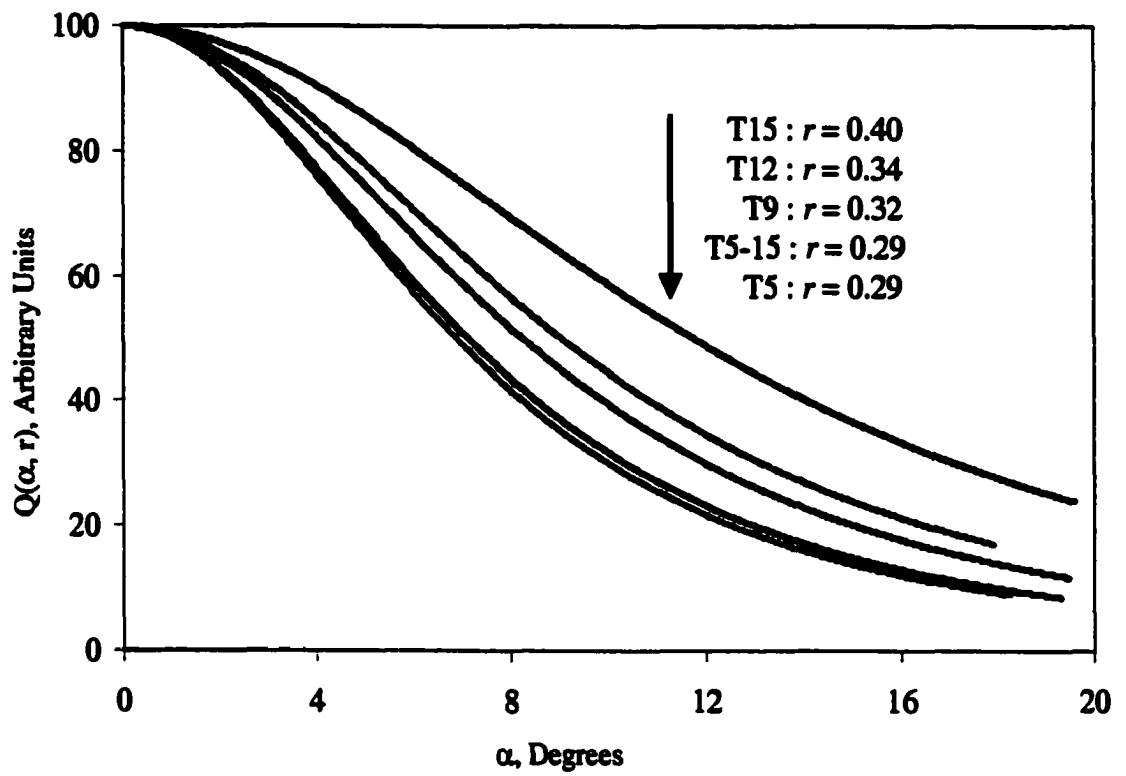


Figure 6.6 Orientation distribution curves for the  $\perp$ -cut samples sintered at 1400°C for 12 h. The curves are March-Dollase fits to the corrected rocking curve data.

### 6.3.3 Electrical Properties

#### 6.3.3.1 Dielectric Properties

Figure 6.7 shows the orientation and temperature dependence of the dielectric properties at different frequencies for the T9 samples sintered at 1400°C from 1 min to 12 h (samples are  $\geq 96.5\%$  dense). Figure 6.7a shows that the room temperature dielectric constants ( $K_{rt}$ ) decrease slightly with increasing sintering time, but the peak dielectric constant ( $K_{max}$ ) strongly improves in the  $c$  direction. Dielectric spectra indicate relaxor behavior with a gradually decreasing  $K_{max}$  with frequency. In addition, the breadth of the phase transformation diminishes with sintering time. The frequency dependence of  $T_{max}$  is more pronounced for the samples sintered for 1 min.  $K_{rt}$  and  $K_{max}$  are much lower in the nonpolar  $a$ - $b$  plane ( $//$  cuts), shown as an inset in Figure 6.7a, and decrease with increasing sintering time. In addition, the frequency dispersion of the dielectric spectra diminishes with sintering time. The anisotropy in the dielectric properties is consistent with data on SBN single crystals. The two orientations also show different dielectric loss behaviors such that the loss is lower in the  $a$ - $b$  plane ( $//$  cuts) than the  $c$  direction ( $\perp$  cuts). Unlike the  $a$ - $b$  plane, loss increases with sintering time in the  $c$  direction (Figure 6.7b).

Figure 6.8 shows the variation of average  $K_{max}$  for the  $\perp$ -cuts samples as a function of composition and  $f$ .  $K_{max}$  increases with increasing initial template content and  $f$ . A maximum  $K_{max}$  of 23,600 at  $f = 0.93$  was measured in the T9 $\perp$  samples.  $K_{max}$  of 1,525 and 860 in the random (R9) and T9 $//$  (same sample) were obtained, respectively. Although the T5-15 samples reached the highest texture fraction ( $f = 0.98$ ), they showed relatively lower  $K_{max}$  (of 17,000).

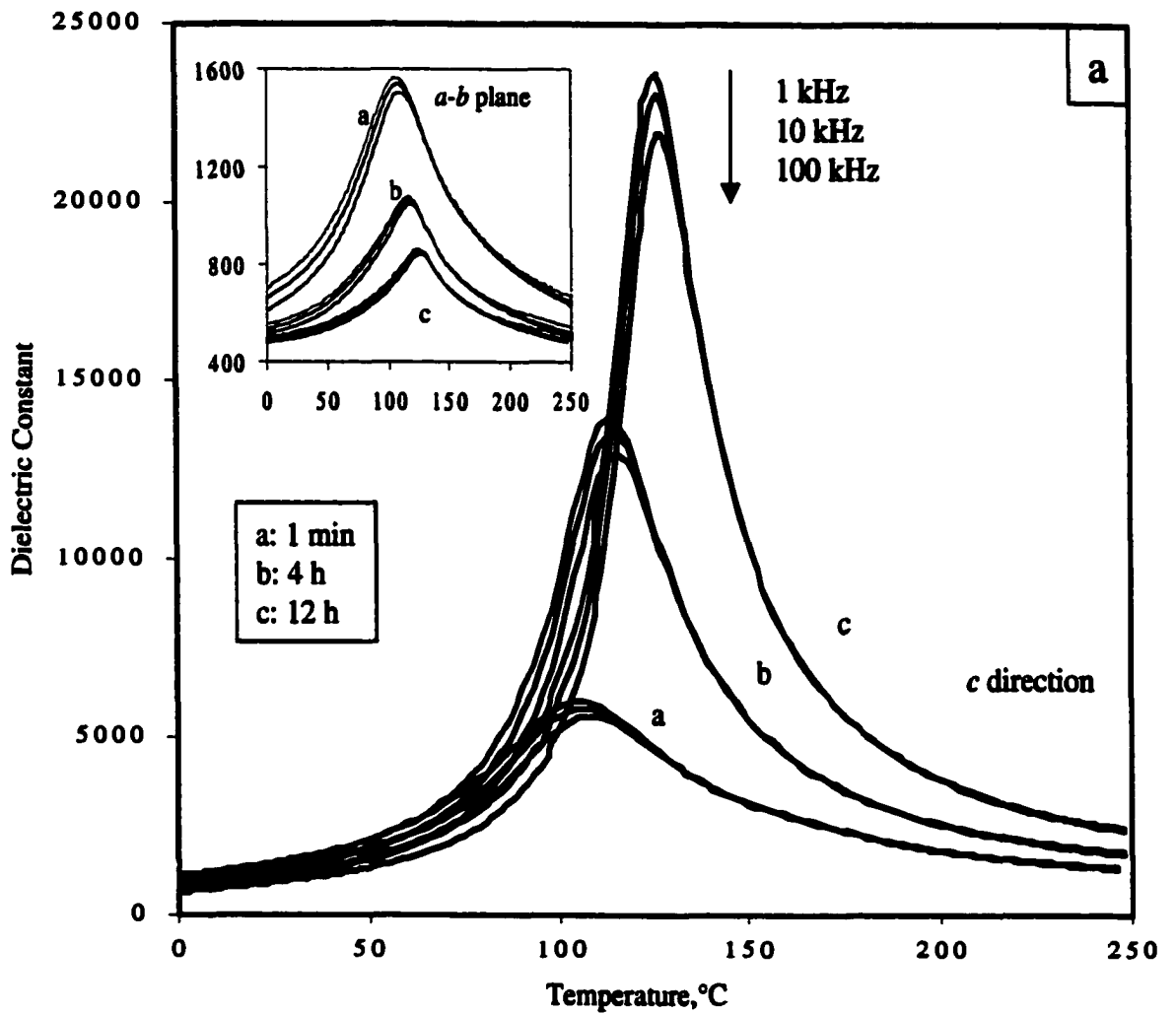


Figure 6.7 Dielectric constant (a) and loss (b) as a function of sintering time and crystallographic (polar *c* and nonpolar *a* or *b*) direction for the T9 samples. Samples were sintered at 1400°C. The inset in (a) gives the data for measurements in the *a-b* plane.

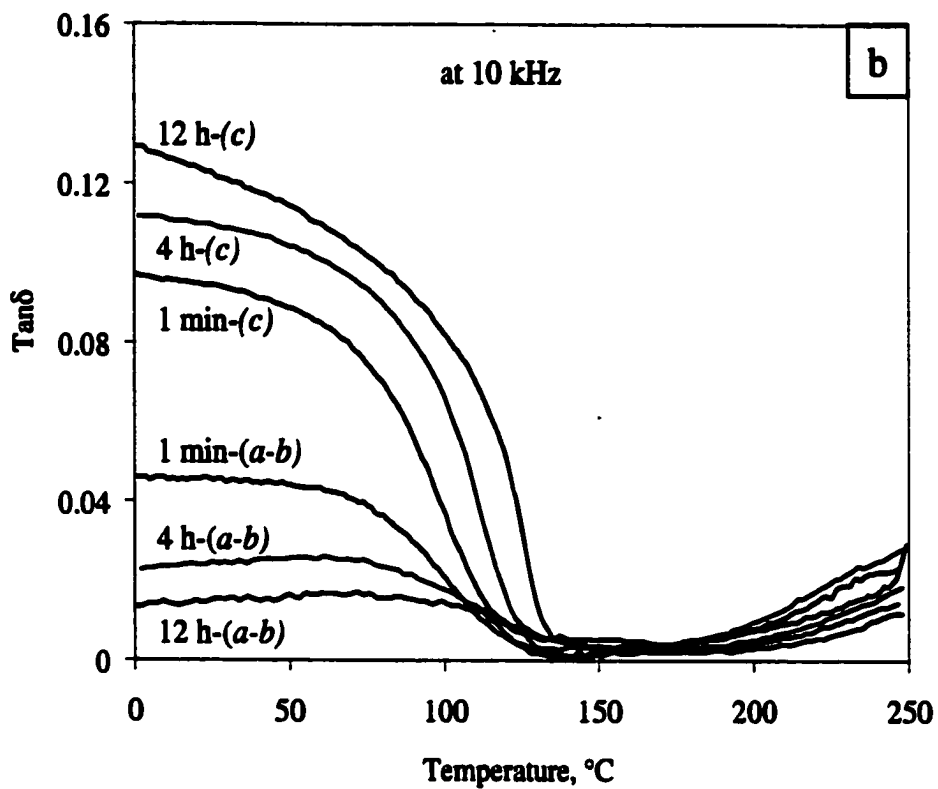


Figure 6.7 Continued.

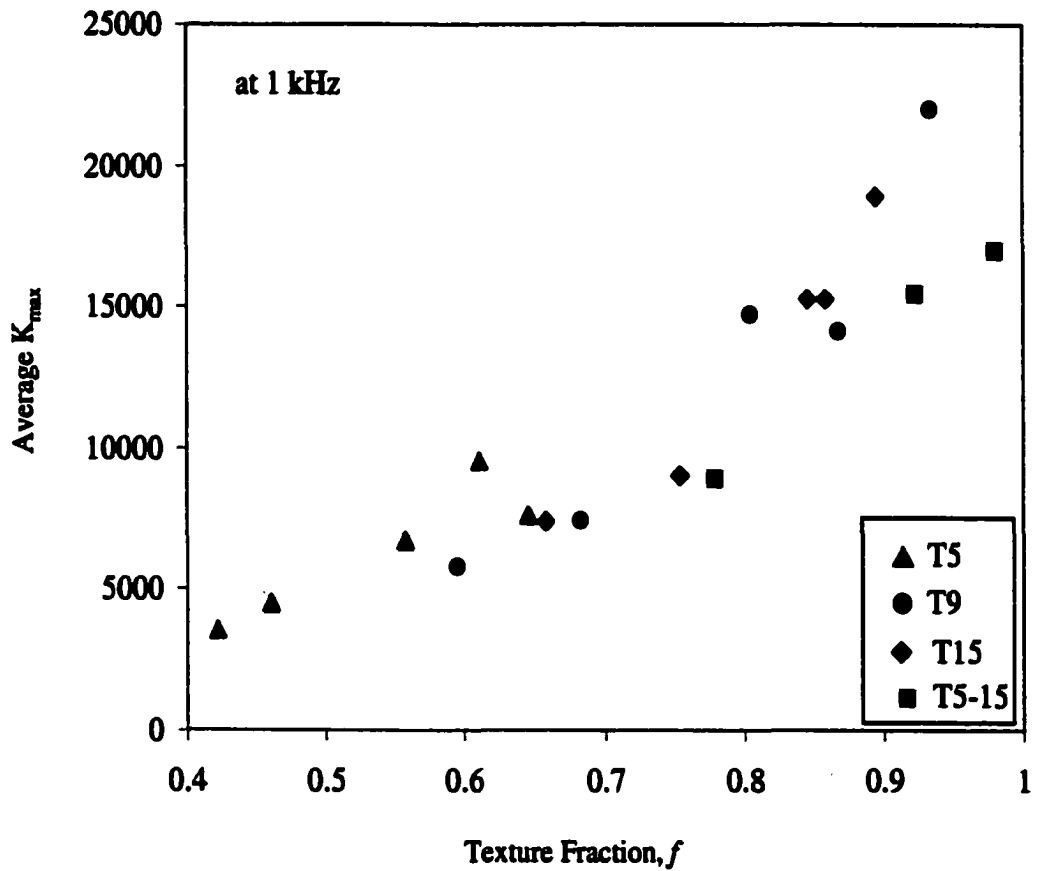


Figure 6.8 Average  $K_{\max}$  as a function of initial template content and texture fraction (by the Lotgering factor) for the  $\perp$ -cut samples. Samples are  $\geq 95\%$  dense.

The diffuseness coefficient ( $\gamma$ ) and degree of diffuseness ( $C/K_{\text{max}}$ ) were calculated using Eqns. (6.1 and 6.2). Figure 6.9 shows an analysis of  $(K_{\text{max}}/K)$  vs.  $(T-T_{\text{max}})^{\gamma}$  at 100 kHz for the T9 $\perp$  samples sintered at various sintering conditions. Each line has a correlation coefficient ( $R^2$ )  $\geq 0.99$  to a linear fit. The inset shows  $f$ ,  $\gamma$ , and  $C/K_{\text{max}}$  (in  $^{\circ}\text{C}$ ) as a function of sintering conditions. Samples sintered at 1400 $^{\circ}\text{C}$  for 1 min and 12 h have the lowest and highest  $K_{\text{max}}$  values (5,600 vs. 23,600), and corresponding  $f$  values (0.6 vs. 0.93), respectively.  $\gamma$  and  $C/K_{\text{max}}$  decrease with increasing  $f$ .

### 6.3.3.2 Switching and Piezoelectric Properties

When hysteresis (P-E) loops were recorded using progressively higher applied fields on highly textured T9 $\perp$  and T15 $\perp$  samples (Type A), it was found that extremely rapid fatigue was observed (See Fig. 6.10a). As a result, the remanent polarization ( $P_r$ ) decreased and coercive field ( $E_c$ ) increased on successive measurements. The decrease in switchable polarization with increasing measurement field could be avoided by heating the sample above  $T_c$  between measurements (Type B in Fig. 6.10b). In this case,  $P_r$  increases with the applied field. Highly textured T5-15 $\perp$  samples, however, did not show strong fatigue dependence and reached the highest  $P_r$  values (e.g.,  $P_r = 20.3 \mu\text{C}/\text{cm}^2$  at 50 kV/cm in Fig. 6.10b). In the  $a$ - $b$  plane,  $P_r$  decreased with increasing texture fraction, and there was no evidence for fatigue.

Comparison of the P-E loops as a function of crystallographic orientation and type of measurement is given in Figure 6.11 for the T5-15 samples sintered at 1400 $^{\circ}\text{C}$  for 12 h. The random sample (R15) was sintered at 1350 $^{\circ}\text{C}$  for only 4 h to prevent abnormal

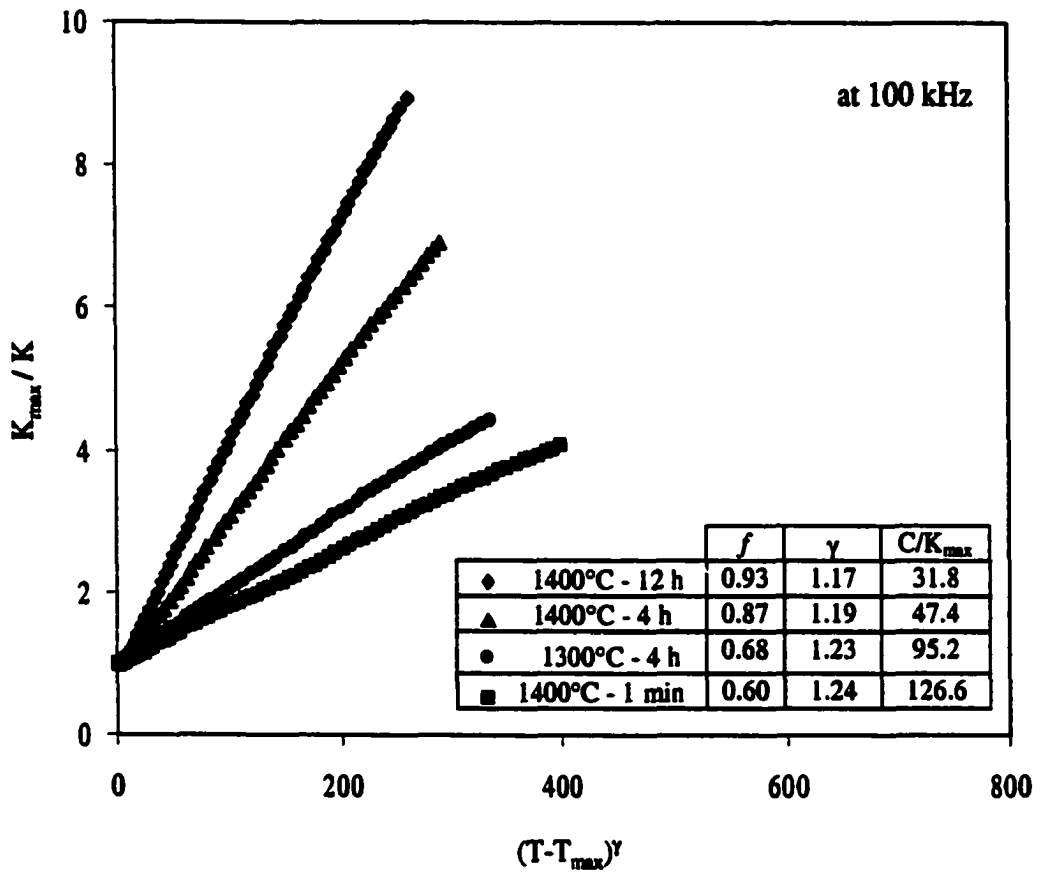


Figure 6.9 Plot of  $K_{\max}/K$  vs.  $(T-T_{\max})^\gamma$ , with calculated values of degree of diffuseness ( $C/K_{\max}$  in  $^\circ\text{C}$ ), as a function of sintering conditions for the T9L samples.  $f$  and  $\gamma$  stand for the texture fraction and diffuseness coefficient, respectively.



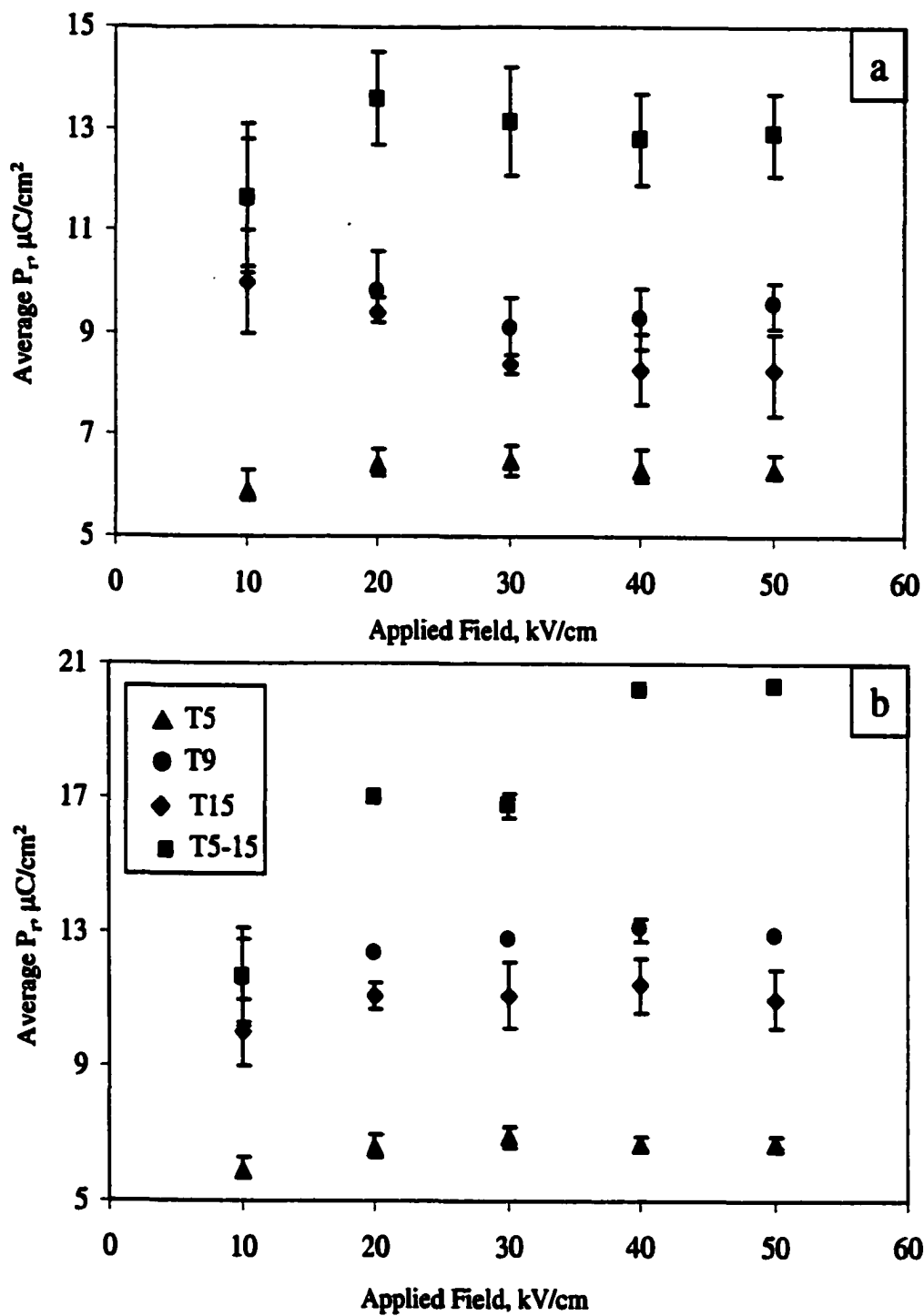


Figure 6.10 Change of average remanent polarization ( $P_r$ ) as a function of initial template content in the  $c$  direction; (a) Type A and (b) Type B. Samples were sintered at  $1400^\circ\text{C}$  for 12 h.

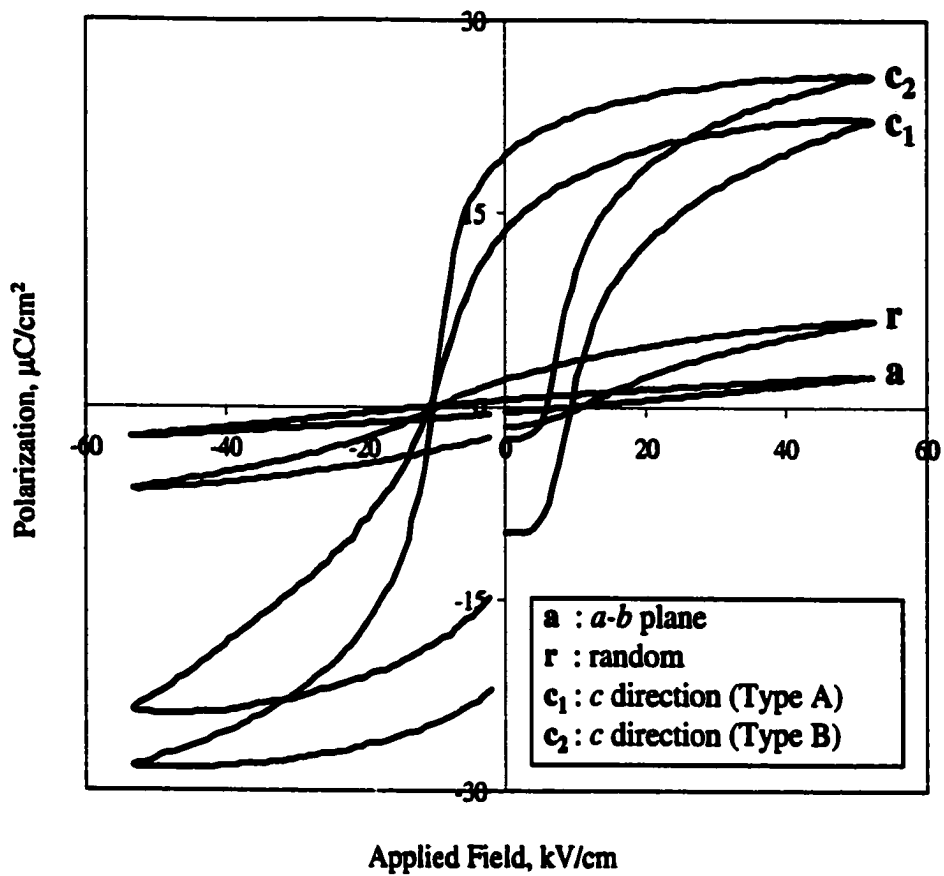


Figure 6.11 P-E hysteresis loops of the T5-15 samples sintered at 1400°C for 12 h and random (R15) sample sintered at 1350°C for 4 h.

grain growth, which decreases  $P_r$  and increases  $E_c$ . The loops do not close because only one cycle of voltage was applied. The textured samples show strong anisotropy.

The change of the remanent polarization ( $P_r$ ) and piezoelectric charge coefficient ( $d_{33}$ ) as a function of  $f$  and template content in the  $c$  direction is given in Figures 6.12 and 6.13. For comparison, SBN50 single crystal properties are also provided. The  $P_r$  (Fig. 6.12a) and  $d_{33}$  (Fig. 6.13) approach single crystal values with increasing  $f$ . Maximum  $P_r = 20.3 \mu\text{C}/\text{cm}^2$  and  $d_{33} = 84 \text{ pC}/\text{N}$  were obtained in the T5-15L samples sintered at  $1400^\circ\text{C}$  for 12 h ( $f = 0.98$ ). SBN50 single crystal has average reported saturation polarizations ( $P_{\text{max}}$  or  $P_r$ ) =  $27.4 \mu\text{C}/\text{cm}^2$  and  $d_{33} = 97 \text{ pC}/\text{N}$ .

Measured  $P_r$  data were fit to a model (see Appendix B), using  $f$  and  $r$  values for each composition. Calculated data from this modeling are also given in Figure 6.12a. Calculated data yield the maximum polarization that can ideally be obtainable for a given set of  $f$  and  $r$  (like single crystals cut at certain angles and combined together). Figure 6.12b shows normalized  $P_r$  (i.e.,  $P_r$  (measured) /  $P_r$  (calculated)) as a function of  $f$  for the  $\text{V}_2\text{O}_5$ -free and  $\text{V}_2\text{O}_5$ -containing samples (data from Chapter 5). It is clear that  $P_r$  remains constant until  $f \sim 0.5$  and then increases sharply.

## 6.4 DISCUSSION

### 6.4.1 Densification and Phase Formation

SBN phase formation takes place by forming necks between the particles in the early stage of reactive sintering. Compositional homogenization takes place as interdiffusion of the ions occurs through these necks. The chemical gradient difference between different regions during homogenization promotes the diffusion of the ions. The

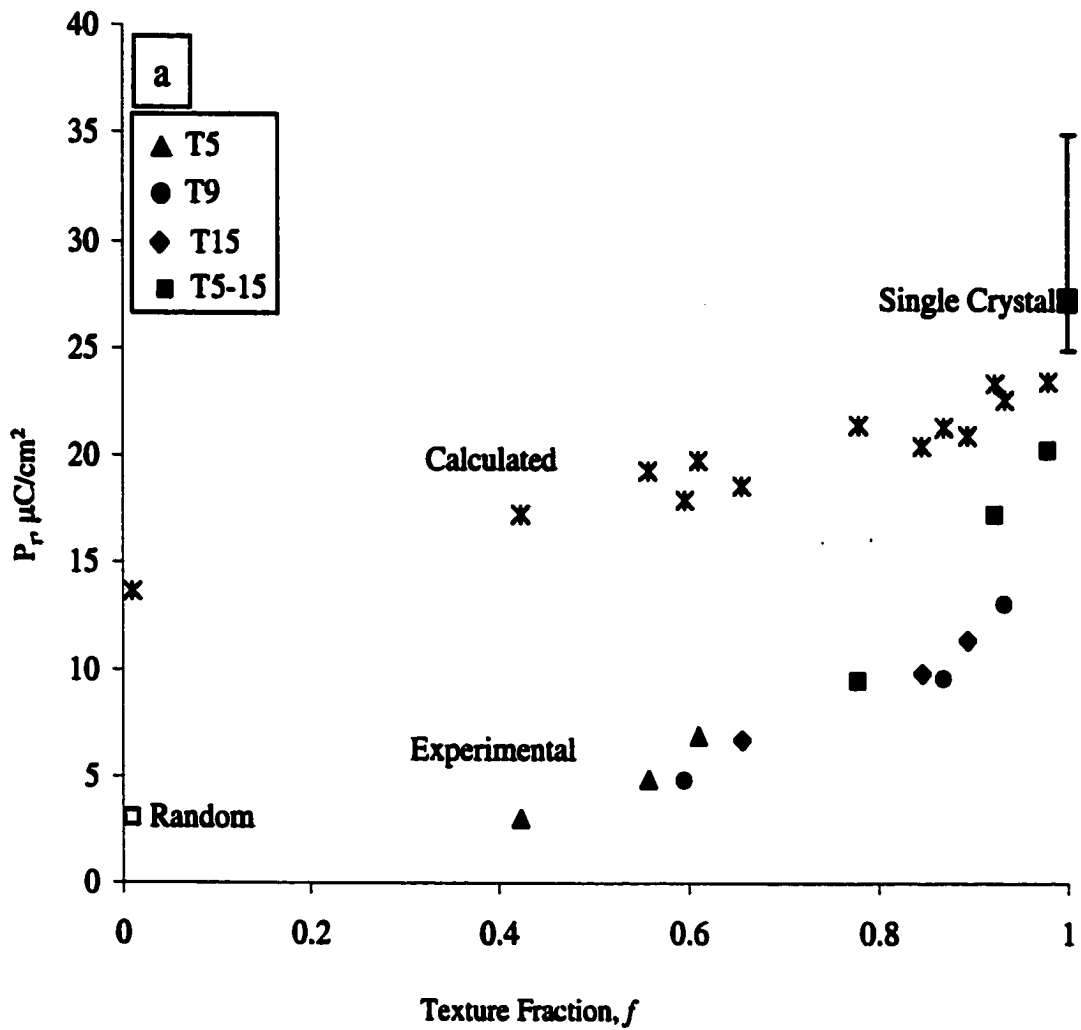


Figure 6.12 (a) Change of average  $P_r$  (Type B) as a function of initial template content and  $f$  (by the Lotgering factor) and (b) normalized  $P_r$  as a function of  $f$  for the  $\perp$ -cut samples. Samples are  $\geq 95\%$  dense.

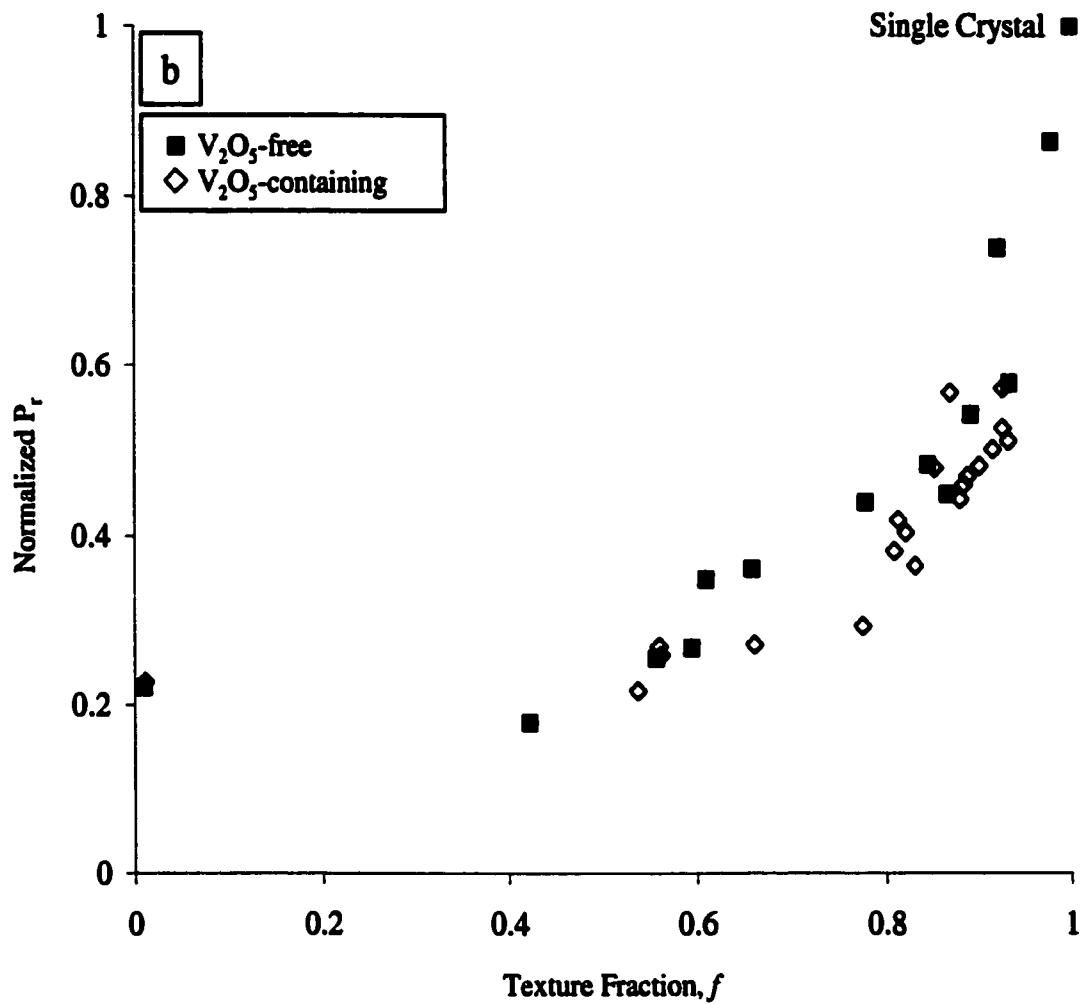


Figure 6.12 Continued.

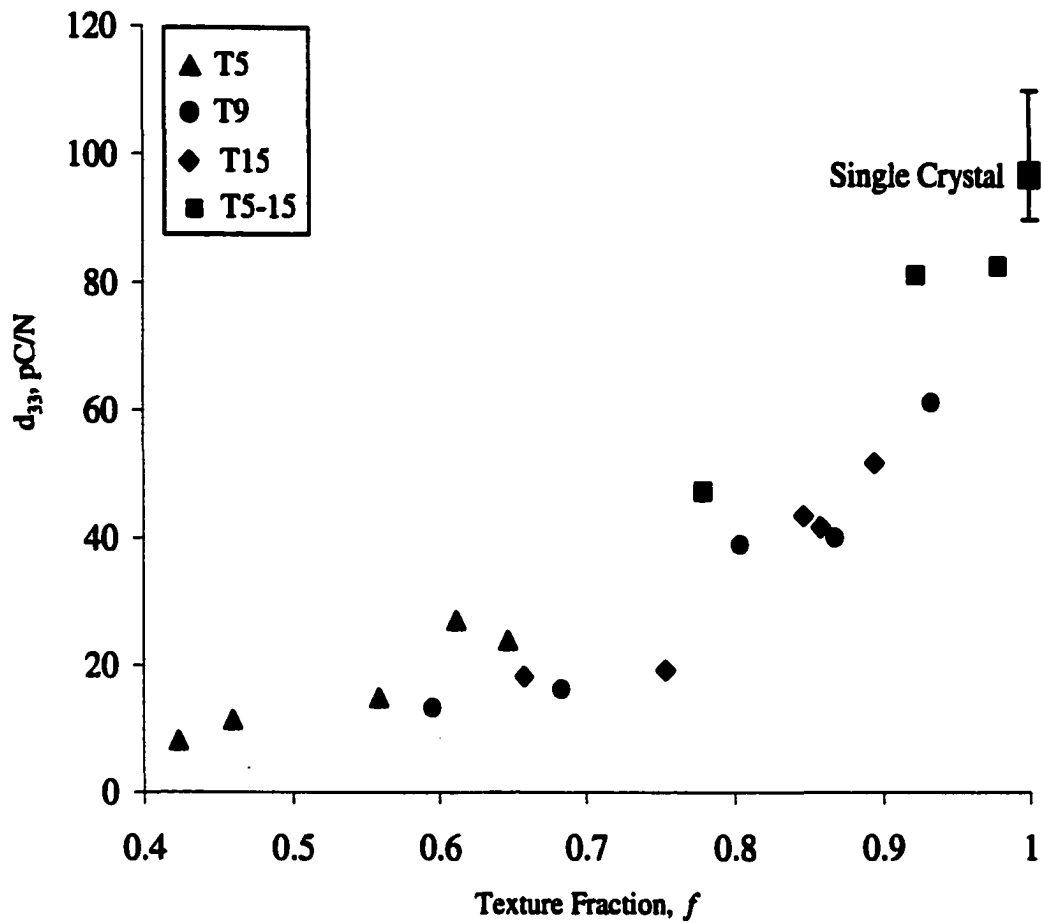


Figure 6.13 Change of average piezoelectric charge coefficient ( $d_{33}$ ) as a function of initial template content and texture fraction (by the Lotgering factor) for the  $\perp$ -cut samples. Samples are  $\geq 95\%$  dense.

densification rate during reactive sintering can be pronouncedly enhanced when the homogenization is almost complete [5]. The reason is that homogenization due to the chemical gradient does not change the state of the microstructure because it happens through the necks. For example, phase analysis by XRD (Fig. 6.2b) indicates that SBN formation is complete at 1200°C, and Figure 6.3a shows that a uniform, highly porous, and fine grain microstructure is retained during SBN formation. Interdiffusion is a dominant process when the necks form because the material transport due to the chemical gradient is more important than the material flow due to the surface curvature [6]. When the necks grow larger, the interdiffusion becomes easier and predominant, which stops additional sintering until homogenization is further advanced [5,7]. After the disappearance of the chemical gradient, the retained microstructure with high surface area induces a high driving force for further densification, which can sharply increase the density. Therefore, fast densification between 1200 and 1300°C can be attributed to the completion of SBN53 phase formation from the reactive mixture (Figure 6.1). The T5-15 samples have lower densification below 1300°C because these samples have K<sub>2</sub>O and Nb<sub>2</sub>O<sub>5</sub> in the matrix. Compositional homogenization, and thus densification, is retarded to higher temperatures. In other words, SBN53 phase formation and compositional homogenization (i.e., especially K<sup>+</sup>) should be completed before densification. The effect of K<sub>2</sub>O and Nb<sub>2</sub>O<sub>5</sub> during reactive sintering of SBN53 ceramics was discussed in detail in Chapter 4.

The densification slightly decreases with increasing template loading for the T5-T15 samples. This may be because template tangling during tape casting increases with increasing template concentration. When the template particles start to grow by

consuming the matrix particles, porosity may form due to templates that are not well aligned (see Fig. 6.4d). In addition, during matrix densification, porosity concentrates in the regions of high template concentration (Figs. 6.3b&c). In fact, template particles inhibit the densification if they form a rigid framework, as is the case of shear forming of only template particles [8]. Pressure or a liquid phase is required to attain high density in such cases. In TGG, however, the template particles are separated by a matrix powder; therefore, rigid template networks are less likely. Figure 6.1 shows that the density difference between T5 and T15 is not considerable (i.e., 97.9 % for T5 and 95.7 % for T15 samples sintered at 1450°C for 4 h), which suggests that template particles do not constrain sintering. Similar results were also found in other examples of templated grain growth [9-11].

Because extra BN was added to compensate for the SN from the KSN templates, the SBN matrix composition may differ from the desired SBN53 composition during phase formation. XRD shows the formation of a TTB structure by  $T = 1200^{\circ}\text{C}$  for all compositions (see curve "b" in Fig. 6.2 for the T9 samples). However, it is very difficult to distinguish KSN and SBN phases based on XRD results because they have a lattice parameter difference of  $\leq 0.5\%$  at room temperature. However, SEM pictures (see Fig. 6.3a) and energy dispersive spectroscopy (EDS) analysis indicate that there is almost no growth of SBN on the KSN template particles at 1200°C. This suggests that when the TTB structure forms, KSN and SBN phases exist together and the SBN formation in the matrix is independent of the presence of KSN templates. At this stage, therefore, the SBN composition in the matrix is probably barium rich. The estimated matrix composition and



the corresponding Sr/Ba molar ratio are given in Table 6.3 as a function of initial KSN content. The amount of extra BN increases with increasing KSN concentration, and results in the most deviation from the SBN53 composition. In addition, the samples can be thought of a composite material. The density can change due to the lower density of KSN phase (5.0 g/cc [12]) but the change is very slight (<1%).

The final solid solution (e.g., SBN53) between the KSN and SBN starts at the template-matrix interface. This process is accelerated by a liquid phase. Lee *et al.* [13,14] found in SBN60 ceramics that the  $\text{Nb}_2\text{O}_5/(\text{SrO}+\text{BaO})$  ratio is different between the grains (<1) and grain boundaries (>1) and that  $\text{Nb}_2\text{O}_5$ -excess grain boundaries lead to liquid formation at  $T \geq 1260^\circ\text{C}$ . The ratio is equal to 1 in the stoichiometric solid solution and the temperature at which the liquid phase forms decreases with more excess  $\text{Nb}_2\text{O}_5$ , [15]. Therefore, liquid may form at the matrix/template interface due to the presence of excess  $\text{Nb}_2\text{O}_5$  contributed from the KSN templates. The regions where matrix grains are not in contact with the template particles are not affected by this liquid and remain dense (Figs. 6.3b-d). The T5-15 samples, however, also have a liquid phase in the matrix due to the presence of  $\text{Nb}_2\text{O}_5$ , which makes the cation distribution more uniform in the matrix. Upon template growth, local homogenization (e.g., diffusion of  $\text{K}^+$ ,  $\text{Sr}^{2+}$ ,  $\text{Nb}^{5+}$ , and  $\text{Ba}^{2+}$  ions) can start inside the grown region with increasing sintering temperature and/or time (see Fig. 5.7 in Chapter 5).

#### 6.4.2 Texture Development

As mentioned in the preceding paragraph, liquid formation takes place due to excess  $\text{Nb}_2\text{O}_5$ . Because the template particles are isolated by the surrounding matrix

**Table 6.3 Estimated matrix composition before KSN-SBN solid solution formation starts.**

<b>KSN Content, wt%</b>	<b>Sr/Ba ratio</b>	<b>Matrix Composition</b>
<b>0*</b>	<b>1.13</b>	<b>SBN53</b>
<b>5</b>	<b>1.04</b>	<b>SBN51</b>
<b>9.1</b>	<b>0.96</b>	<b>SBN49</b>
<b>12</b>	<b>0.89</b>	<b>SBN47</b>
<b>15.4</b>	<b>0.85</b>	<b>SBN46</b>

**\* given as a reference calculation.**

grains, the amount of excess  $\text{Nb}_2\text{O}_5$  supplied from each KSN template would be the same. Only the amount of the liquid changes with the KSN content (see Table 6.1 for the additive contribution). Table 6.2 shows that the average length and thickness of the elongated grains are very close to each other at  $1300^\circ\text{C}$  for the T5-T15 samples, which further indicates that the onset temperature of the liquid formation from the templates would be the same. The presence of a liquid in the matrix promotes template growth for the T5-15 samples. The liquid phase facilitates template particles growth preferentially at the expense of matrix grains. Growth of templates occurs by solution-precipitation in which small matrix particles dissolve in the liquid and then reprecipitate on the larger template particles [16]. Consequently, for TGG the aspect ratio of the template particles must be high and the matrix grain size must be as fine as possible at the time of densification and template growth. During template growth, the matrix grain size still remains fine, that is, the average size is  $\sim 1.8$  to  $1.9 \mu\text{m}$  for T5-T15 and  $\sim 2.4 \mu\text{m}$  for the T5-15 samples at  $1300^\circ\text{C}$ . Therefore, matrix grain growth does not compete with the anisotropically growing grains and hinder texturing. The thermodynamic driving force for TGG decreases with matrix grain growth due to a decrease in the total grain boundary area [10]. Some elongated grains (particularly  $<10 \mu\text{m}$ ) that are off-axis to the casting direction in the T5 sample (Fig. 6.4a) can be attributed to the intrinsic nucleation of anisotropic grains in the matrix. The evidence for this is that abnormal grain growth is observed even in the stoichiometric mixture (e.g., SBN53 with no templates) when the samples are sintered only at high sintering temperatures and for long times (see Chapter 4). However, these secondary and randomly nucleated anisotropic grains are constrained, depending on the template frequency, by the template particles. Thus, the random and

intrinsic growth is limited with increasing template content. Only those grains that are near the initial template orientation can grow.

Figure 6.14 shows texture evolution as a function of densification for the samples sintered between 1200 to 1450°C for various times. The lines are drawn to guide the eye. Significant template growth is observed at high densities. Up to ~90 to 95% relative density,  $f$  is limited and almost constant for each set, but is higher at higher template loadings. Note that the T5-15 sample has a similar trend as the T5 samples. The SEM micrograph of the sample heated at 1200°C (Fig. 6.3a) shows that the matrix is still very porous and there is almost no overgrowth on the KSN template particles. However, the XRD (“curve b” in Fig. 6.2) shows that there is remarkable crystallographic orientation in the [001]. This suggests that texturing is mainly due to the oriented KSN template particles at lower densifications. Above ~95% relative density, however,  $f$  increases sharply, which indicates that densification of the matrix is required for template particles to grow. Due to size differences between the template and matrix grains, and the presence of a liquid, template particles keep growing by consuming the fine matrix grains, which results in a sharp increase in  $f$  with sintering conditions (Figs. 6.2 and 6.5). The highest  $f$  (0.98) was obtained in the T5-15 samples (Fig. 6.5b), which can be attributed to a liquid in the matrix. Note that  $V_2O_5$ -containing samples had almost constant  $f$  with densification (Fig. 5.10 in Chapter 5) because texture development started at  $T < 1000^\circ\text{C}$  due to melting of  $V_2O_5$ .

Although  $f$  is expected to increase with template content, the microstructure evolution in Figure 6.4 indicates that some anisotropically-grown grains deviate from the texture orientation with increasing template loading. Figure 6.6 indicates that the degree

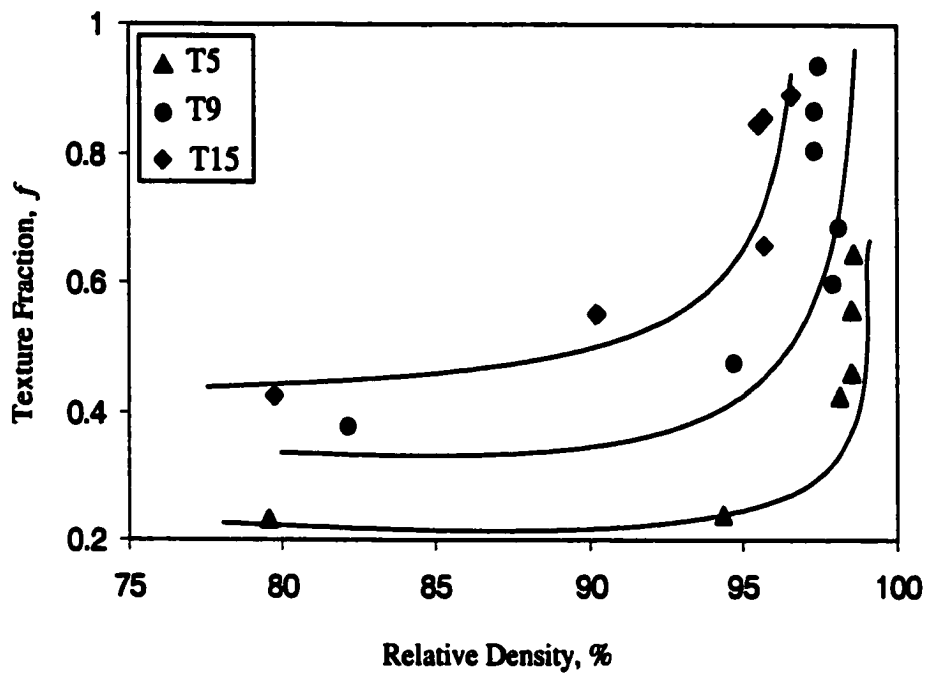


Figure 6.14. Density vs. texture fraction (by the Lotgering factor) for the samples sintered at  $1200 < T < 1450^{\circ}\text{C}$  for 1 min to 12 h.

of orientation parameter,  $r$ , increases with increasing initial template concentration, which results in a broadening of the orientation distribution. A low  $r$  value shows a narrow distribution of anisotropic grains in [001]. Broadening of the orientation distribution with increasing template content can be attributed to increased template-template interactions (e.g., tangling) during tape casting, especially when the template loading exceeds a critical template concentration. Therefore, a lower  $f$  coupled with a higher  $r$  is observed at template loadings greater than this critical concentration. An initial template concentration around 9 wt% is adequate to produce a highly textured microstructures ( $f = 0.93$ ) with a narrow distribution of anisotropic grains ( $r = 0.32$ ) in SBN53 ceramics when there is no liquid phase present in the matrix (for the T5-T15 samples). However, if the template growth is assisted by a liquid in the matrix, template concentrations as low as 5 wt% (e.g., T5-15) are enough to attain a  $f = 0.98$  while keeping  $r = 0.29$ . A similar result was also observed in the literature [9].

The greatest growth of template particles, in both the longitudinal and thickness directions, is observed in the T5-15 system. It was found that template growth and average aspect ratio decrease with increasing initial template content (Table 6.2). This suggests that when template growth in the longitudinal direction is obstructed by impingement with other growing template particles and/or matrix grains, template growth continues in other directions, leading to thickening of the needle-shaped grains. As seen in Figures 6.4a-d and Table 6.2, anisotropic grains are smaller in size for higher template contents after sintering for 12 h at 1400°C. Thus, a microstructure of anisotropic grains with a narrow size distribution and smaller aspect ratio is produced at higher template loadings. Comparison of the T5 and T5-15 samples reveals that templates grow more in

the T5-15 due to a liquid in the matrix, which results in faster consumption of the matrix grains.

### **6.4.3 Electrical Properties**

#### **6.4.3.1 Dielectric Properties**

The phase transition becomes narrower with increasing sintering conditions for all compositions (see Fig. 6.7a for the T9<sub>L</sub> samples). In other words,  $\gamma$  and  $C/K_{\max}$  decrease with increasing  $f$  (Figure 6.9). These results suggest that SBN53 compositions behave more like normal ferroelectrics (e.g.,  $\gamma$  is closer to 1), with relatively little dispersion with frequency. The higher  $C/K_{\max}$  for samples with a lower  $f$  can be attributed to the inhomogeneous distribution of cations (e.g., more  $K^+$  and  $Sr^{2+}$  in the KSN templates and more  $Ba^{2+}$  in the matrix due to SN compensation) between the elongated (e.g., textured) and equiaxed (or matrix) grains in the T5-T15 samples. At this stage, the compositional fluctuation from one grain to another can give rise to a range of Curie points, which broadens the phase transition [17,18]. The compositional fluctuations can be reduced with increasing sintering temperature or time. Therefore, the sharpening of the dielectric peak with increasing  $f$  may be attributed to the gradual homogenization of cations on the A sites. Note that the T5 samples still have weak relaxor behavior ( $T_{\max}$  changes about 2°C between 1 kHz and 100 kHz) even after sintering 1400°C for 12 h presumably because of incomplete  $K^+$  homogenization between templates and matrix grains (Fig. 6.4a). The T5-15 samples, however, have  $\gamma = 1.07$  and  $C/K_{\max} = 25.9^\circ\text{C}$  with no frequency dispersion, probably due to more uniform distribution of cations caused by a liquid phase

sintering.  $V_2O_5$ -containing SBN53 and random samples do not demonstrate relaxor behavior.

Figure 6.8 shows that the average  $K_{max}$  improves with increasing  $f$ . The highest peak dielectric constant is obtained in the T9 $\perp$  samples ( $K_{max} = 23,600$ ) because the T9 samples attained a high  $f$  (0.93) (Fig. 6.5b) and a low  $r$  parameter (0.32) (Fig. 6.6) with a minimum of liquid phase. However, like  $V_2O_5$ -containing samples in Chapter 5,  $K_{max} = 23,600$  is substantially less than the single crystal values. For example,  $K_{max} = 81,000$  [5] and 40,000-63,000 [5,50] were measured for SBN50 and SBN60 single crystals, respectively. The lower dielectric properties in textured samples can be attributed to the existence of nonferroelectric grain boundary phase(s). Excess  $Nb_2O_5$ , contributed by KSN templates forms a liquid during sintering and possibly forms a grain boundary phase(s) after cooling. This is more prevalent for the T5-15 samples because the excess  $Nb_2O_5$  is present both in the elongated grains and in the matrix, while excess  $Nb_2O_5$  is contained only in the elongated grains in the T5-T15 samples. Therefore, the T5-15 samples probably have much thicker grain boundaries. Grain boundary phases considerably suppress the observed dielectric properties, especially at the  $T_{max}$ . Therefore, the T5-15 samples had a lower  $K_{max}$  (17,000) although they reached the highest  $f$  (0.98) and lowest  $r$  (0.29). SBN53 ceramics textured with a  $V_2O_5$  liquid former had much lower  $K_{max}$  (~7,900). The effect of grain boundary phases is discussed in Chapter 7.

Another reason for the lower dielectric properties may be due to the presence of  $K^+$  ions. Analysis of dielectric properties in  $\geq 97\%$  dense random samples, with no abnormal grain growth, indicates that  $K_{max}$  decreases from 3520 for undoped sample to 2250 for 5 wt% and 1725 for 15.4 wt% KSN powder containing samples.  $K_{max}$  drops off



very quickly when abnormal grain growth starts for each set. Similar results in  $K^+$ ,  $Li^+$ , and  $Na^+$  doped SBN ceramics were also observed by Bhanumathi *et al.* [19].

The increase in dielectric loss ( $\tan \delta$ ) in the  $c$  direction and decrease in the  $a$ - $b$  direction with increasing sintering time (Fig. 6.7b) can be attributed in part to the domain wall loss because the volume of the grains with uniform polarization increases with increasing  $f$ , which results in easier domain wall movement in the polar  $c$  direction. The evidence for this is that the dielectric loss of poled samples, measured as the temperature increased from 20 to 250°C, was almost half of the dielectric loss of unpoled samples (e.g., 6.1% vs. 12.3%). The difference is probably attributable to a smaller number of domains and domain walls in the poled samples than the unpoled samples. Matrix grains that give isotropic properties are consumed by the template particles and, therefore, dielectric loss decreases in the nonpolar  $a$ - $b$  direction with increasing  $f$ .

$T_c$  mainly depends on the amount of KSN and the distribution of cations.  $T_c$  increases steadily after the completion of densification at 1300°C, which may be due to (i) increase in  $f$  (and, thus, grain size (see Table 6.2)) and (ii) diffusion of cations (primarily  $K^+$ ) into the SBN lattice, that is, compositional homogenization. 5 out of 6 A sites are occupied by  $Sr^{2+}$  and  $Ba^{2+}$  ions; therefore, SBN is an empty bronze [20]. Alkali elements, such as  $Na^+$ ,  $K^+$  partially or fully occupy the interstitial vacant sites without vacancy formation [19,21,22], which stabilizes the ferroelectric structure. Therefore,  $T_c$  increases due to the increased degree of filling of interstitial A sites with KSN content. Samples with  $\geq 9.1$  wt% templates ( $f = 0.89$  to  $0.93$ ) have a  $T_c$  of 124-128°C compared to 102°C in the T5L samples ( $f = 0.61$ ) after sintering at 1400°C for 12 h. The T5-15 samples had a  $T_c$  of 154°C, possibly due to more uniform cation distribution and, thus,

more A site filling by the  $K^+$  ions. These results indicate that  $T_c$  in TGG samples is strongly correlated with  $f$  due to changes in KSN content. Similar results were also found for the textured KSN42/58 ceramics (stoichiometric composition is KSN33/67) prepared by hot-pressing. It was stated that elongated grains impart less stress on each other with increasing grain orientation, which results in a lower internal stress and, thus,  $T_c$  increases [23]. Pure SBN50 single crystal has a  $T_c$  between 115 and 128°C, depending on the crystal quality [24-29]. This difference can be attributed to the different compositional variations and doping levels in the textured samples.

#### **6.4.3.2 Switching and Piezoelectric Properties**

As is the case for the dielectric properties, the polarization is strongly enhanced in the  $c$  direction ( $\perp$  cuts) with increasing  $f$  (Fig. 6.12a). The T5-15 $\perp$  samples reached a maximum  $P_r = 20.3 \mu\text{C}/\text{cm}^2$ . The estimated saturation polarization ( $P_{\infty}$ ) from P-E loop is  $\sim 24 \mu\text{C}/\text{cm}^2$ , which is 69-96% of reported SBN50 single crystal values. The average  $P_{\infty}$  for single crystal is  $27.4 \mu\text{C}/\text{cm}^2$ , and it ranges from 25 to  $35 \mu\text{C}/\text{cm}^2$  [29-31] depending on the quality of the grown crystal. While  $P_r$  improves with  $f$  in the  $c$  direction, it decreases in the  $a$ - $b$  direction ( $\parallel$  cuts). For example, the T5 $\parallel$  samples have a  $P_r = 1.6 \mu\text{C}/\text{cm}^2$  compared to  $0.8 \mu\text{C}/\text{cm}^2$  for the T5-15 $\parallel$  samples after sintering at 1400°C for 4h. In addition,  $P_r$  ( $\parallel$ ) continuously decreases with increasing  $f$  due to the consumption of unoriented matrix grains (random samples have higher  $P_r$  than the  $\parallel$ -cut samples due to averaging of properties (Fig. 6.11)).

The calculated maximum polarization from the model is substantially higher than the measured data, particularly at lower  $f$  values (Fig. 6.12a). Summary of processing

(i.e.,  $f$  and  $r$ ) and  $P_r$  values used in the calculation is given in Table 6.4. Possible reasons for lower  $P_r$  may be porosity, insulating grain boundary phase(s), pinning sites for domains within the grains, poor continuity in the polarization, and randomly oriented matrix grains. Figure 6.12b compares normalized  $P_r$  for  $V_2O_5$ -free (this chapter) and  $V_2O_5$ -containing (Chapter 5) samples. They show similar trends but  $V_2O_5$ -containing compositions have slightly lower normalized  $P_r$ , which may be attributed to  $V_2O_5$  grain boundary phases. In addition, relatively lower texture (maximum  $f = 0.93$ ) in the  $V_2O_5$ -containing samples allows the attainment of only 57% of single crystal value, while 86% is obtained in the  $V_2O_5$ -free samples (maximum  $f = 0.98$ ).

Figures 6.12a and b also indicate that the remanent polarization remains steady (and low) until nearly  $f = 0.5$  but increases considerably for higher  $f$ . As shown in Appendix B, the maximum polarization from a random sample is theoretically half of the single crystal saturation polarization for  $180^\circ$  domain reversal. Nevertheless, it is common for low symmetry samples to display much lower remanent polarization values, as was the case here. This is believed to be because the random grains effectively decrease the measured polarization at lower  $f$  values, by preventing the charge transfer (to elongated grains) necessary for switching. That is, there are so few possible polarization directions that misoriented grains seriously degrade the ability to maintain continuity in the polarization vector during switching. As a result, comparatively little of the material is actually able to switch. It is intriguing that the remanent polarization is virtually unchanged for  $f < 0.5$ . This suggests that in order for the cooperative switching process to occur effectively, it is necessary for well-oriented grains to have good connectivity. This would also account for the dramatic rise in the switchable polarization for  $f > 0.5$ . This

Table 6.4 Summary of processing (i.e.,  $f$  and  $r$ ) and  $P_r$  values used in Figure 6.12a for the  $V_2O_5$ -free samples.

$f$	$r$	$P_r$ (experimental)	$P_r$ (calculated)
0.01 (Random*)	1	3	13.7
0.423 (T5)	0.38	3.1	17.3
0.558 (T5)	0.29	4.9	19.3
0.596 (T9)	0.46	4.8	18
0.611 (T5)	0.29	6.9	19.8
0.658 (T15)	0.44	6.7	18.6
0.779 (T5-15)	0.29	9.5	21.5
0.846 (T15)	0.41	9.9	20.5
0.868 (T9)	0.36	9.6	21.4
0.894 (T15)	0.4	11.4	21
0.923 (T5-15)	0.26	17.3	23.4
0.934 (T9)	0.32	13.1	22.6
0.98 (T5-15)	0.29	20.3	23.5
1.00 (Single Cryst. <sup>#</sup> )	0.035	27.4	27.4

\* R5-R15 samples.

<sup>#</sup> SBN50 single crystal.

requirement for percolation of well-oriented material should be less important in systems with more possible polarization directions, since continuity of the polarization vector is much easier to achieve there. These results suggest that higher  $f$  and lower  $r$  are required to maximize the charge transfer to orient the domains and hence to increase the macroscopic polarization. Because the  $a$ - $b$  plane is nonpolar, higher  $r$  value also degrades the percolation of the switchable grains.

The type of measurement, namely, Type A and Type B, also affects the piezoelectric properties in the  $c$  direction. Figure 6.10a shows several possible behaviors for  $P_r$  as a function of the amplitude of the field.  $P_r$  for T5 $\perp$  ( $f = 0.61$ ) increases with the field.  $P_r$  for T15 $\perp$  ( $f = 0.89$ ) decreases monotonically.  $P_r$  for T9 $\perp$  ( $f = 0.93$ ) shows an initial decrease followed by a shallow rise, that was coupled with increased asymmetry in the P-E loops. In Type B measurements, however, no asymmetry was observed in any of the samples, and  $P_r$  was found to be higher (Fig. 6.10b). The T5-15 samples reached the highest  $P_r$  in both measurements and did not experience fast polarization fatigue (Fig. 6.10a) or asymmetric loops (Fig. 6.11). The reason for higher  $P_r$  may be higher  $f$  and lower  $r$ , fewer grain boundaries, and more uniform cation distribution.

The above-mentioned results indicate that polarization fatigue becomes dominant with increasing  $f$  in the T5-T15 compositions. Polarization fatigue is defined as the gradual reduction of switchable charge with polarization reversal under bipolar drive. In order to further investigate the fatigue behavior in textured ceramics, the T15 $\perp$  sample sintered at 1400°C for 12 h was subjected to a cycling experiment at 50 kV/cm, 10 Hz, and 25°C.  $P_r$  decreased very fast from 12.5 to 6.8  $\mu\text{C}/\text{cm}^2$  after 10,000 cycles, and gradually to 5.4  $\mu\text{C}/\text{cm}^2$  at 130,000 cycles.  $E_s$ , however, decreased slightly from 7 to 6.2

kV/cm after 130,000 cycles. No asymmetry was observed in the P-E loops during cycling. Note that the T15L sample with V<sub>2</sub>O<sub>5</sub> liquid phase former did not experience polarization fatigue even after 140,000 cycle. Also, fatigue did not always increase with increasing P<sub>r</sub>.

Fatigue is commonly observed in SBN single crystals. It was found in SBN50 that after repeated switching under high fields, a major fraction of the total polarization rapidly locks into unswitching domain configurations after a few initial reversals. For example, P<sub>r</sub> drops from ~ 28 μC/cm<sup>2</sup> (1<sup>st</sup> cycle) to 10 μC/cm<sup>2</sup> (2<sup>nd</sup> cycle) and to 6 μC/cm<sup>2</sup> (3<sup>rd</sup> cycle) at 60 Hz and 25°C [17]. A similar drastic decrease was also observed in SBN75 single crystals [32]. Single crystals usually have imperfections such as striation bands (perpendicular to the *c* direction) that are mainly introduced during crystal growth, which results in a change in the stoichiometry [17,32]. Therefore, the switchable polarization could be clamped due to charges being stored at defects such as domain walls, dislocations, imperfections, and grain boundaries (for ceramics), which tends to break up the ferroelectric coupling. It was also observed that there was no asymmetry with respect to the electric field, indicating no net internal electric field and, therefore, E<sub>i</sub> remained almost constant [32].

The changes in polarization which occur on application of a cyclic field are principally due to the intrinsic (i.e., volume polarizability of the individual domains) and extrinsic (i.e., domain wall motion and reorientation effects) contributions [33]. There are at least two possible reasons for the effect of texture and processing on the observed fatigue behavior: changes in the sample homogeneity and changes in the character of the grain boundaries. As mentioned previously, SBN is an empty bronze in that 5 Sr<sup>2+</sup> and

$\text{Ba}^{2+}$  ions occupy the 6 available interstitial sites in the TTB structure. Therefore, high intrinsic channel defect concentrations due to vacant sites already exist in SBN. These channel defects are electrically neutral; however, short-range strain interactions may exist due to non-uniform distributions of  $\text{Ba}^{2+}$  and  $\text{Sr}^{2+}$  in the  $A_1$  and  $A_2$  sites, respectively [20]. For the T5-T15 samples,  $\text{K}^+$  ions may also contribute to this non-uniform cation and vacancy distribution. In addition, similar to the striation bands in the single crystals, the stoichiometry of TGG samples varies inside the elongated grains because there are more  $\text{Sr}^{2+}$  and  $\text{K}^+$  ions in the center region (e.g., at the original KSN template position) and more  $\text{Ba}^{2+}$  ions in the grown region (due to excess BN in the matrix). This variation in stoichiometry increases with increasing  $f$  because the homogenous matrix grains dissolve and precipitate on the relatively inhomogeneous, anisotropically growing grains. Because  $\text{Ba}^{2+}$  and  $\text{K}^+$  ions diffuse slowly within the grains (e.g., by solid state diffusion), there may be an uneven distribution of cations and vacant sites. Similar to charge trapping in the single crystals, compositional gradients within each grain could behave as defect sites for pinning the domains, which results in a decrease in  $P_r$  during polarization reversal. The fatigue rate intensifies with increasing  $f$  due to increased single crystal regions (e.g., elongated grains) with more defect sites. For the T5-15 samples, however, lower polarization fatigue is due to more uniform distribution of cations because these samples have  $\text{K}^+$  and  $\text{Nb}^{5+}$  ions both in the matrix and elongated grains, which results in less available pinning sites inside the elongated grains. A second possibility is that the differences in the fatigue behavior is due to differences in the electrical conductivity of the specimens due to changes in the grain boundary conductivity. In general, both  $\text{V}_2\text{O}_5$ -containing and T5-15 specimens had comparatively low dielectric loss values. These

same samples had more marked suppression of the peak permittivities due to grain boundary phases. It is possible that lowered dielectric loss was partially associated with a change in the electrical conductivity, and that resulting changes in charge injection also affected the fatigue rates.

Increased  $P_r$  after Type B measurements in Figure 6.10b suggest that fatigue is completely recoverable by annealing the samples above  $T_c$  (e.g., 500°C for 1 h). These results indicate that domain wall pinning either by defect sites or by injected charge during polarization reversal is the main reason for the observed polarization fatigue in the highly textured SBN53 ceramics. Similar results were observed in  $\text{Pb}(\text{Zn}_{1/5}\text{Nb}_{2/5})\text{O}_3$ -4.5PbTiO<sub>3</sub> single crystals [34].

In Figure 6.10a, the increase in  $P_r$  (in the T9 $\perp$ ) can be attributed to charge injection or a possible internal electric field because the P-E loop became asymmetric with respect to the applied field axis and  $E_c$  increased more after 30 kV/cm. Under the application of an ac field, the domains may break away from the pinning sites, resulting in a partial deaging or randomization of the defect-domain configurations, which results in an increased polarization due to switchable domains [35].

The best piezoelectric charge coefficient ( $d_{33}$ ) of 84 pC/N was obtained in the highly textured ( $f = 0.98$ ) T5-15 $\perp$  samples after sintering at 1400°C for 12 h (Fig. 6.13). This value is 76 to 93% of the SBN50 single crystals ( $d_{33} = 90$  to 110 pC/N for single crystals [26,29,35-37]). This sample also showed the highest  $P_r$ . For the T5-T15 samples, the maximum  $d_{33} = 63$  pC/N was measured in the T9 $\perp$  samples. This lower value can be attributed to inefficient poling. This is supported by the observation that  $P_r$  measured from hysteresis loops and pyroelectric measurements are smaller than  $P_{\text{max}}$  measured in P-



E loops. For example, the T15 $\perp$  sample sintered at 1400°C for 4 h has a  $P_{\text{max}}$  of 12.6  $\mu\text{C}/\text{cm}^2$  at room temperature obtained from a pyroelectric measurement (as the poled sample was heated from room temperature to 250°C). However,  $P_{\text{max}} = 17 \mu\text{C}/\text{cm}^2$  was estimated from the P-E loop (Type B) recorded at 50 kV/cm. This indicates inefficient domain orientation and, therefore, the  $d_{33}$  values are lower.

The pertinent average room temperature dielectric and piezoelectric properties for random and textured samples prepared without  $\text{V}_2\text{O}_5$  and sintered at 1400°C for 12 h are summarized in Table 6.5 as a function of crystallographic direction and composition. Random samples have higher Curie temperatures compared to textured samples. The reasons could be more effective  $K^+$  homogenization in the random samples (i.e., fine KSN powder vs. acicular template particles) and stress relief due to cracking (see Chapter 4).

These results, like shown in Chapter 5, indicate that electrical properties are considerably improved, compared to randomly oriented samples, and highly anisotropic properties can be achieved.

## 6.5 CONCLUSIONS

Highly textured  $\text{Sr}_{0.53}\text{Ba}_{0.47}\text{Nb}_2\text{O}_6$  (SBN53) ceramics were reactively sintered in a matrix of  $\text{SrNb}_2\text{O}_6$  and  $\text{BaNb}_2\text{O}_6$  powders. Acicular  $\text{KSr}_2\text{Nb}_5\text{O}_{15}$  particles were used to texture the samples in [001]. Samples had phase-pure tetragonal tungsten bronze structure by 1200°C and reached  $\geq 95\%$  of the theoretical density after sintering for 4 h at 1300°C. Extra BN, added to the stoichiometric matrix powder mixture for compositional adjustment, modified the matrix composition before template particles start to grow.

**Table 6.5** The average room temperature dielectric and piezoelectric properties for random and textured samples sintered at 1400°C for 12 h.

Sample	$T_c$ , °C	$K_{max}$	K at 25°C	$\tan\delta$ (%)	$d_{33}$ , pC/N	$P_r$ , $\mu\text{C}/\text{cm}^2$	$E_c$ , kV/cm
R0*	129	2965	443	6.6	37	3.8	12.2
R5*	138	2150	485	5.5	27	3.4	12.8
T5//	108	1063	612	1.9	1.4	1	8.5
T5 $\perp$	102	9525	1485	7.7	27	6.7	5.9
R9*	150	1525	290	3.8	26	2.7	15.8
T9//	124	859	522	1.1	0.9	0.8	11
T9 $\perp$	126	21952	1324	10.1	61	12.9	6.9
R15*	162	1056	300	2.1	30	1.5	13.9
T15//	133	863	481	1.2	1.1	0.9	13.2
T15 $\perp$	128	18914	1324	10.3	52	11	6.9
T5-9//	144	567	325	0.6	1	0.3	5.9
T5-9 $\perp$	144	16067	900	8.6	78	16.8	9.3
T5-15//	150	645	428	0.7	1.5	0.5	10.8
T5-15 $\perp$	154	17000	935	7.4	83	20.3	10.6

\* : Dielectric properties were measured at 100 kHz due to space charge effect.

$T_c$ : Temperature at the  $K_{max}$ ; measured at 1 kHz during cooling.

$P_r$  and  $E_c$ : Measured at room temperature and 10 Hz, for an applied field of 50 kV/cm (Type B).

$K_{max}$  and K at 25°C: Measured at 1 kHz during cooling.

$\tan\delta$  (%): Measured at room temperature and 1 kHz during cooling.

$d_{33}$ : At 100 Hz and room temperature, after poling at 10 kV/cm at temperatures ~ 10-15°C above  $T_c$ .

Significant template growth was observed after ~90-95% densification. As sintering conditions and initial template concentration increase, the texture fraction ( $f$ ) (as measured by the Lotgering factor) also increased due to the preferential growth of the template particles, assisted with a liquid formed due to the excess  $\text{Nb}_2\text{O}_5$  (either from the templates or present in the matrix). Samples without a liquid in the matrix (i.e., liquid is at the template-matrix interface), reached a maximum  $f = 0.93$  (9.1 wt% templates) compared to 0.98 (5 wt% templates) in the samples with a liquid in the matrix after sintering at 1400°C for 12 h. It was found that the degree of orientation distribution ( $r$ ) in the texture direction (e.g., [001]) widens with increasing template content (e.g.,  $r = 0.29$  for 5 wt% and 0.40 for 15.4 wt% templates) due to the increased template-template interaction (e.g., tangling) during tape casting. Template particles controlled matrix grain growth and, therefore, no cracking or abnormal grain growth were observed in the samples textured by TGG.

The dielectric and piezoelectric properties were affected particularly by  $f$ ,  $r$ , and grain boundary phases. Properties were enhanced in the samples with higher  $f$  and lower  $r$  values. In addition, the presence of nonferroelectric phases (mainly  $\text{Nb}_2\text{O}_5$ -based) at the grain boundaries suppressed the observed dielectric properties, especially at the  $T_c$ . For the samples with uniform cation distribution, dielectric spectra showed normal ferroelectric behavior and fast polarization fatigue was not observed. The best electrical properties obtained are; the peak dielectric constant of 23,600 (at  $T_c = 128^\circ\text{C}$ ), the remanent polarization ( $P_r$ ) of  $20.3 \mu\text{C}/\text{cm}^2$ , the estimated saturation polarization of  $24 \mu\text{C}/\text{cm}^2$  (69-96% of SBN50 single crystal), and the piezoelectric charge coefficient of 84

**pC/N (76-93% of SBN50 single crystal). A model was developed to correlate processing parameters ( $f$  and  $r$ ) to the polarization.  $P_r$  increased sharply (i.e., after  $f = 0.5$ ) when the percolation (or charge transfer) between elongated grains was effectively established.**

## 6.6 REFERENCES

- 1- V. V. Kirillov and V. A. Isupov, "Relaxation polarization of  $\text{Pb}(\text{Mg}_{1/3}\text{Nb}_{2/3})\text{O}_3$  - A ferroelectric with a diffuse phase transition," *J. Mater. Res.*, 5[1-2], 3-9 (1973)
- 2- K. Uchino and S. Nomura, "Critical exponents of the dielectric constants in diffused-phase-transition crystals," *Ferroelectric Lett. Sect.*, 44[3], 55-61 (1982)
- 3- S. J. Butcher and N. W. Thomas, "Ferroelectricity in the system  $\text{Pb}_{1-x}\text{Ba}_x(\text{Mg}_{1/3}\text{Nb}_{2/3})\text{O}_3$ ," *J. Phys. Chem. Solids*, 52[4], 595-601 (1991)
- 4- C. L. Choy, W. P. Leung, T. G. Xi, Y. Fei, and C. F. Shao, "Specific heat and thermal diffusivity of strontium barium niobate ( $\text{Sr}_{1-x}\text{Ba}_x\text{Nb}_2\text{O}_6$ ) single crystals," *J. Appl. Phys.*, 71[1], 170-73 (1992)
- 5- W-J. Lee and T-T. Fang, "Densification and microstructural development of the reaction sintering of strontium barium niobate," *J. Am. Ceram. Soc.*, 81[4], 1019-24 (1998)
- 6- P. F. Stablein Jr. and G. C. Kuczynski, "Sintering in multicomponent metallic systems," *Acta Metall.*, 11, 1327-37 (1963)
- 7- G. C. Kuczynski, "Sintering in multicomponent systems," 685-711 in *Sintering and Related Phenomena*. Edited by G. C. Kuczynski, N.A. Hooton, and C.F. Gibbon, Gordon and Breach, NY (1967)
- 8- H. Watanabe, T. Kimura, and T. Yamaguchi, "Sintering of platelike bismuth titanate powder compacts with preferred orientation," *J. Am. Ceram. Soc.*, 74[1], 139-47 (1991)
- 9- E. Suvaci and G. L. Messing, "Critical factors in the templated grain growth of textured reaction-bonded alumina," *J. Am. Ceram. Soc.*, 83[8], 2041-48 (2000)

- 10- S. H. Hong and G. L. Messing, "Development of textured mullite by templated grain growth," *J. Am. Ceram. Soc.*, 82[4], 867-72 (1999)
- 11- B. Brahmaroutu, "Templated grain growth of textured strontium niobate ceramics," Ph.D. Thesis, The Pennsylvania State University (1999)
- 12- E. A. Giess, G. Burns, D. F. O'Kane, and A. W. Smith, "Ferroelectric and optical properties of  $\text{KSr}_2\text{Nb}_5\text{O}_{15}$ ," *Applied Physics Letters*, 11[7], 233-34 (1967)
- 13- H-Y. Lee and R. Freer, "The mechanism of abnormal grain growth in  $\text{Sr}_{0.6}\text{Ba}_{0.4}\text{Nb}_2\text{O}_6$  ceramics," *J. Appl. Phys.* 81[1], 376-82 (1997)
- 14- H-Y. Lee and R. Freer, "Abnormal grain growth and liquid-phase sintering in  $\text{Sr}_{0.6}\text{Ba}_{0.4}\text{Nb}_2\text{O}_6$ , (SBN40) ceramics," *J. Mater. Sci.*, 33, 1703-08 (1998)
- 15- J. R. Carruthers and M. Grasso, "Phase equilibria relations in the ternary system BaO-SrO-Nb<sub>2</sub>O<sub>5</sub>," *J. Electrochem. Soc.: Solid State Science*, 117[11], 1426-30 (1970)
- 16- M. M. Seabaugh, I. H. Kerscht, and G. L. Messing, "Texture development by templated grain growth in liquid-phase sintered  $\alpha$ -alumina," *J. Am. Ceram. Soc.*, 80[5], 1181-88 (1997)
- 17- T. W. Cline, "Domain contributions to the dielectric response in ferroelectric crystals," Ph.D. Thesis, The Pennsylvania State University (1977)
- 18- G. A. Smolenski and V. A. Isupov, *Zhur. Tekh. Fiz.*, 24, 1375 (1954)
- 19- A. Bhanumathi, S. N. Murty, K. Umakantham, K. C. Mouli, G. Padmavathi, K. T. Rao, and V. Syamalamba, "Ferroelectric properties of tungsten bronze ceramics," *Ferroelectrics*, 102, 173-81 (1990)

- 20- D. Viehland, Z. Xu, and W-H. Huang, "Structure-property relationships in strontium barium niobate, I. Needle-like nanopolar domains and the metastably-locked incommensurate structure," *Phil. Mag. A*, 71 [2], 205-17 (1995)
- 21- S. N. Murty, K.V. R. Murty, K. C. Mouli, A. Bhanumathi, S. B. Raju, G. Padmavathi, and K.L. Murty, "Relaxor behaviour in certain tungsten bronze ceramics," *Ferroelectrics*, 158, 325-330 (1994)
- 22- K. Umakantham, S. N. Murty, K. S. Rao, and A. Bhanumathi, "Effect of rare-earth ions on the properties of modified SBN ceramics," *J. Mater. Sci. Letters*, 6, 565-67 (1987)
- 23- T. Kimura, S. Saiubol, and K. Nagata, "Effect of grain orientation on the Curie temperature of  $\text{KSr}_7\text{Nb}_3\text{O}_{15}$  solid solution," *J. Ceram. Soc. of Japan*, Int. Edition, 103 [2], 132-37 (1995)
- 24- R. R. Neurgaonkar, W. K. Cory, J. R. Oliver, E. J. Sharp, G. L. Wood, and G. J. Salamo, "Growth and optical properties of ferroelectric tungsten bronze crystals," *Ferroelectrics*, 142, 167-188 (1993)
- 25- A. M. Glass, "Investigation of the electrical properties of  $\text{Sr}_{1-x}\text{Ba}_x\text{Nb}_2\text{O}_6$  with special reference to pyroelectric detection," *J. Appl. Phys.*, 40[12], 4699-713 (1969)
- 26- R. R. Neurgaonkar, W. K. Cory, and J. R. Oliver, "Growth and applications of ferroelectric tungsten bronze family crystals," *Ferroelectrics*, 51, 3-8 (1983)
- 27- R. Guo, A. S. Bhalla, G. Burns, and F. H. Dacol, "Studies on annealing and quenching of strontium barium niobate (SBN) single crystals: A-site cation ordering-disordering effect," *Ferroelectrics*, 93, 397-405 (1989)

- 28- M. DiDomenico, Jr. and S. H. Wemple, "Oxygen-octahedra ferroelectrics. I. Theory of electro-optical and nonlinear optical effects," *J. App. Phys.*, 40[2], 720-34 (1969)
- 29- R. R. Neurgaonkar, W.F. Hall, J. R. Oliver, W. W. Ho, and W. K. Cory, "Tungsten bronze SBN: A case history of versatility," *Ferroelectrics*, 87, 167-79 (1988)
- 30- S. B. Deshpande, H. S. Potdar, P. D. Godbole, S. K. Date, "Preparation and ferroelectric properties of SBN50 ceramics," *J. Am. Ceram. Soc.*, 75[9], 2581-85 (1992)
- 31- I. Camlibel, "Spontaneous polarization measurements in several ferroelectric oxides using a pulsed-field method," *J. Appl. Phys.*, 40[4], 1690-93 (1969)
- 32- B. Jimenez, C. Alemany, J. Mendiola, and E. Maurer, "Polarization reversal in SBN inhomogeneous crystals," *Ferroelectrics*, 38, 841-43 (1981)
- 33- D. A. Payne, "The role of internal boundaries upon the dielectric properties of polycrystalline ferroelectric materials," Ph.D. Thesis, The Pennsylvania State University (1973)
- 34- K. Takemura, M. Ozgul, V. Bormand, S. Trolier-McKinstry, and C. A. Randall, "Fatigue anisotropy in single crystal  $\text{Pb}(\text{Zn}_{1/3}\text{Nb}_{2/3})\text{O}_3\text{-PbTiO}_3$ ," *J. Appl. Phys.*, 88[12], 7272-77 (2000)
- 35- Q. Tan, J- F. Li, and D. Viehland, "The influence of mobile vs. randomly quenched impurities on ferroelectric phase transformations," *Ferroelectrics*, Vols. 206-207, 275-91 (1998)
- 35- R. R. Neurgaonkar, J. R. Oliver, W. K. Cory, L. E. Cross, and D. Viehland, "Piezoelectricity in tungsten bronze crystals," *Ferroelectrics*, 160, 265-76 (1994)
- 36- S.T. Liu, "Pyroelectric properties of dislocation-free ferroelectric SBN50 crystals," *Ferroelectrics*, 22, 709-10 (1978)



**37- T. W. Cline, L. E. Cross, and S. T. Liu, "Dielectric behavior of SBN50 crystals," *J. Appl. Phys.* 49[7], 4298-4300 (1978)**

## CHAPTER 7

### SUMMARY AND FUTURE WORK

#### 7.1 SUMMARY

##### 7.1.1 Template Particle Synthesis

The availability of anisometric single crystal particles (e.g., templates) is very critical in the fabrication of textured ceramics prepared by templated grain growth (TGG). Therefore, template particles such as  $\text{KSr}_2\text{Nb}_3\text{O}_{15}$  (KSN),  $\text{Sr}_{0.5}\text{B}_{0.5}\text{Nb}_2\text{O}_6$  (SBN50), and  $\text{SrNb}_2\text{O}_6$  were synthesized in the SrO-BaO-Nb<sub>2</sub>O<sub>5</sub> system, using KCl and  $\text{SrCl}_2 \cdot 6\text{H}_2\text{O}$  salts. The use of other salts like LiCl and NaCl did not yield anisometric particles.

In the  $\text{SrCl}_2 \cdot 6\text{H}_2\text{O} + \text{Nb}_2\text{O}_5$  system (salt to powder ratio = 2), acicular  $\text{SrNb}_2\text{O}_6$  particles formed by solid state reaction of the salt and  $\text{Nb}_2\text{O}_5$ . Large, irregularly-shaped (Sr-rich)  $\text{Sr}_2\text{Nb}_2\text{O}_7$  particles also formed with increasing reaction temperature and time.

SBN50 needles were always  $\leq 3 \mu\text{m}$  in length regardless of the processing variables (e.g., salt to powder ratio, cooling rate, and reaction time and temperature), which indicates that SBN50 is not very soluble in KCl. In order to increase the size of the particles, seeded molten salt synthesis was performed, using pre-synthesized SBN50 needles. However, the final product phase (or needles) did not behave as nucleation sites for further growth. The nucleation frequency to form SBN50 from the reactant oxides was found to be higher.

Small but finite solubility of SrO in the  $\text{KCl} + \text{SrNb}_2\text{O}_6$  system (ratio = 1) favored the formation of acicular KSN and blade-like  $\text{Sr}_2\text{Nb}_2\text{O}_7$  particles. The amount of the latter

increased with increasing reaction temperature. Unreacted  $\text{SrNb}_2\text{O}_6$  particles remained fine ( $\sim 1 \mu\text{m}$ ) for all conditions examined. KCl evaporation limited complete KSN formation but increasing the KCl content (ratio = 1.25) yielded more KSN. The physical separation of as-synthesized particles by differential settling in water eliminated almost all of the unreacted, smaller SN particles.

Acicular KSN particles (isostructural with SBN) were selected as the most suitable templates for SBN matrix crystallization during TGG because these particles are more uniform and easier to reproduce in size relative to SBN50 and SN needles.

### 7.1.2 Reactive Sintering of $\text{Sr}_{0.53}\text{Ba}_{0.47}\text{Nb}_2\text{O}_6$ Ceramics

$\text{Sr}_{0.53}\text{Ba}_{0.47}\text{Nb}_2\text{O}_6$  (SBN53) ceramics were reactively sintered from  $\text{SrNb}_2\text{O}_6$  (SN) and  $\text{BaNb}_2\text{O}_6$  (BN). KSN powder (0 to 15.4 wt%) was added to investigate the effect of seeding on the SBN53 formation.

Phase evolution was studied as a function of quenching temperature, heating rate, and the presence of a liquid phase. The formation temperature for SBN53 was lowered substantially by adding more seeds, decreasing the heating rate, and introducing a liquid. For example, the temperature decreased from  $1260^\circ\text{C}$  for the samples with no seeds to  $1130^\circ\text{C}$  for the samples with 15.4 wt% seeds + 0.8 mol %  $\text{V}_2\text{O}_5$  at a heating rate of  $4^\circ\text{C}/\text{min}$ . For the  $\text{V}_2\text{O}_5$ -free samples, the activation energy was considerably lowered from  $554 \pm 15 \text{ kJ/mol}$  for the samples with no seeds to  $241 \pm 17 \text{ kJ/mol}$  for the samples with 15.4 wt% seeds. In addition, for all compositions, the SBN53 was formed directly, rather than via a variety of intermediate SBN solid solutions (i.e., other than SBN53).

An unknown phase started to form in the samples during the SBN53 formation. The amount of this phase was greater in the  $V_2O_5$ -containing samples, and decreased with increasing seed content and reaction temperature. Also, its formation was found to be almost independent of the heating rate. This phase might form on the surface of the BN particles because the strontium ion diffuses faster (compared to barium and niobium) due to its smaller size. No phases in the SrO-BaO-Nb<sub>2</sub>O<sub>5</sub>-V<sub>2</sub>O<sub>5</sub> system were found to match the unknown phase.

$V_2O_5$ -containing samples densified at lower temperatures due to melting of  $V_2O_5$  at 690°C and they reached maximum density at  $T \leq 1250^\circ\text{C}$ , compared to  $T \geq 1350^\circ\text{C}$  in the  $V_2O_5$ -free samples. The heating rate did not affect the densification much, except that the density was slightly higher at lower heating rates. It was found that KSN slowed the densification in the  $V_2O_5$ -containing samples, and improved it in the  $V_2O_5$ -free samples. All samples had nearly 17% shrinkage in the thickness direction upon full densification. In addition, the densification curves revealed that there was no volumetric expansion during reactive sintering.

The presence of a liquid changed the sequence of the reactive sintering. In the  $V_2O_5$ -containing samples, densification and phase formation occurred simultaneously. In the  $V_2O_5$ -free samples, however, the phase formation was completed before densification. In both cases, ceramics with  $\geq 95\%$  relative density were obtained, indicating that it is not critical whether the densification or phase formation takes place first during reactive sintering.

Samples with high density and uniform grain size were obtained at different KSN contents. Unlike the  $V_2O_5$ -containing samples, abnormal grain growth in the  $V_2O_5$ -free

compositions took place because of off-stoichiometric grain boundary phases (i.e.,  $\text{Nb}_2\text{O}_5$  excess), only when the samples were oversintered.

### 7.1.3 Templated Grain Growth of $\text{Sr}_{0.53}\text{Ba}_{0.47}\text{Nb}_2\text{O}_6$ Ceramics

Textured  $\text{Sr}_{0.53}\text{Ba}_{0.47}\text{Nb}_2\text{O}_6$  (SBN53) ceramics with ~ 95% of the theoretical density were successfully fabricated by templated grain growth (TGG), in a matrix of  $\text{SrNb}_2\text{O}_6$  and  $\text{BaNb}_2\text{O}_6$  powders. Acicular  $\text{KSr}_2\text{Nb}_5\text{O}_{15}$  particles (5 to 15.4 wt%) were used to texture the samples in the  $c$  direction (i.e., [001]).  $\text{V}_2\text{O}_5$  was added to some compositions to form a liquid (melting temperature is 690°C).

When  $\text{V}_2\text{O}_5$  was present, SBN53 phase formation initiated on the KSN templates and texture development started at temperatures as low as 950°C, even before the phase formation was completed (by  $T = 1100^\circ\text{C}$ ). Phase formation in the  $\text{V}_2\text{O}_5$ -free samples, however, initiated in the matrix (e.g., independent of the KSN templates) and was complete by 1200°C.

As sintering conditions and initial template concentration increased, the texture fraction ( $f$ ) (as measured by the Lotgering factor) also increased due to the preferential growth of the template particles. The liquid phase affected template growth in that anisotropic grain growth in the matrix prevented the attainment of higher  $f$  in the  $\text{V}_2\text{O}_5$ -containing samples at low template contents ( $\leq 9.1$  wt%) and, hence, caused broader texture distribution ( $r$ ) in [001]. For example, an  $f = 0.56$  and  $r = 0.32$  for the 5 wt%, and  $f = 0.93$  and  $r = 0.24$  for the 15 wt% templates were obtained at 1400°C. However, high quality texture (i.e.,  $f = 0.93$  and  $r = 0.29$ ) was also obtained with only 5 wt% templates

when the matrix grain growth was slowed by adding  $K_2O$  and  $Nb_2O_5$ . In the  $V_2O_5$ -free samples, intrinsic liquid phase formation took place (at  $\sim 1300^\circ C$ ) around each template due to excess  $Nb_2O_5$  present in the template particles. A template content about 9-10 wt% was found to be adequate to reach an  $f = 0.93$  because of the lack of a liquid (and anisotropic grain growth) in the matrix. It was found that the texture distribution widens with increasing template content (e.g.,  $r = 0.29$  for 5 wt% and 0.40 for 15.4 wt% templates) due to the increased template-template interaction (e.g., tangling) during tape casting. When template growth was assisted with a liquid (by adding excess  $Nb_2O_5$  to the matrix), an  $f = 0.98$  was obtained at template content as low as 5 wt%.

Template particles controlled the matrix grain growth and, therefore, crack-free specimens with high density and uniform grain size were fabricated by TGG.

#### 7.1.4 Electrical Properties of Textured $Sr_{x,53}Ba_{1-x}Nb_2O_6$ Ceramics

The dielectric and piezoelectric properties were affected by  $f$ ,  $r$ , and grain boundary phases. It was found that the ferroelectric properties were enhanced in the samples with higher  $f$  and lower  $r$  values. The presence of nonferroelectric phases ( $V_2O_5$  or  $Nb_2O_5$ -based) at the grain boundaries suppressed the observed dielectric properties, especially at the  $T_c$ . Therefore, maximum  $K_{33} = 7,900$  in the  $V_2O_5$ -containing and 23,600 in the  $V_2O_5$ -free samples were obtained, which are low compared to single crystal ( $K_{33} = 81,000$ ).  $T_c$  was found to be higher than that of SBN50 single crystals due to filling of interstitial sites with  $K^+$  ions from the KSN templates and  $V^{5+}$  ions from the liquid phase former. Dielectric spectra showed normal ferroelectric behavior for the  $V_2O_5$ -containing and weak relaxor behavior for the  $V_2O_5$ -free samples.

Polarization fatigue decreased the remanent polarization on successive application of the field in the  $V_2O_5$ -free samples.  $V_2O_5$ -containing samples, however, did not experience any evidence of polarization fatigue, possibly due to a more uniform cation distribution. However, some samples showed aging in the form of “pinched” loops during polarization reversal. This was eliminated by increasing the number of driving field cycle.

The best room temperature electrical properties obtained in the  $c$  (polar) direction for the  $V_2O_5$ -containing samples are a remanent polarization ( $P_r$ ) of  $13.9 \mu\text{C}/\text{cm}^2$ , an estimated saturation polarization ( $P_m$ ) of  $21 \mu\text{C}/\text{cm}^2$  (60-84% of single crystal), and a piezoelectric charge coefficient ( $d_{33}$ ) of  $88 \text{ pC}/\text{N}$  (80-98% of single crystal). For the  $V_2O_5$ -free samples, the maximum values are  $P_r = 20.3 \mu\text{C}/\text{cm}^2$ ,  $P_m = 24 \mu\text{C}/\text{cm}^2$  (69-96% of SBN50 single crystal), and  $d_{33} = 84 \text{ pC}/\text{N}$  (76-93% of SBN50 single crystal).

A model was developed to correlate the processing parameters ( $f$  and  $r$ ) to the polarization. It was found that the  $P_r$  increased sharply (after  $f = 0.5$ ) when the percolation (or charge transfer) between elongated grains was effectively established.

These results indicate that textured ceramics have superior electrical properties than the reported values in SBN ceramic literature (over the whole solid solution range), which makes the TGG approach viable for fabricating ceramics with single crystal-like properties.

## **7.2 FUTURE WORK**

### **7.2.1 Templated Grain Growth**

In this study, it was shown that highly textured specimens showing anisotropic electrical properties were successfully fabricated by TGG. Acicular template particles were aligned by applying a two dimensional shear force (i.e., tape casting). In most cases, this resulted in high texture fraction with some degree of in-plane orientation of template particles. It was found that the resulting electrical properties were strongly related to the texture distribution in the polar direction. Therefore, other methods that impart three dimensional shear force such as extrusion (for the acicular templates) should be applied to orient template particles more efficiently because orientation distribution is very critical for the low symmetry crystals like SBN.

### **7.2.2 Texture Characterization**

The texture evaluations which have been performed on TGG systems so far have been macroscopic, using x-ray rocking curves and the Lotgering factor. In these techniques, hundreds of crystals are analyzed at the same time, resulting in a distribution of grain orientations. These techniques are simple but have some disadvantages. First, the sample size should be rather large (15 x 15 mm), which can be, sometimes, difficult to produce regularly on an experimental basis. Second, only the crystallographic information from a fraction of the depth of the sample is obtained. Therefore, texture characterization from the volume can not be determined. Texture characterization from a SEM-based techniques (i.e., stereological analysis) also give information from the surface. Therefore, other characterization techniques (i.e., neutron diffraction) should be



applied to analyze the volume, rather than only surface. This is important because measured electrical properties are obtained from the bulk samples.

### 7.2.3 Modeling of Electrical Properties

The macroscopic polarization was successfully correlated to the processing parameters by taking polarization and texture distribution functions into account, and plotted as a function of texture fraction. For uniaxial ferroelectrics, the polarization distribution can be expressed as  $P_3 \cdot \cos\theta$ . This function can be modified for other systems (based on symmetry elements and the number of possible polarization directions), and processing-property relation can be established. In particular, it would be intriguing to determine the critical texture fraction for efficient polarization percolation as a function of the number of polarization directions in the ferroelectric.

In Chapters 5 and 6, it was shown that dielectric properties, especially at  $T_c$ , were substantially suppressed due to existence of non-ferroelectric grain boundary phases.  $V_2O_5$ -containing compositions had the lowest dielectric properties. It would be useful to be able to correlate the effect of texture directly with the measured permittivity values. This is complicated by the need to decouple the effect of the grain boundary phases.

The dielectric behavior can be explained by a series mixing theory for diphasic systems [1]. For a sample with a grain boundary phases, it can be shown that

$$1 / K_s = 1 / K_g + 1 / R \cdot K_{gb} \quad (7.1)$$

where  $K_s$  is the dielectric constant of the sample,  $K_g$  is dielectric constant of the SBN grains (equal to the dielectric constant of SBN50 single crystal),  $K_{gb}$  is dielectric constant of grain boundary phases, and  $R$  is the thickness ratio of the grain ( $D_g$ ) to the

grain boundary layer ( $D_{gb}$ ). Figure 7.1 shows that for the TGG samples, the textured grain length is directly proportional to  $f$ . It is seen that the constant of proportionality changes with the template content. As a first approximation, in Eqn. 7.1, it is assumed that  $D_g$  was proportional to  $f$ . Figure 7.2 shows the variation of  $D_{gb} / K_{gb}$  as a function of  $f$  for calculations made using the peak permittivities. It is clearly seen that  $V_2O_5$ -containing samples have higher  $D_{gb} / K_{gb}$ . In addition,  $D_{gb} / K_{gb}$  decreases continuously with increasing  $f$  for each composition, indicating that as the template particles consume the matrix grains, the volume of the grain boundary phase changes due to the elimination of grain boundaries parallel to the electrodes.

This semi-quantitative analysis gives a trend for the effect of grain boundary phases for various compositions. However, additional experiments to determine the thickness and composition of the grain boundary phases by transmission electron microscopy (TEM) should be done. These results could then be used to refine the model, and should allow determination of the dielectric constant of grain boundary phases as a function of temperature.

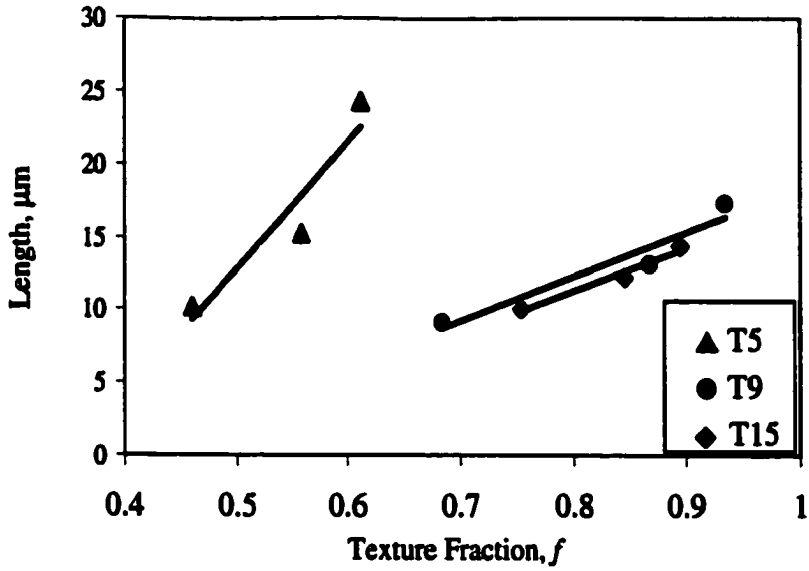


Figure 7.1 Textured grain length (from stereological analysis) vs. texture fraction (from the Lotgering factor).

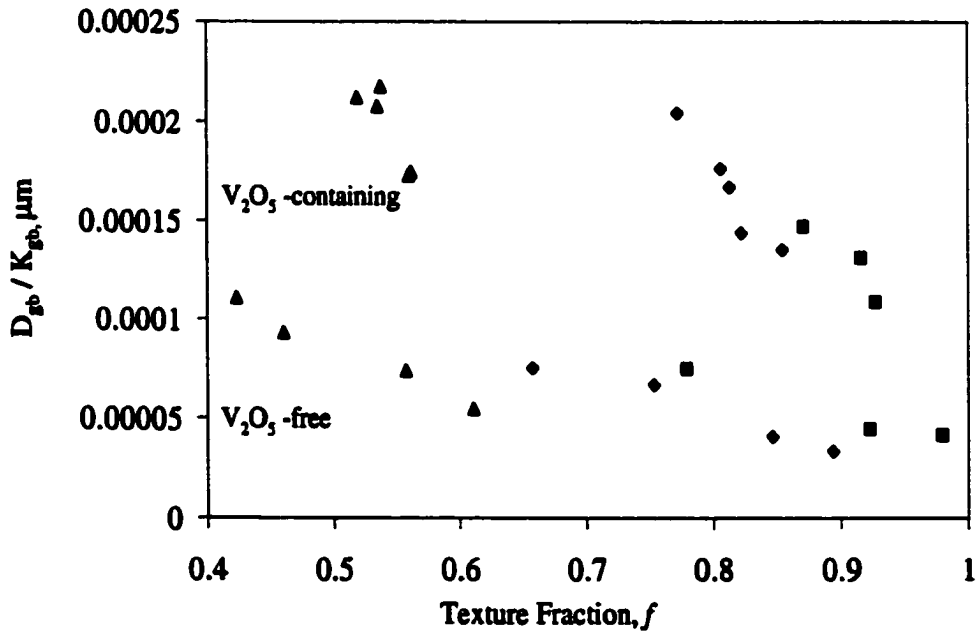


Figure 7.2  $D_{(gb)} / K_{(gb)}$  vs. texture fraction for the  $V_2O_5$ -free and  $V_2O_5$ -containing samples.  $\blacktriangle$ : T5 or TV5,  $\blacklozenge$ : T15 or TV15, and  $\blacksquare$ : T5-15 or TV5-15.

### **7.3 REFERENCES**

- 1- H. C. Wang and W. A. Schulze, "The role of excess MgO or PbO in determining the microstructure and properties of lead magnesium niobate," *J. Am. Ceram. Soc.*, 73, 825-32 (1990)

**APPENDIX A**  
**DETERMINATION OF CORRECTION FACTORS FOR STEREOLOGICAL**  
**ANALYSIS**

Figure 1 shows the coordinate system used for stereological analysis. The template particles (or elongated grains) are considered to be cylindrical in shape with a circular cross-section.  $L$  and  $t$  stand for the length and thickness at any location, respectively. For perfectly oriented template particles, the actual length is equal to the measured length. However, the thickness changes between 0 and  $2r$ , the diameter of the elongated grain.

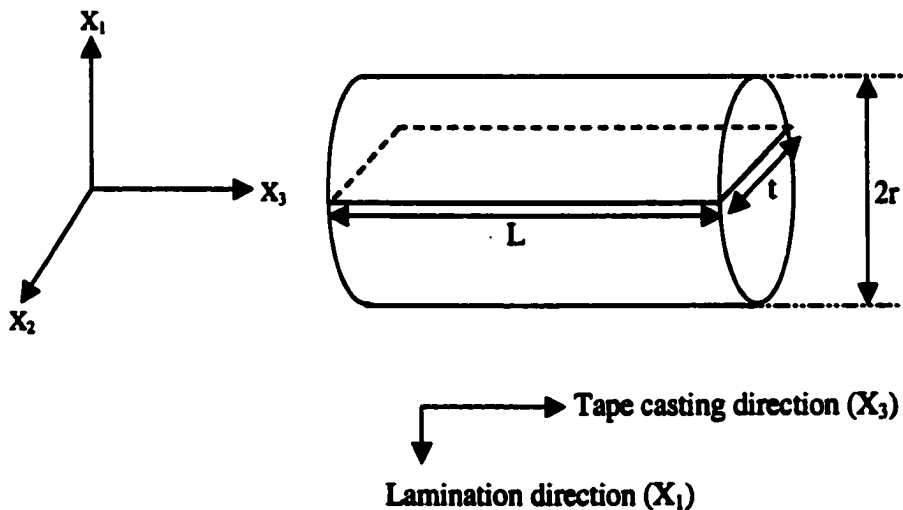


Figure 1. Coordinate system used for stereological analysis.

### **Determination of the Mean Length**

After tape casting, template particles are aligned mainly in the  $X_2$ - $X_3$  plane, making an angle,  $\alpha$ , with the  $X_1$  axis. The lamination process decreases  $\alpha$ . Distribution of elongated grains (namely,  $\alpha$ ) around the  $X_3$  axis is obtained from rocking curves, and the degree of orientation parameter,  $r$ , is obtained using the March-Dollase equation (see Chapter 5 and Appendix B). A correlation between measured and actual lengths, as a function of  $r$ , can be found if the probability of each orientation for elongated grains and the probability of cutting a grain at any particular angle are multiplied by the measured length. The details of this calculation are reported elsewhere [M. Seabaugh, "Texture development in liquid phase sintered alpha alumina via anisotropic template growth," Ph.D. Thesis, The Pennsylvania State University, 1998]. For textured SBN53 ceramics,  $r$  ranges between 0.2 and 0.46. The correction factor calculated for this range is 0.99 and 0.96, respectively. This shows that orientation distribution in the textured SBN53 ceramics is mainly due to in-plane (i.e., in the  $X_2$ - $X_3$  plane) orientation of elongated grains because the measured and actual lengths are very close to each other.

### **Determination of the Mean Thickness**

After polishing the sample, the measured mean thickness in the  $X_2$ - $X_3$  plane,  $[t]$ , can vary between 0 and  $2r$ . Therefore, the thickness,  $t$ , at any location can be given as  $2r \sin\theta$ , where  $\theta$  ranges from 0 to  $\pi$  (Figure 2).

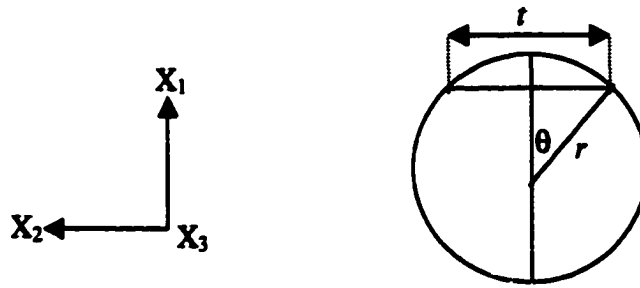


**Figure 2. Cross-sectional view of elongated grains.**

**The mean thickness,  $[t]$ , can be calculated by taking the integral over all possible angles:**

$$[t] = \int_0^{\pi} 2r \cdot \sin\theta \cdot d\theta / \int_0^{\pi} d\theta = 4r/\pi$$

**Therefore, the measured thickness (i.e.,  $[t]$ ) is multiplied with  $\pi/4$  to find the actual thickness because variation in the thickness is directly proportional to that in the radius.**

## APPENDIX B

### AN EQUATION TO MODEL THE CORRELATION BETWEEN THE ELECTRICAL PROPERTIES AND PROCESSING PARAMETERS

(Sr,Ba)Nb<sub>2</sub>O<sub>6</sub> (SBN) single crystals have the prototypic point group *4/mmm* and the ferroelectric phase transition is from *4/mmm* (tetragonal) to *4mm* (tetragonal). There exists only one unique fourfold axis and non-180° domain walls are absent [1,2]. Grain-oriented samples possess axisymmetric (i.e., fiber) texture and belong to the Curie group *∞/mm* (when unpoled) and *∞m* (upon poling) symmetry. In the *∞m* symmetry, the ∞-fold axis is along the X<sub>3</sub> (or *c*) direction and *m* is parallel to the X<sub>3</sub>. SBN has a spontaneous polarization only in the *c* direction, that is, P<sub>1</sub> = P<sub>2</sub> = 0 and P<sub>3</sub> ≠ 0 (i.e., average spontaneous polarization is 27.4 μC/cm<sup>2</sup> for SBN50 single crystal). Therefore, for misoriented grains, the polarization distribution can be expressed as P<sub>3</sub>·cosα, where α is the angle from the texture axis (Figure 1).

The orientation distribution in the *c* direction can be calculated from the March-Dollase equation [3,4]:

$$Q(f,r,\alpha) = f (r^2 \cos^2 \alpha + r^{-1} \sin^2 \alpha)^{-3/2} + (1-f)$$

where *f* is the texture fraction and *r* is the degree of orientation. The March-Dollase equation is simulated in Figure 2 for the random sample (i.e., *r* = 1 and *f* = 0) and a single crystal (or fully textured sample) (i.e., *r* = 0 and *f* = 1). In a random orientation distribution, the volume of material oriented at an angle α changes as sinα [5-8]. Therefore, Q(*f,r,α*) can be multiplied by the sine function to determine the fraction of



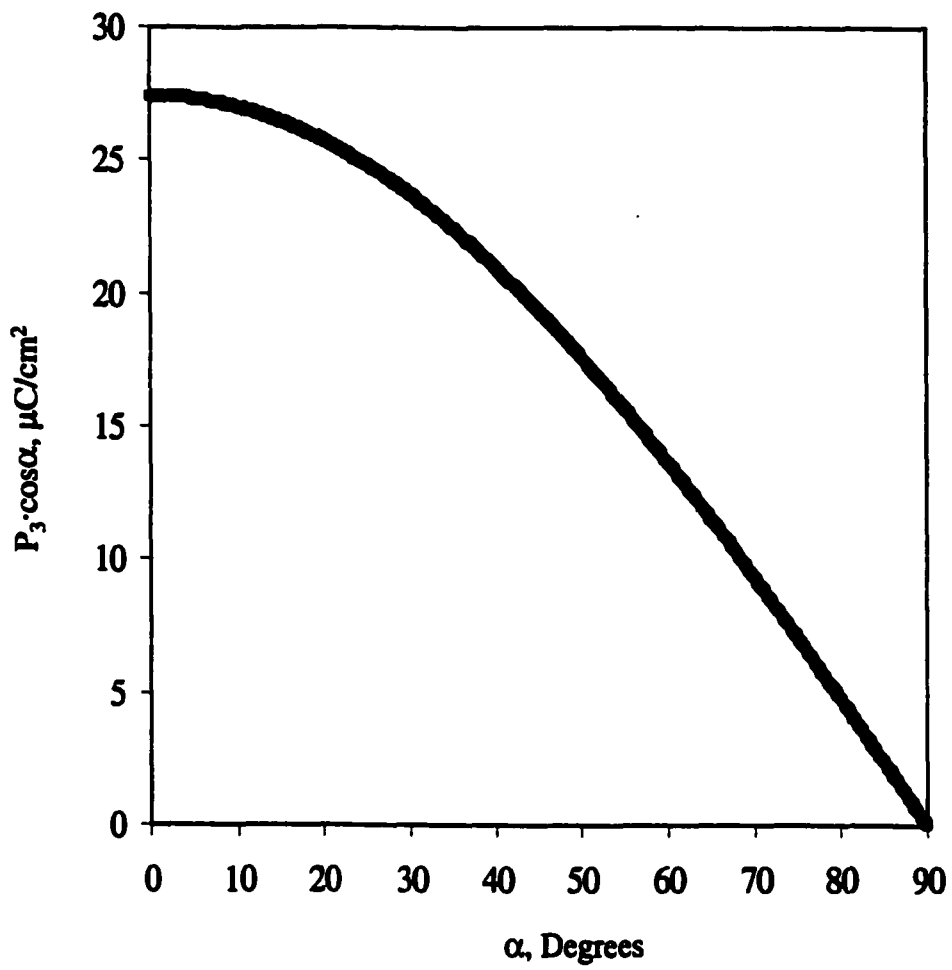


**Figure 1 Polarization distribution for SBN50 single crystal as a function of the angle,  $\alpha$ , from the  $c$  direction.**

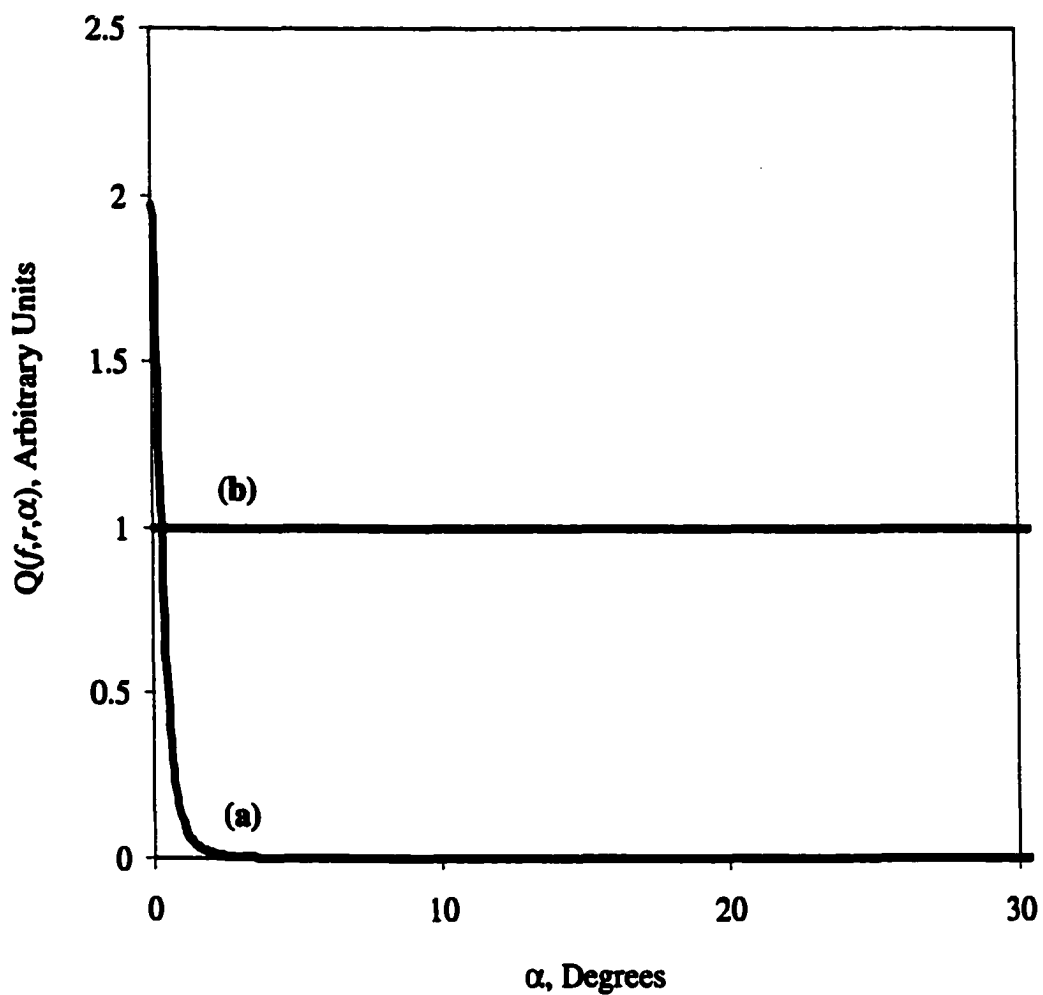


**Figure 2** The March-Dollase equation (i.e.,  $Q(f,r,\alpha)$ ) for; (a) single crystal or fully textured sample ( $r = 0$  and  $f = 1$ ) and (b) random sample ( $r = 1$  and  $f = 0$ ).

material as a function of  $\alpha$ . The normalization condition, that is,  $Q(f,r,\alpha) \cdot \sin\alpha$  ( $\alpha \rightarrow 0$  to  $\pi/2$ ) is simulated in Figure 3 for the random sample and a single crystal (or fully textured sample).

The polarization at any angle can be found by multiplying the polarization distribution function with the normalized March-Dollase function, and taking the integral from the limits 0 to  $\pi/2$ :

$$P(r,f) = \int_0^{\pi/2} P_3 \cdot \cos\alpha [Q(f,r,\alpha) \cdot \sin\alpha] d\alpha$$

This equation calculates the maximum expected polarization as a function of experimentally determined  $r$  and  $f$  values. It is simulated in Figure 4 for the random sample and single crystal (or fully textured sample). The area under the curve gives  $27.4 \mu\text{C}/\text{cm}^2$  for the single crystal (Fig. 3a) and  $13.7 \mu\text{C}/\text{cm}^2$  for the random sample (Fig. 3b). Note that for the random orientation case, the maximum polarization is  $13.7 \mu\text{C}/\text{cm}^2$  (i.e.,  $P_3/2$ ), which is consistent with the theoretical calculation for random polarization, using Euler's angles in 3 dimensions when *only*  $180^\circ$  domain switching takes place [9].

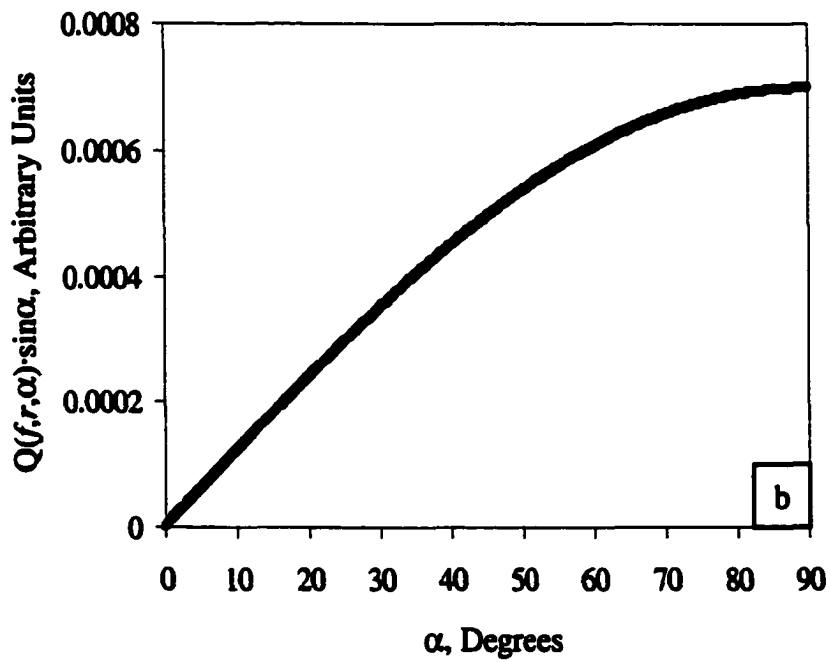
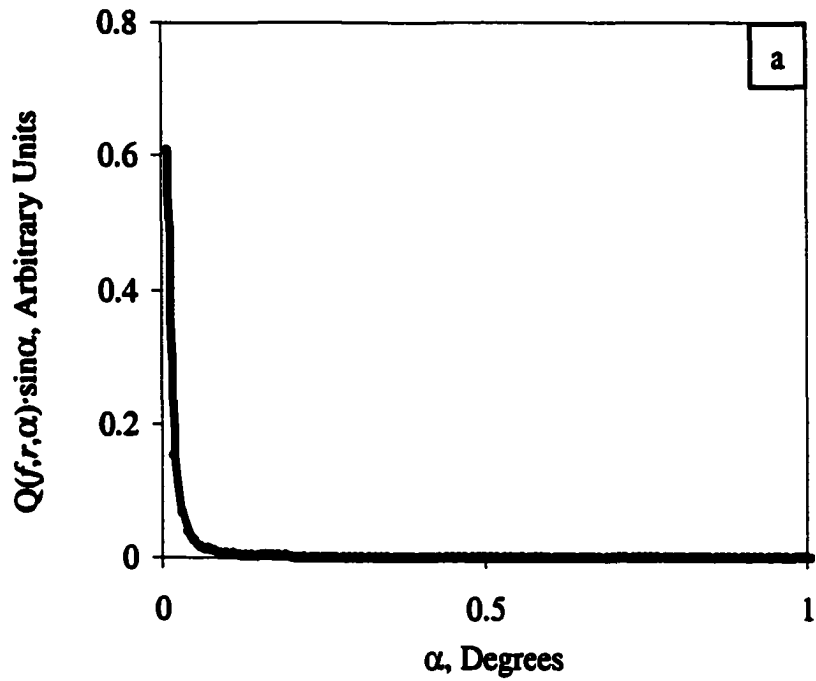


Figure 3 Normalized March-Dollase equation (i.e.,  $Q(f,r,\alpha) \cdot \sin\alpha$ ) for; (a) single crystal or fully textured sample ( $r = 0$  and  $f = 1$ ) and (b) random sample ( $r = 1$  and  $f = 0$ ).

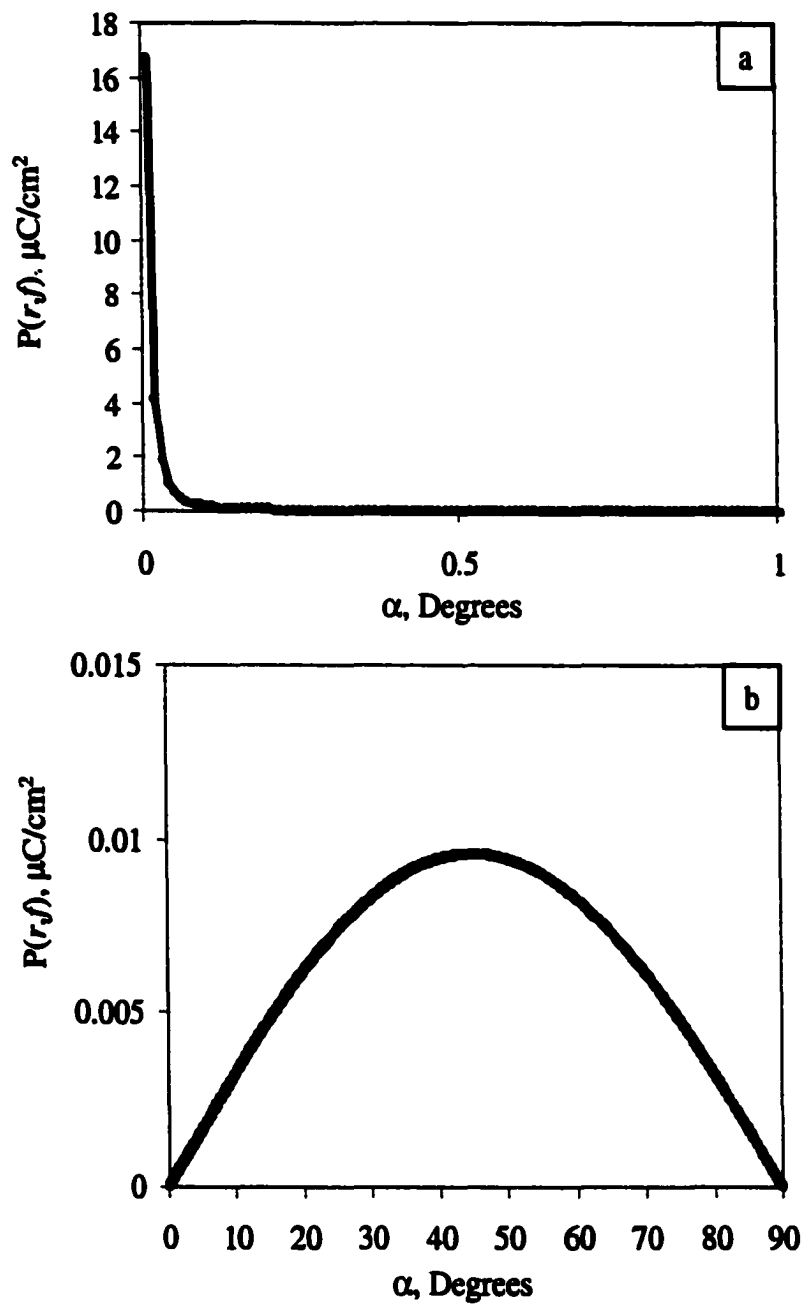


Figure 4 Polarization distribution (i.e.,  $P(r,f)$ ) as a function of misorientation angle; (a) single crystal or fully textured sample ( $r = 0$  and  $f = 1$ ) and (b) random sample ( $r = 1$  and  $f = 0$ ).

## REFERENCES

- 1- R. R. Neurgaonkar, J. R. Oliver, W. K. Cory, L. E. Cross, and D. Viehland, "Piezoelectricity in tungsten bronze crystals," *Ferroelectrics*, 160, 265-76 (1994)
- 2 - R. R. Neurgaonkar, W. K. Cory, J. R. Oliver, E. J. Sharp, G. L. Wood, G. J. Salamo, "Growth and optical properties of ferroelectric tungsten bronze crystals," *Ferroelectrics*, 142, 167-88 (1993)
- 3 - A. March, "Mathematische theorie der regelung nach der korgestalt bei affiner deformation," *Z. Kristallogr.*, 81, 285-297 (1932)
- 4 - W. A. Dollase, "Correction of intensities for preferred orientation in powder diffractometry: Application of the March model," *J. Appl. Cryst.*, 19, 267-72 (1986)
- 5 - M. M. Seabaugh, M. D. Vaudin, J. P. Cline, and G. L. Messing, "Comparison of texture analysis techniques for highly oriented  $\alpha$ -Al<sub>2</sub>O<sub>3</sub>," *J. Am. Ceram. Soc.*, 83[8], 2049-54 (2000)
- 6 - J. E. Blendell, M. D. Vaudin, and E. R. Fuller, Jr., "Determination of texture from individual grain orientation measurements," *J. Am. Ceram. Soc.*, 82[11], 3217-20 (1999)
- 7- A. Böcker, H. G. Brokmeier, and H. J. Bunge, "Determination of preferred orientation in textured Al<sub>2</sub>O<sub>3</sub> ceramics," *J. Eur. Ceram. Soc.*, 8, 187-94 (1991)
- 8- M. S. Sandlin, F. Lee, and K. J. Bowman, "Simple geometric model for assessing whisker orientation in axisymmetric SiC-whisker-reinforced composites," *J. Am. Ceram. Soc.*, 75[6], 1522-28 (1992)
- 9 - T. Takenaka and K. Sakata, "Grain orientation and electrical properties of hot-forged Bi<sub>4</sub>Ti<sub>3</sub>O<sub>12</sub> ceramics," *Jpn. J. Appl. Phys.*, 19[1], 31-39 (1980)

## **VITA**

### **Cihangir Duran**

**Cihangir Duran was born September 30, 1971 in Konya, Turkey. He obtained his B.Sc. in Metallurgical Engineering at the Middle East Technical University in 1994. After graduation, he joined the graduate program in Materials Science and Engineering at the Gebze Institute of Technology in 1994, and obtained his M.Sc. in May 1996. Mr. Duran received a Higher Educational Council Scholarship from Turkish Government, and began his attendance in Materials Science and Engineering at the Pennsylvania State University in August 1996. He has since been working towards his Ph.D. He will be employed as an assistant professor at the Gebze Institute of Technology in Turkey.**

